UNIVERSITÄT HAMBURG
DEPARTMENT PHYSIK

The Magnetic Fine Structure of Thin-Film Elements

Dissertation
zur Erlangung des Doktorgrades
des Department Physik
der Universität Hamburg

vorgelegt von
Sebastian Hankemeier
aus Lemgo

Hamburg
2010

Gutachter der Dissertation:	Prof. Dr. Hans Peter Oepen *Universität Hamburg, Germany* PD Dr. Rolf Allenspach *IBM Rüschlikon & ETH Zürich, Switzerland* Dr. Daniel T. Pierce *National Institute of Standards and Technology, USA*
Gutachter der Disputation:	Prof. Dr. Hans Peter Oepen *Universität Hamburg, Germany* Prof. Dr. Andreas Schreyer *Helmholtz-Zentrum Geesthacht, Germany*
Datum der Disputation:	22. Oktober 2010
Vorsitzender des Prüfungsausschusses:	Prof. Dr. Alexander Lichtenstein
Vorsitzender des Promotionsausschusses:	Prof. Dr. Jochen Bartels
Dekan der Fakultät für Mathematik, Informatik und Naturwissenschaften:	Prof. Dr. Heinrich Graener

Abstract

In this thesis the magnetic fine-structure of thin films and patterned soft-magnetic thin-film elements is investigated via Scanning Electron microscopy with Polarization Analysis (SEMPA) and magnetotransport measurements. Such small ferromagnets display a variety of domain configurations which strongly depend on their exact geometry and magnetic history.

Fife topics are discussed in this thesis. They are in particular:

- **The characteristics of our newly designed scanning electron microscope with polarization analysis (SEMPA or Spin-SEM) for the acquisition of magnetic images.** Optimization of the instrument, long time stability of the detector, sample preparation, details of the data analyzing process and the newly installed cryostat are discussed.

- **The evolution of the magnetic domain pattern in temperature driven spin-reorientation transition in $NdCo_5$ thin films.** A reversible transformation of the domain pattern is observed and the ratio K_1/K_2 was obtained from the images of the domain evolution.

- **The magnetic fine-structure of single (sub)micron-sized permalloy rectangles with a thickness of 20 nm and an aspect ratio of 2:1 is investigated with SEMPA and magnetotransport measurements.** The focus is on the influence of magnetostatic coupling in arrays of rectangles and the influence of the magnetic history on the actual domain configuration. The magnetic fine-structure of the Landau state is found to be strongly sensitive to stray fields. The energy density of micromagnetic states is obtained from anisotropic magnetoresistance hysteresis loops.

- **The seeding of domain walls in soft magnetic nanowires.** The predominant domain wall configuration in dependence on the geometry of the nanowires and the orientation of the (domain wall) seeding field is investigated. A method for the deliberate tuning of domain wall properties is presented.

- **The manipulation of aforementioned domain walls via (spin-polarized) currents.** The transformation of a domain wall was observed via SEMPA and the magnetotransport technique was utilized to investigate the magnetically switching of nanowires caused by external fields and supported by electrical currents. A separation of the influence of Oersted-field, temperature and spin-torque effects on the switching behavior is realized.

The experimental investigations via imaging techniques (SEMPA) and integrative methods (magnetotransport) are numerically supported and quantified with micromagnetic simulations.

Kurzzusammenfassung

Im Rahmen dieser Doktorarbeit wurde die magnetische Feinstruktur von dünnen Filmen und Dünnschichtelementen sowohl mit Rasterelektronenmikroskopie mit Polarisationsanalyse als auch mit Magnetotransportmessungen untersucht. Weichmagnetische mikrometergroße Ferromagnete zeigen eine Vielzahl von Domänenkonfigurationen welche stark von der exakten Geometrie und der magnetischen Geschichte abhängen.

Im Einzelnen wird in dieser Arbeit über fünf Themen berichtet:

- **Die Eigenschaften unseres neu entwickelten Rasterelektronemikroskops mit Polarisationsanalyse (SEMPA oder Spin-SEM) für die Aufnahme von magnetischen Bildern.** Optimierung des Instruments, Langzeitstabilität des Detektors, Probenvorbereitung, Datenanalyse und der neu installierte Kryostat werden diskutiert.

- **Die Entwicklung des magnetischen Domänenmusters während des temperaturgetriebenen Spin-Reorientierungsübergangs in dünnen $NdCo_5$ Filmen.** Ein reversibles Domänenmuster wird beobachtet und das Verhältnis K_1/K_2 wurde aus den Bildern der Domänenentwicklung bestimmt.

- **Die magnetische Feinstruktur einzelner (sub) mikrometergroßer Permalloy Rechtecke mit einer Dicke von 20 nm und einem Seitenverhältnis von 2:1 wird mit SEMPA und Magnetotransportmessungen untersucht.** Der Schwerpunkt liegt auf dem Einfluss der magnetostatischen Kopplung in Gittern von Rechtecken und dem Einfluss der magnetischen Geschichte auf die tatsächliche Domänenkonfiguration. Die magnetische Feinstruktur der Landauzustandes erweist sich als hochempfindlich auf magnetostatische Streufelder. Die Energiedichte von bestimmten mikromagnetischen Zuständen wurde aus Hystereseschleifen unter Zuhilfenahme des anisotropen Magnetowiderstandes bestimmt.

- **Das Einsähen von Domänenwänden in weichmagnetischen Nanodrähten.** Die vorherrschende Domänenwandkonfiguration wird in Abhängigkeit von der Nanodrahtgeometrie und der Orientierung des externen Feld untersucht. Ein Verfahren für die absichtliche Veränderung von Domänenwandeigenschaften wird vorgestellt.

- **Die Manipulation der vorhergenannten Domänenwände durch (spinpolarisierte) Ströme.** Die Umwandlung von Domänenwänden wurde mit SEMPA beobachtet und Magnetotransportmessungen werden genutzt um das magnetische Schalten von Nanodrähten, hervorgerufen durch äußere Felder und unterstützt durch elektrische Ströme, zu untersuchen. Eine Trennung der von Oersted-Feld, Temperatur- und Spin-Torque-Einflüsse auf das Schaltverhalten ist realisiert worden.

Die experimentellen Untersuchungen mit bildgebenden Verfahren (SEMPA) und integrative Methoden (Magnetotransport) werden numerisch unterstützt und quantifiziert unter Zuhilfenahme mikromagnetischer Simulationen.

Contents

1. Introduction

I must have been around ten years old when my parents got our first personal computer. It had a harddisk with a typical capacity of 250 MB and I was confident that the available space would last more or less forever. Well, the 250 MB did not last very long. As next generation harddrives were available for reasonable prices, we usually bought one and stored useful and not so useful data on them, causing the next generation harddrive being soon too small. I believe everyone who reads these sentences had a similar experience, properly with different numbers (probably smaller, in case of the reviewers).

When new technologies become available to improve things, it will be done and when it is done, people will use them in one or the other way. I do not know why this is so, but it seems to be a general law that the pursuit of improvement and a childlike curiosity, especially in the scientific community, is an important motivation for advance. It has something of the olympic motto "altius, citius, fortius" [Did24] (higher, faster, stronger).

Classical examples for this trend in the field of technology are Moore's law [Moo65] which predicts the exponential improvement of computing hardware, or Kryder's law [Kry09] for the growth of storage capacity. A fundamental article on the development of data storage concepts is probably R. P. Feynmans famous publication "There is plenty of room at the bottom" [Fey60] where he asks "Why cannot we write the entire 24 volumes of the Encyclopedia Brittanica on the head of a pin?" and proposes some ideas to do this in the future. Today we can write huge amounts of data in very small space, although "The entire 24 volumes of the Encyclopedia Brittanica" would still need $\approx(1.0\text{ cm})^2$ of space with nowadays available consumer technology at an area density of $\approx$300 Gbits/in^2 [Hit10b]. But there is still plenty of room at the bottom as magnetically stored bits are theoretically stable in FePt dots at densities approaching 100 Tbits/in^2 [Kry09].

Furthermore, different alternative technologies have been proposed for the succession of harddrives, as the improvement of harddisks is restricted by the superparamagnetic limit, which is probably reached in the year 2020 [Kry09]. Among these technological concepts for future nonvolatile memory devices is the magnetic RAM (M-RAM) [Gal97, Eng05], the racetrack memory [Par08, Hay08a], spin-transfer-torque RAM [Hos06], single electron memory [Guo97] and the vortex RAM (V-RAM) concept [Boh08]. In this context, the magnetic fine structure of patterned micro-/nano-elements as discussed in this thesis is of fundamental interest, as harddrive technology as well as some of the proposed succession technologies are based on magnetics. They are limited by the decrease of bit stability with shrinking dimensions. For the improvement of such technologies a precise knowledge about details of the actual domain configuration of real world microstructures and their possible magnetostatic interaction is of great importance.

A strongly related field to the aforementioned storage technology is the young field of spintronics [Wol06, Cow07], also connected to this work. Spintronic or spin-electronic means that not only the electric charge is utilized for data processing and storage, but also the spin of the electron is employed herein. When the aim is to use the electron spin for data processing, magnetic nanowires containing domain walls come into play [All06]. These magnetic structures are the topic of chapter five: The influence and different effects of electrical currents on certain types of domain walls and the reason for domain wall transformations are investigated.

Even while not considering potential applications in the first place, there is always a pleasure in finding things out [Fey88]. For example the exciting domain evolution during the temperature driven spin-reorientation transition in $NdCo_5$ thin films in chapter three, which reveals some unexpected domain patterns.

In this thesis the magnetic fine structures of thin films and patterned elements are investigated chiefly with the Scanning Electron Microscope with Polarization Analysis (SEMPA or spin-SEM) [Ung86, Koi87, All90, Oep91]. The second experimental technique utilized are magnetotransport measurements. The former gives direct access to a real space map of the surface magnetization while the latter is an integrative method, which not necessarily yields a distinct result regarding the exact domain configuration. The interpretation of magnetotransport measurements has to be confirmed by SEMPA measurements or supported by numerical simulations. This is done in chapters four and five where the advantages of all three techniques are combined to investigate the global picture of a micromagnetic situation.

The thesis is structured as follows: Chapter two deals with a detailed discussion of our SEMPA experiment and in particular with the properties of the spindetector. Two publications are integrated in chapter two which deal with certain topics in the context. The articles are merged with the text via an introduction. Comments as well as additional information are given in the context. The procedure of implementing articles into the thesis is followed throughout the other chapters, but always a classification of the results is given as well as a comment on my contribution to the work.

In chapter three the aforementioned SEMPA investigation of the temperature driven spin-reorientation transition in $NdCo_5$ thin films is presented. Chapter four discusses the magnetic fine structure of soft magnetic rectangles and V-shaped nanowires. In case of the rectangles, strong influence of magnetostatic coupling is observed, which may have consequences for magnetic storage devices. It is shown that the domain wall properties in V-shaped nanowires can be purposely manipulated which provides a possible application for e.g. V-RAM modules [Boh08].

The last chapter discusses the manipulation of domain walls in aforementioned V-shaped nanowires via external magnetic fields supported by ultra-high static current densities, which gives new insights into the spin transfer torque effect and may affect the development of the racetrack memory concept [Par08, Hay08a].

The SEMPA technique, however, is the central investigation technique which connects all parts of the thesis. An example of the unique possibilities of SEMPA can be seen in Fig. 1.1. Many aspects of the physics of micromagnetism and the features of SEMPA become apparent in this single measurement: The magnetization map in (a) shows the configuration of a cross-tie wall which consists of a sequence of

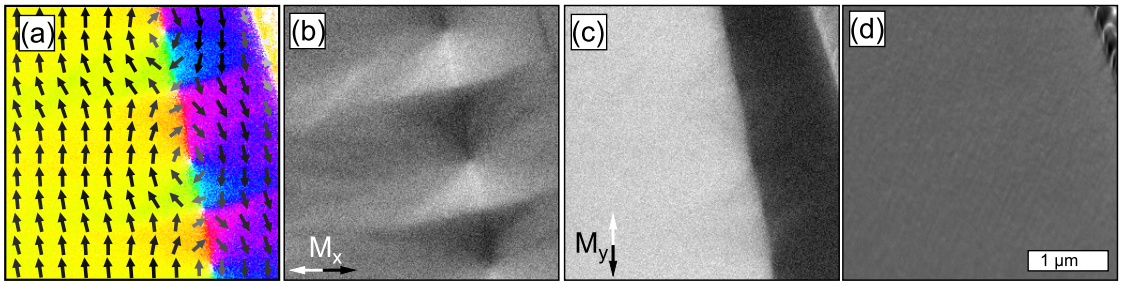

Figure 1.1.: SEMPA image of a cross-tie wall in a soft magnetic thin film. (a) displays the magnetization map. (b) and (c) show the two components of the in-plane magnetization and (d) displays the simultaneously acquired SEM image.

vortices and anti-vortices, which belong to the most interesting structures in micromagnetism [Her07]. Energy minimization is realized in this structure via the distribution of exchange energy and volume charges over a large area (b), several microns away from the actual domain wall, which is best visible in (c). The simultaneously acquired SEM image (d) shows the uniformly illuminated thin film. In the top right corner, the film has been removed via focused ion beam milling. In this area the magnetic signal vanishes, visible as white region in (a) but superimposed by some geometrical edge contrast. The magnetization in the vicinity of this region aligns parallel to the edge due to minimization of surface charges.

The image illustrates that a single SEMPA measurement can open the door to the whole world of micromagnetism and surface physics to an interested mind and the following chapter will show that SEMPA is an excellent tool for the investigation of "The magnetic fine structure of thin-film elements".

2. SEMPA: Scanning Electron Microscopy with Polarization Analysis

Many different techniques for the observation of the magnetic microstructure are nowadays used to investigate micro- and nano-magnetism. The most prominent methods are Lorentz microscopy [Cha84], X-ray PhotoEmission Electron Microscopy (X-PEEM) [Möl63, Stö93], Magneto-Optical-Kerr-Effect (MOKE) microscopy [Fel67, Hub86], magnetic x-ray holography [Eis04, Eis08, Sti10], the Bitter technique [1] [Bit32], Magnetic Force Microscopy (MFM) [Mar87, Har91], Spin Polarized Scanning Tunneling Microscopy (SP-STM) [Wie94] and Scanning Electron Microscopy with Polarization Analysis (SEMPA) [Kir84]. An overview of the different imaging techniques and a detailed discussion of their individual advantages and disadvantages can be found for example in [Hub98, Oep05, Haw10].

Throughout this thesis, all experimental investigations of magnetic microstructures are performed with the SEMPA technique. The development of SEMPA was triggered by the investigation of the spin polarization of secondary electrons in 1982 [Cel82, Kir84] and the idea to use this effect in a microscope to image magnetic structures emerged. The first experimental setup for imaging the sample magnetization was then realized by Koike et al. in 1984 [Koi84]. Since then, SEMPA or spin-SEM has been established as a high resolution technique for the direct observation of magnetic microstructures.

An advantage of SEMPA is that a high spatial resolution of approx. 10 nm [Koh, Kon04] is combined with the full quantitative information of the in-plane[2] magnetization orientation accessible with a small error of only $\pm 1\%$. The high surface sensitivity of the method makes ultrahigh vacuum conditions mandatory, which put some restrictions on samples and handling. For the acquisition of a single high quality image, a measurement time of around 15 min is necessary which sets some limitations to a time resolving approach. Imaging in external fields to observe e.g. the hysteresis of a nano-particle is only feasible with the limitation of a weak magnetic field which in addition must be strongly localized [Ste02]. Within this limitations, SEMPA gives direct real space access to the surface magnetization ori-

[1] The Bitter technique was the first method for domain observation and further improved over the years. Nowadays it is sometimes called high-resolution Bitter SEM (HRBS) method. A spatial resolution better 50 nm can be achieved [Kit96] with small magnetic particles, 15-30 nm in size [Sha06].

[2] With our detector the two components of the in-plane magnetization are accessible. Detectors with a 90° deflector for the SE give one in-plane component and the out-of-plane component of the magnetization [Fed81].

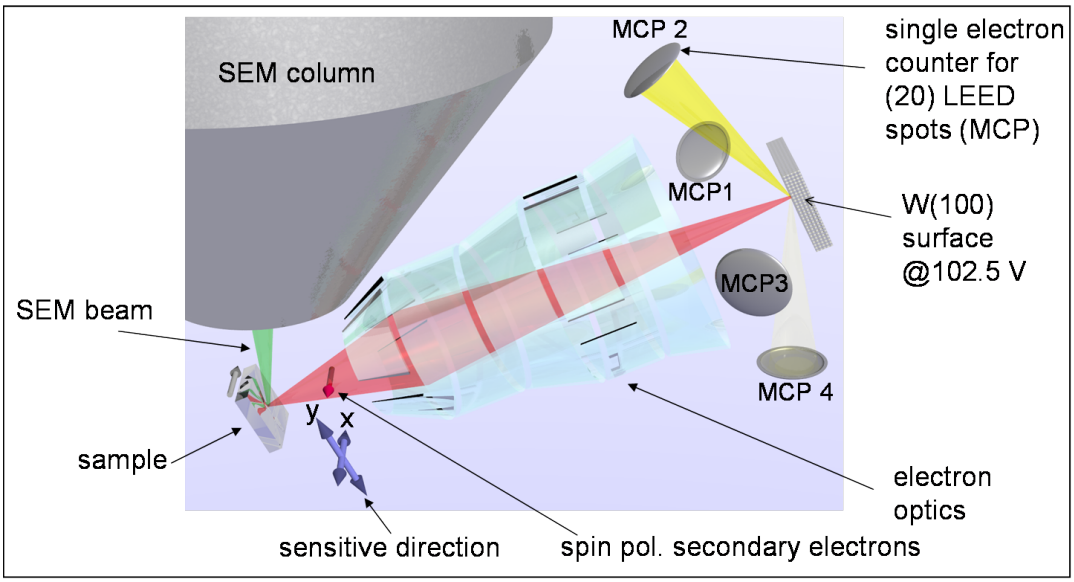

Figure 2.1.: Schematic of the LEED scattering process of the spin polarized secondary electrons (red beam) at the (100) surface of a tungsten single crystal. The yellow cones illustrate the intensities of the (2,0) beams in case the sample is magnetized as indicated by the gray arrow.

entation of ferromagnetic materials. Furthermore, a standard SEM contrast image is acquired simultaneously with the magnetic images, allowing the direct correlation of magnetic structure and topography.

In the following section an introduction to the principle of operation is given, together with an overview of the necessary data analysis. A detailed investigation of the detector's energy filtering properties and its efficiency is following. After that, the long time stability of the detection process in dependence of hydrogen contamination is presented followed by a discussion about sample preparation. The last part of the chapter deals with the calibration and the properties of the newly installed cryostat component for sample cooling.

2.1. Introduction to the principle of operation

In Fig. 2.1 a schematic sketch of the principle of operation of the SEMPA technique is shown. A scanning electron microscope (SEM) [Rus31, Rei88] column creates the primary electron beam which scans over the surface. At the position where the primary beam hits a ferromagnetic sample, spin polarized secondary electrons (SE) are created. The SE originate from the topmost 1-2 nm of the surface due to the short mean free path of electrons within a metal [Sea79] which is the reason for the high surface sensitivity of the SEMPA technique. The SE are guided via the electron optics into the key element, the spin detector. The angle between primary electron beam and sample is 64°, thus allowing normal take-off geometry for the detector optics to have the same coordinate system for the sample magnetization and polarization vectors of the SE. The whole trick about SEMPA is now to detect

these polarization vectors by a preferably simple and efficient approach. Three different basic detector types for polarization analysis have been developed over the last years: The Mott- [Koi84], LEDS [Sch89a] and LEED [Kir84, Oep91] detector. All have in common a very low efficiency compared to a mere intensity measurement, which means that it takes roughly 10^4 times longer to acquire a polarization measurement than an intensity measurement of the SE with identical statistics [Sch90]. Furthermore, compared to a Faraday cup [Bro56] used for electron counting, they exhibit a very high level of complexity.

In the following, the LEED spin detector is discussed which utilizes low energy electron diffraction of the SE at a W(100) surface for polarization analysis: In case the magnetization at the sample surface points along the x-direction (gray arrow, Fig. 2.1), the magnetic moment of the SE points also in the x-direction. As the magnetic moment of the electron is defined as $\mu_\mathrm{S} = -g_\mathrm{s}\mu_\mathrm{B}\frac{\vec{S}}{\hbar}$ the spin $\vec{S}$ is antiparallel[1] aligned to the magnetization of the sample (red arrow, Fig. 2.1).

The quantum mechanical observable "spin" is associated with the spin operator $\mathbf{S} = (S_x, S_y, S_z) = \frac{\hbar}{2}\boldsymbol{\sigma}$, where $\boldsymbol{\sigma}$ are the Pauli spin matrices which are unitary and self-adjunct [Kir85b](p6). The spin operator satisfies the commutation rules $S_xS_y - S_yS_x = -i\hbar S_z$ and cyclic.

General spin states of, for example a beam of electrons along the z-axis with partial or complete alignment of the projection of the spin along the x-axis can be characterized by the spin function χ with complex coefficients a_1 and a_2:

$$\chi = a_1|\alpha\rangle + a_2|\beta\rangle = a_1\begin{pmatrix}1\\0\end{pmatrix} + a_2\begin{pmatrix}0\\1\end{pmatrix}, \tag{2.1}$$

$|\alpha\rangle$ and $|\beta\rangle$ are eigenfunctions of σ_x with eigenvalues ± 1 of the Pauli spin matrices $\boldsymbol{\sigma} = (\sigma_\mathrm{x}, \sigma_\mathrm{y}, \sigma_\mathrm{z})$. The probability to find the value $+\hbar/2$ or $-\hbar/2$ with respect to the x-axis in a measurement is given by the squares $|a_1|^2$ and $|a_2|^2$. The polarization vector is then defined by the expectation value of the spin operator $\boldsymbol{\sigma}$:

$$P_x = \frac{\langle\chi|\sigma_x|\chi\rangle}{\langle\chi|\chi\rangle} = \frac{|a_1|^2 - |a_2|^2}{|a_1|^2 + |a_2|^2} \tag{2.2}$$

The degree of polarization P_x of a beam of electrons polarized along the x-axis is then:

$$P_x = \frac{N_\rightarrow - N_\leftarrow}{N_\rightarrow + N_\leftarrow}, \tag{2.3}$$

where $N_\rightarrow$ and $N_\leftarrow$ are the numbers of electrons with spin parallel and antiparallel to the x-axis.

Such a spin polarized beam of the SE impinges upon the W(100) surface at normal incidence with an average electron energy of $E = 104.5$ eV. From the generated LEED pattern, the (2,0) beams are utilized for the spin detection process. The intensity of each diffracted (2,0) beam is sensitive to the degree of spin polarization

[1] The spin polarization of the sample conduction band is not exactly reproduced by the SE, as one might expect, but the SE with very low energy have a three times higher degree of polarization [Hop83]. The increase of spin polarization can be interpreted in terms of different mean free paths of spin-up and spin-down electrons in the sample [Pen85].

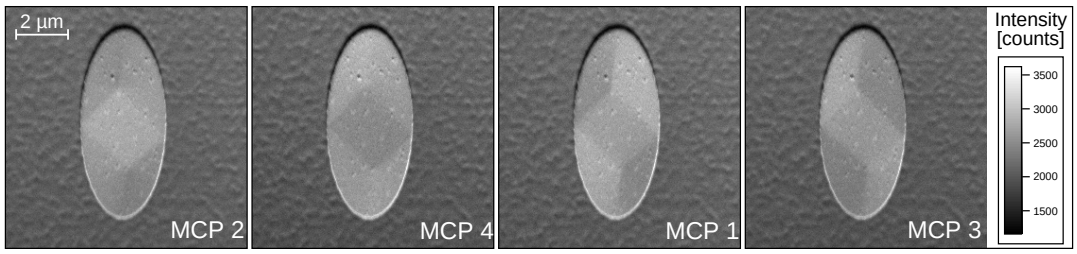

Figure 2.2.: Raw data from the individual detector channels MCP 1 - MCP 4, acquired by imaging a Permalloy ellipse on a silicon wafer. The intermixing of the spin-contrast (areas within the ellipse) and SEM contrast (fabrication defects) is visible.

in the direction orthogonal to its scattering plane [Kir85b](p66). The degree of polarization P along this axis, the sensitivity $S(E)$ of the spin dependent scattering process and the energy dependent reflectivity $R(E)$ specify the (2,0) beam intensities. The intensity of each diffracted electron beam is amplified by a double stack multi channel plate device (MCP) for single electron counting and detected via an anode plate. The assembly generates a nanosecond voltage pulse with an amplitude of some ten mV per incoming electron which is then further processed. In the following, the four single electron detector channels are referred to as "MCP 1" to "MCP 4".

For the situation sketched in Fig. 2.1 the (2,0) beam intensity in channel MCP 2 is given by:

$$I_{(2,0)} = I_0 \cdot R(E)\,[1 + P \cdot S(E)] \tag{2.4}$$

and the intensity of the opposite $(\overline{2},0)$ beam (MCP 4) is

$$I_{(\overline{2},0)} = I_0 \cdot R(E)\,[1 - P \cdot S(E)]\,, \tag{2.5}$$

where I_0 is the intensity and P the degree of polarization perpendicular to the scattering plane of the primary electron beam. The reflectivity is defined as $R = I_{(2,0)}/I_0$ for an unpolarized primary beam of intensity I_0 [Kir85b](p67). $R(E)$ and $S(E)$ are experimentally obtained curves [Fed81] and for the scattering energy utilized here (104.5 V), their values are $R = 0.11$ % and $S = 27$ %. The only difference between Eqs. 2.4 and 2.5 is the sign change within the brackets which comes from the fact that the normal to the scattering plane changes its direction, thus inverting the contrast in respect to a non-polarized incident beam [Kir85b](p65).

In brief, a sample magnetization pointing along the x-direction increases the MCP 2 intensity compared to an unpolarized SE beam. The MCP 4 intensity is then reduced by the same amount as the MCP 2 intensity is enhanced. With the intensity map of MCP 2 or MCP 4 it is then possible to derive the x-component of the magnetization of the sample in case I_0 is constant throughout an acquired image.

According to Eqs. 2.4 and 2.5 the intensities of the diffracted beams are proportional to the total number of electrons entering the spin detector (I_0). Thus the intensity variation due to the spin detection process is superimposed by an intensity variation at different positions at the sample either caused by a variation of the SE

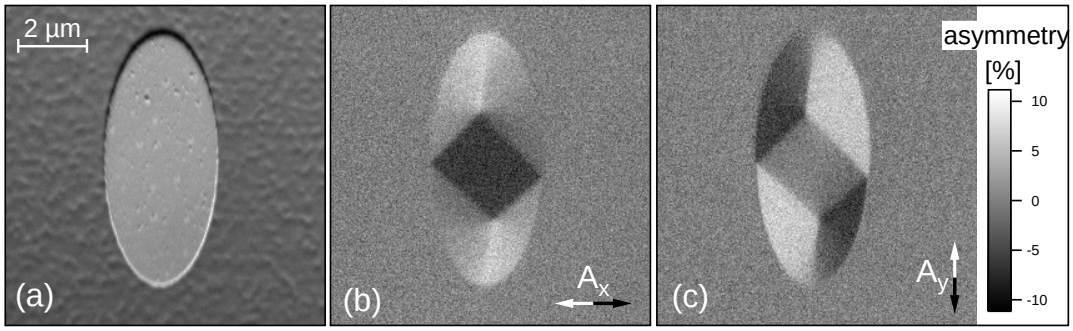

Figure 2.3.: Images derived from the raw data: The sum image of all four channels gives the standard SEM contrast in (a). In (b) (MCP 4-MCP 2)/(MCP 4+MCP 2) is shown, which gives the magnetic contrast along the x-direction; In (c) (MCP 1-MCP 3)/(MCP 1+MCP 3) is plotted, showing the magnetic contrast along the y-direction.

yield due to different materials or by some surface texture [Rei10](p186) which is equivalent to the conventional SE contrast in SEM imaging.

Fig. 2.2 shows exemplarily a set of the four simultaneously acquired intensity maps from MCP 1 to MCP 4. The sample is a 20 nm thick Permalloy (Py, $Ni_{80}Fe_{20}$) ellipse on a silicon wafer. The darker area around the ellipse is the region where the Permalloy has been totally removed via focused ion beam milling. The total SE yield of silicon is lower compared to Py [Rei88], therefore it appears darker. Within the Py ellipse, the magnetic contrast is visible. In Fig. 2.2 the central region appears bright in the MCP 2 channel and dark in the MCP 4 channel. From the above discussion of the different beam intensities it is then clear that the sample magnetization must point to the right in this region. The magnetic contrast, however, is superimposed on the conventional SEM contrast which is in this case some intensity fluctuations caused by Py texture defects and surface roughness.

Adding up the intensity maps of two opposite MCP channels results in the canceling out of the magnetic contrast and the conventional SEM contrast remains:

$$I_{(2,0)} + I_{(\bar{2},0)} = I_0 \cdot R \cdot (1 + P \cdot S + 1 - P \cdot S) = 2 \cdot I_0 \cdot R \tag{2.6}$$

Summing up all four detector channels increases the image statistics of the SEM image by a factor two, which decreases the Poisson error of the intensity measurement by a factor of $\frac{1}{\sqrt{2}}$ thus resulting in a high quality SEM contrast image shown in Fig. 2.3(a), usually called sum- or SEM image.

To extract only the magnetic information, the intensity maps of two opposite detectors channels are subtracted and the results normalized by the sum of their intensities, thereby canceling out the SEM contrast. The procedure gives a magnetic intensity map in units of asymmetry A which can be interpreted as the ratio between the magnetic contrast and the intensity generated by an equivalent unpolarized SE beam. The four diffracted (2,0) beams yield the two components of the asymmetry perpendicular to the scattering planes:

$$A_x = \frac{I_{2,0} - I_{\bar{2},0}}{I_{2,0} + I_{\bar{2},0}} = P_x \cdot S, \quad A_y = \frac{I_{0,2} - I_{0,\bar{2}}}{I_{0,2} + I_{0,\bar{2}}} = P_y \cdot S \tag{2.7}$$

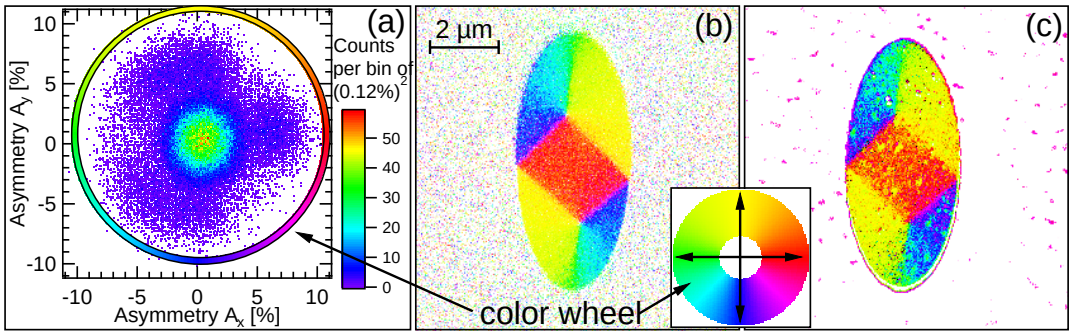

Figure 2.4.: (a) shows the 2D-histogram calculated from the magnetization maps of Fig. 2.3(b) and (c). Non polarized SE from the silicon wafer are causing the large green accumulation point in the center. By appointing a color to each position, a magnetization map was derived which is shown in (b). (c) shows a color map calculated only from the two channels MCP 1 and 2, the structural signal is here still visible, i.e. superimposed with the magnetic signal.

In Fig. 2.3(b) and (c) both asymmetry maps of the Py ellipse are shown giving the magnetic information along the x- and the y-axis, respectively. As expected, the SEM contrast of Fig. 2.2 is no longer visible and only the magnetic signal remains. The observed asymmetry is in the range of ± 8 % (Fig. 2.3(c)) and agrees well with a first approximation using an average polarization $P = 30$ % for iron and an average sensitivity of the scattering process $S = 27$ % [Kir85b](p67) giving a theoretical asymmetry $A = S \cdot P = 8.1$ %.

For the physical interpretation of the images and the ongoing data analysis a statistical investigation of the obtained magnetic information is often quite useful. A common approach is the evaluation of a 2D-histogram: The asymmetry doublets of each acquired pixel are counted in a 2d-bin array which is then plotted similar to a scatter plot. Fig. 2.4(a) shows such a 2D-histogram of the Py ellipse. The major accumulation point in the center is caused by the outer non magnetic area (silicon substrate) and defines the origin of the magnetization vectors [All92]. The dark rectangular domain in the center of the ellipse (Fig. 2.3(b)) is responsible for the second circular accumulation point on the right side of the origin. The continuous rotation of the magnetization orientation due to shape anisotropy in the top and button domains of the ellipse which can be seen best as bright and dark regions in Fig. 2.3(c) causes the smeared satellites in the 2D-histogram.

By appointing a color to each magnetization doublet (vector) a color map of the magnetization can be calculated which is shown in Fig. 2.4(b). The color wheel (Fig. 2.4(a)) is somewhat arbitrarily chosen, different solutions are presented in the literature [vG10, Bac07, Bed07, Jun07, Frö08], none totally satisfying[1]. The color coding in Fig. 2.4(b) is additionally extended with the association of white to magnetization vectors which are shorter as a specified critical length, thus representing non magnetic regions.

[1]For a magnetic system with a four fold symmetry, no color wheel can be perfect due to the fact that there are seven main colors visible to the human eye, thus one color or direction is always

The color map shown in Fig. 2.4(c) is calculated from only two orthogonal channels (MCP 1 and MCP 2). Again, the information about the magnetization orientation is superimposed with the conventional SEM contrast. It shows that the intensity maps of two orthogonal channels are quite sufficient to derive the complete magnetization map in case homogenous samples are imaged where the variation of the total electron yield is low, e.g. homogenous thin films or parts of it.

The advantages, however, which come with the definition of the asymmetry images (Eq. 2.7) displayed in Fig. 2.3(b) and (c) can be summarized to:

- the conventional SEM contrast cancels out, only magnetic information remains
- the image statistics increases by a factor of two, which decreases the Poisson error of the polarization measurement by a factor $1/\sqrt{2}$
- the image comes in units of polarization asymmetry, thus supplying a direct value for comparison of different samples

2.2. Optimization of the LEED detector design

The details of the actual physics and the technical aspects of the spin detection process are much more complex than presented in the former introduction. The most important effects which have to be taken into account are:

- the SE have an energy distribution between 0-15 eV peaked around 2 eV [Rei10](p166), thus resulting in different scattering energies at the tungsten crystal
- with the energy distribution comes a polarization distribution [Oep05] with a maximum polarization at a SE energy of 0 eV. At this energy, the spin-polarization for 3*d*-ferromagnets is strongly enhanced due to minority d-hole scattering on their way to the surface [Sch93]. Only above ≈10 eV a constant value is obtained, which corresponds to the polarization of the conduction band.
- the sensitivity S of the scattering process changes rapidly (sign-change!) with a variation of scattering energy [Kir84] which comes with the energy distribution of the SE.

These three effects have to be considered when designing a spin detector for the purpose of imaging. In contrast to the concept of the classic design of a spin polarimeter where an sharp energy filter (e.g. FWHM=0.4 eV [Kir85a]) is used to analyze the polarization of a more or less monochromatic electron beam, the purpose of a detector for imaging is to transmit and analyze as many electrons as possible as long as the sensitivity does not changes sign. The approach allows to gain a high image quality (Figure of Merit) which is proportional to $N \cdot S^2$ for images acquired in reasonable time (<10 min).

missing.

The design optimization was carried out primarily by R. Frömter and H.P. Oepen and the result as well as a detailed discussion of the detector properties is presented in our following article [P1]. My contribution to the work was the high resolution measurement of the exemplary SEMPA image of an iron whisker shown in [P1, Fig. 9 and Fig. 10]. As one can see from the discussion in [P1] the image properties like asymmetry, error and count rate (i.e. transmission) agree very well with the predicted values from the calculation carried out by R. Frömter. The magnetism observed at the surface of the Fe-whisker is not topic of [P1]. A subsequent discussion together with an interpretation of the details of the associated 2D-histogram is then following after the article.

Optimizing a LEED spin polarization analyzer for imaging of magnetic structures

R. Frömter, S. Hankemeier, H.P. Oepen and J. Krischner

submitted to *Review of Scientific Instruments* in July 2010

accepted for publication in *Review of Scientific Instruments*; 13th December 2010

Preprint

P1

The numbers by which citations are referenced in the following article are only valid within the article.

Optimizing a LEED spin-polarization analyzer for imaging of magnetic surface structures

Robert Frömter, Sebastian Hankemeier, and Hans Peter Oepen
Institut für Angewandte Physik, Universität Hamburg, Jungiusstr. 11, 20355 Hamburg, Germany
Fax: +49 (40) 42838-6368, Tel.: +49 (40) 42838-3312
E-mail: rfroemte@physik.uni-hamburg.de

Jürgen Kirschner
Max-Planck-Institut für Mikrostrukturphysik, Weinberg 2, 06120 Halle, Germany

ABSTRACT

A newly designed scanning electron microscope with polarization analysis (SEMPA or Spin-SEM) for the acquisition of magnetic images is presented. Core component is the spin detector, based on the scattering of low-energy electrons (LEED) at a W(100) surface in ultra-high vacuum (UHV). The instrument has been optimized with respect to ease of handling and efficiency. The operation and performance of a general LEED detector for SEMPA has been modeled in order to find the optimum operating parameters and to predict the obtainable image asymmetry. Based on the energy dependence of the secondary electron polarization and intensity the detector output is simulated. For our instrument with optimized performance we demonstrate experimentally 8.6 % polarization asymmetry in the domain structure of an iron whisker, which corresponds to 17.2 % image contrast, in excellent agreement with the predicted simulated value. A contrast to noise ratio (CNR) of 27 is achieved at 5 ms acquisition time per pixel.

I. INTRODUCTION

For more than 20 years, the scanning electron microscope with polarization analysis (SEMPA or spin-SEM) has been used to study magnetic patterns at surfaces, in ultrathin films, and in nanostructures. During that period it has proven its potential to address various topics e.g., the magnetic structure of domain walls [1,2], ultrathin films [3], exchange coupled films [4], antiferromagnetically coupled oxides [5], and the spin-reorientation transition [6]. Recently, special attention has been paid to widen the range of application of spin-SEM by utilizing various techniques for surface preparation, like dusting [7] or sputtering. Meanwhile, procedures have been established that make the investigation of nearly all kind of material and sample feasible and spin-SEM has developed to a standard technique for the investigation of magnetic structures in the range from several microns down to 5 nm[8].

The unique feature of the technique is that the magnetization orientation is directly measured. This can be achieved by detecting the spin-polarization of the secondary electrons (SE), which are anti-parallelly aligned to the magnetization. Hence, utilizing SEMPA means to create secondaries point by point and analyze the electrons with respect to their spin-polarization, i.e. combining a SEM and a polarization detector in one instrument. To achieve optimal performance, the conditions dictated by the physical process of spin polarized secondary electron emission have to be considered. To obtain best results, both components, SEM-column and spin detector have to be optimized. In this paper, we report on the design of a polarization detector optimized for the use in a spin-SEM. This detector is designed and already used in combination with a new SEM column that is as well optimized for the application in a SEMPA.[9]

Worldwide, three different types of detectors are used in spin-SEMs for polarization analysis, i.e. the Mott[10] -, LEDS[11] -, and LEED[12,13] detector. The Mott detector is based on the scattering of high-energy electrons at atom cores, while the low energy detectors utilize the multiple scattering of electrons at surfaces of a single crystal (low energy electron diffraction, LEED) or at amorphous films (low energy diffuse scattering, LEDS). Common to all these detectors is a low efficiency in the range of 2×10^{-4} or less.[14] The up to two orders of magnitude more efficient exchange-based detectors, Fe(001)-p(1×1)O [15] and Co/W(110) [16], require two successive measurements for each component of spin polarization and they rely on scattering of electrons with a narrow energy distribution. Their advantage in efficiency would be completely lost in SEMPA application as the energy spread is disjunctive to that of the secondaries. Thus, low efficiency is the crucial point that makes the optimizing of the instruments in all respects necessary. Due to our continuous experience with LEED detectors, we have explored the possibility to optimize the performance of this detector with respect to its application for SEMPA.

The paper is organized as follows. In the first paragraph, we introduce our new spin-SEM system

and the realization of a new LEED detector. In the following paragraph we work out theoretically the optimized performance of a detector when LEED at W(001) is utilized in the SEMPA application. From these considerations, certain design criteria follow, which are discussed in the third paragraph. Finally, the performance of our new detector design is compared with the results from the modeling.

II. Experimental Setup

The microscope is set up in a UHV chamber, which can be baked to at least 150° C and is operated at 5×10^{-11} mbar residual gas pressure. Under these conditions, the magnetic contrast from an iron sample has proven to be largely preserved for several days. Samples can be quickly inserted into the microscopy chamber by means of a load-lock and can be transferred into a directly attached preparation chamber under UHV conditions.

One design criterion has been to achieve as much flexibility as possible for applying the high resolving electron beam from the SEM column. For that purpose, several UHV ports have been oriented with straight view onto the sample. On such flanges, there are mounted the spin analyzer, an Ar-ion sputter gun, a hemispherical energy analyzer for Auger electron analysis, and an electron beam evaporator for iron film deposition. In order to achieve high detection efficiency, it is important to keep the distance sample/spin detector optics small. Thus, to maintain unhindered sample access for the other devices, the spin detector can be retracted.

Geometric design considerations

The important issue for an optimized spin-SEM is to maximize the angular acceptance of the polarization analyzer. For that reason, normal take-off geometry was chosen. Additionally, the distance between sample and detector optics was minimized. The two conditions put strong limitations on the geometrical arrangement. The angle between SEM column and detector optics should be much smaller than 90° to maintain an acceptable sample tilt with respect to the column axis. Too large angles will cause a serious deterioration of lateral resolution in the tilt direction. Too small angles will strongly reduce the size of the extraction optics cross section. The final solution is illustrated in Fig. 1: Straight access to the sample at a collection distance of 8 mm (to front end of detector) is possible at a sample tilt of 64° for a conical extractor optics with full opening angle of 49°. In this geometry, a SEM working distance of 8 mm is feasible.

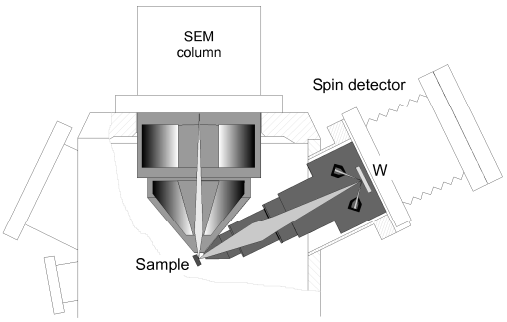

FIG. 1. Arrangement of column, sample, and spin detector within the UHV chamber. Both, SEM and retractable detector operate at a working distance of 8 mm. Since the detector is oriented in normal take-off geometry to maximize sensitivity, the SEM is scanning at 64° tilt angle with respect to the sample surface. The sample is mounted on a 5-axis goniometer stage (not shown). The interior of column and detector schematically indicates the primary and secondary electron beams, together with one scattering plane of the W-crystal and two electron counters for the (2,0) beams (not to scale).

The objective lens of the SEM is responsible for a magnetic stray field along the optical axis, which decreases with increasing working distance. An additional shielding reduces the stray field to 250 µT at the sample under typical working conditions (7 kV). A precessional rotation of the measured spin polarization vector has not been observed within an error margin of 1°. This most advantageous result is due to the fast acceleration of the electrons towards the spin detector by the first elements of the optics. The electric field of the SEM column at the sample surface is quite small and is easily overcome by the potential gradient of 56 $\mathrm{Vmm^{-1}}$ from the first acceleration lens of the transfer optics, which has been calculated including the outer ground shield. The effects of the column's electrostatic and magnetic stray fields on the SE trajectories are compensated by the beam steering elements (quadrupole deflectors) of the detector optics.

Spin detector

The detector for the spin-SEM is displayed in Fig. 1 Scattering at the W(001) surface is performed at normal incidence. For that geometry, at a kinetic scattering energy of $E_0 = 104.5\,\mathrm{eV}$, the (2,0) LEED beams appear at a fixed angle of $\vartheta_0 = 40.64°$ (see Equation (9)) with respect to the surface plane. To preserve the propagation direction of the scattered electrons, the complete surroundings of the crystal including the drift tube and lens 6 are held at the same potential, termed scattering potential U_s. The (2,0) beams can leave the field-free region around the W(001) crystal

through grids at the same potential, which separate the scattering from the counting section. A second set of grids (retarding grids) is used to separate the elastically scattered electrons from the SE generated at the W crystal as well as to suppress the inelastic background. The retarding grids act as high-energy pass filters and are set to a potential close to sample ground. An electron, which has passed both grids, is then attracted into a dual microchannel plate (MCP) assembly for pulse amplification. Between the retarding grid and the MCP entrance, a tapered optical element is mounted. With this electrode, the electron beam is defocused before hitting the front of the first channel plate. Due to the defocusing, the whole plate area can be illuminated by the electrons. This is important to increase the expected lifetime, i.e. to increase the total number of detected events before the MCP quality degrades. In addition, the lower area intensity reduces the dead time of the plate assembly, as subsequent electrons will not hit exactly the same microchannel. The current pulses generated in the MCP stack are collected with an anode plate and, after high-voltage decoupling, fed into counting electronics.

To clean the W(001) surface, the single crystal can be flash-heated above 2000 K from its rear by electron bombardment from a hot filament. Within 30 seconds after flashing the detector is ready again for measuring. The whole cycle requires less than a minute.

As will be discussed in the following paragraphs, the SE emission is characterized by a wide energy spread with varying polarization and an emission into half space. To fulfill the conditions for optimized spin detector performance (small angle/energy spread) would imply, however, that only a small fraction of the total SE emission could be utilized for spin analysis. Hence, the spin polarization analyzer in a spin-SEM has to work at less favorable conditions in order to cover a large part of the SE spectrum. The goal is to find the optimum in the antagonism of degrading polarization sensitivity versus increasing count rates upon increase of the angle and energy acceptance. From general considerations about the SE emission, it was deduced that the detector with best performance (for spin-SEM application) should accept all the SE up to at least 10 eV, while the acceptance angle of the detector should be as large as possible [17]. The solution for the latter requirement is, to put the sample into the focal plane of the detector system. By this, a large emission angle is transformed into a quasi-parallel beam configuration. This means that the majority of all the electrons transferred into the detector are scattered at conditions close to normal incidence. In our design (see Fig. 2), there is a drift tube at the end of the optics, which is essential for adjusting the beam. The drift tube allows tuning of the electrons into a parallel beam configuration just by maximizing the sum of the four scattered intensities. The tube permits only electron beams with an angular spread of at maximum ±5º to be transmitted.

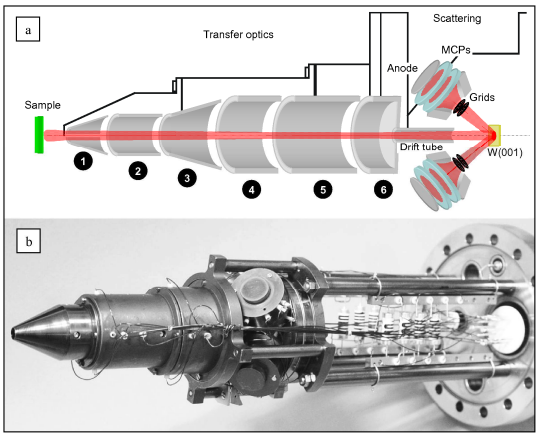

FIG. 2a). Schematic of the spin detector. The transfer optics consist of a series of electrostatic tube lenses labeled 1 to 6 and a drift tube to define the beam divergence. Lenses 1 and 4 have been doubly split to form quadrupoles for beam steering. After scattering at the W-crystal, the elastically scattered electrons that form the four (2,0) beams are first filtered by a retarding grid and amplified by a double MCP setup. The resulting current pulses on the four anodes can then be recorded by external electronics. A photograph of the entire spin detector with cabling is shown in part b). The transfer optics on the left are followed by the scattering section in the center of the image. Adjacent is the voltage divider network for supplying the MCP stacks. It is suspended between the standoffs that mount the detector onto the CF 100 base flange containing all required electrical feedthroughs.

Electrons with different energies are scattered into different angles. Hence, LEED with fixed exit apertures gives a discrimination of energy in itself via the limitation of the angular spread of the scattered beams. In our setup, the grid support mounts act as such apertures (Fig. 2). For idealized normal incidence conditions, these apertures define an energy spread of roughly ± 10 eV around the nominal scattering energy. Details will be discussed later on.

The first two lens elements of the transfer optics in front of the detector are set to high potential (2 – 3 kV) to accelerate as many SE as possible into the optics. The first and fourth lens elements have been split into four segments each, so they can act as beam steering elements (electrostatic quadrupoles). They correct for angular deviations due to electrostatic and magnetic fields of the SEM column and sample tilt. The main effect of the first quadrupole is to center the field of view of the

detector with respect to the SEM scan area, while the second quadrupole adjusts the LEED pattern with respect to the MCP entrance apertures by minimizing the experimental asymmetry.

SEM column

The UHV version of the Zeiss Gemini system is used in our microscope. This column was designed as primary source for SAM and SEMPA. It is equipped with a Schottky field emission cathode and a combined electromagnetic/electrostatic objective lens. The electron optical properties are superior to conventional microscopes, as the column combines high current with high spatial resolution, even at relatively low primary beam energies. It thus fits very well the requirements for a SEM column to be used in spin-SEM. At a working distance of 8 mm (see below), a resolution of 7.5 nm is specified for a beam current of 1 nA at 3 keV primary energy. This current value fits well into the range that offers good working conditions, while the low primary energy is superior as it allows to operate close to the energy range where the SE yield becomes high [17].

III. PRINCIPLES OF OPERATION

Standard spin polarized LEED detector

In the LEED polarization detector the diffraction of low energy electrons at a W(100) single crystal surface is used to measure the spin polarization. Almost 30 years ago, the spin dependent scattering properties of the W(100) surface have been determined both experimentally and theoretically [18,19]. The optimum working condition when utilizing the scattering at W(001) as a polarization detector were found using the (2,0) diffraction beams at 104.5 eV scattering energy. At this energy, a sensitivity $S = -0.27$ was obtained [12,20].

In normal incidence, two orthogonal components of the spin polarization *P* of the incoming electrons can be determined from the normalized intensity differences (asymmetries) of two pair-wise opposed beams $\dot{N}_{\uparrow}$ and $\dot{N}_{\downarrow}$, or $\dot{N}_{\rightarrow}$ and $\dot{N}_{\leftarrow}$.

$$P_x = \frac{1}{S}\frac{\dot{N}_{\uparrow} - \dot{N}_{\downarrow}}{\dot{N}_{\uparrow} + \dot{N}_{\downarrow}},\ P_y = \frac{1}{S}\frac{\dot{N}_{\rightarrow} - \dot{N}_{\leftarrow}}{\dot{N}_{\rightarrow} + \dot{N}_{\leftarrow}} \qquad (1)$$

The total statistical error of a single polarization measurement using single electron counting is governed by Poisson statistics. It can be expressed as [21]

$$\Delta P = 1/\sqrt{NS^2} \qquad (2)$$

For the LEED detector, $N = N(2,0) + N(\bar{2},0)$ is the total number of counts in two opposed beams for any fixed acquisition time. As *N* is proportional to *R*, maximizing RS^2 minimizes ΔP. The detector efficiency is twice the product of reflectivity *R* times the square of the polarization sensitivity *S*, i.e. $2RS^2$.[12] This so-called "Figure of Merit" allows for direct comparison of spin detectors, since it is derived from the statistical uncertainty in the polarization detection of each acquired data point. In calibration experiments, it turned out that the highest Figure of Merit of 1.6×10^{-4} is found at a kinetic energy of 104.5 eV [12], with an energy spread of 1.5 eV and an angular spread of 0.5° at normal incidence. The reflectivity was determined to be *R* = 0.0011.

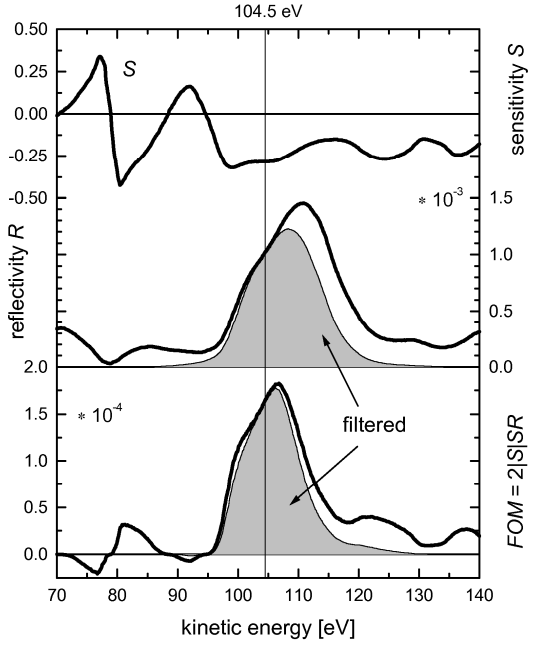

FIG. 3. Characteristics of spin-dependent scattering at the W(100) surface and the result of energy filtering in the detector. Energy dependent detector spin-sensitivity *S* and reflectivity *R* data in normal incidence are reproduced from Ref. [12] for the (2,0) diffracted beams. The Figure of Merit in the lower panel is a measure of detector efficiency at the given energy. In order to illustrate the sign-changes of the sensitivity, FOM has been redefined incorporating the sign of the sensitivity. The filtered curves indicate how the transmission (reflectivity) and the resulting FOM are affected by the exit apertures of the scattering section of our detector.

The LEED detector in SEMPA

If the LEED detector is used for polarization measurement in a SEM, such a simple relation is no longer meaningful. The reason for this is that three experimental conditions, which are more or less fulfilled in a typical spectroscopy experiment, are no

longer valid for a secondary electron polarization detector with high efficiency in spin-SEM application:

The SEs cannot be considered monochromatic, compared to a scattering energy as low as 104.5 eV. SEs show a characteristic energy distribution, which is peaked around 2 eV, and extends up to a kinetic energy of 50 eV by definition. This distribution can be approximated by [22]

$$\frac{\mathrm{d}\,n}{\mathrm{d}\,E_{\mathrm{SE}}} \propto \frac{E_{\mathrm{SE}}}{\left(E_{\mathrm{SE}}+\phi_{\mathrm{W}}\right)^{4}}, \qquad (3)$$

with ϕ_{W} the work function as sole material parameter (see also Fig. 4). In this approximation, the peak position is given by $\phi_{\mathrm{W}}/3$.

The spin-polarization of the secondary electrons is energy dependent within the relevant energy range. For 3*d*-ferromagnets the spin-polarization of SEs at the lowest energy is strongly enhanced due to minority *d*-hole scattering on their way to the surface [23]. Only above 10 to 15 eV a constant value is obtained, which corresponds to the electron polarization of the occupied 3*d*-bands. Other classes of ferromagnetic materials can behave quite differently.

The SE emission is not directional. Instead, it shows a cosine-type angular distribution, centered along the surface normal, with emission into the full half-space [22]. This angular spread can be strongly reduced by an accelerating collection field, but the remaining angular divergence at the W crystal still has to be taken into account.

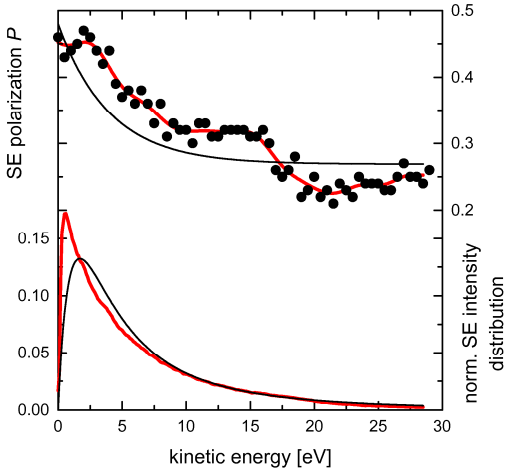

FIG. 4. Spin-polarized secondary electron emission from iron. The upper panel shows the spectral distribution of the SE spin-polarization. Two slightly different cases are shown: the dots are measured data for a clean Fe (110) single crystal, taken from ref. [24]. The thick (red) line gives a smoothed version of this data, which is used for the following calculations. The thinner (black) line approximates the SE polarization from a polycrystalline or amorphous iron sample (see text). The same color-coding is used in the lower panel to describe the normalized energy distribution of the SE for the two cases. While the Fe(110) data are taken directly from the above-mentioned experiment, the distribution assumed for the polycrystalline case is calculated from equation (3) using a work function of 5 eV.

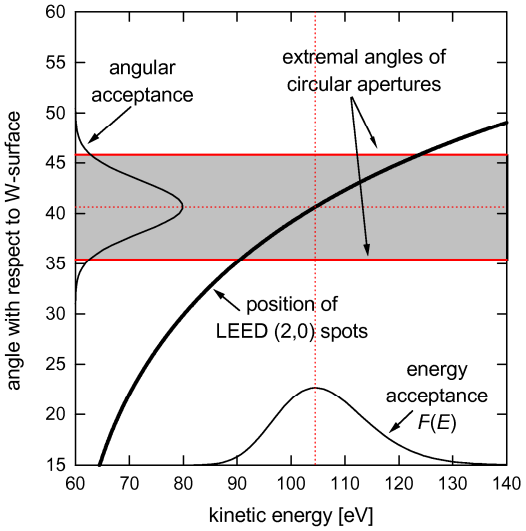

FIG. 5. Illustration of the energy filtering properties of our LEED detector design. The calculated angular variation of the (2,0) LEED spots is shown as function of kinetic energy together with the limiting angles at ±5° of the circular entrance apertures of the MCP section. The working point of the detector at 104.5 eV, and the center position of the exit aperture at 40.64° are indicated as dotted lines. The Gaussian shaped angular acceptance on the left axis is transformed by the nonlinear energy dependency into the non-symmetric energy acceptance shown on the bottom axis (both in arbitrary units and offset to the respective axes as zero).

Strategy

In principle, it is possible to use an energy and angle resolving detector system, which selects electrons with a narrow energy and angle distribution out of the total SEs, while the majority of the SEs is discarded. The scattering intensity will be very low and measuring time has to be increased for statistical reasons. While such a detector can answer - according to equation (1) - the question for the exact spin-polarization of the SE of a narrow energy-interval at one spot, it cannot be practically used to visualize the lateral distribution of the polarization for typical imaging conditions with some ten thousand pixels per image. As the focus is on the local orientation of the magnetization in the

SEMPA investigation, the relative value of the polarization in different directions is of interest. Hence, it is recommendable to use a detector that accepts a wide range of SE energies and emission angles for the spin polarization analysis in order to improve the signal to noise ratio by increasing intensity at the expense of polarization sensitivity. In addition, a large angular acceptance avoids possible image artifacts on polycrystalline samples with a pronounced angular dependence of spin polarization.

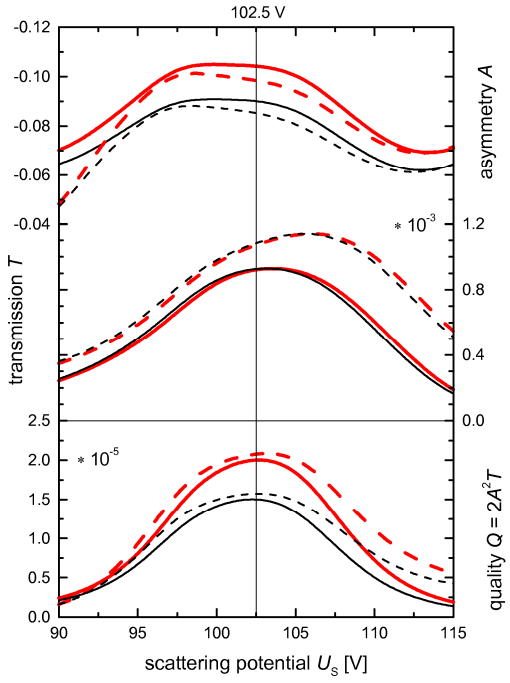

FIG. 6. LEED detector output as function of the scattering potential U_S for SEs from Fe. The graphs show the asymmetry (top panel), transmission (middle panel), and quality (bottom panel), obtained by a convolution of sample and detector properties. Dashed lines show the results without filtering by a geometric exit aperture, while solid lines are calculated using the energy filter characteristic illustrated in Fig. 5. Due to its higher spectral weight at lowest energies, the single crystalline model (broad, red lines) achieves a higher asymmetry at the working point, compared to the polycrystalline model (narrow, black lines). The optimum voltage to be applied to the scattering crystal is 102.5 V, independent of the model, as can bee seen from the quality graph.

The experimental data of the double scattering experiment at W(100) [12], which are reproduced in the upper two panels of Fig. 6, reveal that both, sensitivity and reflectivity, vary strongly with energy around the optimum working point of 104.5 eV. Even a sign change of the sensitivity occurs some 9 eV below the optimum energy. Above 104.5 eV the reflectivity still increases up to 111 eV while the spin sensitivity gradually drops. These data indicate that the inclusion of electrons with wider energy spread will actually reduce the polarization sensitivity and thus the obtainable contrast. The lower panel of Fig. 6 shows the figure of merit *FOM* for a nearly ideal detector with a small energy and angular spread like the one used in Ref. [12]. We define the *FOM* as $FOM = 2|S|SR$. The latter formula differs from the conventional definition (Eq. (2)) to account for the effect of the sign changes of the sensitivity on the attainable detector properties when the energy spread is enlarged. The plot in Fig. 6 (lower panel) gives a hint to an operation window with an energy span fitting the SE energy distribution. The energy range between 99 and 112 eV with a slightly asymmetric peak in the *FOM* seems to be well suited.

The 13 eV energy interval is sufficient to analyze most of the SE with an energy distribution similarly to Eq. (3). It can be expected that tuning a detector to this working point will increase the performance of the spin-SEM. This qualitative argument, however, has to be quantified. The quantification is closely related to answers to the following questions:

Which is the optimum scattering potential, i.e., the voltage to apply between sample and W crystal? In other words, how can the SE polarization and energy distributions be optimally mapped onto the distribution of the analyzer FOM?

What asymmetry can be expected for a measurement at a given sample? This question asks for the obtainable image contrast in the polarization maps.

What is the total detector performance for a given sample? This asks for the obtainable contrast/noise ratio per SE, which determines the quality of the local magnetization direction map calculated from the two polarization maps.

Can angular- and/or energy-filtering apertures be beneficial to improve the detector performance?

In order to answer these questions, a numerical convolution of sample and detector properties in

energy-space will be carried out in the following.

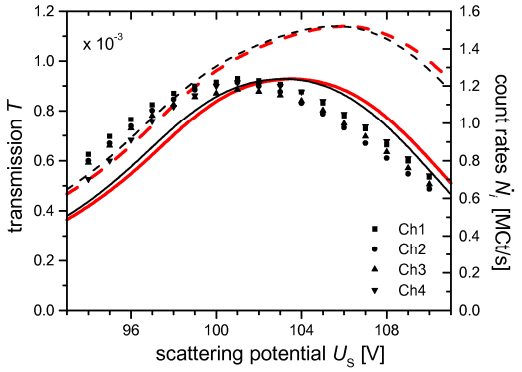

FIG. 7. Comparison of the theoretical transmission curves from Fig. 6 (dashed and solid lines, as described there) with measured count rates (different style dots) as function of the scattering potential. Data points are recorded for the four channels Ch1-Ch4 simultaneously. The -2 eV shift of the measured data is attributed to hydrogen contamination of the detector crystal (see also text).

Spin polarized secondary electron emission

At first, the exact polarization- and energy distribution of the SE from a particular sample has to be known. We take the SE emission from Fe as the model system. Experimental data obtained at Fe(110) single crystal surface are reproduced in Fig. 4 [24]. The primary beam of 2 keV hits the surface at an angle of 60° while the SE emission was investigated in normal emission. The polarization is highest (P ~ 45 %) at lowest energies and drops to about 25 % for energies above 15 eV. Due to band-structure effects, a variety of substructures is superimposed onto the general trend [25]. The latter features depend on and vary with emission angle. Hence, when the angular acceptance is increased, a weighted average of all emission angles has to be used for maximum accuracy. In the following, we will just consider the normal emission data as prototype. In Fig. 4 the normalized SE distribution from Ref. [12] is plotted. The intensity is peaked at a very low energy of 0.6 eV. The angular acceptance is given as ±3° in the reference. Although energy and angular resolution are limited, we take this distribution as a good approximation of the true distribution.

As second sample we consider an amorphous/polycrystalline Fe sample because thin Fe films are frequently used as dusting layer for imaging in spin-SEM. Ultrathin polycrystalline Fe films are deposited onto samples that are otherwise not accessible for SEMPA, like oxides, non-itinerant ferromagnets, or samples with contaminated surfaces [26]. The decoration (or dusting) layer mirrors the magnetic structure of the underlying sample and provides the clean surface for spin-polarized SE emission, that is required for imaging [7]. Due to a lack of published energy-resolved polarization data from polycrystalline iron, measurements on the Fe-rich amorphous metallic glass $Fe_{80}B_{15}Si_4$ [27] have been rescaled to describe pure Fe. The plot in Fig. 4 is the result of linearly scaling the metallic glass polarization data to match at higher energies (> 20eV) the expected Fe band polarization of 27 %. The polarization distribution resulting from this procedure is in reasonable accordance with Monte-Carlo simulation for non-crystalline iron [28]. Likewise, it fits more or less the general trend of the Fe(110) data, shown in the same panel. Numerically, we can represent the latter distribution, by $P_{\mathrm{SE}}(E) = 0.27 + 0.21\mathrm{e}^{-0.25E}$ for Fe.

The normalized intensity distribution for the amorphous Fe has been calculated from Eq. (3), assuming a work function of 5 eV for Fe (Fig. 4). This distribution is commonly believed to fit the general intensity distribution of SE in case of low angle and energy resolution [22]. The latter distribution has a peak at a significantly higher energy than the Fe(110) measurement, however it coincides well with the experimental curve for Fe (110) above 10 eV.

Convolution of sample and scattering properties

As the most simple approach we first consider a detector without apertures, which detects scattered electrons from the (2,0) beams only. In that case, the transmission is solely determined by the reflectivity at the W crystal. For a monochromatic beam of polarization P and kinetic energy E being scattered at the target, the observable intensity asymmetry A is given by (compare Eq. (1))

$$A \equiv \frac{N_\uparrow - N_\downarrow}{N_\uparrow + N_\downarrow} = P\,S(E). \qquad (4)$$

In order to facilitate the understanding, we will first consider a case were only electrons of two discrete scattering energies E_1 and E_2 were incident upon the crystal. The two electron beams are characterized by the relative frequencies n_1 and n_2, and the polarizations P_1 and P_2. The resulting asymmetry is then given by the weighted average of the individual asymmetries

$$A = \frac{n_1 R(E_1)}{n_1 R(E_1) + n_2 R(E_2)} P_1 S(E_1) + \frac{n_2 R(E_2)}{n_1 R(E_1) + n_2 R(E_2)} P_2 S(E_2), \qquad (5)$$

where weighting takes into account both, the initial frequency and the energy-dependent reflectivity at the crystal. If the incoming frequencies are

normalized ($n_1 + n_2 = 1$), then the denominator gives directly the total transmission *T*, defined as the number of detectable electrons in each (2,0) LEED spot per incoming electron.

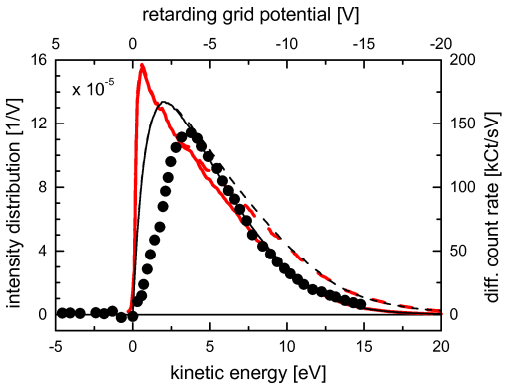

FIG. 8. Energy distribution of the SE after scattering at W(001). Dots give the experimental results when the retarding grid voltage was varied between +5 and −15 V (top axis). The data shown are differentiated with respect to energy (right axis), to obtain the distribution. From the model, we obtain the dashed lines as energy distributions per channel and incoming electron (left and bottom axes). The energy filtering at the entrance apertures, which is included in the solid line calculations, is the reason for the gradual cutoff above 5 eV that is in perfect agreement with the measured data. At energies below 4 eV the grid transmission becomes less than unity, so the measured data falls off more rapidly. A scattering potential of 102.5 V has been used in the experiment and in the model.

In SEMPA, we have to consider the continuous polarization and energy distributions of the incoming electrons, $P(E_{\mathrm{SE}})$ and $n(E_{\mathrm{SE}})$, the latter normalized by $\int_0^\infty n(E_{\mathrm{SE}})\,\mathrm{d}E_{\mathrm{SE}} = 1$. E_{SE} is the initial kinetic energy of the SE. To facilitate the notation further, we define $n(E_{\mathrm{SE}} < 0) = 0$. The total apertureless transmission *T* can be calculated in analogy to the denominator of the simple two-energy case by integrating the product of energy distribution and associated reflectivity over the SE energy:

$$T(U) = \int_0^\infty n(E_{\mathrm{SE}})R(U + E_{\mathrm{SE}})\,\mathrm{d}E_{\mathrm{SE}} \equiv (\tilde{n} * R)(U) \quad (6)$$

Here $U = E - E_{\mathrm{SE}}$ is the potential difference between sample and scattering crystal. By a simple substitution, it can be shown that this integral is mathematically equivalent to the convolution of a reversed energy distribution $\tilde{n}(E) = n(-E)$ with the reflectivity, as is given by the last part of Eq. (6). The numerator of Eq. (5) can be extended in a similar manner to continuous distributions by including the initial polarization and the spin sensitivity at the respective energies into the product in the integral. Thus, the resulting apertureless asymmetry is given by

$$A(U) = \frac{1}{T(U)}\int_0^\infty n(E_{\mathrm{SE}})P(E_{\mathrm{SE}})R(U + E_{\mathrm{SE}})S(U + E_{\mathrm{SE}})\,\mathrm{d}E_{\mathrm{SE}} \equiv \frac{1}{T(U)}\left(\tilde{n}\tilde{P} * RS\right)(U)$$

Again, this can be equivalently expressed in form of a convolution, if one uses the notation $\tilde{P}(E) = P(-E)$ for the energy-reversed polarization distribution. Note that *U* will be the only remaining free parameter in this simple model, if the four distributions used as input are known.

The quality of a SEMPA image, which is obtainable from a given total number of emitted SE, is entirely determined by knowing *A* and *T*. In analogy to the Figure of Merit of a spin detector for spectroscopy, as it is derived from the measurement uncertainty in Eq. (2), the quality parameter of a SEMPA measurement can expressed as

$$Q(U) = 2A^2(U)T(U)\,. \quad (8)$$

Q is no longer a pure detector property, as it also includes the information about the spin polarization and energy distribution of the SE from a particular sample. Only for a sample that caused 100 % spin polarization at all relevant SE energies, *Q* would be equal to the *FOM*. For an Fe sample, *Q* is found to be roughly one order of magnitude smaller than the *FOM*.

Next, we apply these formulas to the two above discussed model distributions for Fe samples. As three of the input distributions are available as experimental data points only, both convolutions have been carried out by discrete summation, instead of using the integral form. Prior to summation, the distributions have been interpolated and discrete values generated on a common energy abscissa with 0.1 eV resolution. The results of the calculations are shown in Fig. 6 (dashed lines). The transmission curves for both cases are very similar. This is due to the normalization of the SE intensities and to the fact, that the reflectivity maximum is broader than the two energy distributions, so their differences are washed out by the convolution. Both have a maximum of 1.15 ‰ at around 106 eV, which means a 25 % reduction compared to the maximum of the “monochromatic” reflectivity from Fig. 3. The optimum working point for SEMPA, however, is at the maximum in the *Q* graphs and turns out to be around 102.5 V for both sample systems. The latter

is the best voltage to operate the detector. The transmission of 1.0 ‰ found at this voltage is equal to the one of a detector operating on monochromatic electrons at the respective working point (104.5 eV). So from the apertureless approximation no losses are expected.

The asymmetry values are 10 % for Fe(110) and 8.5 % for the amorphous sample at the working point (Fig. 6). Monochromatic SE from Fe just above the work function barrier with an initial polarization of 48 % would yield 13 % asymmetry. The total spin sensitivity is thus clearly reduced by accepting a large number of less polarized SE. However, this is outweighed by the gain in transmission: Estimating the detector performance for monochromatized electrons gives $Q_{mono} = 4 \times 10^{-6}$, by assuming a 1 eV wide energy acceptance window around the intensity maximum (12 % of all emitted electrons). In comparison, the quantity Q is five times higher when all secondary electrons are accepted. Around the working point, the asymmetry in the non-filtered case (Fig. 6) is depending on the potential. The asymmetry drops towards higher scattering potentials while it stays constant when reducing the potential. The fall-off may cause artifacts when scanning or looking at inclined objects. We will show in the next section, how an energy filtering aperture can strongly reduce this effect.

The difference in asymmetry calculated for the two sample systems is also reflected in the Q graphs. Its main origin is the SE distribution, which is shifted for Fe(110) towards lower energies and thus enhances the weight of the strongly polarized electrons. If one calculates an average spin polarization of all SE for the two samples, weighting with the respective energy distributions, the Fe(110) model gives 39 %, while the amorphous Fe gives 34 %. This difference in average polarization is roughly proportional to the asymmetry difference found in the calculation

Energy filtering and angular distribution

In order to calculate the properties of the detector precisely, the full trajectory of each SE has to be calculated, including the emission, the transmission to and scattering at the W crystal, and finally the transmission to the multiplier. In a simplified picture, three main effects have to be considered as function of initial emission angle and kinetic energy:

First, the spin sensitivity and reflectivity of the scattering at W (100) depend on the angle of the incoming electrons. The angle dependence has been experimentally studied for deviations from normal incidence of ±1° [12] and up to ±2° [19]. A slight variation of the energy dependent sensitivity was observed, with an increase/decrease when tilting in the one/opposite direction. As long as the angular divergence of the incoming electrons stays within these limits, which can be ascertained by appropriate entrance apertures, these effects can be neglected.

Secondly, special features of the electron optics in front of the detector can cause losses. Possible origins are geometric apertures at the entrance or a limited strength of the collecting field. The latter are responsible for a loss of electrons at the fringes of the emission cone. Besides these limiting properties, which are directly correlated with details of the SE emission, a reduced transmission of the optics and/or retarding grids has to be considered. All these losses, together with reduced detection efficiency of the electron counting facility are put together into the global transmission figure. This figure is relevant for the final detector performance, and it can be determined experimentally from comparison with the ideal calculation, which will be finalized in the following. The above-mentioned effects will not be modeled throughout the paper since they are largely independent of the polarization properties of sample or scattering crystal and have an effect on the experiment that is similar to a variation of the primary current of the SEM column.

Thirdly, if an aperture is placed after the W crystal in front of the electron counters this exit aperture, in addition to angular filtering, will also have energy filtering properties. The reason for this behavior is that the scattering angle is energy dependent. Thus, by an adequate shape and placement of apertures centered around the nominal direction of the (2,0) beams an energy window is defined. Only scattered electrons within a limited energy spread can be counted. Such an energy filter could improve the overall performance by rejecting electrons far away from the optimum energy that add only very little or even have a negative contribution to the detector performance. The implications of such an aperture will be modeled here, because it directly affects the polarization sensitivity.

The specific size and location of the exit apertures are taken from our detector design, which is described in detail in the preceding chapters. As indicated in Fig. 5, the four exit apertures are of circular shape and allow for a maximum angular divergence of ±5° when viewed from the center of the W crystal. Their positions are centered with respect to the outgoing (2,0) LEED spots of an optimum kinetic energy of 104.5 eV. The electron beam impinging on the W-crystal has the same divergence of ±5°, which is defined by the drift tu be geometry (see Fig. 2). The same angle is also defined in the reverse beam direction by the lateral extension of the W crystal, when it is viewed from the center positions of the exit apertures, so no electrons from further off angles can enter the apertures. Because of this consistent angular geometry, a very simple approximation is made to include the energy filtering properties: The angular intensity distribution after the exit aperture is

assumed to be of Gaussian shape with a width of $4\sigma = 10°$, the full angular opening of the apertures. This shall account for the divergence of the incoming beam in two dimensions, as well as for the size and intensity distribution of the illuminated area on the crystal. The symmetric Gaussian shape of the angle acceptance (Fig. 5) can be converted into an energy acceptance utilizing the non-linear energy dependence of the (2,0) scattering angle

$$\cos\vartheta(E) = \frac{2\lambda(E)}{a} = 7.757\sqrt{\frac{\mathrm{eV}}{E}}\,, \qquad (9)$$

as illustrated in Fig. 5. The result is an asymmetric filter function

$$F(E) = \exp\left[-\frac{1}{2}\left(\frac{\vartheta(E)-\vartheta_0}{\sigma}\right)^2\right]$$
$$= \exp\left[-2\left(\frac{\arccos\left(7.757\sqrt{\mathrm{eV}/E}\right)-40.64°}{5°}\right)^2\right], \qquad (10)$$

which falls off more rapidly to the low energy side. The validity of this simplified filter model will be justified in the next section by the good agreement to experimental findings. The filter function has been normalized to a peak value of 1, which by construction is located at $E_0 = 104.5\,\mathrm{eV}$. This accounts for the assumption that appropriate angular filtering has been performed by the drift tube before scattering, so all electrons scattered by the crystal with the exact energy E_0 can pass the exit apertures, irrespective of their initial angle. In order to include this filter characteristic into the detector model it has to be multiplied by the reflectivity *R* of the W crystal. The resulting filtered transmission *FR* is shown in the reflectivity graph of Fig. 6.

Looking at the polarization distribution, the asymmetric shape of the filter characteristics has the positive side effect to reduce the transmission for the electrons of reversed sensitivity at the lower energy side to at least 0.4, while maintaining reasonable transmission at the higher energy side where *R* is maximum and *S* is still acceptable. How well this chosen geometry matches to the scattering properties can be seen from the filtered FOM graph, which is given by $2|S|SFR$ and shown in the lower panel of Fig. 6. Under the assumption of unity transmission at E_0, most of the area with positive FOM around the working point can be made use of.

The consequences of the energy filtering apertures for the performance of the detector are shown in Fig. 7 as continuous lines. All calculations for both sample systems have been repeated, with $R(E)$ replaced by $F(E)R(E)$ in Eq. (6) and (7). A first observation is that the working point from the maximum of the quality graphs is unchanged, which is due to the matched aperture position. Since the part of the electron energy distribution with reduced or even reversed asymmetry contributions have been filtered out, the expected asymmetry at the working point has risen to 10.5 % for Fe(110) and 9 % for the polycrystalline sample model compared to 9.8 % and 8.5 % without filtering. In addition, the dependency of the asymmetry on the scattering voltage is reduced, which should help to reduce image artifacts. On the other hand, the transmission with aperture is reduced by 14 %. This is not fully compensated by the gain in asymmetry, so the quality is still slightly reduced (Fig. 7).

IV. System Performance

In this section we conclude the predictions of the model and compare them to measured data. The ideal detector transmission *T*, as predicted by the model, is plotted in Fig. 7 as function of the scattering voltage U_S applied to the W(001) crystal. For comparison, the scattering intensities of the four diffraction-channels, which have been obtained from an iron film, are plotted in the same graph (note the different ordinates). The experimental data are from a 2 nm thick *in-situ* deposited Fe film on an oxidized Fe-whisker. As the film exhibited a multitude of apparently random oriented domains within the field of view, no net magnetic contrast is observed in the area-integrated measurements. A primary beam of 1 nA / 2 keV electrons was impinging at 64° onto the film. The upper curves in Fig. 7 (dashed lines), give the energy dependent reflectivity of W(001) convoluted with the two SE energy distributions, i.e. the result of the simple model. Comparing the latter with the more precise model (solid lines), the effect of the limiting apertures becomes evident. The latter elements shift the maximum of transmission towards lower energies, where the spin-sensitivity is higher (see the following discussion). The shape of the aperture filtered transmission curve coincides very well with the observed single-channel transmission data. This demonstrates that the intended energy filtering can be obtained in a predictable way by limiting the diffracted beams by means of apertures. The energy shift of roughly –2 V in the experimental data can be explained by hydrogen contamination of the W-surface. Such peak shifts as function of hydrogen coverage have been observed and interpreted in terms of different surface reconstructions that affect the W-interlayer spacing[29]. The dataset shown has been measured at a H_2 residual gas pressure of 2×10^{-9} mbar. Already some minutes after flash-cleaning the peak position reaches a stable value although the surface is not yet hydrogen saturated. Under the improved vacuum conditions mentioned in the beginning, we find within 50 minutes a linear shift of the maximum of the distribution, starting from above 104 V to the shown value of 101 V. During this period, and at a fixed

scattering voltage of 102.5 V, the measured image asymmetry remains stable within the span of 0.8 to 0.9. A detailed analysis of the effects of hydrogen adsorption on SEMPA measurements will be in the focus of a forthcoming paper.

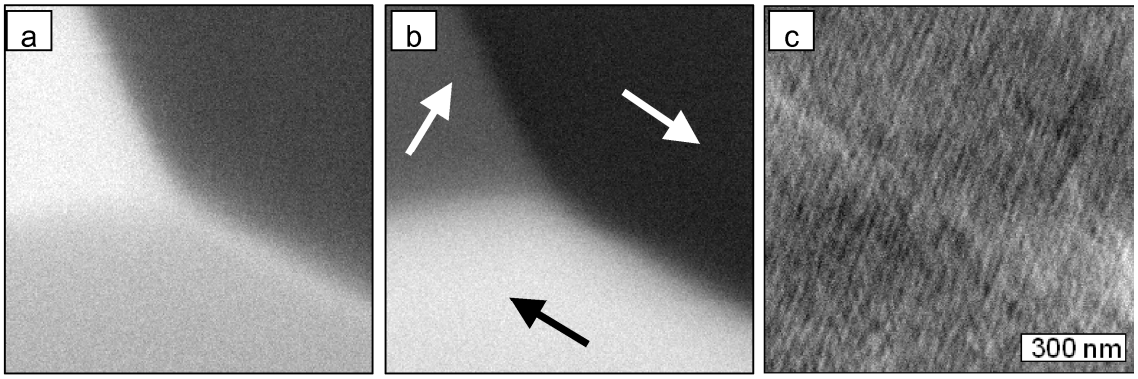

FIG. 9. SEMPA images from an Fe(100) whisker. The three images have been calculated from the simultaneously acquired intensity maps of the four detector channels. Panels (a) and (b) display the asymmetries corresponding to the *y* and *x* components of magnetization, respectively. Three magnetic domains are visible, with the magnetization (arrows) pointing along easy axes of magnetization. The surface Néel cap of the 180° wall is seen to extend as brig ht line from the center to the bottom-right (a). Panel (c) gives the sum of all four channels and thus equals standard non-magnetic SEM contrast. The lines running diagonally over the surface are grooves created by the low-angle sputter-cleaning process.

detector, which is not easy to measure for experimental reasons. If one assumes an incoming SE current of 1 nA at the tungsten crystal, the calculation predicts a count rate of 5.5 MCt s^{-1}. This value is about 5 times larger than the count rates experimentally observed here. As the SE yield is not precisely known, we cannot calculate the exact SE current and count rates, the uncertainty in the yield is less than a factor 2. Thus, we might conclude that the reduction of the count rates is due to a reduced transmission and a reduction of the acceptance angle at the transfer optics. In addition, low-energy losses at the retarding grid have to be considered (see below). As those effects are not included in the model, we call that theoretical result the ideal transmission. Still, the obtained count rate, above one million per second and channel, allows for taking quick overview images from iron samples within less than a minute, or taking high quality images within 5 – 10 minutes.

An important crosscheck of the detector performance, especially concerning the cleanliness and quality of the W crystal, can be experimentally performed by varying the retarding grid voltage while keeping the scattering potential fixed. In Fig. 8 the energy derivative of the measured count rates versus retarding grid potential is plotted. The plot looks (and actually should look) very similar to the principal SE intensity distribution. The dashed line in the plot is the SE intensity distribution convolved with the W(001) reflectivity, while the solid curve is the same distribution corrected for the influence of the energy-filtering aperture. Again, the results of the experiment and the latter model curve fit very well. In order to compare absolute numbers, one has to know the number of SE actually entering the

From the plot, the effect of the aperture becomes evident. Electrons above 10 eV, which have lower polarization, are suppressed. The noticeable reduction of transmission between 0 and 3 eV is a common detriment of a retarding grid setup [30]. In the present detector this breakdown of low energy transmission at the retarding grid will strongly reduce the higher image asymmetry of the single crystalline Fe sample, predicted in the model calculation. The total detector intensity distribution found here is roughly 20 times wider than the distribution that has been calculated for a standard SPLEED operating at high resolution [20]. It is still twice the width found in the same study for the optics running in a high transmission mode.

The latter experiment, measuring the energy distribution via modulation of the retarding grid potential, has turned out to be a very useful tool for checking the operation of the LEED detector. For instance, if the surface of the W(001) crystal is not well prepared, there will be a noticeable diffuse background at positive retarding grid voltages in the differentiated signal. Any charging at the sample can immediately be noticed from a peak shift in this distribution.

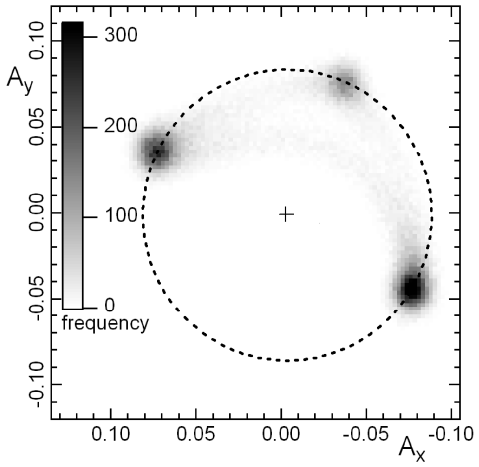

FIG. 10. Histogram of the two-dimensional asymmetry distribution from the two component images in Fig. 9 (a) and (b) of the sputtered Fe-whisker. The scale bar is given in occurrences per bin of $(0.25\ \%)^2$. Almost all of the intensity is concentrated in only three spots, which correspond to the three domains within the field of view. The radius of a circle drawn through the spots gives an asymmetry of 8.6 %, which is in perfect agreement with our model calculation for polycrystalline iron. The domain walls show up in the histogram as faint curved lines interconnecting the accumulation spots.

Image contrast and noise

So far, we have only shown energy resolved experimental data without considering magnetic properties. In order to characterize our detector and to test the model calculation on sensitivity, the analysis of magnetic images is required. Fig. 9 shows the domain image of a detail at the surface of an Fe(100) oriented single crystal (whisker). The whisker is several 100 µm in profile, about 1 cm long, running at an angle of 30° with respect to the image frame. We have sputtered the whisker by extended 1 keV Ar ion bombardment to obtain a clean ferromagnetic surface. The three images of Fig. 9 have been calculated from the four simultaneously acquired intensity maps of the independent detector channels. Panels (a) and (b) display the local asymmetry corresponding to the *y* and *x* components of magnetization. The magnetic structure of an unstrained (100) oriented iron whisker is governed by the cubic volume anisotropy with easy axes along <100> directions in the surface plane. Therefore, aside from domain walls, only four in-plane directions of magnetization exist at the (100) surface and no out of plane component is expected. Of these four directions, only three magnetic domains are visible in the image. They form two 90° walls oriented at 45° to the easy axes. The surface Néel cap of a 180° wall[1] is seen to extend as white line from the center to the lower-right. Panel (c) gives the sum of all four channels and thus the standard non-magnetic SEM contrast. The lines running diagonally over the surface are grooves originating from the low-angle sputter-cleaning process. This set of images demonstrates the perfect separation of magnetic and non-magnetic information within one dataset that is possible with a well-balanced detector on a nearly flat surface. For strongly corrugated objects, however, topographic effects can lead to artifacts in the magnetic contrast. The image has been acquired with a primary beam of 3 nA at 10 keV. It consists of 64 kpixels and has a total size of 1 µm². The dwell time per pixel was 5 ms, yielding roughly 13 kCt per pixel and per channel, and a total acquisition time of 5.5 minutes.

In order to analyze such an image quantitatively, the statistical distribution of all measured asymmetry (*x*,*y*) doublets within the image has to be evaluated[31]. This is done using the two-dimensional asymmetry histogram given in Fig. 10, which has been calculated from the data of Fig. 9 (a) and (b). Three dark spots visible in the histogram indicate the presence of three predominant asymmetry doublets in the data. They can thus be identified with the three magnetic domains of the image. The fourth possible domain orientation, which is absent from the image, would complete the isosceles triangle formed by the three spots into a square. The center of this square (marked by a cross) corresponds to zero spin polarization and thus gives the experimental asymmetry of the detector for this measurement. From the radius of a circle that is centered on this point, and passes through the accumulation points, the magnitude of the image asymmetry can be determined. We find a value of 8.6 %, which is only slightly less than the 9 % predicted from our model calculation for polycrystalline iron (see upper panel of Fig. 6). Because the whisker was not annealed after sputtering, the surface layers defining the spin polarization will be disordered, so this comparison is reasonable. The image contrast, by common definition the difference of the darkest and the brightest areas of an image normalized by the average intensity, is twice this value and thus 17.2 %. A second quantitative measure to be extracted from the histogram is the noise of the image. It is given by the uncertainty of the asymmetry measurement due to limited statistics and can be extracted from the profile of an accumulation point. A Gaussian fit to the line-profile across one of the spots in Fig. 10 yields a standard deviation of $\sigma = 0.0065$, which conforms to the error of $1/\sqrt{26{,}000} = 0.0062$ for the Poisson statistics of a single measurement. The image quality can be quantified by the contrast to noise ratio CNR, which is about 26.5 for the image shown. It scales with $\sqrt{Q\,\Delta t}$, where Δt is the acquisition time per pixel

and *Q* the quality of the detector. Beyond these numbers, further quantitative information about the magnetization pattern can be extracted from the histogram: The possibility to determine the in-plane angle of the local magnetization with small uncertainty ($\arctan(\pm 0.0065/0.086) \cong \pm 4°$) has been used to investigate fine magnetization details of artificially patterned nanostructures, which reveal information about dipolar coupling and edge roughness.[32]

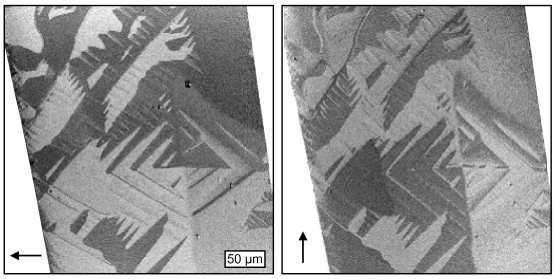

FIG. 11. Overview asymmetry images showing the full width of a second, less perfectly grown, Fe whisker. The observed fir-tree domain pattern indicates that its surfaces are only vicinal to {001} and that several twin boundaries are present. There is almost no shift in the sensitivity or the experimental asymmetry over the entire field of view of 350µm.

By analyzing the radius between the center and each asymmetry point in the histogram, the magnitude of the projected magnetization onto the detector plane can be determined. This has been applied together with the angular information to the analysis of the complex three-dimensional domain structure of the canted phase of ultrathin films close to spin reorientation transition[33]. An additional feature of the detector is demonstrated in Fig. 11. Due to the well-defined divergence of the beam in the drift tube, it is easy to find lens settings that allow for a wide field of view, while a homogeneous instrumental asymmetry and homogeneous spin sensitivity are maintained. The example given shows the full lateral extent of a less perfectly grown Fe-whisker. The non-ideal structure can be deduced from the observed fir-tree domain patterns which are typical for vicinal {001} surfaces. Several changes of pattern orientation, together with the sum image (not shown), hint at the presence of twin boundaries within the image. Image sizes of about (500 µm)² are feasible. In the example given, the local magnetic structure can hardly be understood without such an overview image – a fact that equally well holds e.g. for the study of coupling in arrays of magnetic nanostructures.

Acknowledgement

Financial support by the German Federal Ministry of Education and Research has been granted under BMBF 13N7484. We acknowledge additional funding by SFB668. We thank F. Lofink for critical reading and discussions.

References

[1] H.P. Oepen and J. Kirschner, Phys. Rev. Lett. **62** (7), 819 (1989).

[2] M.R. Scheinfein, J. Unguris, R.J. Celotta, and D.T. Pierce, Phys. Rev. Lett. **63** (6), 668 (1989).

[3] H.P. Oepen, J. Magn. Magn. Mater. **93**, 116 (1991).

[4] J. Unguris, R.J. Celotta, and D.T. Pierce, Phys. Rev. Lett. **67** (1), 140 (1991); H. Hopster, Phys. Rev. Lett. **83** (6), 1227–1230 (1999).

[5] M. Konoto, T. Kohashi, K. Koike, T. Arima, Y. Kaneko, T. Kimura, and Y. Tokura, Phys. Rev. Lett. **93** (10), 107201 (2004); M. Konoto, T. Kohashi, K. Koike, T. Arima, Y. Kaneko, T. Kimura, and Y. Tokura, Phys. Rev. B **71**, 184441 (2005).

[6] R. Allenspach and A. Bischof, Phys. Rev. Lett. **69** (23), 3385–3388 (1992); R. Allenspach, M. Stampanoni, and A. Bischof, Phys. Rev. Lett. **65** (26), 3344 (1990); M. Speckmann, H.P. Oepen, and H. Ibach, Phys. Rev. Lett. **75** (10), 2035 (1995).

[7] T. VanZandt, R. Browning, and M. Landolt, J. Appl. Phys. **69** (3), 1564 (1991).

[8] T. Kohashi and K. Koike, Jpn. J. Appl. Phys. **40**, L1264 (2001).

[9] developed in cooperation with Carl Zeiss NTS GmbH, CEOS GmbH, and Omicron NanoTechnology GmbH

[10] K. Koike and K. Hayakawa, Jpn. J. Appl. Phys. **23** (3), L187 (1984); R. Allenspach, J. Magn. Magn. Mater. **129** (2-3), 160 (1994).

[11] M.R. Scheinfein, D.T. Pierce, J. Unguris, J.J. McClelland, R.J. Celotta, and M.H. Kelley, Rev. Sci. Instrum. **60** (1), 1 (1989).

[12] J. Kirschner, *Polarized Electrons at Surfaces*. (Springer-Verlag, Berlin, 1985).

[13] H.P. Oepen and J. Kirschner, J. Phys. -Paris **49 C-8** (Colloque C8), 1853 (1988); H.P. Oepen and J. Kirschner, Scanning Microsc. **5** (1), 1 (1991).

[14] M.R. Scheinfein, J. Unguris, M.H. Kelley, D.T. Pierce, and R.J. Celotta, Rev. Sci. Instrum. **61** (10), 2501 (1990).

[15] R. Bertacco, M. Merano, and F. Ciccacci, Appl. Phys. Lett. **72** (16), 2050 (1998); A. Winkelmann, D. Hartung, H. Engelhard, C.T. Chiang, and J. Kirschner, Rev. Sci. Instrum. **79** (8), 083303 (2008); T. Okuda, Y. Takeichi, Y. Maeda, A. Harasawa, I. Matsuda, T. Kinoshita, and A. Kakizaki, Rev. Sci. Instrum. **79** (12), 123117 (2008).

[16] C. Jozwiak, J. Graf, G. Lebedev, N. Andresen, A.K. Schmid, A.V. Fedorov, F. El Gabaly, W. Wan, A. Lanzara, and Z. Hussain, Rev. Sci. Instrum. **81** (5), 053904 (2010).

[17] H.P. Oepen and H. Hopster, in *Magnetic Microscopy of Nanostructures*, edited by H. Hopster and H.P. Oepen (Springer, Berlin Heidelberg New York, 2005), pp. 137.

[18] J. Kirschner and R. Feder, Phys. Rev. Lett. **42** (15), 1008–1011 (1979); R. Feder and J. Kirschner, Surf. Sci. **103** (1), 75 (1981).

[19] G.C. Wang, R.J. Celotta, and D.T. Pierce, Phys. Rev. B **23** (4), 1761 (1981).

[20] D. Yu, C. Math, M. Meier, M. Escher, G. Rangelov, and M. Donath, Surf. Sci. **601** (24), 5803 (2007).

[21] J. Kessler, *Polarized Electrons*, 2nd ed. (Springer-Verlag, Berlin Heidelberg New York Tokyo, 1985).

[22] L. Reimer, *Scanning electron microscopy: physics of image formation and microanalysis*, 2nd ed. (Springer-Verlag, Berlin Heidelberg New York, 1998).

[23] G. Schönhense and H.C. Siegmann, Annalen der Physik **2** (5), 465 (1993).

[24] J. Kirschner and K. Koike, Surf. Sci. **273** (1-2), 147 (1992).

[25] H. Hopster, R. Raue, E. Kisker, G. Güntherodt, and M. Campagna, Phys. Rev. Lett. **50** (1), 70 (1983); M.S. Hammond, G. Fahsold, and J. Kirschner, Phys. Rev. B **45** (11), 6131–6141 (1992).

[26] H. Hopster and H.P. Oepen, in *Nanoscience and Technology* (Springer, Berlin, 2005), pp. 313.

[27] H. Hopster, Phys. Rev. B **36** (4), 2325 (1987).

[28] M. Yasuda, K. Tamura, H. Kawata, and K. Murata, Journal of Physics D-Applied Physics **34** (13), 1955 (2001).

[29] D.A. King and G. Thomas, Surf. Sci. **92** (1), 201 (1980); R.A. Barker and P.J. Estrup, J. Chem. Phys. **74** (2), 1442 (1981).

[30] D.A. Huchital and J.D. Rigden, J. Appl. Phys. **43** (5), 2291 (1972).

[31] R. Frömter, C. Menk, H. Stillrich, and H.P. Oepen, Vacuum **82** (4), 395 (2007).

[32] S. Hankemeier, R. Frömter, N. Mikuszeit, D. Stickler, H. Stillrich, S. Pütter, E.Y. Vedmedenko, and H.P. Oepen, Phys. Rev. Lett. **103** (14), 147204 (2009).

[33] R. Frömter, H. Stillrich, C. Menk, and H.P. Oepen, Phys. Rev. Lett. **100** (20), 207202 (2008).

2.2.1. Image formation

In this section I would like to comment on the image formation and beam focussing as well as on the difference between lateral magnetic resolution and the resolution observable in the sum image.

Fig. 2.5 (a) and (b) shows the 2D-histogram of a three domain pattern observed at the surface of an Fe(100) whisker acquired with a primary beam energy $E_{\mathrm{prim}} =$ 10 kV and $E_{\mathrm{prim}} = 5$ kV, respectively. The associated domain pattern is plotted in [P1, Fig. 9]. The physics of the domain formation in an Fe(100) whisker is well understood and discussed e.g. in [Oep89, Sch91b]. Here, it is focused on the 180° wall separating two domain along the ⟨100⟩ crystal direction. Within the volume of the crystal the wall is a 180° Bloch wall, which changes to an asymmetric 180° Néel wall in the vicinity of the surface [Sch89b]. Within an 180° Néel wall the magnetization rotation happens completely in-plane. Therefore, when imaging the wall with SEMPA, one would expect to obtain the full magnetic signal (asymmetry) from the wall, which would be represented by a "signal stripe" interconnecting the three accumulation points and running on the black circle in the 2D-histogram in Fig. 2.5(a), (b). The actual measurement shows this signal stripe with significantly reduced signal, emphasized with a red arc in Fig. 2.5(a), (b). With a primary beam energy of $E_{\mathrm{prim}} = 10$ kV, $E_{\mathrm{prim}} = 5$ kV the signal is reduced to 52 %, 64 % of the maximum asymmetry, respectively.

One reason for signal loss could be an insufficient lateral resolution of the primary beam to resolve the domain wall, thus giving the average of two magnetization orientations resulting in a reduced degree of spin polarization. From the simultaneously acquired sum image the lateral resolution was appointed 15 nm which is much smaller as the domain wall width of 220 nm, thus canceling out this explanation.

To find the key for the understanding of the measurement one has to look at the origin of the spin polarized secondary electrons. In Fig. 2.5(c) a sketch of the interaction volume of the primary electron beam in a sample is shown. Secondary electrons of type one (SE1) are created directly at the position of the incoming primary beam carrying the full lateral resolution as the escape depth of the SE is ≈1.5 nm for the 3*d*-metals [Ono79]. Secondary electrons of type two (SE2), however, are created from backscattered electrons (BSE) at a distance from the primary beam position up to the escape depth of the BSE [Rei10](p168). In the sum (intensity) image, the SE2 give only a constant offset, while the SE1 are responsible for the contrast with full lateral resolution.

The magnetic signal in SEMPA is coming from both the spin polarized SE1 and SE2. While imaging a domain wall the average spin polarization of the SE2 is strongly reduced due to the large surface area which can have opposite orientation of magnetization at the positions where the SE2 originate. Only the polarization of the SE1 remains, resulting in a reduced total polarization as observed in Fig. 2.5(a), (b) (red arc).

The escape depth of the BSE and therefore the area of origin of the SE2 is roughly proportional to the primary beam energy [Sei76]. Copper, as example for medium atomic number elements like Fe,Co and Ni, has a BSE escape depth of 55 nm / 175 nm for $E_{\mathrm{prim}} = 5$ kV / $E_{\mathrm{prim}} = 10$ kV [Rei85]. This explains the different

intensities of the magnetic signal of the 180° wall at 10 kV and 5 kV in Fig. 2.5(a), (b): At lower primary energy the area of origin of the SE2 is smaller thus resulting in an increased magnetic signal of the domain wall compared to higher primary energies.

The knowledge of the local origin of the secondary electrons is of great importance for the interpretation of magnetic images. A misinterpretation of magnetic images [Li06] for example has recently caused some irritation and debate [Bod08] throughout the community concerning the diameter of a vortex core in a nanodisc [Gus04].

The same applies for secondary electrons which emerge from a textured surface thus causing geometrical edge contrast. When the primary SEM beam impinges onto a sharp edge in an otherwise flat surface, e.g. caused by deep FIB milling, the SE will exit the sample at this position at a different angle than the electrons from the flat reference surface. This changes the SE trajectories and may favor the diffraction of the electrons during the LEED spin-detection process into one of the four MCP's for geometrical reasons. A non-magnetic intensity asymmetry is then caused which results in a "fake" magnetic signal at sharp edges [Oep07]. The effect can be seen for example in the top right corner of Fig. 1.1(a). In literature, however, examples have been given for clear magnetic contrast despite strong sample morphology [Mat91].

To finish this section, I would like to comment on the focussing procedure necessary for SEMPA imaging. At a standard SEM, one usually focuses the electron column based on the live image which comes from the SE. The problem when doing SEMPA is that all SE are guided into the spin detector and only the BSE remain which have an intrinsically much lower lateral resolution (Fig. 2.5(c)), thus high quality alignment of the primary beam guiding optics based on the BSE image is impossible. A work-around is to feed the four MCP signals of the spin detector in real-time into the image formation device of the SEM, thus accessing the high resolution of the SE. Due to the low reflectivity of the W(100) crystal the so achievable count rates are three orders of magnitude lower as the usual SEM intensity rates. Nevertheless, the implementation of this technique proved to be a valuable addition to the microscope setup. It was necessary to develop a fast electronic compound which adds and converts the count rates of the MCPs into an analog signal which can be processed by the SEM electronics. The circuit diagram of the electronics can be found in the appendix on page 130.

2.3. Long time stability

The question for the long time stability of the detector, i.e. what influence have hydrogen adsorbates on the image quality and how often is it necessary to flash the tungsten crystal in order to achieve best image quality during a measurement session, has been addressed previously for a specific detector in [Yu07] and in general for the spin dependent scattering process in [Saw92]. Both, however, do not discuss the connection between the asymmetry variation and the energy peak shift of the sensitivity mentioned in [P1, Fig. 7] with time that is caused by hydrogen absorbtion on the detector crystal. In the context of [P1] it is referred to a forthcoming paper.

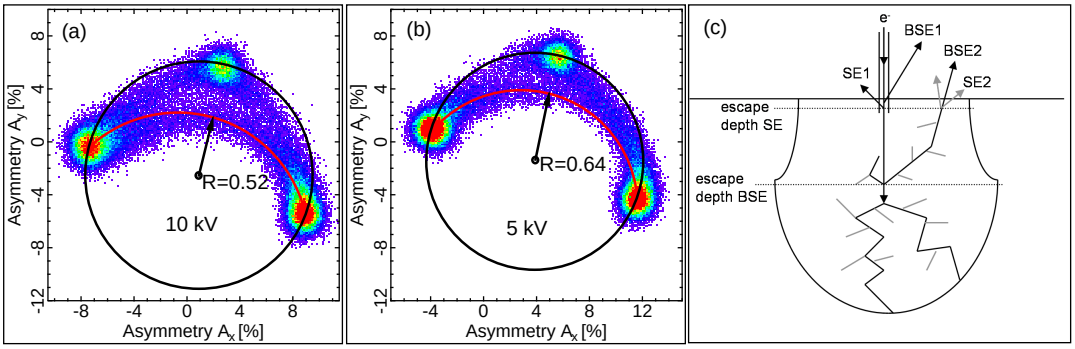

Figure 2.5.: (a) reproduces the 2D-histogram shown in [P1, Fig. 10] associated to three domains at the surface of an Fe(100) whisker. (b) shows a 2D-histogram of the same area imaged with $E_{\mathrm{prim}} = 5$ kV instead of $E_{\mathrm{prim}} = 10$ kV. The black circle indicates the maximum asymmetry of the measurement. The red arc emphasizes the magnetic signal of the 180° wall which separates the two main domains. In (c) a schematic illustration of the generation of secondary electrons SE1 and SE2 and backscattered electrons BSE1 and BSE2 is shown.

The detailed analysis of the effects of hydrogen adsorption on the quality of SEMPA measurements are discussed herein. A preliminary version of this work is attached in the following [P2].

The asymmetry measurement in dependence of time after flash cleaning in [P2, Fig. 3] are obtained from the analysis of many images of the three domain area of the Fe-whisker [P1, Fig. 9]. They triggered the detailed investigation of transmission curves in dependence of time after flash cleaning [P2, Fig. 1] which revealed the peak-shift as well as the intensity variation with time [P2, Fig. 2]. The key to the understanding gave the review paper of the "Interaction of hydrogen with solid surfaces" [Chr88] and in particular [Kin80]. The literature research and the analysis of the already published data (LEED I-V-curves) was conducted together with F. Lofink who also wrote large parts of the paper.

Long time stability of an optimized SPLEED-detector for magnetic imaging / SEMPA

F. Lofink and S.Hankemeier et al.

in preparation, to be submitted to
Journal of Vacuum Science and Technology (2010)

Preprint

P2

The numbers by which citations are referenced in the following article are only valid within the article.

APS/123-QED

Long time stability of an optimized SPLEED-detector for magnetic imaging / SEMPA

F. Lofink* and S. Hankemeier et al.
Institut für Angewandte Physik, Universität Hamburg,
Jungiusstr. 11, 20355 Hamburg, Germany

(Dated: January 27, 2011)

In this paper we present the results of our investigation on the long time stability of our SEMPA system. We discusses the causes of the variation of image quality and its application as a diagnostic tool. The time-related decrease of image quality is commonly attributed to the adsorption of impurities such as hydrogen and carbonoxids onto the surface of the W(001) single crystal. We measure a time dependent energy shift of the (2,0) LEED beams of the W(001) single crystal, starting with a flash cleaned W(001)-surface. The information is important to characterize and optimize the SEMPA detector especially related to long time stability. We found that hydrogen induced ordered reconstruction of the W(001) single crystal surface has no significant effect on the detector quality. Eventually, the onset of the disordering process at about 0.25 monolayers (ML) of hydrogen coverage decreases the quality measurably. This is equivalent to a time window up to 60 minutes at a hydrogen pressure of about 9×10^{-10} mbar in the surrounding area of the detector crystal. The time dependent behavior of the shift allows the correlation between hydrogen coverage and time after flash cleaning under consideration of the H_2 sticking probability. With this knowledge, one can easily estimate the hydrogen pressure in the vicinity of the detector crystal.

PACS numbers:

I. INTRODUCTION

The aim of SEMPA (secondary electron microscope with polarization analysis) is to map the magnetization of ferromagnetic surfaces. The discovery of the fact that the secondary electrons extracted from a ferromagnetic sample due to excitations by either electrons or photons have their magnetic moment parallel (and hence the spin anti-parallel) to the sample magnetization vector at their origin has triggered the development of SEMPA [1–3]. A high surface sensitivity of this imaging technique is caused by energy losses of the escaping secondary electrons (SE) due to stoner excitation [4] in combination with a high scattering cross section for these electrons in 3*d*-ferromagnets.

The unique feature of SEMPA is that it generates a map of the magnetization orientation and relative magnitude by measuring the SE spin-polarization direct and point by point. Today SEMPA is an established imaging technique for the investigation of magnetic structures in the range from a few hundred microns down to nanometers.

Presently three different types of polarization detectors are used: (I) the conventional high energy (100 keV) Mott polarimeter. It uses the scattering of high energy electrons at atom cores [5, 6] for polarization analysis. (II) detectors which realizes the polarization analysis via low electron scattering at an amorphous thin film (low energy diffuse scattering, LEDS [7, 8]) and (III) scattering at a tungsten single crystal (low energy electron scattering, LEED [5, 9, 10]) which is applied here. The LEED detector is distinguished from the Mott detector by an intrinsic energy filter which automatically discriminates inelastically scattered electrons. This leads to a better transmission for the secondary electrons originating from the sample. With respect to the LEDS detector the LEED detector is distinguished by a significantly higher value of the Sherman function (0.27 in comparison to 0.15) at the optimum working point, thus giving images with a better magnetic contrast. This optimum working point is an average scattering energy of the SE at the W(001) single crystal of 104.5 eV which is equivalent to a potential of 102.5 V at the W(001) [4]. A relative low efficiency (described by the figure of merit, FOM) in the range of 2×10^{-4} is common with all these detector types. That is why optimization is necessary for all these detectors. To evaluate the optimization, it is best to consider the detector quality instead of the efficiency as it was recently introduced [11]. The assessment of the stability of the detector discussed in this article will be carried out via the so defined quality $Q = 2AT^2$. Here T is the total transmission of SE's originating from the sample into the detector and A is the achieved image asymmetry. We discuss the evolution of both parameters independently. The major focus of this study is the investigation of the long time stability of our SEMPA system. The time-related decrease of image quality is commonly attributed to the adsorption of impurities such as hydrogen and carbonoxids onto the surface of the W(001) single crystal. Especially a time-dependent decreasing trend of the ability for polarization detection was observed earlier [12, 13]. This article presents measurements on the time-related changes of the detector quality of our LEED detector, discusses its reasons and its possible application as a diagnostic tool.

*Electronic address: flofink@physnet.uni-hamburg.de

II. EXPERIMENTAL

The experimental setup of our detector system as well as a careful discussion of the energy filtering and transmission properties can be found in [11]. The important aspects of our detector system for the following discussion are briefly summarized:

Our LEED detector was optimized with respect to its application for SEMPA. With this design it is possible to take overview images in less than a minute and high quality images within 5-10 minutes with a primary beam current of about 5 nA. Basically the detector utilizes the intensities of the four (2,0) LEED beams to analyze the spin polarization of the secondary electrons.

There are two crucial qualities of SE which must be considered, if one is comparing a classical polarimeter with an energy resolution of about 0.2 eV [14] and a LEED detector in SEMPA with a broad energy acceptance due to the stated optimization. First, the secondary electrons cannot be considered monochromatic; second, the polarization of those electrons is energy dependent. Another key difference is that we have a fixed setup which is optimized for a scattering potential of 102.5 V resulting in filtered energy acceptance of the detector. Thus, our detected intensity as well as the asymmetry represents a combination of all these facts, e.g. the intensity can be described as a convolution of the mentioned energy acceptance with the associated monochromatic resolved I-V-curve as obtained from a classical polarimeter experiment and the secondary electron distribution which has to be determined experimentally.

The main feature of the scattering process we investigate throughout this paper is the intensity of the (2,0) beams in respect to the scattering potential and the (time-dependent) surface condition. A scan of the scattering voltage at a specific time after cleaning yields an intensity curve which is correlated to the surface condition of the scattering crystal. This intensity curves aren't monochromatic resolved, but nevertheless give a fingerprint of the crystal scattering properties, in particular when one takes the filtering properties of the detector as well as the secondary electron distribution into account. The properties of interest are reflectivity and beam-shift which can be accessed via the experimentally observable transmission as long as the beam is situated inside the detector, as described further below in detail.

Due to the high surface sensitivity of the LEED scattering process only a few monolayers (ML) of adsorbates are needed to completely change the LEED pattern and to diminish the quality of the spin analyzing process. Crystal cleaning before imaging and very good UHV conditions are essential for a successful experiment. The hydrogen partial pressure in our chamber is 4×10^{-10} mbar. We start with a CO flash of the detector crystal, hereby assuming a clean surface thereafter [12, 15] and analyze the detector properties in dependence on time after flash cleaning.

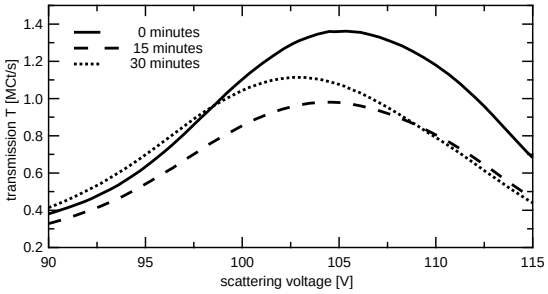

FIG. 1: The plot shows the intensity distribution of the detected transmission depending on the scattering potential of the W(001) single crystal for different times after flash cleaning. The asymmetric shape of the curves reflects the asymmetric energy filtering distribution [11]. By means of the intensity maximum and its position one receive the results in Fig.2a and Fig.2b.

III. RESULTS AND DISCUSSION

The detector system is designed for a scattering potential of 102.5 V. Around this working point the detector has a slightly asymmetric energy acceptance due to a Gaussian angle acceptance (α=40.64° with respect to the tungsten surface plane, σ=5°). A variation of the crystal potential therefore necessarily yields a decrease of the transmission. In particular a change of ±5 V around 102.5 V yields a projected intrinsic intensity decrease of 4 %.

Three exemplarily measurements of beam intensity versus scattering potential are plotted as black lines in Fig.1. The SE originate from an oxidized copper surface in order to obtain a constant SE yield throughout the experiments. The three curves are correlated to the elapsed time after flash cleaning. The differences between the three curves are much larger than the expected maximum intrinsic intensity decrease of 4 %. The observed variation of transmission curves can therefore be attributed to a change of the scattering process itself. Direct after flash cleaning the peak of the intensity curve is located at 105.4 V with a transmission of 1.35×10^6 counts. After 15 min the peak is located at 104.6 V and the transmission has decreased by approximately 30% to 0.95×10^6 counts. After 30 min the peak has moved to 102.7 V while the transmission has again increased to 1.1×10^6 counts. Thus, we observe a time related peak shift as well as a significant variation in intensity.

The resulting evolution of the position of the peak intensity is plotted in Fig.2a versus time (bottom x-axis). The peak shifts nearly linearly from 105 V to 101 V during the first 60 minutes. After 60 minutes a clear kink in the curve is visible. Only a slight peak-shift follows. Correlated to the change of the peak position is the peak-

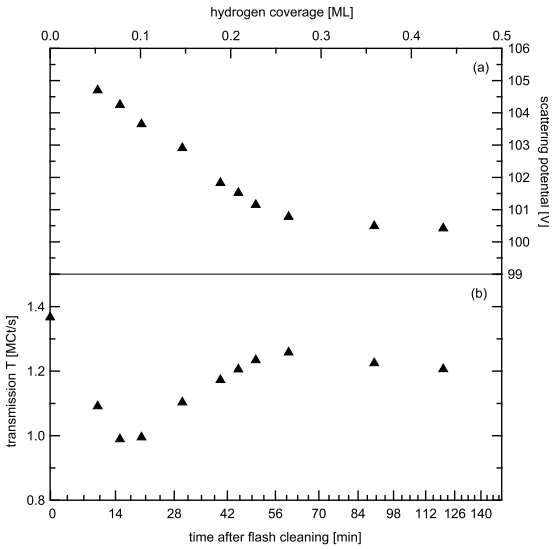

FIG. 2: (a) Peak shift and (b) variations of the peak intensity due to hydrogen induced surface reconstruction of the transmission curve (Fig.1) witch is obtained here via a variation of the scattering potential of the W(001) single crystal plotted versus time after flash cleaning as well as hydrogen coverage.

intensity plotted in the lower part of the graph (Fig. 2b). During the first 60 minutes a considerable intensity variation is evident. After 60 minutes the curve is marked by a nearly linear and slightly decreasing intensity. In conclusion the results of Fig.2a and Fig.2b show a clear influence of time after flash cleaning on the scattering properties of the W(001) divided in two intervals before and after 60 minutes, related to different surface conditions of the scattering crystal:

Possible reasons for a beam shift as observed in Fig.2a of a LEED spot are changes in temperature, interlayer spacing or the inner potential. As temperature effects can be ruled out in this case, a variation of interlayer spacing or inner potential must cause the shift. From the literature it is known that a hydrogen induced reconstruction of a W(001) surface has a strong influence on both interlayer spacing and inner potential [16–18]. It was shown that increasing hydrogen coverage shifts the major peaks in the I-V-curve towards lower energies until saturation. These beam-shifts are in the range of about 4 eV and therefore significantly larger then the observed change of the work function (0.85 eV) [17]. Thus, the dominating influence comes from a variation of interlayer spacing. The studies show that the interlayer spacing shifts from 1.48 Å for the clean surface to 1.51 Å at saturation. This shift is already completed at hydrogen coverage of about 0.25 ML [17]. On the basis of this fact one can associate the kink in Fig.2a (60 min) with hydrogen coverage of 0.25 ML. This interpretation leads us to the correlation between hydrogen coverage and time after flash cleaning under consideration of the H_2 sticking probability [17]. We calculated the hydrogen pressure in the surrounding area of the tungsten single crystal to be 9×10^{-10} mbar.

Interpretation of the curves in Fig. 2 and Fig. 3 based on the hydrogen coverage (top axis) gives then following results: The crystal starts with an ordered 1x1 surface direct after flash cleaning. The surface structure is undergoing several ordered phase transitions during the first 60 minutes to become a largely-ordered 2x2-H surface at about 0.25 ML (associated with the kink in Fig.2a). A phase transition to a disordered surface follows. From 0.4 ML coverage on, the surface slowly regains an ordered 1x1-H surface, which is completed at saturation (1 ML). The disordering process above 0.25 ML of the surface causes random scattering and decreases the intensity as well as the asymmetry of the order beams [17]. This explains the intensity decrease in Fig. 2b above 0.25 ML (60 min). The variations up to 0.25 ML (60 min) are caused by ordered surface reconstructions, as one might expect. However, the exact course of these intensity variations can only be reproduced by full dynamical LEED calculations. This is out of the scope of this work. The important question is now the influence of peak-shift and intensity variation on the quality of the detector at its optimum working point. To determine the impact we have imaged an Fe(100) single crystal (Fe-whisker) at different times after flash cleaning always with the same scattering potential of 102.5 V. From these images one can derive the time-related evolution of asymmetry and transmission under working conditions. The results of this investigation are presented in Fig. 3a and Fig. 3b. The recording duration for one image amounts to eight minutes which gives a time error of ±4 minutes.

The intensity curve in Fig. 3b is marked by a weak increase up to 0.1 ML hydrogen coverage, a broad maximum between 0.1 ML to 0.2 ML followed by a weak decrease up to 0.25 ML and a significant decrease thereafter. All caused by the fact that the (20) LEED beam shifts through the field of view. The following significant decrease can attributed to random scattering as also observed in Fig. 2b. The obtainable asymmetry (Fig. 3a) is basically constant with a value of 9 % up to 0.25 ML hydrogen coverage. Only a weak maximum at 0.15 ML can be recognized. Again, the onset of the decrease in asymmetry coincides with the completion of the peak shift (Fig. 2a). The asymmetry, therefore, is not susceptible for the ordered surface reconstructions of the tungsten single crystal. Because of the quadratic dependency of the quality on the asymmetry, this fact is crucial for the long time stability of the spin detection ability. Eventually, the time dependence of the detector quality is shown in Fig. 3c. Up to 0.25 ML hydrogen coverage we receive nearly unchanged quality. The optimum working range is between 0.1 ML and 0.2 ML hydrogen coverage. One might expect that the quality increases again when the

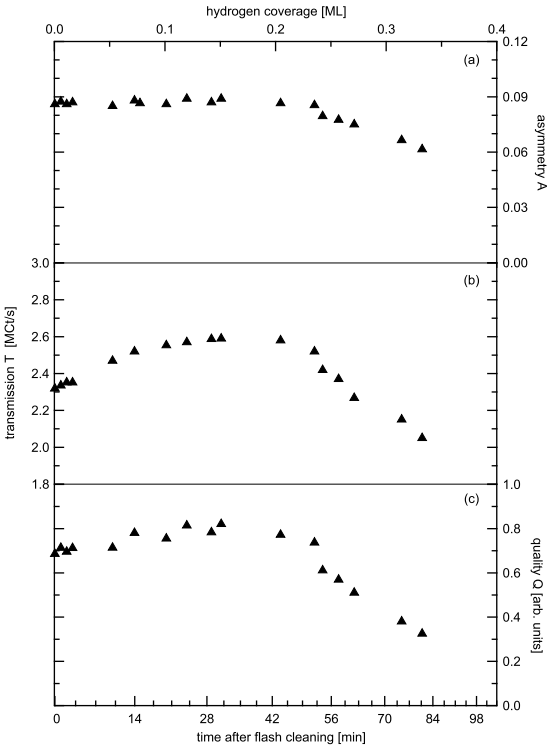

FIG. 3: The variation in the achieved asymmetry of two opposite (20)-beams diffracted from the W(001)@102.5 V (a), the transmission into the detector (b) and the detector quality $Q = 2AT^2$ (c) based on the analysis of the images of an Fe-whisker is plotted versus time after flash cleaning as well as hydrogen coverage. The measured values are obtained via repeated imaging of the same position of an iron whisker.

surface exhibits an ordered structure (1x1-H) at saturation. At that time, however, the strong influence of a small amount of heavier contaminants such as CO on the scattering properties is dominating and therefore the scattering will be mostly random.

How can one use the results of this study for the characterization as well as to optimize a LEED detector for magnetic imaging (SEMPA)? On the one hand it gives clear evidence that the hydrogen induced ordered reconstruction of the W(001) single crystal surface has no significant effect on the detector quality. This gives a constant imaging conditions until finally the onset of the disordering process at about 0.25 ML hydrogen coverage decreases the quality measurably. This is equivalent to a time window up to 60 minutes at a hydrogen pressure of about 9×10^{-10} mbar in the surrounding area of the detector crystal. Consequently it is necessary to flash clean the crystal after 60 minutes to keep constant imaging conditions. On the other hand the hydrogen pressure around the detector is usually not well known. We present a diagnostic procedure to determine this pressure: By observing the time dependence of the peak shift of the (20)-beam one can easily estimate the amount of hydrogen in the vicinity of the crystal. The information is important to characterize as well as to optimize the SEMPA detector in order to achieve long time stability of detection quality.

Acknowledgments

Financial support by DFG via SFB 668 is gratefully acknowledged.

[1] G. Chrobok and M. Hofmann, "Electron spin polarization of secondary electrons ejected from magnetized europium oxide", *Physics Letters A*, **57**, 257 (1976)
[2] J. Kirschner and R. Feder, "Spin Polarization in Double Diffraction of Low-Energy Electrons from W(001): Experiment and Theory", *Phys. Rev. Lett.*, **42**, 1008 (1979)
[3] G.-C. Wang, J. Unguris, D. Pierce, and R. Celotta, "Pleed study of temperature and hydrogen induced reconstruction and reordering of W(100)", *Surface Science Letters*, **114**, L35 (1982)
[4] J. Kirschner, *Polarized Electrons at Surfaces*, Springer, Berlin (1985)
[5] K. Koike, H. Matsuyama, and K. Hayakawa, "Spin-Polarized Scanning Electron Microscope Equipped with a Thumb-Size Spin Detector", *Jpn. J. Appl. Phys.*, **27**, L1352 (1984)
[6] T. J. Gay and F. B. Dunning, "Mott Electron Polarimetry", *Review of Scientific Instruments*, **63**, 1635 (1992)
[7] M. R. Scheinfein, J. Unguris, M. H. Kelley, D. T. Pierce, and R. J. Celotta, "Scanning electron microscopy with polarization analysis (SEMPA)", *Rev. Sci. Instrum.*, **61**, 2501 (1990)
[8] J. Uunguris, G. G. Hembree, R. J. Celotta, and D. T. Pierce, "High-resolution Magnetic Microstructure Imaging Using Secondary-electron Spin Polarization Analysis In A Scanning Electron-microscope", *Journal of Microscopy-oxford*, **139**, RP1 (1985)
[9] H. Oepen and J. Kirschner, "Imaging of magnetic microstructures at surfaces - The scanning electron microscope with spin polarization analysis", *Scanning Microsc.*, **5**, 1 (1991)
[10] R. Allenspach, "Ultrathin films: magnetism on the microscopic scale", *J. Magn. Magn. Mater.*, **129**, 160 (1994)
[11] R. Frömter, S. Hankemeier, H. P. Oepen, and

J. Kirschner, "Optimizing a LEED spin-polarization analyzer for imaging of magnetic surface structures", *submitted to Review of Scientific Instruments* (2010)

[12] D. Yu, C. Math, M. Meier, M. Escher, G. Rangelov, and M. Donath, "Characterisation and application of a SPLEED-based spin polarisation analyser", *Surf. Sci.*, **601**, 5803 (2007)

[13] D. Venus and J. Kirschner, "Momentum dependence of the Stoner excitation spectrum of iron using spin-polarized electron-energy-loss spectroscopy", *Phys. Rev. B*, **37**, 2199 (1988)

[14] J. Kirschner, "Direct and Exchange Contributions in Inelastic Scattering of Spin-Polarized Electrons from Iron", *Phys. Rev. Lett.*, **55**, 973 (1985)

[15] S. Krause, L. Berbil-Bautista, G. Herzog, M. Bode, and R. Wiesendanger, "Current-Induced Magnetization Switching with a Spin-Polarized Scanning Tunneling Microscope", *Science*, **317**, 1537 (2007)

[16] K. Christmann, "Interaction of hydrogen with solid surfaces", *Surface Science Reports*, **9**, 1 (1988)

[17] D. A. King and G. Thomas, "Displacive surface phases formed by hydrogen chemisorption on W 001", *Surf. Sci.*, **92**, 201 (1980)

[18] R. A. Barker and P. J. Estrup, "Surface structures and phase diagram for the H/W(001) chemisorption system", *J. Chem. Phys.*, **74**, 1442 (1981)

2.4. Sample preparation

A major restriction of the SEMPA technique is the requirement for clean ferromagnetic samples, as the escape depth of the SE is rather low. For Nickel and SE with $E = 10$ eV one expects an escape depth of 1-2 nm from the so called universal curve of the energy dependence of the mean free path [Sea79]. Abraham and Hopster [Hop89] have shown that the escape depth from Ni and its oxides is actually much smaller with 0.4-0.5 nm. For iron a longer escape depth of 2.2(2.9) nm for an energy of 10(2) eV was measured [Van90]. Whatever sample system is in the focus of an investigation, the numbers show that magnetic information of the SEMPA images comes from the topmost 5 monolayers (ML) of the sample. In case the surface is oxidized or covered with an adsorbate, the SE are no longer spin polarized and SEMPA imaging is impossible.

There are three ways around this problem: In-situ preparation of the sample, cleaning by soft sputtering or "dusting" with a thin ferromagnetic layer of cobalt or iron [Van91]. In all cases ultrahigh vacuum conditions are necessary to minimize the degradation of the surface over time, e.g. with a base pressure of 1×10^{-10} mbar, it takes roughly three hours to adsorb a single ML of "dirt" (residual gas) [Ede97] which already makes imaging unpleasant in most cases.

2.4.1. Iron dusting

A simple way of contrast enhancement is to dust the sample with a thin iron layer [VanZandt1990]. Iron has the highest spin polarization of Fe,Ni and Co [Oep05, All94] thus giving high contrast but is relatively sensitive to oxidation. The technique is comparable to the well known Bitter decoration method [Bit32] where external particles on the surface are imaged. The basic differences to the Bitter method are that a very thin homogeneous marker film is used and that SEMPA observes the magnetization of the Fe film directly, while the Bitter particles align in the gradient of the magnetic field of the sample. Of decisive importance is the film thickness. The film should be thick enough to be ferromagnetically ordered thus giving a high spin polarization, i.e. thicker than approximately 1.5 ML [Dür89]. It must, at the same time, be thin enough so that the contribution of the film to the magnetic free energy does not change the domain structure upon deposition.

Fig. 2.6(a) shows MOKE measurements of iron films with different thickness evaporated on naturally oxidized silicon wafer substrate with a 2 nm Pt seed layer. The iron film with a thickness of 4 nm shows a ferromagnetic hysteresis with remanence. For 1.0 nm and 1.5 nm a paramagnetic signature without remanence is visible. In between, the hysteresis curves show the emerging ferromagnetism of the film.

In Fig. 2.6(c) a SEMPA image of an in-situ fabricated iron film with an evaporation time of 25 min (4 nm) is shown. A ferromagnetically ordered in-plane maze domain pattern is visible as expected for thick Fe films [Zav00]. As no thickness measurement via a quartz crystal-oscillator rate monitor is available in the SEMPA chamber, the Fe evaporation time was measured and the thickness calibrated via the onset of ferromagnetism at 4 nm (Fig. 2.6(a)(c)). The evaporation rate was kept constant via the built-in flux monitor with I_{flux}=20 nA in the evaporator, thus resulting in

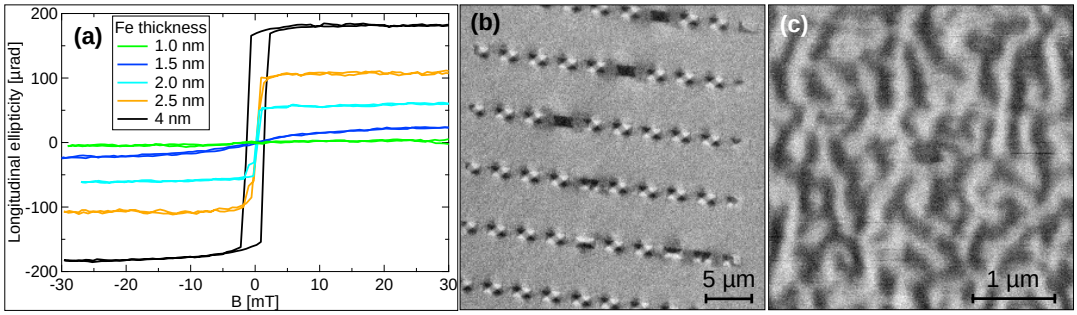

Figure 2.6.: (a) shows MOKE measurements of iron films with different thicknesses deposited on a silicon wafer substrate. The plot is shown by courtesy of M. Hille. In (b) a SEMPA image of Py rectangles on a silicon wafer is displayed. Prior to imaging an iron film of approx. 2 nm was evaporated. The stray-field of single domain particles is visible. In (c) approx. 4 nm iron were evaporated on a clean silicon wafer substrate. A maze magnetization pattern is visible.

the standard dusting rate of 0.16 nm/min.

The SEMPA images of the Py ellipse shown in Fig. 2.3 and Fig. 2.4 were also acquired with an iron dusting layer present. The evaporation time was much shorter, 8 min, resulting in a thickness of approx. 1.3 nm. In Fig. 2.3, magnetic contrast is only visible on-top of the Py ellipse. For this thickness the iron is paramagnetic on the silicon wafer (Fig. 2.6(a)) resulting in zero spin polarization. On the Py, however, the iron couples via exchange interaction [Van91] to the Py and enhances the magnetic contrast.

In Fig. 2.6(b) a SEMPA image of small Py rectangles with an approx. 2 nm thick Fe film (12 min evaporated) is shown. Most of the rectangles are in the flux closure Diamond state, three are in a single domain state. The stray-field from the single domain particles is visible in the image. In accordance to the MOKE measurements, the strong stray-field induces the iron layer to become ferromagnetic, thus producing magnetic contrast in the vicinity of the rectangles even on the silicon substrate. The image demonstrates that not only exchange coupling is responsible for the magnetic alignment of the dusting film as proposed in [Van91] but also stray-fields can lead to the arising of a signal in the SEMPA images.

2.4.2. Argon sputtering

Another method to enhance the magnetic contrast in case the sample consists of a material with an intrinsic high spin polarization, is just removing the topmost of the non magnetic material by soft sputtering. The sputtering procedure is only feasible when the sample thickness is relatively high (>10 nm) and the removed material does not significantly change the magnetic free energy and thus influences the outcome of an investigation. The Ar^+ particles may also damage the atomic order of underlying material and change its magnetic structure as recently demonstrated for a Co(0.6nm)/Pd(0.4nm) multilayer system [McM10].

To minimize the sputter damage, all sputter processes throughout this work were

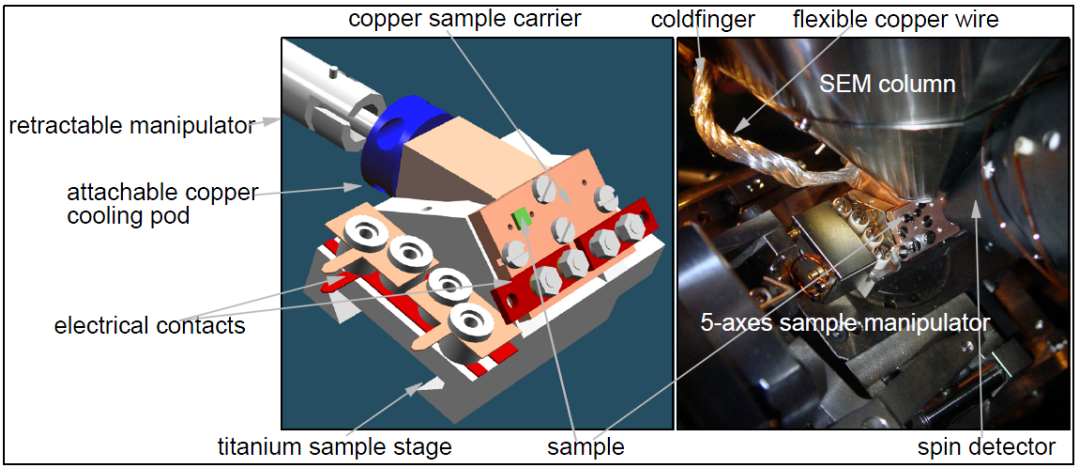

Figure 2.7.: On the left side a sketch of the new cooled sample stage is shown. The right shows a photograph of the setup under working conditions. The cold-finger is attached via two braided copper wires to the copper sample carrier.

carried out with a relatively low acceleration voltage of 1 keV. The angle of incidence was 45°. With an emission current of 20 mA and an Argon partial pressure of 3.8×10^{-7} mbar an ion current of 0.1 µA was realized[1] at a sample area of $(5\ \text{mm})^2$. For a sputter angle of 45° and 1 keV acceleration voltage, the sputteryield of Ni,Fe,Co,Pt, and Nd is approx. 3 [Nat05]. The numbers give a sputter rate of approx. 0.1 ML/min. To regain the magnetic contrast of a slightly oxidized or contaminated sample, e.g. an iron whisker preserved at UHV conditions for a few weeks, sputtering for 15 min, thus removing 1.5 ML, is sufficient. When not otherwise noted, sputtering / re-sputtering means in the following the above mentioned sputter procedure carried out for 15 minutes.

2.5. Cryostat calibration

The possibility of efficient sample cooling is a mandatory precondition for SEMPA investigation of a temperature driven spin-reorientation transition (see Chapter 2) or for the realization of ultrahigh current densities in nanowires (see Chapter 4). As no cryostat device was present in the SEMPA UHV chamber, the design of an appropriate solution was a necessary. The main design criteria were:

- compatibility with the present mechanical five axes sample manipulator
- easy sample transfer (UHV - air)
- flexible coupling of the cold-finger to the sample to minimize vibrations
- a reasonably short timescale to reach thermal equilibrium of sample, coldfinger and manipulator (vanishing thermal drift during imaging)

[1] For the measurement, the sample was kept at a potential of +27 V and the sample current was recorded. This gives approximately the primary ion beam current.

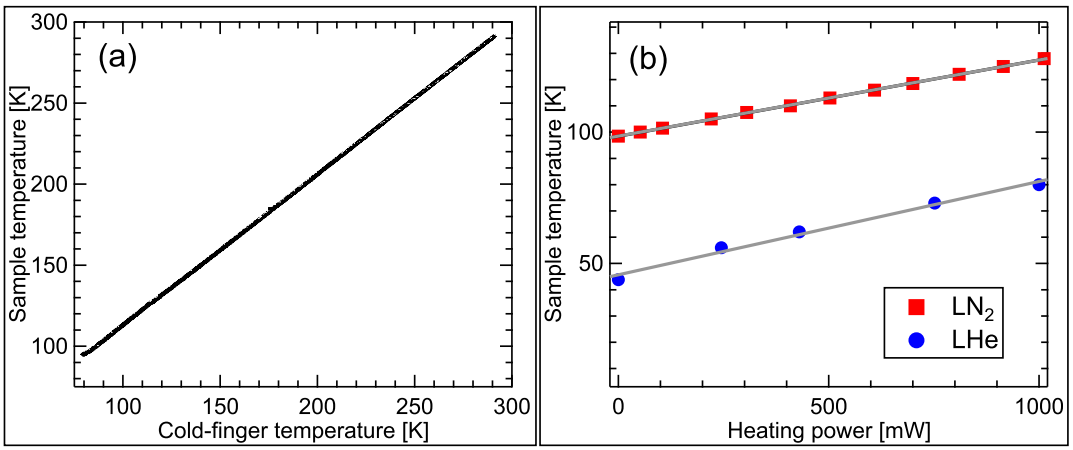

Figure 2.8.: Temperature at the sample position versus cold-finger temperature (a). In (b) the sample temperature is plotted versus heating power applied at a distance of 5 mm on the copper sample carrier.

A sketch of the realized technical solution is displayed on the left side in Fig. 2.7. On the right, a photograph of the operational cooling device under SEMPA imaging conditions is shown. Two flexible silver coated copper wires (only one visible) connect the cold-finger to the copper cooling pod (blue). The cooling pod can be attached in-situ to the copper sample carrier via a retractable manipulator thus acting as heat-sink. The cooling pod and the sample carrier are electrically and thermally isolated from the titanium sample stage, in order to keep the cooled material volume small. Approximately one hour is needed to cool the sample down from room temperature with liquid nitrogen (ℓN_2) and to reach thermal equilibrium of the setup. The lowest temperature achievable at the sample position is 95 K / 40 K with ℓN_2 / ℓHe as coolant, respectively.

Fig. 2.8(a) shows the temperature at the sample position versus cold-finger temperature. The calibration measurement is important as it is not always possible to mount a temperature sensor at the sample position. Therefore, by measuring only the cold-finger temperature with the built-in sensor in case ℓN_2 is used as coolant, the sample temperature can be derived from the linear relation:

$$T_{\text{sample}} = 19.3\ \text{K} + 0.932 \cdot T_{\text{coldfinger}} \tag{2.8}$$

All temperature information given in the next chapter about the temperature driven spin-reorientation transition has been obtained this way.

In Fig. 2.8(b) the dependence of the sample temperature on the applied heating power is plotted. The temperature increase is independent on the used coolant and can be approximated via a linear slope. On application of 1000 mW near the sample (5 mm distance on copper sample carrier) the temperature rises only approx. 30 K. The increase of the temperature is a fundamental information in case e.g. nanowires under ultrahigh current density are investigated, as it is crucial that the cooling capability of the setup is maintained under the conditions. 500 mW of dissipated heat at a current density of 1×10^{12} A/m^2 is a common value (see Chapter 4) which

causes the copper temperature just to increase by 15 K which makes a SEMPA investigation at high current densities possible.

3. Spin-Reorientation Transition in $NdCo_5$

Alloys of cobalt and rare earth metals generally posses a strong magnetocrystalline anisotropy and usually high curie temperatures. In case such intermetallics exhibit a single crystalline structure, the individual contributions of the cobalt- and the rare earth metal sublattice to the magnetocrystalline anisotropy lead in some cases to the interesting effect of a temperature driven spin-reorientation transition. This is due to the fact that the anisotropy of both compounds can vary strongly with temperature. The investigation of the spin-reorientation transition in thin films of such cobalt / rare earth metal alloys is a topic of modern research, as recent publications about $SmCo_5$ [Sin06], $PrCo_5$ [Pat06] and $NdCo_5$ [Sei09] show. In case of 60 nm thick $NdCo_5$ films, a temperature driven spin-reorientation occurs completely within the film plane in a moderate temperature interval between 255 K and 310 K. In combination with the high cobalt content of the alloy and the therefore high spin polarization of the secondary electrons, the alloy makes an excellent candidate for a SEMPA investigation of the domain structure during spin-reorientation transition. The temperature interval previously mentioned is easily accessible with the cryostat present in the SEMPA UHV chamber and the full in-plane sensitivity of the spin detector matches the in-plane spin-reorientation. Dr. Volker Neu and his colleagues in the group of Dr. Rudolf Schäfer of the IFW Dresden are experts in characterization and preparation of rare earth / Co_5 compounds and therefore a cooperation was initiated, in which the SEMPA imaging of fully characterized $NdCo_5$ samples was the task. The results of the SEMPA investigation are the topic of this chapter.

3.1. Properties of $NdCo_5$

All $NdCo_5$ thin films discussed in this chapter were fabricated by Marietta Seifert of the IFW Dresden via alternating pulsed laser deposition of a neodymium and a cobalt target. The substrate used was a MgO(1 1 0) single crystal with a 15 nm thick chromium seed layer for the $NdCo_5$ film. The film thickness is 60 nm. On top, a 10 nm chromium cap layer was deposited to prevent oxidation during transport of the sample from Dresden to Hamburg at ambient condition.

Such a thin-film system shows an epitaxial growth with a hexagonal crystal structure. The c-axis of the hexagonal lattice is aligned in-plane along the MgO[001] direction, the a-axis is parallel to the MgO[010] direction and the b-axis is oriented out-of-plane. The neodymium sublattice of a $NdCo_5$ bulk single crystal favors an easy direction of magnetization within the basal plane for low temperatures below 240 K. Due to the shape anisotropy of the thin film, the easy basal plane anisotropy

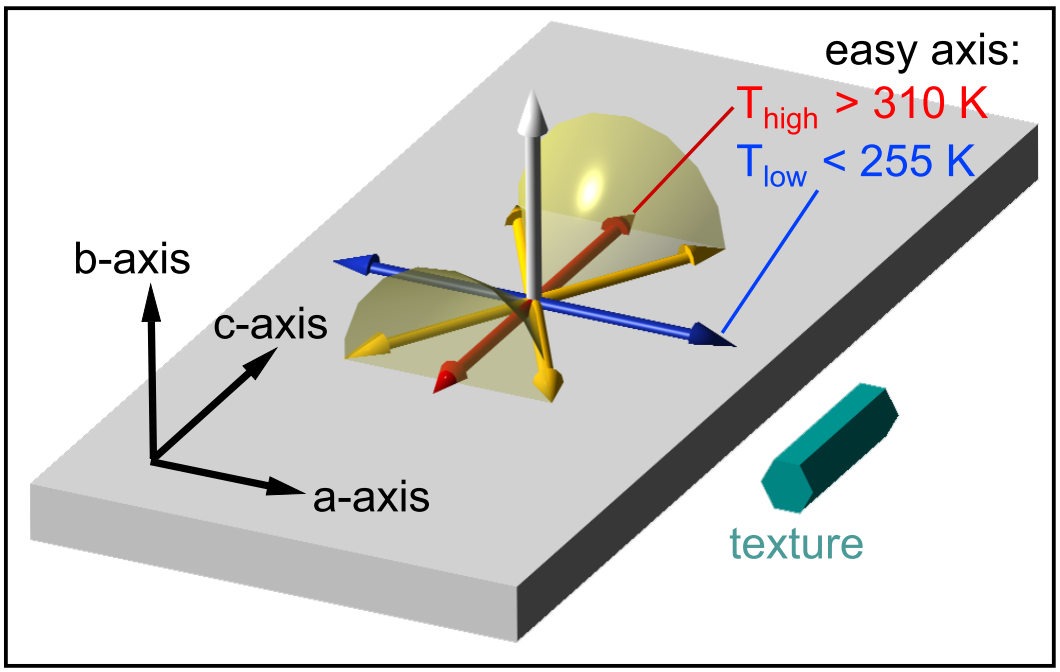

Figure 3.1.: Sketch of substrate, texture orientation and temperature dependence of the easy axis of magnetization.

is confined to the film plane and an easy magnetic direction along the a-axis remains. The cobalt sublattice has uniaxial anisotropy with easy direction along the c-axis and dominates the total magnetocrystalline anisotropy for high temperatures above 310 K.

Between 255 K and 310 K the spin-reorientation transition occurs. A sketch of the temperature dependent easy axis of magnetization and the alignment of the crystal structure with respect to the substrate is shown in Fig. 3.1. Detailed information about the crystal structure and magnetic properties of the $NdCo_5$ thin film are published in [Sei09] and the references herein. To give a brief summary: The nominal $NdCo_5$ film consists of a Co rich $Nd_{1-y}Co_{5+2y}$ phase and the Nd_2Co_7 phase, both with the same relation to the substrate, as x-ray diffraction experiments suggest. The anisotropy constants K_1 and K_2 have been determined to be 1.2 and 0.26 MJ/m^3 at 400 K and -4.8 and 1.15 MJ/m^3 at 200 K, respectively.

3.2. Domain pattern of $NdCo_5$ at room temperature

The first $NdCo_5$ thin-film sample sent to Hamburg for the purpose of SEMPA imaging was in the as-grown state. No external fields or temperature cycles were applied to the sample before first imaging. The sample had been capped with a 10 nm thick layer of chromium, which was removed by six hours of soft Ar^+ sputtering at 1 kV and an angle of incidence of 45°. After such cleaning of the surface, SEMPA imaging was possible, with a maximum signal asymmetry of ±7 % at room temperature. Fig. 3.2(b) shows the SEMPA image at 296 K, a complicated but regular

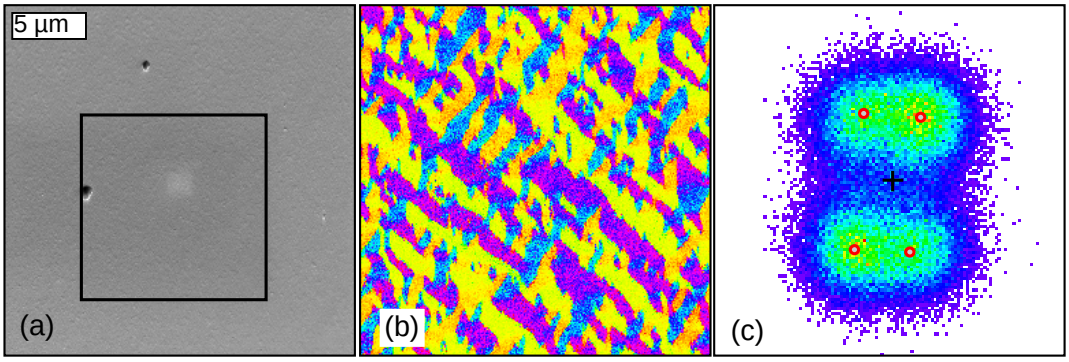

Figure 3.2.: SEMPA data of the $NdCo_5$ thin film at 296 K. (a) shows the sum image with conventional SE contrast, the black square indicates the region of interest for the following images (Fig. 3.4). In (b) the magnetic contrast for the whole area of (a) is visible. (c) gives a 2D-histogram of the distribution of the magnetization directions. The open red dots indicate the center of the accumulation points.

domain pattern with four predominant directions of magnetization and an average domain periodicity of 4 µm^2 is visible. The temperature of 296 K is in the interval of the spin-reorientation transition, where two easy axes of magnetization are present (orange arrows in Fig. 3.1). Both axes of magnetization, as well as both directions per axis, accounting to a sum of four directions of magnetization, are occupied. These directions are clearly visible as four accumulation points in the 2D-histogram marked with red circles in Fig. 3.2(c). To study the temperature driven spin-reorientation transition of this system, a higher magnification as in Fig. 3.2 was chosen in order to observe more details of the domain structure and to obtain more distinct accumulation points in the 2D-histogram as less domain walls are present when the magnification is higher. The selected region for a detailed investigation of the domain structure is indicated by a black square in Fig. 3.2(a). The large particle near the left edge of the box acts as positioning marker during the cooling and heating cycles.

Unfortunately, a decrease of the signal asymmetry after (re)sputtering the sample for 15 min to remove the topmost monolayer is observed. The evolution of the domain pattern is plotted in Fig. 3.3. After 60 minutes the obtainable image asymmetry has decreased by a factor of two which correlates to a loss of image quality by a factor of four [P1]. Flashing the detector crystal did not recover the signal, the loss of asymmetry is therefore caused by a decrease of the polarization of the SE. The signal loss over time is all in all a well known difficulty in SEMPA imaging, but the speed of the decrease is rather unusual. In imaging $Co_{39}Fe_{54}Si_7$ for example, after more than a day a signal decrease of only ∼30 % was observed with the same base pressure of the UHV-chamber. Some specific contamination or oxidation of the sample surface is probably responsible for the fast diminishing signal. As rare earth metals like Neodymium tend to be very reactive, they are known to be very sensitive to contamination [Get96]. Especially CO adsorbates are known to dramatically decrease the spin polarization from cerium alloys in spin polarized scanning tunneling microscope experiments [Get10]. To regain the contrast a new sputter-cleaning cycle

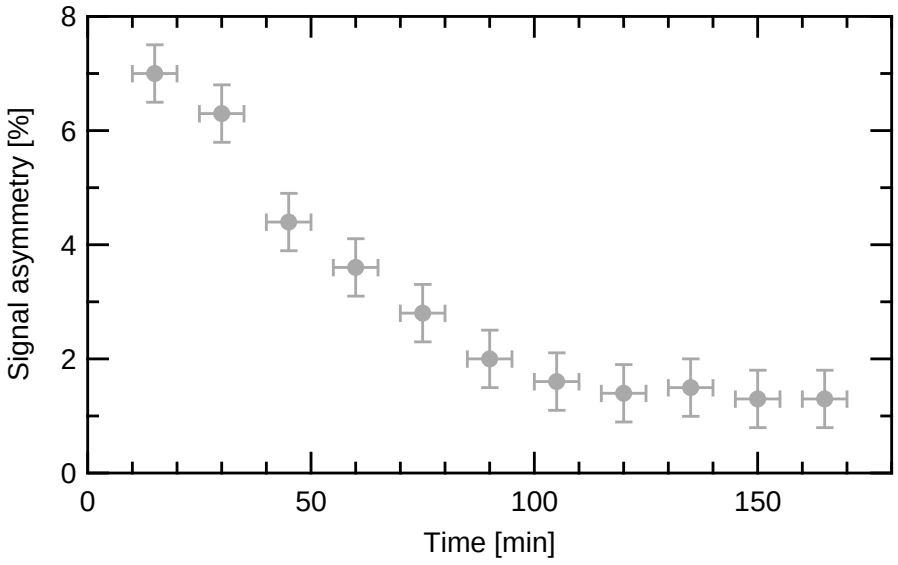

Figure 3.3.: Development of the magnetic contrast (asymmetry) of a $NdCo_5$ sample after sputter-cleaning vs time at room temperature.

of the surface is mandatory. For each high quality image of the spin-reorientation transition one day of total lab time was needed.

3.3. Evolution of the domain pattern during spin-reorientation

The evolution of the $NdCo_5$ domain pattern as a function of temperature can be seen in Fig. 3.4(a)-(e). The image size is $(11.8\ \mu m)^2$, in all images the same area of the sample was imaged with a slight lateral shift of $\pm 1\ \mu m$. At 240 K (Fig. 3.4(a)) the majority of the magnetization is aligned along the a-axis and distributed equally in both directions, as can be seen from the two pronounced accumulation points in the correlating 2D-histogram. The same applies for 320 K, with the difference that the direction of magnetization is tilted 90° in-plane and is now aligned along the c-axis. The predominant directions of magnetization above and below the transition interval agree with earlier investigations utilizing vibrating sample magnetometer measurements [Sei09]. The spin-reorientation transition occurs between $T_{\mathrm{low}} = 255$ K and $T_{\mathrm{high}} = 310$ K in agreemnet with [Sei09]. The change of the domain pattern is visible in the images in Fig. 3.4(b)-(d) for 274 K, 285 K and 296 K. The two accumulation points in the 2D-histogram at 240 K split into four above T_{low}. With increasing temperature they move on a circle until they merge again into two accumulation points above $T_{\mathrm{high}} = 310$ K.

The accumulation points indicate domains with the same direction of magnetization. Therefore the spin-reorientation transition happens via a splitting of the two domains into four domains until they merge again into two domains (Fig. 3.4(a)-(e)). The important parameter of this process is the angle between each predominant di-

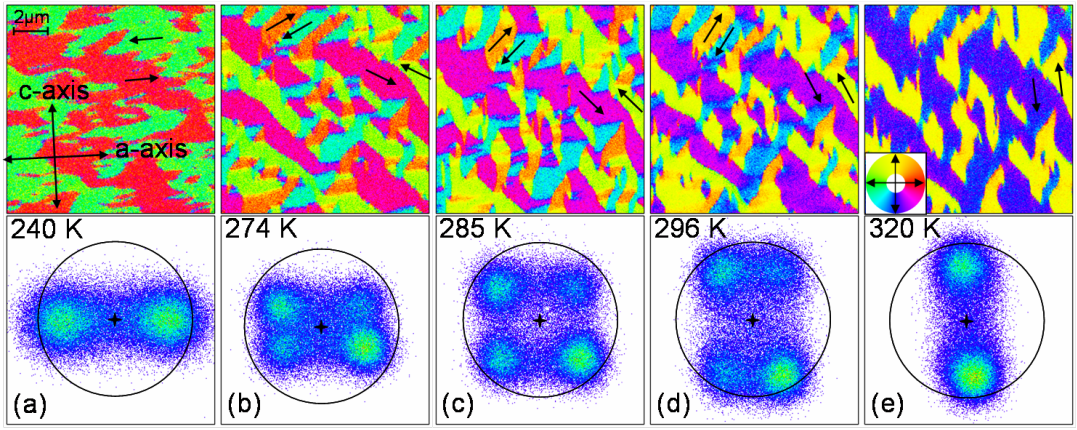

Figure 3.4.: SEMPA images of the as grown state of a $NdCo_5$ film at different temperature. In the upper part of the figures, the domain pattern is shown. The black arrows indicate the direction of magnetization according to the color wheel. In the lower part, the corresponding 2D-histogram is plotted. The rotation of the accumulation points on a circle around the center in the 2D-histograms throughout the temperature series is clearly visible. The black circles act as guide to the eye and each has a diameter of 8 % asymmetry.

rection of magnetization and the x-axis (arbitrary chosen) called spin-reorientation angle (SRA) in the following and its evolution with temperature.

3.4. Determination of the spin-reorientation angle Θ

To determine the spin-reorientation angle Θ for each domain in the different images at different temperatures, a mathematical approach is mandatory. The predominant direction of magnetization and therefore Θ(T) for each domain is defined as shown in Fig. 3.5(a). The necessary information to calculate Θ(T) is an accurate knowledge of the peak position for each accumulation point. The four peaks in the 2D-histograms can be fitted via four 2-dimensional symmetrical normal distributions. Additionally, one has to include one wide normal distribution into the fitting procedure, centered around the origin, to account for the domain walls and for some background noise within the 2D-histogram. The origin, however, is defined as the center between the peaks of the four accumulation points:

$$(x_\mathrm{o}, y_\mathrm{o}) = (\sum_{i=1}^{4} x_\mathrm{ci}/4, \sum_{i=1}^{4} y_\mathrm{ci}/4), \tag{3.1}$$

with x_ci and y_ci being the coordinates of the accumulation points. The 2d-curve fitting equation can then be written as:

$$f(x,y) = c + \sum_{i=1}^{4} \frac{A_\mathrm{i}}{\sigma_\mathrm{i} \cdot \sqrt{2 \cdot \pi}} \cdot \left[\exp\left(-\frac{1}{2} \cdot \left(\frac{x - x_\mathrm{ci}}{\sigma_\mathrm{i}} \right)^2 \right) + \exp\left(-\frac{1}{2} \cdot \left(\frac{y - y_\mathrm{ci}}{\sigma_\mathrm{i}} \right)^2 \right) \right]$$
$$+ \frac{A_5}{\sigma_5 \cdot \sqrt{2 \cdot \pi}} \cdot \left[\exp\left(-\frac{1}{2} \cdot \left(\frac{x - x_\mathrm{o}}{\sigma_5} \right)^2 \right) + \exp\left(-\frac{1}{2} \cdot \left(\frac{y - y_\mathrm{o}}{\sigma_5} \right)^2 \right) \right], \tag{3.2}$$

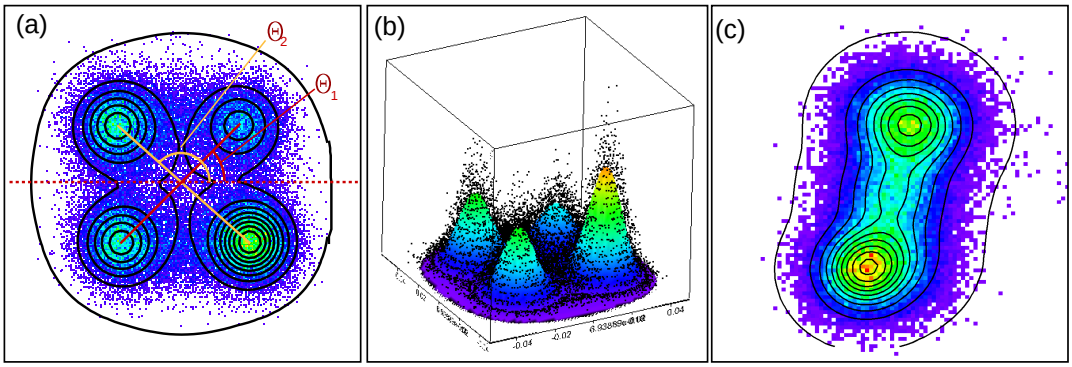

Figure 3.5.: 2D-histograms and corresponding fits for 285 K ((a),(b)) and 257.5 K (c). In (a) and (c), the blue and green points are the measured data. The black solid lines indicate a contour plot of the result of the fit function. Two spin-reorientation angles for two domains are indicated Θ_1 and Θ_2 in red. In (b), a 3D view of the 2D-histogram of (a) is given. In (c) result of the fit function for 257.5 K is plotted.

where A_i, c, x_ci and y_ci and σ_i are free fit parameters. x_ci and y_ci give the fitted position of the accumulation points. An exemplarily result of the fit procedure can be seen in Fig. 3.5(a) and (b) as 2D-contour plot and 3D illustration, respectively. From the origin and the peak positions, the spin-reorientation angle Θ(T) can be calculated for each domain via

$$\Theta_\mathrm{i}(\mathrm{T}) = \mathrm{Arctan}\left(\frac{y_\mathrm{ci} - y_\mathrm{o}}{x_\mathrm{ci} - x_\mathrm{o}}\right). \tag{3.3}$$

The fitting procedure is surprisingly stable and even works when the accumulation points (i.e. the domains) are nearly merged near 255 K and 310 K, as can be seen in Fig. 3.5(c) where the 2D-histogram and the associated fit for the image acquired at T=257.5 K is shown. The fitting procedure yields an average splitting of the two domains of $\Theta(275.5\ K)$=9°±2° in this case[1].

The so evaluated spin-reorientation angles for different temperatures are shown in Fig. 3.6 as color coded solid dots. In the temperature interval of the spin-reorientation a linear dependence of Θ(T) is visible. The black dotted lines act as guide to the eye. From the crossing the spin-reorientation interval was determined to be between T_low = 252 K and T_high = 318 K ±1 K, which fairly agrees with T_low = 255 K and T_high = 310 K from [Sei09] as well as the gray solid points fit into the graph which are also taken from [Sei09]. The onset of the spin-reorientation transition at T_low was of particular interest and it was tried to find deviations of the linear behavior of Θ(T). Within the angular- and temperature resolution of the experiment (±2° and ±1 K) no such deviation could be resolved. An open question

[1] As discussed in [P1] the angular error of an individual pixel for an average SEMPA measurement is ≈ ±4° depending on the count rate and obtained asymmetry. Calculation of the error of the fitting procedure with the propagation of uncertainty yields an absurdly small error of ≈ ±0.1° due to the quantity of pixels in the 2D-histogram. In my opinion an error must give an information on "How far do I trust my data". In this case I do not trust it to be ±0.1° thus giving a much larger value of ±2° based on an educated guess.

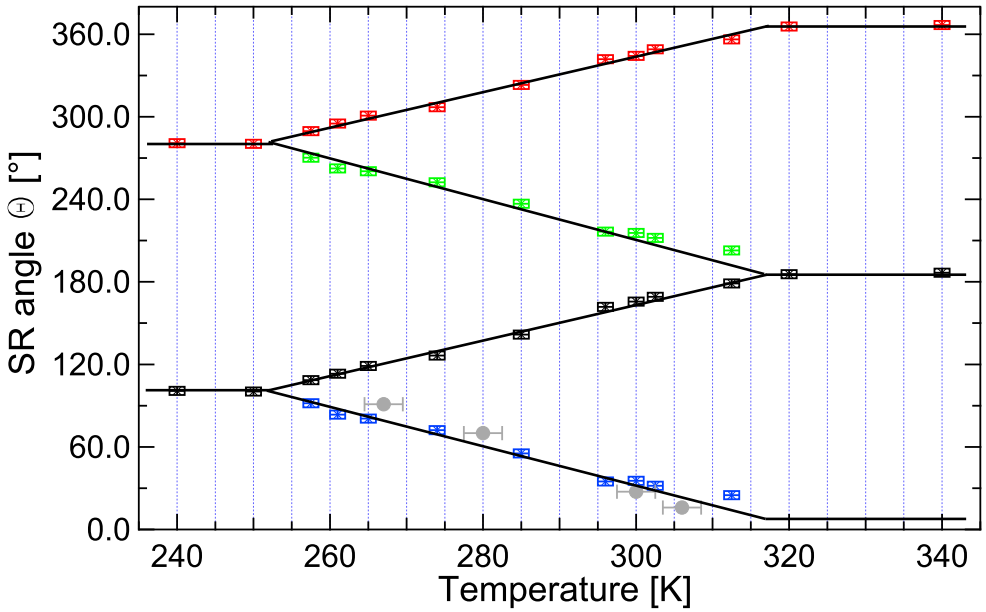

Figure 3.6.: Dependence of the four spin-reorientation angles of the four domains on the temperature. The angles were calculated form the histograms and are plotted as red, green, black and blue marks. The black solid line acts a guide to the eye. For comparison, earlier VSM data form [Sei09] is plotted as gray points.

is the nature of the linear dependence of Θ(T), which has its root in the temperature dependence of the first and second order anisotropy constants of the material and will be discussed in the next section.

3.5. Determination of the ratio K_1/K_2 from $\Theta(T)$

In an undisturbed crystal, the crystal anisotropy, which basically results from spin orbit coupling, is associated to the direction of magnetization relative to the structural axis of the material. Hexagonal crystals like thin films of $NdCo_5$ show a uniaxial anisotropy. The anisotropy energy density γ_{Ku} for a hexagonal system can be expressed as [Dar74]:

$$\gamma_{Ku} = K_0 + K_1 \cdot \sin^2(\theta) + K_2 \cdot \sin^4(\theta) + K_3 \cdot \sin^6(\theta) + K_4 \cdot \sin^6(\theta)\cos^6(\phi)\ldots, \quad (3.4)$$

where θ is the angle between the magnetization direction and the anisotropy axis, in our case the c-axis and ϕ is the angle between the magnetization component in the basal plane and one of the a-axis. In the following, only the first two significant terms are considered, since thermal excitation of the spins usually averages out the higher order terms for temperatures above 10 K and Eq. 3.4 becomes [Hub98](p115):

$$\gamma_{Ku} = K_1 \cdot \sin^2(\theta) + K_2 \cdot \sin^4(\theta) \quad (3.5)$$

A large positive K_1 describes an easy axis along the c-axis, a large negative K_1 an easy plane perpendicular to the c-axis. Due to shape anisotropy of the thin film, the

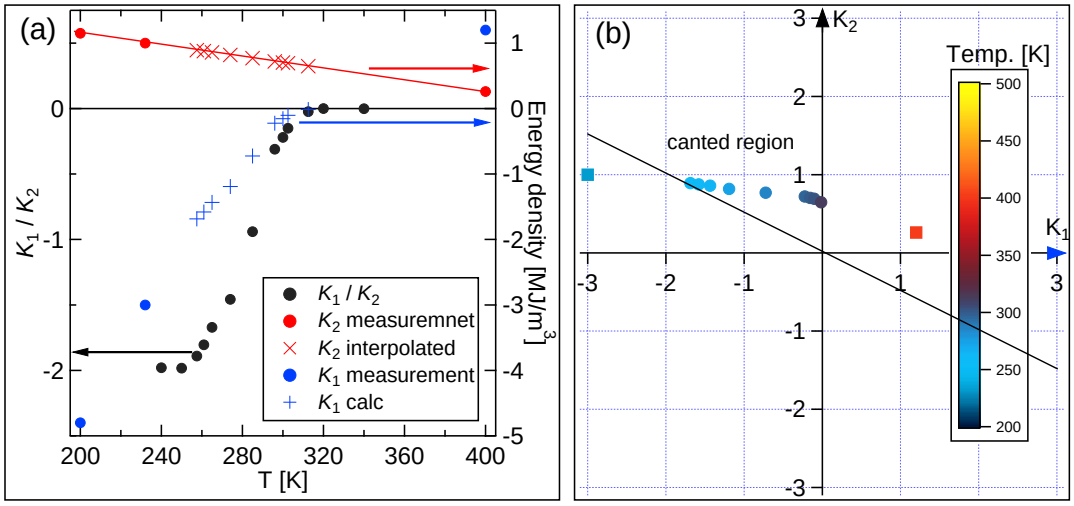

Figure 3.7.: Overview of K_1 and K_2 of $NdCo_5$ and their dependence on the temperature. The black solid points in (a) represent the calculation of the ratio K_1/K_2 from the SRT angles. The blue and red solid points indicate the values of K_1 and K_2 at three different temperatures taken from [Sei09]. The red crosses show a linear interpolation of K_2. The blue crosses are the calculated values of K_1 using the interpolated values of K_2. In (b) the temperature-trajectory in the K_1 vs K_2 phase diagram is shown.

magnetization is confined to the film plane and the easy plane becomes an easy axis parallel to the a-axis for large negative K_1. For intermediate values of K_1, i.e. under the condition of $0 > K_2/K_1 > -2$ a spin-reorientation occurs and the magnetization points along a direction in-between the c- and a-axis. The angle between the easy direction of magnetization and the c-axis is then given by [Mil96]:

$$\frac{K_1(T)}{K_2(T)} = -2 \cdot \sin^2\left(\Theta(T)\right) \tag{3.6}$$

With this relation, the ratio K_1/K_2 can be derived from the knowledge of the spin-reorientation angle Θ(T) which was measured and calculated above (Fig. 3.6), as long as $0 > K_1/\ K_2 > -2$.

The black solid dots in Fig. 3.7(a) represent the ratio K_1/K_2 derived from Eq. 3.6. The first two and last two points do in principle not fulfill the $0 > K_1/K_2 > -2$ criteria, but are also plotted for the purpose of illustration. As discussed above, K_1 exhibits a zero crossing and is mainly responsible for the spin-reorientation process, while a slight variation of K_2 is a correction of higher order. At 200 K, 240 K and 400 K, values for K_1 and K_2 were determined before (Fig. 3.7(a), solid red and blue discs) using the Sucksmith-Thompson relation [Suc54] on VSM measurements, as discussed in [Sei09]. This approach does not apply in the temperature range of the spin-reorientation transition. Due to only slight changes of K_2 between 200 K and 400 K, the values for 255 K < T < 310 K were interpolated via a linear slope and are plotted as red crosses in Fig. 3.7(a). From the interpolated K_2 values and the ratio K_1/K_2, the values for K_1 were derived and are plotted as blue crosses in Fig. 3.7(a). These values fit very well into the K_1 curve (solid blue) and also agree with earlier

measurements [Kle75]. Fig. 3.7(b) shows the phase diagram K_1 vs K_2 with the temperature color coded as indicated in the legend. In agreement to the principal phase diagram shown in [Mil96], the path of the measured K_1 vs K_2 values during spin-reorientation runs through the "canted region" in the second quadrant yielding a smooth, continuous connection between the two final domain states beyond the SRT temperature interval [Ved02].

3.6. Reversible domain pattern

As discussed above, due to the decreasing magnetic signal over time, it was possible to acquire only one to two images per day. Before acquiring an image, one would usually wait until the sample mount is in thermal equilibrium and the thermal drift of the sample is negligible. Unfortunately, this can take up to 30 minutes. After this time, the signal quality is already significantly lower (see Fig. 3.3). Therefore, one has to accept some image drift in order to achieve images with a higher signal to noise ratio. The thermal drift as well as slightly different positions of the different images have to be corrected for an investigation of variations of the fine structure of the domain pattern during different cooling cycles or measurement sessions. The image alignment was done using a free software algorithm [Bus00] usually employed in the alignment of medical images, e.g. sets of computer tomography images. The method works very well on the sum images due to the textured surface of the thin film (see Fig. 3.2(a)). The image at 296 K was used as master image due to the absence of thermal drift at room temperature. The series of aligned and corrected images is shown in Fig. 3.8. The first number in the top right corner of each image gives the measurement session (day), the second number the image number at this specific day. During two sessions, the sample was heated at least to room temperature and re-sputtered to remove the topmost 1.5 ML.

As can be seen from the image series, the overall domain pattern does not change between all the heating/cooling cycles. Some slight deviations of the magnetic fine structure between the different sessions can be observed, an example is marked in Fig. 3.8 (1.2)(7.1)(5.2) with a black circle where the south end of the green changes from cycle to cycle. But all in all, the system takes the same path of domain and domain wall nucleation / annihilation within the different SRT cycles. The domain walls are therefore probably pinned by some magnetic impurities or defects of the crystallographic structure, which are surprisingly not correlated to the surface texture visible in the sum images as discussed later in detail.

Another question that arises from the image series of Fig. 3.8 is, if this domain pattern is the state of lowest energy? Would not a single domain state without domain walls be much more favorable? The orientation of a single domain could just rotate by 90° during cooling, and then rotate back during heating. To answer this question, another sample of a $NdCo_5$ thin film was fabricated and this time saturated at 320 K in a magnetic field of 9 T along the easy c-axis. The first image after saturation, acquired at 296 K, is shown in Fig. 3.9(a). Basically a single domain state is visible. Some slight variations (purple and cyan in the blue background) can be seen, caused by the SRA of 20° at 296 K (Fig. 3.6). But there can be no doubt that

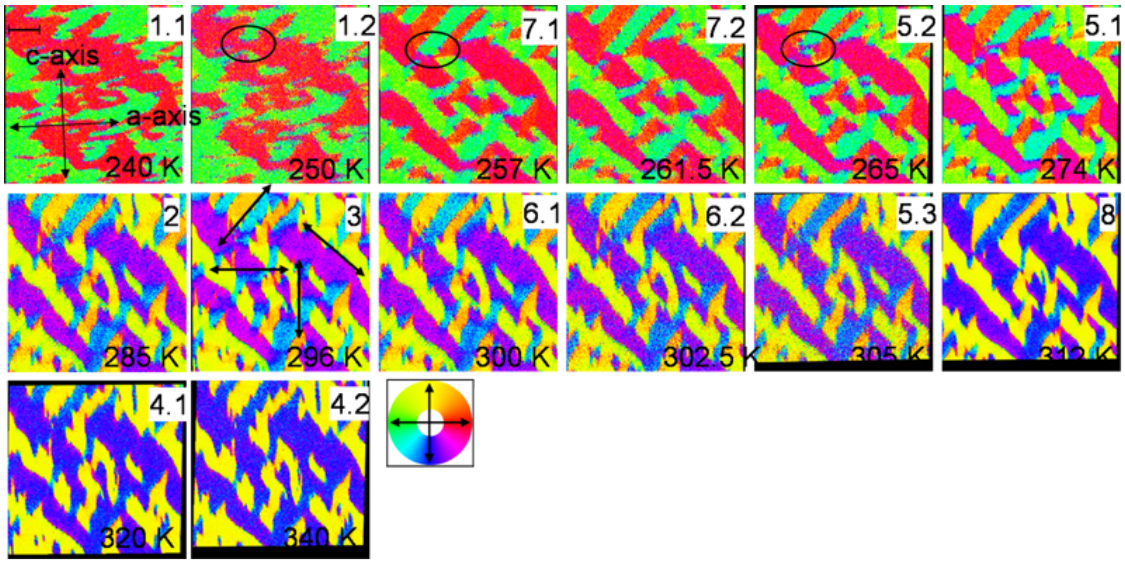

Figure 3.8.: SEMPA image series of the same position (see Fig.3.2(a)) of the thin film under variation of the temperature. Image drift has been corrected (black frames) and the images are aligned to the master image (3) at 296 K.

after saturation at 320 K the magnetization in remanence was totally aligned along the c-axis. In Fig. 3.9(b) the magnetization of the same area is shown at 100 K. The single domain state has split into two, showing a stripe domain pattern. Fig. 3.9(c) shows the domain pattern again at 296 K. Four directions of magnetization are now clearly visible. A single cooling/heating cycle of the sample created the four fold domain pattern observed in the as grown sample (Fig. 3.8). This measurement shows that a breakup into domains during the spin-reorientation transition is energetically more favorable than the rotation of the direction of magnetization of one large single domain.

3.7. Domain wall direction and average domain size

Another remarkable feature of the domain transformation during spin-reorientation transition are the stationary domain walls. Despite the fact that the magnetization within the domains rotate, the domain walls themselves stay at their places. The domain wall angle changes and can become 0°. The domain walls are no longer visible, but reoccur on the next heating (cooling) cycle. Four dominant directions of the domain walls are visible: along the a-axis, along the c-axis and along the two directions 45° in-between. These four directions are indicated in Fig. 3.8(3) with black arrows. Looking at Fig. 3.8(1.1) at 240 K, the majority of the walls along the c-axis have vanished, as well as some of the 45° walls. The remaining walls are mostly oriented parallel to the easy a-axis in order to reduce the net magnetic charge of the wall [Hub98](p220). In Fig. 3.8 at 340 K the situation is rotated by 90°: Only the walls parallel to the easy c-axis and some along the 45°-direction remain. In Fig. 3.10(a) the distribution of the directions of the domain walls is

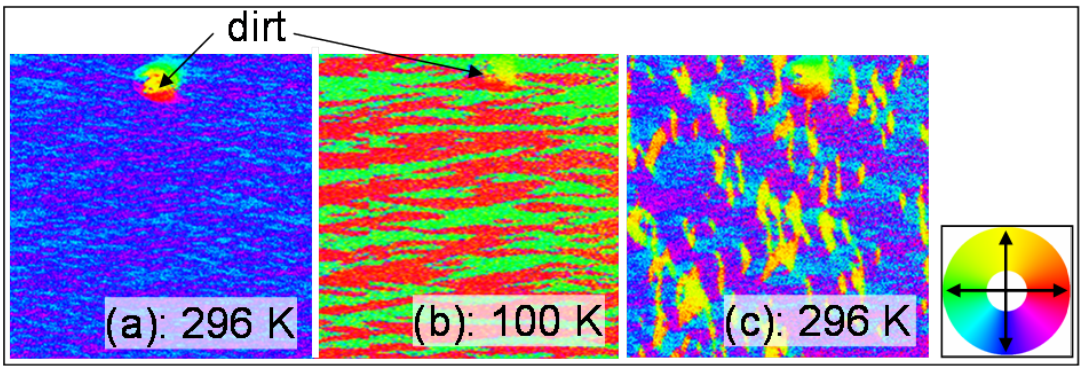

Figure 3.9.: SEMPA images of a second $NdCo_5$ sample, which was saturated at 320 K along the c-axis. In (a), a single domain state is visible at 296 K. (b) shows a two domain state at 100 K of the same position as in (a). Heating again to 296 K shows a four domain state in (c).

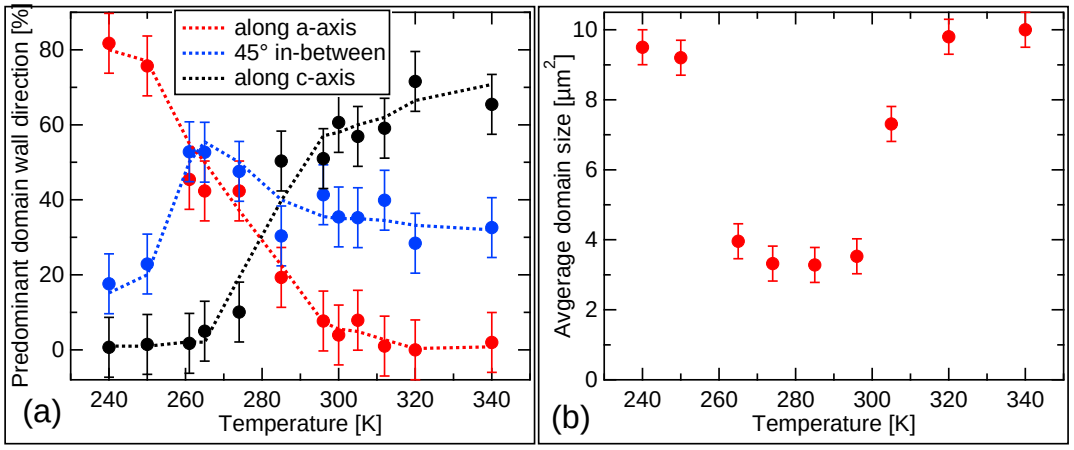

Figure 3.10.: In (a) the distribution of domain wall directions versus temperature is shown. In (b) the average domain size vs temperature is plotted.

plotted versus the temperature. The intuitive impression from the image series of Fig. 3.10 is confirmed: Below T_{low} domain walls along the a-axis are dominating. During spin-reorientation there is a maximum number of domain walls along both 45°-directions and above T_{high} most domain walls are aligned along the c-axis. In the temperature range, where the majority of the domain walls are aligned along both 45° directions, nearly twice as much domain walls are present compared to the situation when the domain walls are aligned along one of the crystal axes. Due to the increased number of visible domain walls, the average domain size has to decrease which can be seen in the plot in Fig. 3.10(b). Above and below the spin-reorientation transition, basically two large interconnected domains are present (Fig. 3.10) with a size of around 10 µm^2. During spin-reorientation the additional domain walls along the 45° directions emerge. As soon as they are visible in the SEMPA images, i.e. when the spin-reorientation angle becomes larger 10°, the average domain size drops

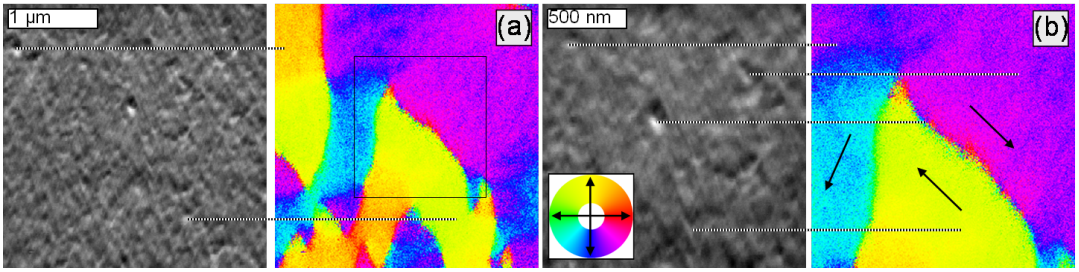

Figure 3.11.: Fine structure of the centered magnetic feature of Fig. 3.4(d). The image size in (a) is (2.9 µm)^2 and (1.7 µm)^2 in (b), respectively. The dotted lines correlate apparent defects in the sum image to the corresponding position in the magnetic image.

to a constant level of 4 µm^2. Below 255 K the average domain size increases to the former value of 10 µm^2.

3.8. Domain fine structure & Domain wall pinning

To obtain a deeper insight into the magnetic fine structure during spin-reorientation, high resolution images at room temperature were acquired. Fig. 3.11 shows two zoom images into the central region of Fig. 3.10(296 K). The corresponding sum images are also plotted, in order to correlate the texture of the film to magnetic features. The horizontal dotted lines in Fig. 3.11 point from some significant texture defects visible in the sum image to the corresponding positions in the magnetic image. The defects have a diameter of around 100 nm which is in the range of the film thickness, thus probably continuing throughout the whole film. It is obvious that the majority of marked positions, except one, shows no correlation between texture and magnetic structure.

This is a quite surprising result: On the one hand it is clear from the image series of different cooling/heating cycles (Fig. 3.11) that the recurring domain pattern is governed by strong pinning, on the other hand we see that large defects observable in the SEM image are not responsible for the pinning. So the question remains what causes the pinning of the domain walls and why are the pinning sites not visible in the SEM image?

Next I would like to comment on the two domain walls in Fig. 3.11(b): One 180° wall is running diagonally through the image. The other is a 110° domain wall (green) between the yellow and cyan domain. Both walls have a domain wall width of 100 nm ±40 nm based on the definition introduced by B. Lilley [Lil50]. The relative largely error of 40 nm is determined by the lateral resolution deduced from the sum image. From the measurement of merely the in-plane component and the averaging over an area of 40 nm, it cannot be decided if the walls are of a Bloch- or Néel type in this case. A theoretical approximation of the domain wall width via $W_L = \pi \cdot \sqrt{A/K}$ [Lil50] gives a value W_L=35 nm using $A = 1.05 \times 10^{-11}$ J/m (from [Guo03]) and $K = 1.0 \times 10^5$ J/m^3 (from Fig. 3.7) which is at the lower border of the measured value.

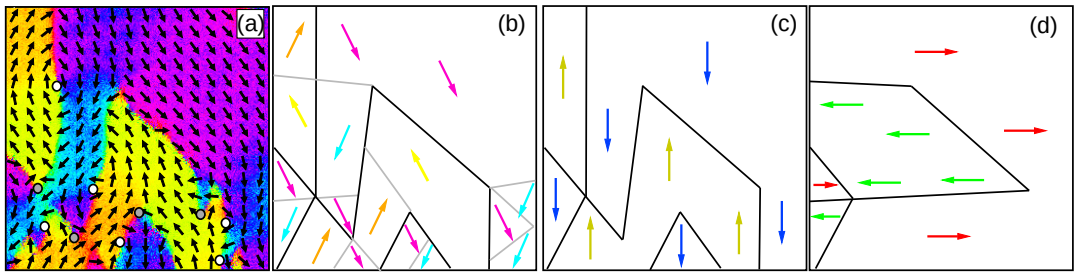

Figure 3.12.: (a) color and arrow plot of Fig. 3.11(a). The white circles indicate vortex cores, the gray circles anti-vortices. In (b) a simplified sketch of the domain pattern of (a) is shown. (c) and (d) indicate the related domain pattern above and below the spin-reorientation process.

3.9. Summary & Conclusion

The evolution of the domain pattern during spin-reorientation transition of $NdCo_5$ was observed via SEMPA. The reorientation transition is mainly driven by the temperature dependence of K_1 and its zero crossing at 310 K. From a statistical investigation of the SEMPA data the spin-reorientation angle was calculated for different temperatures. Surprisingly, a linear dependence of the spin-reorientation angle from the temperature was observed (Fig. 3.6). From the variation of the SRA with temperature and an approximation for K_2(T) the evolution of K_1(T) during spin-reorientation was investigated and compared to literature values (Fig. 3.7).

The SEMPA investigation of the same area during different spin-reorientation cycles revealed a reproducible domain pattern (Fig. 3.8). The domain walls are fixed at their position and only change their domain wall angle during the spin-reorientation process (Fig. 3.10). The source of the strong pinning is probably some local modulation of the anisotropy, although the pinning sites are not correlated to texture defects visible in the SEM images (Fig. 3.11). This local anisotropy modulation may also serve as reason for the breaking-up of the saturated single domain state into the as-grown domain pattern (Fig. 3.9). When the spin-reorientation process starts, some domains "decide" to rotate into the one, some into the other direction influenced by the local anisotropy, therefore irreversibly splitting the single domain state.

It remains the question for the reason of the observed domain pattern during SRT (Fig. 3.12). It seems to me that the energy decrease of the domain walls with a decreasing domain wall angle [Hub98] has a significant influence on the domain pattern and the creation of the additional domain walls along the 45° direction. In case all domain walls would be Néel walls, the argumentation would be the following:

The 90° Néel wall has in the classical model [Née53] only 12 % of the energy of a 180° Néel wall. The strong energetically preference for lower-angle Néel walls has the consequence that energy would be gained by replacing a 180° Néel wall by a multitude of low-angle walls. Although the total length of the low-angle walls within this pattern is much larger, the total wall energy can be smaller. The actual energy of the observed domain pattern is unfortunately impossible to calculate, due to the

fact that it is not known if Bloch- or Néel walls (or a mixed state) are present and both have quite a different energy variation with wall angle [Hub98] (Fig. 3.73 on p.239).

A second reason for the creation of additional domain walls during spin-reorientations is the otherwise creation of massively charged walls: Let the reorientation process start with the observed two domain configuration (Fig. 3.8) which is sketched in Fig. 3.12(c). The pinned domain walls and the rotation of the magnetization with decreasing temperature would cause all vertical walls to gain the maximum possible wall charge after finishing the reorientation process. To avoid the charged walls the two domains split into four domains in the beginning of the SRT creating the additional low-angle domain walls (gray, Fig. 3.12(b)). The final configuration can be seen in Fig. 3.12(c). The vertical domain walls have vanished and a majority of horizontal domain walls remains (see also Fig. 3.10(a)).

The complex domain pattern evolving during the spin-reorientation resembles in parts the cross-tie domain wall structure [Hub58], as the principal constituents of a cross-tie configuration, i.e. vortices and anti-vortices, can be found in the observed domain structure (white and gray circles Fig. 3.12(a)). The occurrence of vortices and anti-vortices is a direct consequence of the creation of the additional domain walls during the spin-reorientation process (see Fig. 3.12(b)). In brief, the complex domain pattern is governed by the huge variation of the anisotropy, strong pinning, energy minimization via the creation of many low-angle domain walls and the attempt to avoid massively charged head-to-head (tail-to-tail) domain walls. To get a deeper inside into the combating energy contributions, sophisticated micromagnetic simulations are mandatory which are at present conducted by M. Seifert with support of Dr. D. V. Berkov from Innovent, Jena [Ber]. The most important remaining questions are:

- Are the domain walls of Bloch- or Néel type?
- What is the cause for the domain wall pinning? What kind of anisotropy modulation would be necessary?
- Why is the 45° direction distinguished?
- Can the domain pattern during spin-reorientation be reproduced by simulations?

4. Ground State of Thin-Film Microstructures

The theory of ferromagnetism in bulk materials is widely discussed in a multitude of publications, e.g. in the famous books of Aharoni [Aha96], Chikazumi [Chi78] and Brown [Bro62]. From the bulk material, the theory was extended to cover the forming of domains in thin ferromagnetic films, where the magnetization $\vec{M}$ tends to remain in-plane due to the film's shape anisotropy. An overview on the theory of thin-film magnetism can be found for example in [Hub98, O'H99, Coh70, Arr05].

Magnetic thin-film materials can be classified into three categories using the quality factor $Q = \frac{K}{2\pi\mu_0 M_s^2}$ as a guiding dimensionless material parameter:

Definition	Name	Typical applications
$Q \ll 1$	Low anisotropy	Soft magnetic materials
$Q \approx 1$	Medium anisotropy	Recording Media
$Q \gg 1$	High anisotropy	Permanent Magnets

The previously discussed $NdCo_5$ thin films have for example a quality factor of $Q = 0.32$ at 200 K and can thus be classified as medium anisotropy material.

In the following chapters, patterned elements from low anisotropy (soft magnetic) thin films with $Q \ll 1$ are discussed, i.e. Permalloy ($Q = 5.9 \times 10^{-5}$) and $Co_{39}Fe_{54}Si_7$ ($Q \simeq 0$).

The magnetic configuration of such soft magnetic small elements is primarily determined by their shape due to the large contribution of shape anisotropy to the total energy density γ_{total} which is the sum of exchange energy density γ_{exchange}, (magnetocrystalline) anisotropy energy density $\gamma_{\text{anisotropy}}$, magnetostatic energy density γ_{demag} and Zeeman energy density γ_{Zeeman}. The Zeeman energy term is caused by a given external magnetic field $\vec{H}_{\text{external}}$ and can be written as

$$\gamma_{\text{Zeeman}} = -\mu_0(\vec{H}_{\text{external}} \cdot \vec{M}). \tag{4.1}$$

It is minimal when $\vec{H}_{\text{external}}$ and $\vec{M}$ have the same orientation and vanishes in case the magnetic configuration in remanence is under investigation, as in the following sections. The (magnetocrystalline) anisotropy energy density which has different forms for uniaxial and cubic systems is usually negligible for soft magnetic, i.e. low anisotropy, elements as in this case γ_{exchange} and γ_{demag} are much larger[1].

The exchange energy density for a cartesian coordinate system is given by

$$\gamma_{\text{exchange}} = A\left[(\nabla m_x)^2 + (\nabla m_y)^2 + (\nabla m_z)^2\right] . \tag{4.2}$$

[1] A micromagnetic simulation yields the following energy contributions for a 5 µm x 400 nmm x 10 nm Permalloy wire containing a vortex wall: $\gamma_{\text{exchange}} \approx 1150$ J/m^3 and $\gamma_{\text{demag}} \approx 4580$ J/m while the uniaxial anisotropy energy density of Permalloy is 285 J/m^3 (see chapter 4.4).

The formula is derived by a Taylor expansion of the isotropic Heisenberg interaction between spins $E_{\mathrm{ex}} \propto -\sum_{\mathrm{i,j}} \vec{S}_{\mathrm{i}} \cdot \vec{S}_{\mathrm{j}}$, when the discrete spins are substituted with a continuous magnetization. It penalizes deviations from the perfect alignment of two neighboring magnetization vectors via an exchange energy increase which is proportional to $-\cos\,\phi_{\mathrm{i,j}}$, where $\phi_{\mathrm{i,j}}$ denotes the angle between the two spins. A is the material dependent exchange stiffness. Its zero temperature value is related to the Curie point T_{C} via $A(0\ \mathrm{K}) \approx k_{\mathrm{B}} T_{\mathrm{C}}/a_{\mathrm{L}}$ (a_{L} = lattice constant).

The magnetostatic energy density

$$\gamma_{\mathrm{demag}} = -\frac{1}{2}\mu_0(\vec{H}_{\mathrm{demag}} \cdot \vec{M}) \tag{4.3}$$

is caused by the demagnetizing field (stray-field) $\vec{H}_{\mathrm{demag}}$, which is caused by magnetic volume and surface charges. The aforementioned shape anisotropy is in fact a magnetostatic effect and results from the formation of magnetic surface charges at the boundary of a magnetic structure. It describes the tendency of the magnetization to align parallel to the sample edges and in the film plane to avoid the formation of magnetic poles.

A detailed discussion of the individual energy terms can be found for example in the book by A. Hubert and R. Schäfer [Hub98](p108ff.) and a presentation of the domain structure of elements with sizes of a few ten microns as well as many experimental examples of domain configurations is following on pages 447ff.

To get a first idea of a possible domain configuration of a structured element, one can apply the Van den Berg method [vdB85, vdB86, vdB87] to the geometry in question. This geometrical domain construction method gives a possible stray-field free magnetic configuration, but the result is not explicit and it will not solve the question for the magnetic ground state, i.e. the state of lowest energy.

Very small elements e.g. thin discs with a diameter smaller than five times the exchange length of the material [Chu10] are usually in a single domain state and their behavior in external fields can be approximated by the Stoner-Wohlfahrt model of coherent rotation of the magnetization [Sto47].

The domain pattern of thin-film elements up to 10 µm^2 is usually accessible via micromagnetic simulations, but here again the question for the ground state is difficult to address and the energetics of different configurations have to be compared. An introduction to micromagnetic simulations with a discussion of difficulties and advantages can be found in [Arr05] and in [Fid00]. As a computational approach in general solves a "perfect world" problem[1] the question arises if the numerical results can be confirmed by experimental observation as it is discussed in the critical review by A. Aharoni [Aha01].

The last years indeed showed a vast list of publications dealing with experimental investigations of small structured elements, numerical simulations and the compar-

[1] Micromagnetic simulations always compute a solution to a simplified problem. The effort to consider a real world situation, i.e. imperfect edges, grains and local variation of material parameters is immense and it is not for sure that then a correct solution is given because like I mentioned "with four parameters I can fit you an elephant" [Dys04]. On the other hand, micromagnetic simulations with simplified assumptions often give surprisingly good agreement to an experiment which make them sometimes quite a valuable tool to get a first idea of the physics.

ison of both (only to name a few: [Bar04, Che05, Cor88, Cow00, Gal97, Gar02b, Gom99, Her87, Her02, McV88, Nov03, Plo93, Rav00, Rem08, Sat06, Wan06]). Due to the technological importance of memory devices two of the most prominent geometrical objects studied are small rectangles important for MRAM devices [Gal97] and nanowires which are relevant to the proposed racetrack memory concept [Par08]. The general interest in the two geometries and the fact that SEMPA is a high resolution experimental method which gives quantitative information of the magnetization orientation of a complete structure is the reason for the following investigation: The magnetic fine structure of soft magnetic rectangles and nanowires investigated by SEMPA imaging.

4.1. Magnetic fine structure of Permalloy rectangles

Permalloy rectangles with dimensions of 2 µm x 1 µm x 20 nm, exhibit seven basic stable or meta-stable magnetic configurations in zero field as shown by micromagnetic simulations [Rav00]. These eight configurations can be divided into two principal classes: The flux-closure states which have a low average magnetization (Landau, diamond, tulip, and cross-tie states) and the high remanence states which have a high average magnetization (flower and C- and S-states).

The widest known of these micromagnetic configurations is probably the so called Landau structure, named after L. Landau who proved together with E. Lifshitz for the first time that a flux closure magnetic configuration can have a lower energy than the uniformly magnetized state due to a massive reduction of the magnetic surface charge density at the edges [Lan35]. The flux-closure Landau state can be found in rectangular geometries of different size: One of the largest Landau states yet observed was found at the (100) surface of Fe single crystals [Col57] with dimensions of a few millimeters in length and width. The Landau state also occurs in Permalloy rectangles of 160 µm x 60 µm x 240 nm [Hub98](p464), as well as in rather small Permalloy particles of 600 nm x 300 nm x 20 nm [Kob09]. Due to the common appearance of the Landau state in a variety of materials and in structures of very different size, it has settled in common knowledge as a paradigm for a flux-closure domain configuration with four predominant domains. The direction of magnetization of each of the four domains is aligned along the edges, separated by four 90° walls and one 180° wall in case of a rectangle. A sketch of such a domain structure is plotted as inset in Fig. 4.1(a) and can be found in a large number of publications, for example in [Kit49, Gar02a, Her02, Han09].

In 1997 the "Micromagnetic Modeling Activity Group" from the "National Institute of Standards and Technology" (NIST) chose a 2 µm x 1 µm x 20 nm Permalloy rectangle to serve as the so called "standard problem #1", intended for the comparison of the reliability of different micromagnetic codes. It was advertised on the web together with three other standard problems [NIS] and attracted wide attention throughout the community [Aha01, Rav00, Rep98]. One of the possible micromagnetic configurations which appears in the rectangle is the Landau state which makes the structure one of the most prominent examples for a thin-film element in a flux closure configuration.

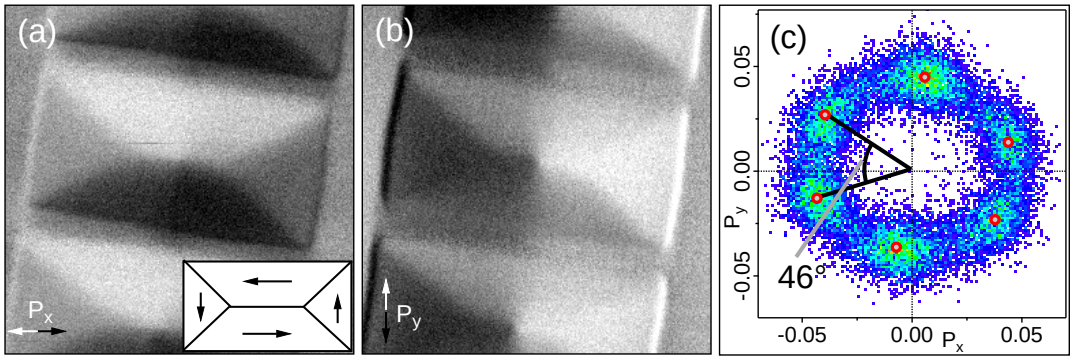

Figure 4.1.: SEMPA image: (a) and (b) show the two components of the direction of magnetization of three coupled Permalloy rectangles (2 µm x 1 µm x 23 nm). In (c) the corresponding 2D-histogram for the central rectangle is plotted. The inset in (a) is a sketch of the magnetization of the so called Landau state.

We decided to investigate the domain structure of "standard problem # 1" with a slightly higher thickness of 23 nm instead of 20 nm from an experimental point of view, additionally including arrays of rectangles which can couple magnetostatically via their stray-field when the separation is small.

In Fig. 4.1(a), (b) the two orthogonal components of the magnetization orientation of three adjacent Permalloy rectangles (2 µm x 1 µm x 23 nm) are shown, separated by a gap of 200 nm between the long edges. The corresponding 2D-histogram for the central rectangle is plotted in Fig. 4.1(c). Surprisingly, instead of the expected four accumulation points, reflecting the four domains of the Landau structure, there are six accumulation points visible. The data reveals that the domains parallel to the long edge split into two domains, with a splitting angle of 46° (Fig. 4.1(c)).

Further SEMPA investigations and additional micromagnetic simulations of the apparent conflict between measurement and common belief led to the insight that even simulations of perfect, uncoupled structures give a splitting of the larger domains with a splitting angle of 15°. The splitting is significantly enhanced in coupled rectangles, which develop a kind of mesoscopic magnetic structure. Furthermore it was found that the splitting angle also depends on the exact shape of the edges. The detailed results of the investigation are published in the following article [P3].

Magnetic ground state of single and coupled Permalloy rectangles

S. Hankemeier, R. Frömter, N. Mikuszeit, D. Stickler, H. Stillrich, S. Pütter, E.Y. Vedmedenko, and H.P. Oepen

Phys. Rev. Lett. **103**, 147204 (2009)

P3

The numbers by which citations are referenced in the following article are only valid within the article.

PRL 103, 147204 (2009) PHYSICAL REVIEW LETTERS week ending 2 OCTOBER 2009

Magnetic Ground State of Single and Coupled Permalloy Rectangles

S. Hankemeier,* R. Frömter, N. Mikuszeit, D. Stickler, H. Stillrich, S. Pütter, E. Y. Vedmedenko, and H. P. Oepen
Universität Hamburg, Institut für Angewandte Physik, Jungiusstrasse 11, D-20355 Hamburg, Germany
(Received 2 February 2009; published 1 October 2009)

We have studied the magnetic domain structure in Permalloy rectangles that reveal flux-closure domain configurations. Arrays with varying spacing between the rectangles are investigated by scanning electron microscopy with polarization analysis as well as by micromagnetic simulation. In contrast to general expectation, rectangles in the flux-closure Landau state show significant coupling and form a magnetic pattern of common chirality. The coupling is due to the stray field that originates from small changes of the magnetization alignment, which is sensitive to the exact shape and the separation of the rectangles.

DOI: 10.1103/PhysRevLett.103.147204 PACS numbers: 75.60.Ch, 75.50.Bb, 75.75.+a

One important aspect of present research on magnetism is the behavior of magnetic structures fabricated from thin films. While apparently the magnetic ground state is well known, the research is mostly dedicated to the dynamic properties after excitation either by short field or current pulses [1]. Particularly, the magnetic ground state in rectangles (1 μm $\times$ 2 μm) of $\sim$20 nm thick Permalloy (Py) has settled as best known structure in the research on micromagnetism in general. The reason for this situation is the fact that thin rectangles are commonly accepted as paradigmatic structure that causes flux-closure domain structure in soft magnetic materials. This concept was reaffirmed when the so-called standard problems [2] were launched in the 1990s to compare the quality and accuracy of micromagnetic simulations. A rectangle with the above dimensions and magnetic parameters to mimic Py was defined as standard problem 1 (SP1). Nowadays, micromagnetic simulations are widely used and generally accepted when domain configurations are studied. In the case of SP 1, it appears to be granted that one of the two prominent flux-closure domain structures, i.e., either the Landau state [Fig. 1(b)] or the diamond state [Fig. 1(c)] is the ground state. Around 20 nm thickness these two states are close in energy [3,4] and small variations of magnetic parameters favor the one or the other. From the experimental point of view, the finding of such a state is taken as a proof for good structuring and magnetic quality. Nobody has ever proven with adequate experimental accuracy the magnetic fine structure of actual fabricated rectangles. As these structures deviate more or less from an idealized geometry, discrepancies between experimental findings and simulations made for perfect structures have to be expected. We show that the Landau structure shows significant deviations of the magnetization orientation from the four commonly assumed predominant magnetization directions. We find that a critical parameter is the exact shape of the rectangle. Since artificially created particles always have small deviations from the ideal shape, like inclined edges or edge roughness [5], the finding is of general importance, particularly when the magnetic behavior of rectangles, e.g., in external fields, is modeled.

The coupling between nano- or microstructures is another important issue in present research, as coupling has to be considered to understand the magnetization reversal behavior in arrays of nanostructures as, for example, in magnetic random access memory (MRAM) devices [6,7]. The general hypothesis is that the coupling will be important in case the single structures create a stray field, although some correlated chirality in vortex structures has been found recently [8–10]. From considerations about the stray field, it is concluded that the effects will show up for small particles [11] or in special geometries where particles with extremely elongated shape are placed head to head with very close spacing [9,12]. In the first case the particle will have a S or C state [Figs. 1(d) and 1(e)], while

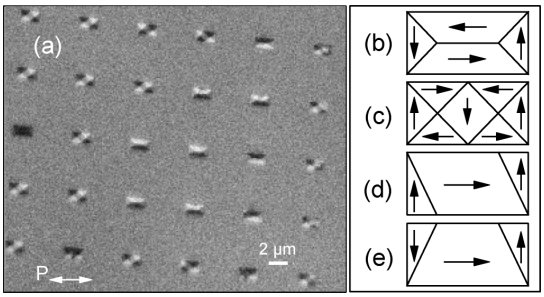

FIG. 1. SEMPA image of an array of well separated Permalloy rectangles (a). The image exhibits the magnetic structure obtained by one polarization component. The polarization sensitive axis is parallel to the horizontal edge. The dimensions of the rectangles are 1 μm $\times$ 2 μm $\times$ 23 nm. The rectangles show either the Landau state or the diamond state, only one structure is in the S state. (b)–(e) Sketch of the Landau state (b), diamond state (c), S state (d), and C state (e). ''S state'' and ''C state'' refer to the flux lines through the rectangle having shapes similar to the letters S and C, respectively.

PRL 103, 147204 (2009) PHYSICAL REVIEW LETTERS week ending 2 OCTOBER 2009

in the latter arrangement the interaction between the charged edges of two structures is stronger than the magnetostatic interaction throughout the ferromagnet. In the case that the ferromagnetic structures create flux-closure domains to minimize the stray field energy, the coupling is assumed to be less pronounced and particularly in the low field range the coupling is believed to be of minor importance for the reversal process. These suppositions are again founded on the unrealistically idealized structure morphology. We show in this Letter that the coupling is important even in the case where the single element exhibits apparently a flux-closure structure. We first present the magnetic fine structure of Permalloy rectangles with dimensions of SP1, and switch over in the second part to the influence of coupling between closely spaced rectangles and its consequences for the micromagnetic fine structure.

The rectangles are grown via the nanostencil technique [13] by *e*-beam evaporation. The mask, a FIB structured 100 nm thick silicon nitride membrane, was brought in direct contact with the Si substrate to minimize blurring of the structure edges. The structures presented here show some edge broadening, i.e., the side faces have an angle of approximately 30° to the film plane (instead of 90° for a perfect particle), as checked by scanning electron microscope (SEM) and atomic force microscope (AFM) measurements [Fig. 2(c)]. The edge roughness was found to be smaller than 20 nm peak to peak, which corresponds to the grain size. The rectangles have lateral dimensions that match the SP1 and a slightly higher thickness of 23 nm. We have performed spatially high resolving investigations of the Py rectangles via scanning electron microscopy with polarization analysis (SEMPA). Magnetic field cycles parallel to the long axis direction of the rectangles have been applied prior to imaging. Because of the high sensitivity of our SEMPA [14] we are able to analyze very accurately the spatial magnetization orientation with an angular resolution of less than 4°. Hard axis magneto-optic Kerr effect measurements of the extended film confirm a negligible uniaxial anisotropy ($\sim$200 J/m^3).

A SEMPA micrograph of an array of uncoupled structures is shown in Fig. 1(a). Within the fraction of the array imaged, mostly Landau and diamond structures appear, while one rectangle is in the S state. A statistical investigation of the whole array (100 rectangles) reveals that Landau and diamond structures appear with equal probability ($\sim$50%). Next we focus on the details of the magnetic domain structure of the two different states [Figs. 2(a) and 2(b)]. The two SEMPA images are taken simultaneously and show the distribution of magnetization components in two perpendicular in-plane directions. The frequency distribution of magnetization orientation versus angle for the two structures is shown in Fig. 3. For the diamond state we find four accumulation peaks, which represent the magnetization of four different domain orientations appearing in the domain structure. The four magnetization directions are parallel to the edges of the rectangle, in exact agreement with general belief. The

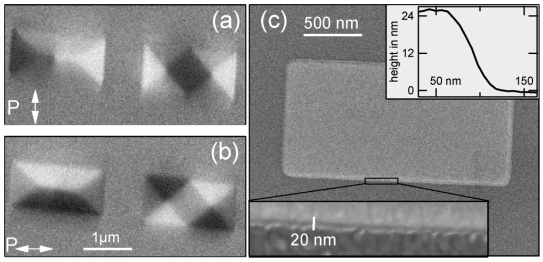

FIG. 2. Magnetic structure of Permalloy rectangles obtained by SEMPA. (a) and (b) give the images obtained via the two polarization sensitive axes oriented perpendicular to each other, parallel to the edges of the images. Both images have been measured simultaneously. (c) SEM image of a single Permalloy structure. In the lower left corner, a zoom into one edge is plotted. The inset displays an AFM line profile of the edge of the structure, which was capped by 2 nm Pt.

situation is completely different in case of the Landau state, where we find six maxima. The plot reveals that the peaks that correspond to the orientation of the long axis domain magnetization split. In the direction parallel to the long edges we do not find a single maximum in the distribution, but a splitting into two closely spaced maxima. In other words, in the Landau structure the magnetization in the larger domains is no longer aligned parallel to the long edges. The majority of the magnetization is slightly ($\sim$17.5°) turned up- or downward within the plane of the rectangle. The diamond state, on the other hand, shows a broadening of the distribution of the same magnetization orientation, which is an indication for contributions from continuously rotating magnetization.

As the splitting of the magnetization for the Landau structure was unexpected, we have performed micromagnetic simulations [15]. The geometric and magnetic parameters are taken from SP1 [2]; the simulation cell size was (5 nm)^3, i.e., $400 \times 200 \times 4$ cells. To attain the Landau structure we relaxed the system, starting from a vortex state. The resultant frequency of magnetization orientation versus angle is plotted in black in Fig. 4. Surprisingly, the simulation shows a splitting of the long edge domain magnetization orientation as well. Such a splitting has not been discussed so far in the literature. Although hints can be found in published domain structures obtained by micromagnetic simulations [3,4,16,17], it was not further investigated as, at most, a small spreading (of no relevance) of the magnetization orientation due to a continuous magnetization rotation around the singularity was expected. Comparing our experimental result with the simulation, it is evident that the splitting angle in the experiment (35°) is larger than in the simulation (15°). To learn about the origin of this discrepancy, we have made cross-checks by varying the magnetic properties in the simulation. First we checked the influence of the magneto-

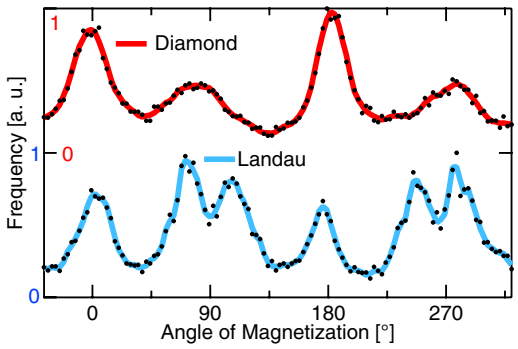

FIG. 3 (color online). Frequency of magnetization orientation as a function of angle. The angle is given with respect to the short edge of the Permalloy rectangle. The experimental data for the diamond- and the Landau structure is shown.

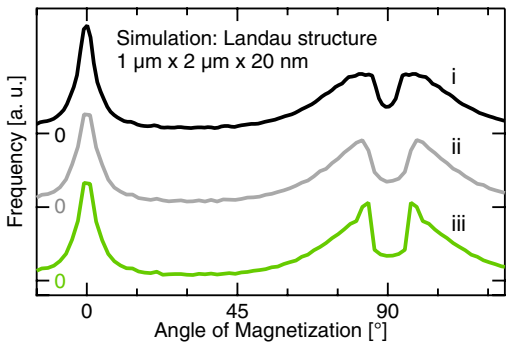

FIG. 4 (color online). Frequency of magnetization orientation as a function of angle for a single Landau structure obtained by simulations [15]. The black curve (i) gives the result for a perfect rectangle with SP1 parameters [2]. The gray plot (ii) additionaly includes edge roughness with a period of 30 nm and a peak-to-peak amplitude of 20 nm. The green curve (iii) gives the result for SP1 including inclined edges with an inclination length of 35 nm.

crystalline anisotropy. Changing the anisotropy from $+500\ \mathrm{J/m^3}$ (SP1) to $-500\ \mathrm{J/m^3}$ does not have any significant influence on the splitting angle. The only variation that showed effects was a change of the morphology of the rectangle. As the fabrication process in general generates rough and inclined edges, we have made simulations to investigate these effects: Based on our experimental findings, we have included edge roughness of a periodicity of 30 nm and a peak-to-peak amplitude of 20 nm and also modeled the edge inclination via stepwise reduction of the thickness over 35 nm. The results of the simulations are plotted as curves (ii) and (iii) in Fig. 4. Notably, the former small splitting becomes larger and more emphasized in both cases. This indicates that edge morphology is a very sensitive parameter that influences the orientation of magnetization. The splitting further increases by mutual amplification. The explanation is straightforward: volume charges are created by the 180°-Néel wall along the center, which cause a locally varying field that stipulates a locally varying magnetization. The torque on the magnetization by the volume charge is counterbalanced by the magnetic poles that will be created at the borderline of the rectangle due to magnetization in-plane tilting. As this magnetic pole density is reduced at rough and inclined edges, the demagnetizing field is smaller than that of a sharp edge [18] and the edge influence is reduced. The in-plane tilting of magnetization due to the volume charges originating from the 180°-Néel wall becomes larger with increasing edge roughness and inclination. Hence, a splitting of the long edge magnetization orientation will be always present, while the splitting angle is a measure for the edge structure. To strengthen that point, the results represented in Fig. 3 are those for the best structures we could fabricate via mask techniques. While for the idealized geometry the peaks in the angular distribution are fairly broad, indicating a gradual rotation, the peaks of the more realistic simulation are much sharper and can thus be seen as footprint of two separate domains.

Next we want to address the coupling of closely spaced rectangles. Figure 5 displays the magnetic structure of arrays of coupled rectangles obtained via SEMPA. The rectangles are arranged in a row with small spacing between the structures (nominal separation 200 nm) to render coupling across the long edges possible. The magnetization distribution of a single rectangle out of the array is shown in Fig. 6(a). The frequency of magnetization orientation taken from the same element is shown in Fig. 6(b). The histogram shows six clearly separated accumulation peaks, which are sharper than those in case of single rectangles. The splitting of the magnetization of the long axis domains is larger (46°) than for the noncoupled elements (35°). The microstructure in the former long axis domain has split up into two well-separated magnetic domains. The splitting is enhanced, which is caused by the magnetostatic interaction of the rectangles. The areas below the different peaks reveal that the size of the two new domains is comparable to that of the domains with magnetization orientation up and down [Fig. 6(a)]. In the SEMPA image the four regions can easily be identified as connected areas, i.e., domains. They are pairwise separated by a small angle Néel wall that runs perpendicular to the long edge through the line of vortices. Such a domainlike structure is known as a detail of the complex cross-tie wall [19,20].

All rectangles in the array exhibit the Landau state. All structures in a row of coupled rectangles show an identical magnetic pattern and have the same chirality of magnetization. Moreover, the vortices of the different rectangles are all perfectly aligned. Apparently, the interplay of long

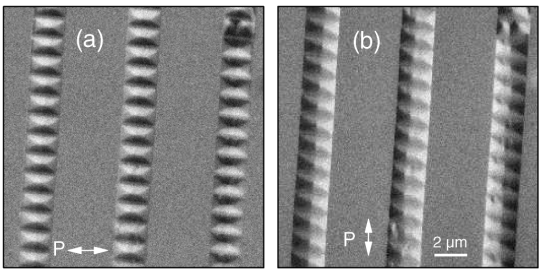

FIG. 5. SEMPA micrograph of an array of coupled Permalloy rectangles. (a) and (b) give the two polarization sensitive axes oriented perpendicular to each other, as indicated by the arrows. Both images have been measured simultaneously.

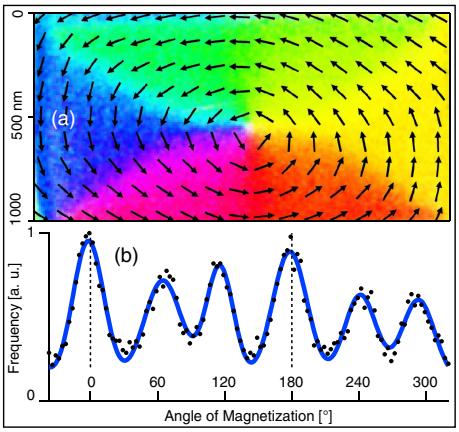

FIG. 6 (color online). Magnetization orientation of one single element from the array of Fig. 5. (a) shows a color (arrow) plot of the magnetic microstructure. The magnetization orientation was calculated from the SEMPA images. For easier understanding, arrows are given which show the direction of magnetization. (b) is the frequency of magnetization versus angle for the element shown in (a).

and short range interactions generate a new mesoscopic magnetic pattern that is originating in the instability of the single structure against in-plane tilting of the long axis magnetization orientation. The driving force is the magnetostatic interaction between the closely spaced edges that supports the creation of opposite poles. As the single-element Landau configuration is susceptive to magnetization rotation of the long edge domains, the magnetization is tilted in opposite directions in the closely spaced domains. The adjacent edges of two neighboring structures are oppositely charged. As a result all the elements are fixed regarding their microstructure and a mesoscopic structure is created throughout the whole assembly of coupled elements. The resultant structure is similar to a cross-tie wall. Typical elements of a cross-tie wall are the vortex and antivortex structures. In the coupled structures the vortices are located within the rectangles while the antivortex structures are suppressed by moving their position into the region between the rectangles. The cross-tie wall-like structure eliminates large angle domain walls in the elements and thus represents a minimum of the total energy.

In summary, we conclude that the domain structure, even in seemingly well-understood systems like Py rectangles, reveals new and surprisingly relevant details when analyzed with appropriate sensitivity. In the Landau configuration we find a splitting of the magnetization orientation of the large domains. The splitting angle increases with decreasing quality of the edges. Inevitably rough and inclined edges in experiments have a strong impact on the magnetic behavior and have to be incorporated in simulations, particularly when the behavior in external fields is considered. The susceptibility to fields is demonstrated by study of the coupling in an array of rectangles. In contradiction to common belief, the magnetostatic coupling of closely spaced rectangles with flux-closure structure is strong. The instability of the magnetization orientation of the Landau structure puts the coupling on an entirely new basis, resulting in a new mesoscopic superstructure to minimize the total energy of the whole assembly of rectangles.

We gratefully acknowledge funding from DFG via SFB 668. We thank G. Hoffmann and M. Scholz for performing the AFM measurements.

*shankeme@physnet.uni-hamburg.de

[1] B. Hillebrands and A. Thiaville, *Spin Dynamics in Confined Magnetic Structures III* (Springer, Berlin, 2006).
[2] NIST Micromagnetic Modeling Activity Group.
[3] W. Rave and A. Hubert, IEEE Trans. Magn. **36**, 3886 (2000).
[4] R. Hertel, Z. Metallkd. **93**, 957 (2002).
[5] R. P. Cowburn *et al.*, J. Appl. Phys. **87**, 7067 (2000).
[6] W. J. Gallagher *et al.*, J. Appl. Phys. **81**, 3741 (1997).
[7] J. Shi, in *Ultrathin Magnetic Structures IV: Applications of Nanomagnetism*, edited by B. Heinrich and J. A. C. Bland (Springer, Berlin, 2005).
[8] V. Novosad *et al.*, Appl. Phys. Lett. **82**, 3716 (2003).
[9] K. Sato *et al.*, J. Magn. Magn. Mater. **304**, 10 (2006).
[10] T. Tezuka *et al.*, Trans. Magn. Soc. Jpn. **4**, 241 (2004).
[11] R. F. Wang *et al.*, Nature (London) **439**, 303 (2006).
[12] A. Remhof *et al.*, Phys. Rev. B **77**, 134409 (2008).
[13] M. M. Deshmukh *et al.*, Appl. Phys. Lett. **75**, 1631 (1999).
[14] R. Frömter *et al.*, Vacuum **82**, 395 (2007).
[15] M. J. Donahue and D. G. Porter, *OOMMF User's Guide: Version 1.0, Interagency Report NISTIR 6376* (National Institute of Standards and Technology, Gaithersburg, MD, 1999).
[16] J. M. García *et al.*, J. Magn. Magn. Mater. **242–245**, 1267 (2002).
[17] S. Cherifi *et al.*, J. Appl. Phys. **98**, 043901 (2005).
[18] S. Pütter *et al.*, J. Appl. Phys. **106**, 043916 (2009).
[19] S. Middelhoek, J. Appl. Phys. **34**, 1054 (1963).
[20] R. Ploessl *et al.*, J. Appl. Phys. **73**, 2447 (1993).

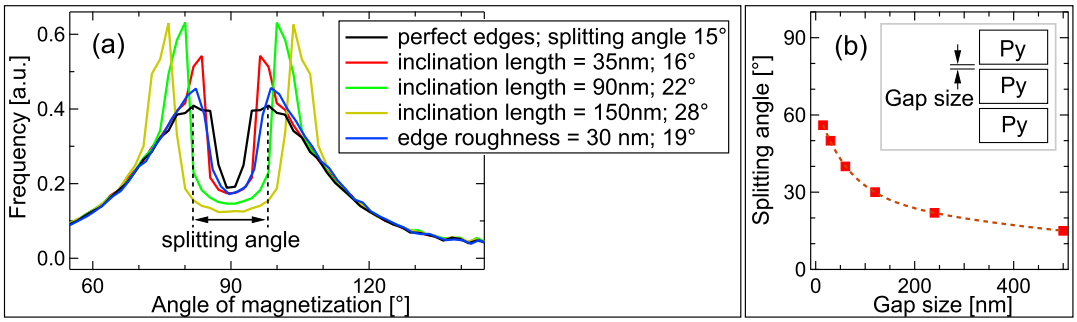

Figure 4.2.: Simulated results for the dependence of the splitting angle on geometrical parameters. In (a) the results for a single rectangle are plotted for different edge geometries. The dependence of the splitting angle on the gap size between three coupled Py rectangles is plotted in (b) as red squares. The dotted line is a guide to the eye.

4.1.1. Additional simulations on the splitting angle

In [P3, Fig. 4] numerical results of the splitting angle of three different edge types of single elements were presented. N. Mikuszeit, who performed the majority of the simulations, conducted further simulations covering a wider set of parameters. The results are plotted in Fig. 4.2. In (a) a zoom into the angular histogram shown in [P3, Fig. 4] is plotted. It is concentrated on the critical feature, the splitting of the domain parallel to the long edge expressed by the splitting angle. As discussed in [P3] even for a rectangle with perfect edges a small splitting (15°) is present in the simulations (black curve). When inclined edges are introduced, an increase of the inclination length causes an increase of the splitting angle as well as more pronounced peaks (red, green and yellow curves). 90 nm inclination length, for example, yield a splitting angle of 22°. The same trend is observed when introducing edge roughness via "postage stamp edges" with an amplitude of 30 nm (blue curve) which gives 19° splitting.

Any alteration of the edge geometry from the perfect rectangular geometry probably causes an increase of the splitting angle. This is due to the fact that any deviation from the perfect edges causes an increase of the edge surface and thus decreases the magnetic pole density at the edge. In return new poles are created which are accompanied by an increased splitting of the large domain.

In Fig. 4.2(b) the effect of coupling between rectangles is presented: Three rectangles in a row have been simulated with the geometrical arrangement shown in the inset. The gap size has been varied and the splitting angle of the central rectangle is plotted versus gap size. The splitting angle increases with a decrease of the gap size as illustrated by the red curve which is a guide to the eye. The trend can be explained by the fact that with low separation magnetic poles at the long edge are counterbalanced by opposite poles at the edge of the next rectangle, thus allowing again for an increase of the splitting angle.

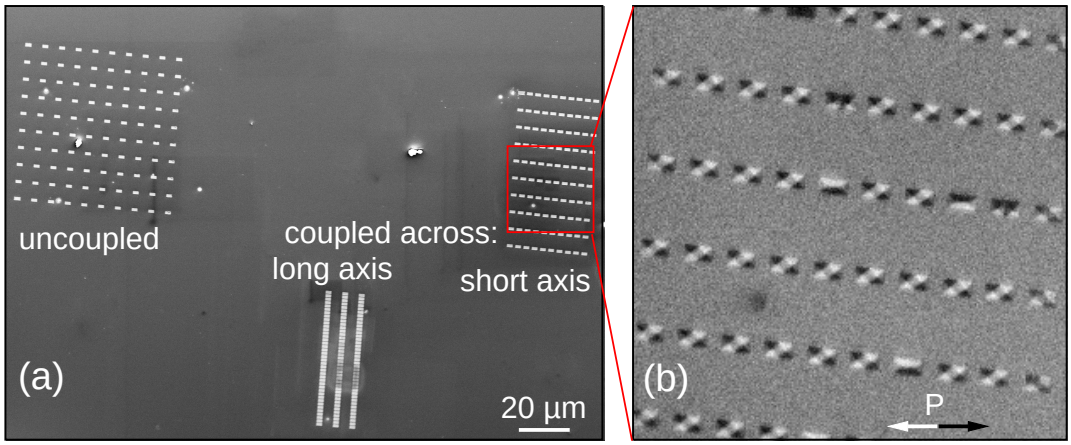

Figure 4.3.: In (a) a SEM image of the three different Py arrays with rectangles of 2 µm x 1 µm x 23 nm is shown. (b) displays the SEMPA image of the indicated area. The distance between short edge of two rectangles is 900 nm.

4.1.2. Long range coupling & Summary

Fig. 4.3(a) shows a SEM image of the arrays of Py rectangles presented in [P3]. As discussed in the article, the rectangles in the uncoupled array exhibit a equal distribution of Landau and diamond state while the rectangles coupled across the long axis are solely in the Landau state with common sense of rotation. The third array on the sample was not discussed in the article thus a brief summary of the results follows: The distance between the short edges of the rectangles is 900 nm and 5 µm in the other direction with a size of the rectangles of again 2 µm x 1 µm x 23 nm. In Fig. 4.3(b) a SEMPA image of the third array is shown. Four Landau states are visible, one single domain state, two double vortices and 46 structures are in the diamond state, all with the same sense of rotation. All three arrays have an identical magnetic history but show a totally different magnetic microstructure of the rectangles which must then originate from the interaction between the elements. Thus, a magnetic coupling between the rectangles in the flux closure diamond state (Fig. 4.3(b)) via their stray-field is evident. This is a rather surprising result as in the literature coupling is only observed for a separation of at most 300 nm for flux closure configurations[1]. In [Nov03], Py squares with 400 x 400 nm^2 and a separation of 100 nm were investigated showing vortices with same sense of rotation. Sato et al. observed the opposite sense of rotation in 1000 x 1000 nm^2 Py squares with 300 nm separation [Sat06]. In [Lua08] it is reported on chains of alternating vortex configurations in arrays of 2 µm large Py hexagons separated by 200 nm. Konoto et al. [Kon08] observed no coupling between 640 x 640 nm^2 rectangles with a spacing of 320 nm and in [Che05] where 600 x 600 nm^2 Co squares with a distant of 300 nm were investigated it is stated that "The elements in the patterns were separated sufficiently so that there was negligible magnetic coupling via their stray-fields". In contrast, the SEMPA measurement in Fig. 4.3(b) shows coupling over a distance of 900 nm which suggests that the influence of stray-fields for the magnetic interaction

of adjacent structures is more important than commonly believed.

A micromagnetic simulation of the problem is challenging due to the large size of such an array which makes significant computational resources necessary if many structures are modeled. A solution of the problem could be the implementation of periodic boundary conditions which was recently realized by K. Lebecki et al. [Leb08]. Thus, a cooperation was initiated with Dr. Lebecki, now at the University of Konstanz, where the diploma student J. Jelli will try to model all three arrays to quantify the experimental findings. A first step will be to repeat our simulations in order to reproduce our experimental findings for the uncoupled rectangles as in our simulation even with inclined and rough edges according to the experimentally observed geometry, the measured splitting angle of 35° could not be reproduced. A solution to this problem could be to additionally include rounded corners to the rectangle geometry as observed in the experiment [P3, Fig. 2(c)] or maybe to further decrease the cell-size of the simulation.

4.2. Interpretation of magnetotransport measurements utilizing SEMPA images

Publication [P3] deals solely with the magnetic fine structure of rectangles with dimensions of "standard problem # 1" (SP1) in the remanent state. In case of SP1 the Diamond state and the Landau state are nearly equal in energy [Rav00] as can also be seen from the equal distribution of both states in the uncoupled rectangles [P3, Fig. 1], while in the coupled rectangles the Landau state dominates. The actual domain configuration found in a given structure can depend on stray-field interaction with structures in the vicinity as observed in [P3], on the magnetic history of the sample or on the direction of some magnetocrystalline anisotropy of the thin-film material [Hub98](p464ff.)

The dependence of the magnetic configuration on treatment in an external field is the topic of our publication [P4], which is discussed in the following: The focus of the article is to present a method to determine the magnetic energy of single submicron rectangles with an aspect ratio of 2:1 via magnetotransport measurements. For that purpose the anisotropic magnetoresistance (AMR) of a single rectangle has been measured while a magnetic field cycle has been applied along the short- and long axis, respectively.

As the name AMR suggests, a resistivity anisotropy is existent in ferromagnetic samples which depends on the angle φ between current flow $\vec{j}$ and direction of magnetization. The difference in resistance is largest between $R_\perp$ in case the magnetization and current are perpendicular to each other and $R_\parallel$ when they are parallel

[1] In the literature, the magnetostatic coupling between elements is often discussed in terms of relative separation, i.e. absolute separation divided by element size [ML06, Vog10]. This approach is advantageously in case small elements are under investigation where the magnetization is far from parallel to the edge. In the text, however, relative large structures are discussed which are in the flux-closure state. Here, the absolute distance is probably a more suited value for comparison.

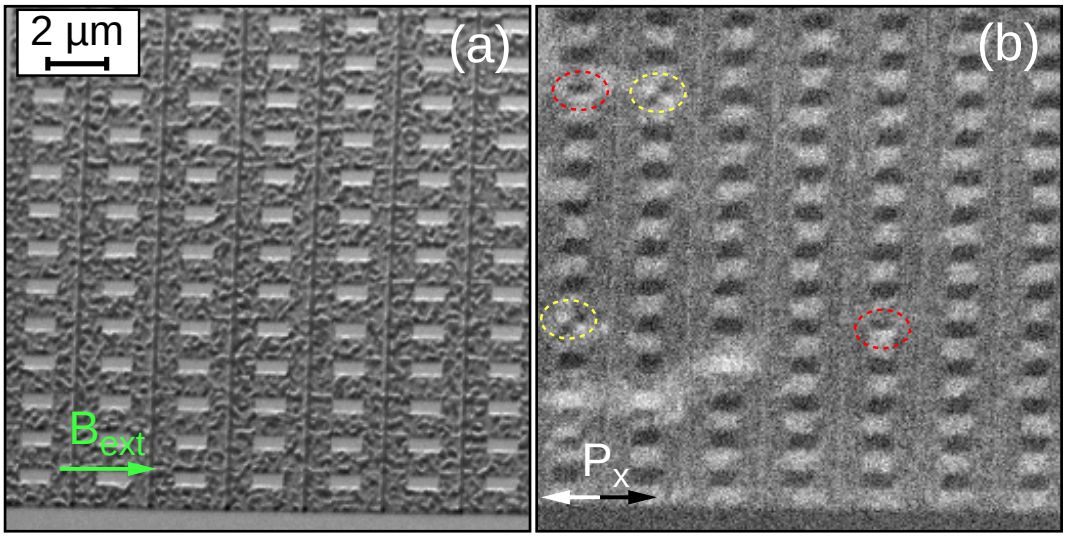

Figure 4.4.: (a): Sum image of 91 Permalloy rectangles with an individual size of 800 x 400 x 20 nm^3; before imaging the rectangles were saturated by an external magnetic field indicated by the green arrow. (b) shows the magnetic contrast along the x-direction, two structures are in the Landau state (red circles), two in the Diamond state (yellow circles), all other structures exhibit a single domain state (S- / C-state).

aligned. The angular dependence can be expressed via [McG75]:

$$R_{\mathrm{AMR}}(\varphi) = R_{\perp} + \Delta R \cdot \cos^2(\varphi), \tag{4.4}$$

where ΔR is defined as $R_{\parallel} - R_{\perp}$. The strength of the AMR is quantified by the expression $\frac{\Delta R}{R_{\perp}}$ which is usually in the range of 0.5-5 % at room temperature. A common value for 20 nm thick Permalloy film is $\frac{\Delta R}{R_{\perp}} = 1.5 - 2$ %. The resistance anisotropy can be explained phenomenologically by different scattering cross sections for the conduction electrons at the non-spherical $3d$-orbitals due to spin orbit interaction [Ebe96]. A first attempt for a quantum-mechanical description of the effect has already been given in 1951 [Smi51] and expanded in [Pot74, McG75]. Considering the spin-orbit interaction operator of the form:

$$\Upsilon_{\mathrm{LS}} = A\mathbf{L}\cdot\mathbf{S} = A\left[L_z S_z + \underbrace{\frac{1}{2}\left(L_x - iL_y\right)\left(S_x + iS_y\right) + \frac{1}{2}\left(L_x + iL_y\right)\left(S_x - iS_y\right)}_{\text{spin-flip operator}}\right], \tag{4.5}$$

where $\mathbf{L}$ is the orbital momentum operator and $\mathbf{S}$ is the spin operator. The effect of the spin-flip operator in Υ_{LS} is an enhancement (decrease) of the spin quantum number with a simultaneous decrease (enhancement) of the orbital angular momentum quantum number. In practice it mixes the spin-up and spin-down states as it establishes the possibility of electron scattering from the $4s^{\uparrow}$ into the $3d^{\downarrow}$ orbitals. From the fact that the spin-flip operator is not symmetrical with respect

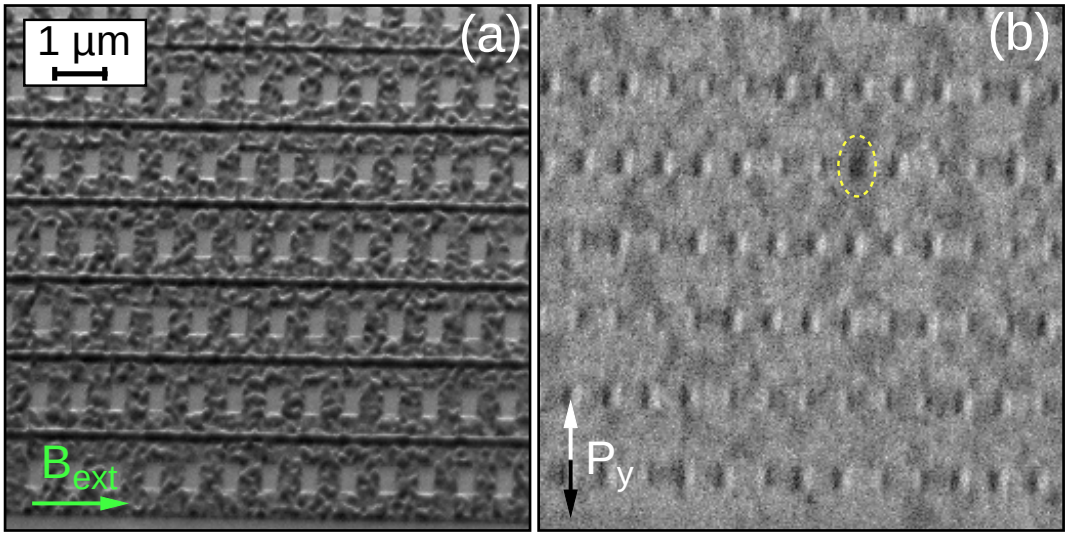

Figure 4.5.: Sum image of 94 Permalloy rectangles of 600 x 300 x 20 nm^3, before imaging the rectangles were saturated by an external magnetic field indicated by the green arrow. (b) shows the magnetic contrast in the y direction, all structures except one are in the Landau state.

to x, y and z, it may be expected that not all orbitals are mixed to the same amount. Writing down the wave-functions and calculating the scattering probability for different cases leads to the results that when $\vec{j} \| \vec{M}$ the $s^{\uparrow}$-$d^{\downarrow}$-scattering is enhanced resulting in a higher electrical resistance compared to $\vec{j} \perp \vec{M}$ when the $s^{\uparrow}$-$d^{\downarrow}$-scattering channel is suppressed [McG75].

Coming back to the experimental investigation, a mandatory information for the correct interpretation of the acquired AMR hysteresis loops is the magnetic microstructure of the elements in zero field. To gain a general quantitative statement regarding the most favorite magnetic configuration for rectangles of a given shape, size and magnetic history, arrays of about 100 uncoupled elements have been imaged for the geometrical configurations of interest. The publication discusses elements with an aspect ratio of 2:1, film thickness 20 nm each, 1000 nm, 800 nm and 600 nm length of the long axis, which have been exposed to external field loops perpendicular and parallel to the long axis. Two exemplary (out of six) SEMPA images of arrays of 91 and 94 structures are presented in Fig. 4.4 and Fig. 4.5. In Fig. 4.4 structures with a size of 800 x 400 nm^2 are shown, the magnetic field was applied along the long axis of the rectangles prior to imaging. It is visible from the magnetic contrast in Fig. 4.4(b) that two structures are in the Landau state (red circles), two in the Diamond state (yellow circles), while all other elements exhibit the C- or S-state. In Fig. 4.5(b) the magnetic contrast of 94 elements with a length of 600 nm is shown, after pretreatment in an external field aligned along the short axis. All elements but one (yellow circle), are in the Landau state. The two measurements already show the enormous effect of the magnetic history on the remanent state.

SEMPA images of arrays of rectangles with all three sizes in combination with both orientations of the external field yielded the statistical information about the

remanent state during the hysteresis loops as discussed in [P4]. With this information it was possible to deduce the complete magnetization procedure of a single rectangle during the hysteresis loop from the AMR signature and then determine the anisotropy of a single element from the so evaluated AMR hysteresis.

Magnetic energies of single submicron permalloy rectangles determined via magnetotransport

A. Kobs, H. Spahr, D. Stickler, S. Hankemeier, R. Frömter, and H.P. Oepen

Phys. Rev. B. **80**, 134415 (2009)

P4

The numbers by which citations are referenced in the following article are only valid within the article.

PHYSICAL REVIEW B **80**, 134415 (2009)

Magnetic energies of single submicron permalloy rectangles determined via magnetotransport

André Kobs,* Hendrik Spahr, Daniel Stickler, Sebastian Hankemeier, Robert Frömter, and Hans Peter Oepen
Institut für Angewandte Physik, Universität Hamburg, Jungiusstraße 11, 20355 Hamburg, Germany
(Received 31 March 2009; revised manuscript received 22 September 2009; published 19 October 2009)

We have investigated the magnetic properties of single submicron permalloy rectangles with a thickness of 20 nm and an aspect ratio of 2:1 via anisotropic magnetoresistance (AMR). Preparation and investigation via magnetotransport are performed *in situ* in ultrahigh vacuum. The field-dependent magnetization behavior of the two generic cases with the magnetic field applied perpendicular and parallel to the long axis of the rectangles is studied. Due to the high sensitivity of our setup, single field sweeps are sufficient to obtain magnetoresistance curves of structures with dimensions as small as 600×300 nm^2. To link features of the AMR to changes in the micromagnetic states, the remanent state has been investigated via scanning electron microscopy with polarization analysis. Our main result is that the energy density of micromagnetic states can be obtained from the hard-axis magnetization behavior. It is demonstrated that a C/S state can be distinguished from a Landau state and the energy difference between both states is determined.

DOI: 10.1103/PhysRevB.80.134415 PACS number(s): 75.60.−d, 75.50.Bb, 75.47.−m, 81.16.−c

I. INTRODUCTION

Present basic research on magnetism is mainly focused on nanostructures, particularly their fabrication and characterization. The ultimate aim is to understand the magnetization behavior of nanostructures and to follow the transition from collective behavior to the quantum-mechanical behavior of atoms and molecules. In a bottom up approach, i.e., depositing single atoms, clusters, or nanoislands on perfect surfaces, big progress has been made over the last years, which is enabled by the improvements of scanning probe techniques.[1–3] A disadvantage of this approach is caused by the method of preparation of the nanosized elements, as it does not allow to tune magnetic or structure parameters on purpose. Therefore, a systematic evaluation of dependences is not possible. A further problem is the fact that magnetic properties are only indirectly accessible via modeling the lateral distribution of the probed quantities. In general, imaging techniques with high spatial resolution are utilized to study the domain pattern.[4] Modeling the domain structure then allows to extract indirectly the magnetic quantities.

The top-down approach, i.e., the fabrication of artificial nanostructures, has also made tremendous progress in recent times.[5] However, the characterization of such structures is still lagging behind because the quantitative analysis of single structures is difficult due to missing sensitivity of conventional characterization techniques. To study, e.g., the size and shape dependence of magnetic properties of single nanostructures, new methods have to be developed. The route to achieve the required sensitivity for measuring magnetic properties of single nanostructures is via miniaturized probes that are combined with conventional macroscopic measurement tools. The pioneering experiment in this field was the successful measurement of magnetic-flux density via microsuperconducting quantum interference device.[6] Nowadays the trend is shifting toward investigating magnetic wires, which are of technological relevance.[7,8] Measuring the anisotropic magnetoresistance (AMR) of wires with two dimensions shrank to the nanoscale has the potential to sensitively detect the switching fields.[9–12] Until recently, the reversal has been interpreted in the framework of homogenous magnetization reversal of the whole wire, as predicted analytically for rotational ellipsoids.[13] On the contrary, latest investigations have demonstrated that the assumption of nonlocal reversal procedures is wrong.[14,15] Instead, a domain wall nucleates at the end of the wire and rushes through the wire, as predicted theoretically.[16,17] This example demonstrates that the combination of domain structure investigation and quantitative studies of switching fields, anisotropies, or other magnetic quantities is mandatory.

While single wires are frequently investigated, the study of real nanostructures (all three dimensions nanosized) is rare and most often performed with the help of nanostructure arrays.[18,19] To address an individual nanostructure is very demanding as the whole measuring device has to be scaled down. In this paper we present an approach for AMR investigation of single structures with lateral dimensions down to some 100 nm. Additionally, this approach gives the flexibility to vary parameters of the nanostructure, such as size and shape, which opens the way to systematically study dependences on particular parameters.

In this paper we demonstrate how this technique allows to quantify the size-dependent energy of the Landau state in single nanostructures below 1 μm lateral size. The quantitative magnetization behavior obtained via AMR is complemented by domain structure investigations via scanning electron microscopy with polarization analysis (SEMPA). The combination of both methods gives direct access to the understanding of the reversal mode and the resultant interpretation.

II. EXPERIMENTAL DETAILS

The experiments are performed in a UHV dual beam system, equipped with a focused ion beam (FIB) and a SEM. The FIB is used to create a microsized electrical circuit including a ferromagnetic rectangle in a film [see Fig. 1(a)]. For the *in situ* magnetoresistance measurements the electrical circuit is contacted by a micromanipulator.[20] The current is driven through the structure to the film, which serves as sec-

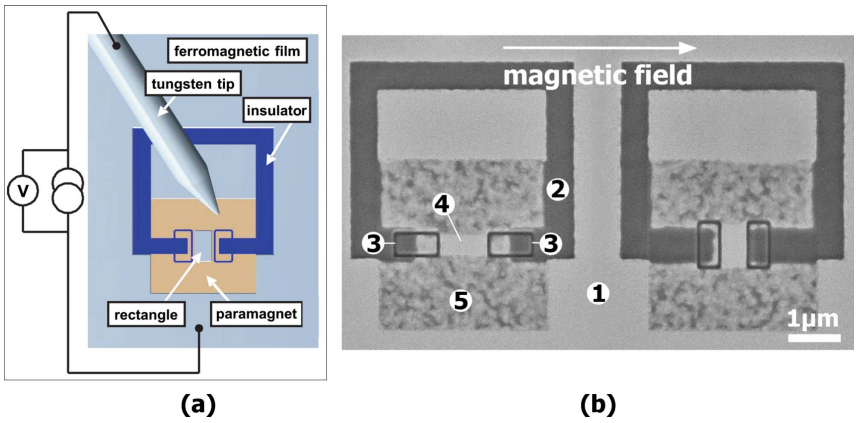

FIG. 1. (Color online) Microsized circuits for magnetoresistance measurements. (a) Sketch of the measurement principle. The tungsten tip can be moved by a micromanipulator to contact the circuit within the framed region. The approach is monitored via SEM. The current is driven from the tip to the film crossing a small ferromagnetic rectangle within the gap of the yoke-shaped frame. (b) SEM micrograph of two microsized circuits with different orientations of the ferromagnetic rectangles (4) with respect to the field direction (arrow). The rectangles of size 800×400 nm^2 are surrounded by paramagnetic material (5), which has been created by Ga^+ ion bombardment out of the ferromagnetic film (1). The dark gray parts (2, 3), where the metal has been totally removed by sputtering, are electrically insulating.

ond electrode. A magnetic field of up to ±23 mT can be applied within the film plane. The orientation of the magnetic field is fixed with respect to the sample. The fabrication process and tip steering is controlled via SEM. The dimensions of the investigated rectangles are 1000×500, 800×400, and 600×300 nm^2. The energy of the Ga^+ ions is 30 keV at a beam current of 40 pA.

An SEM image of two FIB made microcircuits is shown in Fig. 1(b). The bright gray regions show the unperturbed film (1). In the black areas (2, 3) the metal has been completely removed by ion milling. The FIB preparation is performed in three steps: in the first step a yoke-shaped structure (2) is milled, which isolates the framed region from the film (1) except for the small part in the gap of the yoke. In the second step the rectangle (4) in the gap of the yoke is created. For that purpose, the area around the rectangle is irradiated by Ga^+ ions (5) to destroy the long-range magnetic order while conductance is maintained. Narrow isolation lines (3) are prepared in the third step close to the rectangle (nominal distance of 75 nm) so that almost the whole current has to pass through the rectangle and any bypassing current is kept negligibly small. This layout creates the highest current density of the whole electrical circuit in the region of the rectangle, which enhances the sensitivity for the ferromagnetic structure. This preparation procedure guarantees the most precise geometry of the rectangle as any distortion due to thermal drift is minimized. The second microsized circuit on the right-hand side in Fig. 1(b) has a different orientation of the rectangle with respect to the magnetic field and current direction.

For the experiments a Cr (10 nm)/Py (20 nm)/Pt (2.5 nm) multilayer film is used, which has been deposited on an electrically insulating Si_3N_4 substrate using electron-beam evaporation. The deposition rate is 0.5 Å/s at a base pressure of 10^{-8} mbar. The Cr layer serves as a seed layer while the Pt layer on top prevents oxidation.

When destroying the long-range magnetic order by ion bombardment, it is necessary to maintain a low resistance of the leads (5) to keep the sensitivity for magnetogalvanic effects high. This can be achieved by keeping the material removal as small as possible. For that purpose the Cr layer is incorporated into the multilayer stack to induce intermixing of permalloy (Py) and Cr by ion bombardment.[21] As only 8% of Cr in Py causes the Py to become paramagnetic at room temperature,[22,23] the phase transition should be achieved already at low ion doses. For the layer system a gallium ion dose of 6000 μC/cm^2 (3.75×10^{16} Ga^+/cm^2) is needed to destroy long-range order while a film thickness of only about 12 nm is removed (to be published).

The magnetoresistance is measured utilizing pulsed electrical currents with an amplitude of $I=0.3$ mA (duty cycle of 10%), which corresponds to maximum current densities of 3×10^{10} A/m^2. This current density does not cause any detectable heating of the submicron structure[20] and is about one order of magnitude smaller than required to move domain walls in Py.[24] As mentioned above, two different orientations of the rectangles with respect to the magnetic field direction are fabricated while the orientation of the microsized circuit is not changed. This enables the investigation of the two generic cases with the magnetic field applied parallel to the long and short axis of the rectangle, respectively, while current and field are orientated perpendicular to each other.

After the MR measurements the magnetic microstructure has been investigated by means of SEMPA.[25] As the rectangles have two different orientations with respect to the magnetic field, the micromagnetic structure in remanence is obtained for both pretreatments.

III. RESULTS AND DISCUSSION

In a first step, we have checked for parasitic contributions to the resistance due to magnetogalvanic effects in the whole

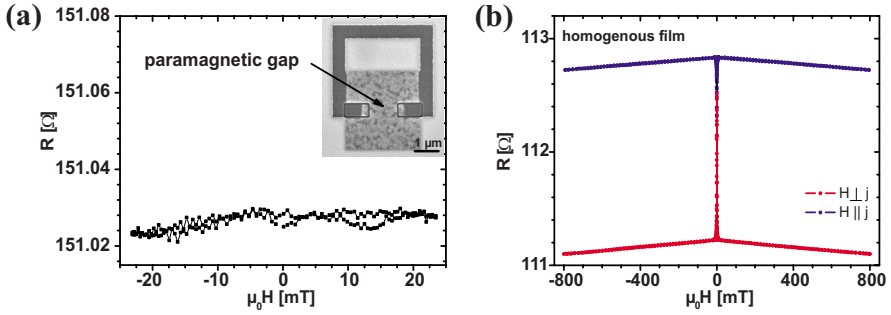

FIG. 2. (Color online) Resistance versus field curves. (a) MR measurement of a paramagnetic gap. An SEM micrograph of the microsized circuit is shown as inset. (b) MR measurements of the film system. The measurements are performed on a macroscopic wire with dimensions of l=6 mm and w=0.5 mm. The current is driven through the whole wire while the voltage drop along 4 mm is measured. The magnetic field is applied in the film plane perpendicular ($H \perp j$) and parallel ($H \| j$) to the current direction, respectively. At low fields the AMR dominates due to magnetization reversal processes. At high fields the isotropic negative MR dominates, which is due to the decrease in spin-wave density on field increase.

circuit including the ferromagnetic film. For that purpose we have created a circuit with identical layout while the rectangle has been rendered paramagnetic in the same way as explained above [see inset of Fig. 2(a)]. The obtained resistance versus magnetic field curve is plotted in Fig. 2(a). Within the resolution of the measurement ($\Delta R/R = 1 \times 10^{-5}$) no dependence of the resistance on the magnetic field is found. This result demonstrates that any MR signal arising from the ferromagnetic film can be neglected. Additionally, it proves that the applied ion dose is sufficient to destroy ferromagnetism. In comparison to the MR curves obtained for the rectangles (see below) this result also shows the high sensitivity for the ferromagnetic nanostructures.

In a second step, we have characterized the MR properties of the homogeneous film in an *ex situ* four-point MR setup in magnetic fields of up to ±800 mT. The dependence of the resistance on field is plotted in Fig. 2(b). The two curves show the resistance for in-plane fields that are oriented parallel/perpendicular to the current direction. At small fields the AMR dominates the resistance change, as the magnetization can easily be field aligned. At large fields in both geometries a slight, linear decrease in resistance of about 1×10^{-6}/mT is found. This isotropic behavior is well known as spin-disorder MR.[26] The measurements reveal that MR contributions arising from classical Lorentz MR are not observable. As the fields in the *in situ* MR measurements are small (±23 mT), the spin-disorder MR contribution will be small (≈2 mΩ) and can be neglected compared to the AMR contribution (see below). The dominating AMR effect is given by[26]

$$R(\alpha) = R_{\|} - \Delta R_{\mathrm{AMR}} \cdot \sin^2(\alpha) = R_{\|} - \Delta R_{\mathrm{AMR}} \cdot \frac{M_{\perp}^2}{M_S^2}, \quad (1)$$

where α is the angle between magnetization and current direction, $R_{\|}$ is the resistance for magnetization aligned parallel to the current, and $M_{\perp}$ the magnetization component perpendicular to current direction. ΔR_{AMR} is the difference of resistance for parallel and perpendicular alignment of magnetization with respect to the current direction. For a quantitative discussion of the MR results we have to determine the value of $\Delta R_{\mathrm{AMR}} = \Delta \rho_{\mathrm{AMR}} \cdot l/(w \cdot t)$ for the rectangles. $\Delta \rho_{\mathrm{AMR}}$ describes the maximum resistivity change in the film due to AMR, w and l are the dimensions of the rectangles and t is the thickness of the Py layer. We obtain $\Delta \rho_{\mathrm{AMR}} = (0.39 \pm 0.02)$ $\mu\Omega$ cm from the *ex situ* four-point MR measurements [see Fig. 2(b)]. Using this value for the nanostructures, we can calculate the maximum resistance change for the two different geometries. When the current runs along the short/long axis, the maximum resistance change is $\Delta R_{\mathrm{AMR,ea}} = (0.10 \pm 0.01)$ Ω and $\Delta R_{\mathrm{AMR,ha}} = (0.39 \pm 0.04)$ Ω, respectively.

A. Easy-axis magnetization behavior

The results of the MR measurements for magnetic fields applied parallel to the long axis of the rectangles (the easy axis of magnetization) are shown in Fig. 3. The arrows indicate the field sweep direction. The curves have been obtained in one single field cycle. For all three sizes the same type of resistance versus field curve is found, which demonstrates almost identical magnetization behavior.

Starting at ±23 mT, the resistance increases continuously toward zero field. The change in resistance is 16–20 mΩ. This increase in resistance is due to the AMR effect. Spin-disorder MR effect can be ruled out (see above). The increase in resistance corresponds to (18 ± 3)% of the maximum value $\Delta R_{\mathrm{AMR,ea}}$. At a field of 0.1 mT applied in the opposite direction the resistance jumps by a value of about 19–23 mΩ, corresponding to (21 ± 3)% of $\Delta R_{\mathrm{AMR,ea}}$. The abrupt resistance increase indicates an irreversible magnetization process most likely due to domain nucleation/annihilation. Further increase in the field causes a slight resistance decrease. At a field of 4–9 mT a resistance drop with the same height as the first jump is found. Again, this sudden change in resistance indicates a domain nucleation/annihilation process. The field at which the resistance drops varies slightly from cycle to cycle, while the positive jump

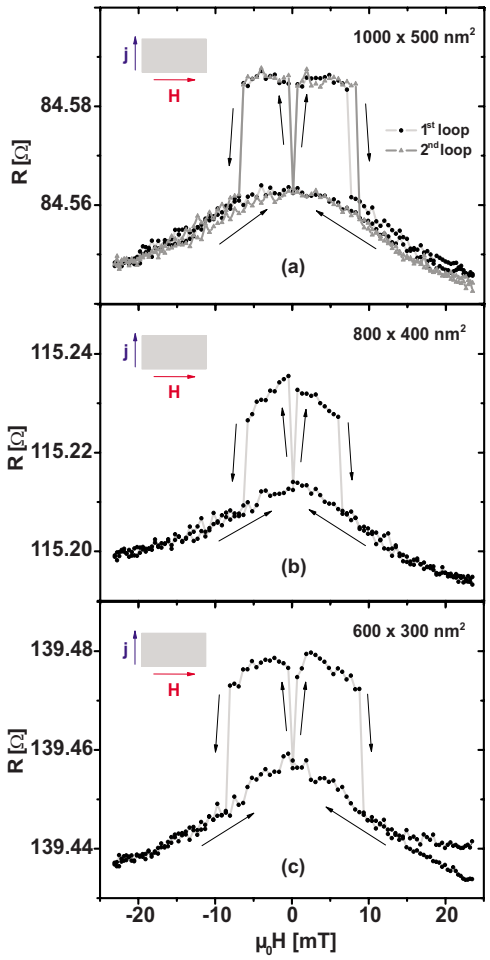

FIG. 3. (Color online) Resistance versus field curves for rectangles with long axis parallel to the field direction. The easy-axis loops for rectangles of size (a) 1000×500, (b) 800×400, and (c) 600×300 nm^2 are plotted. The geometry of the measurement is given as inset.

appears at almost the same field, which is shown in Fig. 3(a), where $R(H)$ curves for two field cycles are plotted.

For the quantitative discussion of the MR measurements information about the magnetic microstructure is necessary. The investigation of the magnetic microstructure in remanence by means of SEMPA reveals that the very same rectangles are either in the C or S state after pretreatment in magnetic fields. In an array of uncoupled rectangles we find that 75 (95/100) out of 100 of the largest (intermediate/smallest) rectangles are in C or S states after the very same pretreatment in magnetic fields. The remaining rectangles exhibit a flux-closure structure, like the Landau or diamond state. From the SEMPA micrographs of the C and S state we can determine the area filling of domains with magnetization parallel to the current direction to be $(27\pm5)\%$. For the Landau and diamond state we obtain $(25\pm6)\%$ and $(50\pm10)\%$, respectively.

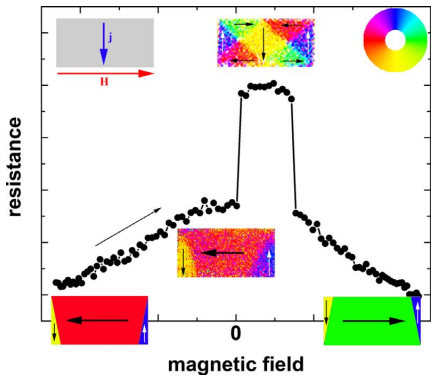

FIG. 4. (Color online) Cartoon of supposed magnetization behavior for fields applied along the easy axis. The domain structures at zero and small positive fields are SEMPA micrographs. The magnetization orientation is color coded according to the given color wheel.

The magnetization behavior of Fig. 3 can be interpreted as follows (see Fig. 4): as the magnetic microstructure in remanence is a C or S state, we can interpret the reversible MR behavior on field decrease either as a reduction in a small tilting of the magnetization of the end domains or as a reversible domain-wall shift that decreases the area of the center domain. The first scenario gives a rotation angle of 54° while in the second situation the area of the end domains has to shrink to $(9\pm5)\%$ at ±23 mT. The relatively high rotation angle of the magnetization in the end domains, which would be accompanied by a considerable increase in magnetostatic energy, indicates that the domain-wall displacement process is the most probable one (see Fig. 4). The latter has been found in micron-sized rectangles before.[27]

The irreversible jump of $(21\pm3)\%$ of $\Delta R_{\mathrm{AMR,ea}}$ at small opposite field indicates that large fractions of the structure exhibit domains with orientation of magnetization along the current direction and perpendicular to the field, respectively. It is reasonable to assume that the system jumps into a flux closure pattern, as the Landau and the diamond state are lower in energy than the C or S states for the dimensions used here.[28,29] As the Landau state would give almost the same resistance as the C/S states, it follows from the resistance jump that the diamond state is created (see Fig. 4). Quantitatively, the height of the jump fits well with the relative difference in area filling of $(23\pm11)\%$ of the parallel to field-orientated domains of the C/S state and the diamond structure normalized to the rectangle area. On further field increase the field degenerated diamond structure is again transformed into the C or S state and a resistance drop appears.

B. Hard-axis magnetization behavior

The results of the MR measurements for magnetic fields applied parallel to the short axis of the rectangle (the hard

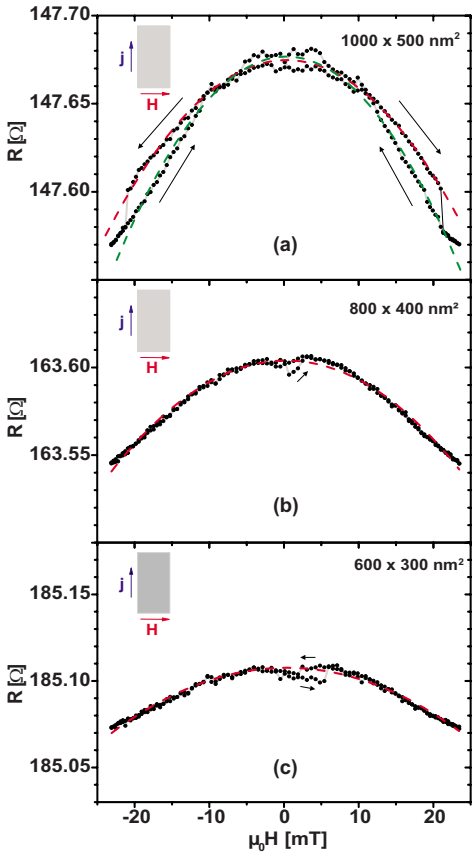

FIG. 5. (Color online) Resistance versus field curves for rectangles with short axis parallel to the field direction. The hard-axis loops for rectangles with dimensions of (a) 1000×500, (b) 800×400, and (c) 600×300 nm^2 are shown. The geometry of the measurement is given as inset. The dashed lines show parabolic fits which indicate (coherent) magnetization rotation during the reversal process.

axis of magnetization) are shown in Fig. 5. For the sake of better comparison the ordinate scales are identical in all plots. The arrows indicate the field sweep direction. The curves have been obtained in one single field cycle.

The same type of parabolic resistance versus field curve is found for all three sizes. Deviations from the parabolic dependence are found around zero field and for the largest rectangle additionally at high fields. The amount of resistance change becomes smaller with shrinking dimensions of the rectangles.

The microstructure in remanence has been obtained via SEMPA. The Landau state is the predominant state for such rectangles, which has been checked for arrays of uncoupled rectangles. After the very same pretreatment in magnetic fields, 60% (90%/99%) exhibit the Landau structure in case of the largest (intermediate/smallest) size. The remaining rectangles show C or S states. From this result we can deduce the following magnetization procedure (see Fig. 6): the

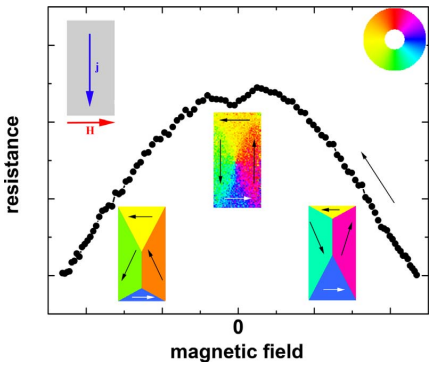

FIG. 6. (Color online) Cartoon of supposed magnetization behavior for fields applied along the hard axis. The domain structure at zero field is a SEMPA micrograph. The magnetization orientation is color coded according to the given color wheel.

Landau state has two large domains that are oriented perpendicular to the field direction, while two small domains at the end have parallel/antiparallel field alignment, respectively. According to Eq. (1), the parabolic field dependence indicates that the magnetization component perpendicular to the current increases linearly with field. When the remanent state is a Landau state, the only mechanism that creates a parabolic MR signal is the rotation of the magnetization of the two large domains. The reason for this assumption is twofold. At first, according to performed simulations[30] the area of the two small oppositely magnetized domains will change by almost the same amount while the one shrinks and the other grows. As both magnetization orientations exhibit the same resistivity, the MR will stay constant within the error margins of the experiment. The second reason is that the Landau state creates stray fields that are caused by a slight tilting of the magnetization in the large domains out of the direction parallel to the long axis.[29,31] External fields along the short axis can easily affect that pre-existing tilting and increase the angle of tilt even at small fields. Hence, a magnetization tilting in the Landau structure occurs.

In the largest structure irreversible changes can be seen at large fields. We appoint that hysteretic behavior to a sudden change in domain structure after the rotation has become so large that a low-angle domain wall can easily be moved and a C/S state is created.

In case the rotation of magnetization is dominant we can calculate from the MR curve the magnetic anisotropy that counterbalances the Zeeman torque. The linear dependence of the magnetization on field is typical for a uniaxial anisotropy. So the equilibrium magnetization orientation in field for a uniaxial system can be put into Eq. (1)

$$R(\mu_0 H) = R_{\parallel} - \Delta R^{\text{Landau}}_{\text{AMR,ha}} \cdot \left(\frac{\mu_0 H M_S}{2K}\right)^2, \qquad (2)$$

where $\mu_0 H$ is the external field, K the first-order uniaxial anisotropy constant, and M_S is the saturation magnetization. $\Delta R^{\text{Landau}}_{\text{AMR,ha}}$ can be determined from the area filling of domains with magnetization perpendicular to the current direction. As

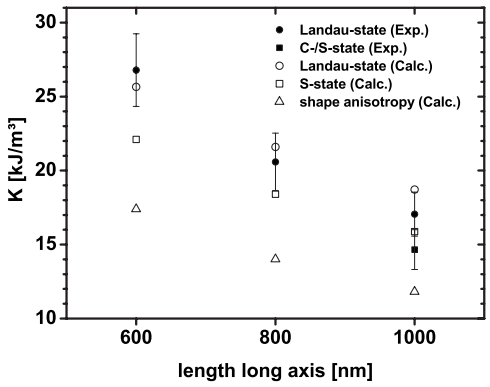

FIG. 7. Anisotropies for different sizes of Py rectangles. The open symbols represent calculated shape anisotropy and calculated energy density differences between the hard-axis saturated state and certain domain structures given as labels in the plot. The filled symbols have been obtained by fitting a uniaxial behavior to the hard-axis curves from Fig. 5.

the large domains of the Landau state occupy roughly 75% of the rectangle we can expect a maximum resistance change of $\Delta R_{\mathrm{AMR,ha}}^{\mathrm{Landau}}=0.75\times\Delta R_{\mathrm{AMR,ha}}=(0.29\pm0.04)\ \Omega$.

The largest structure exhibits a reversible resistance change in about 25% of $\Delta R_{\mathrm{AMR,ha}}^{\mathrm{Landau}}$ when sweeping the field from 0 to 21 mT, i.e., up to the field at which the irreversible jump occurs. This value corresponds to a magnetization rotation of 30°. In case of the smaller structures, the rotation angle at maximum field is 26° (19°) for the intermediate (smallest) rectangle. The smaller rotation indicates a stronger magnetic anisotropy that competes with the Zeeman energy. Finally, we can calculate the first-order anisotropy constant for the different rectangles using a saturation magnetization of $M_S=(820\pm40)$ kA/m, which is determined by means of SQUID measurement. The results are $K=(17\pm2)$ kJ/m^3, $[(21\pm2)$ kJ/m^3/(27 ± 3) kJ/m$^3]$ in case of the largest [intermediate/smallest] size.

The results for the anisotropy constants should be comparable to the shape anisotropy because the magnetocrystalline anisotropy of the film is very small (300 J/m^3) and the only effective anisotropy is due to the shape. In its strict definition the latter is the difference between the energy of the saturated states along the hard (short) and easy (long) axis. The shape anisotropy has been calculated utilizing an open access micromagnetic simulation code (OOMMF).[30] Experimental results (●) and calculated shape anisotropy values (△) are plotted versus long axis size in Fig. 7. It is obvious that the experimental values do not fit the simulated values. The experimental results are systematically larger, meaning that either there do exist some further contributions to the anisotropy or the nanostructure properties diverge considerably from the assumptions. The properties such as saturation magnetization and size have been cross-checked. As they were identical to the values used for the analysis, an additional contribution to the anisotropy has to be considered. To explore the reason for the systematic deviation, we have calculated the energy density of the micromagnetic states that have been found in the SEMPA investigation. The calculated energy density differences between the hard-axis saturated state and the domain structures, i.e., the S state (□) and the Landau configuration (○), are included in Fig. 7. It is evident that these calculated energy density differences fit the experimental results quite good. For the small and intermediate rectangles the experimental values are very close to the calculated values of the most probable domain configuration, i.e., the Landau state. In particular, it turns out that the anisotropy can be used to distinguish between different domain configurations. One direct proof becomes evident from the magnetization behavior of the largest rectangle, where at higher fields the irreversible change from the Landau configuration to the C/S state is found [see Fig. 5(a)]. In the up and down scans the two different curvatures of the parabola demonstrate that the magnetization rotation in the two states is counterbalanced by different torques, yielding different anisotropies (● and ■ in Fig. 7). For the calculation of the anisotropy utilizing Eq. (2), $\Delta R_{\mathrm{AMR,ha}}^{\mathrm{C/S\ state}}=0.73\times\Delta R_{\mathrm{AMR,ha}}=(0.29\pm0.04)\ \Omega$ is used for the down scan, yielding $K=(15\pm2)$ kJ/m^3. This anisotropy (i.e., the energy density difference to the hard-axis saturated state) of the C/S state is smaller than that of the Landau state, which means that the C/S state is higher in energy as predicted from simulation.[29] Quantitatively, the energy density difference between the C/S state and the Landau state can be obtained from the experiments, yielding (2.4 ± 0.7) kJ/m^3, which fits well the value of 2.8 kJ/m^3 from calculations.

The experimental results reveal the amazing fact that we can measure the magnetic energy of the rectangles. The magnetization rotation is not only affected by the shape anisotropy, which is determined by the surface charges at the rim, but also by the domain state in the same functional dependence. In extended systems domain-wall movement allows to bypass energy maxima, i.e., to take a straight path between two local minima on the energy landscape, as well as transformations via metastable transient states are possible.[32] The complexity of the numerous possible paths makes an exact description of the reversal and the extraction of real numbers nearly impossible. In small structures, however, there does not exist any alternative domain structure that can be reached with small to medium fields. The energy landscape is thus apparently fixed to one minimum for a certain span of external field strengths. The potential gradient, respectively, the torque, is caused by the total energy difference between initial and final state. Surprising is still the fact that our results reveal similar field dependence as a uniaxial anisotropy in lowest-order approximation.

In the discussion we have assumed a homogenous current density within the rectangles. We are aware that the current density would be not exactly homogenous. Different magnetization orientations of the domains cause locally varying current densities, which have to be taken into account. Nevertheless, it has been shown that a uniform electrical current density is a good approximation in microstructures,[33] as the AMR ratio is only a few percent. Using this assumption the resistance contribution of the individual domains depends only on the area filling and magnetization orientation. The influence of the domain walls on resistance has been neglected as the area filling of the walls is vanishingly small.

IV. CONCLUSION

We have investigated the magnetization behavior of single submicron Py rectangles (20 nm thick) via AMR using single field cycles. The magnetization reversal for the two generic cases with the magnetic field applied perpendicular and parallel to the long axis of the rectangles has been explained. Particularly, we can quantify reversible and irreversible magnetization processes. In case of the magnetic field applied parallel to the long axis, the dominating feature is the switching between the quasisingle-domain C/S states and the diamond state. In case of the magnetic field applied perpendicular to the long axis, the parabolic MR behavior can be attributed to a coherent rotation of the magnetization within the large domains of the Landau and C/S state, respectively. The coherent rotation curves are used to determine the first-order anisotropy constant for the individual rectangles. Surprisingly, the anisotropies deviate from pure shape anisotropy. In comparison to calculated energy densities of the involved micromagnetic states, i.e., the Landau and the C/S states, it turns out that in fact the energy density of these states is obtained. Particularly, the difference of the energy density between both states is measured. The results demonstrate that the magnetization rotation is not only affected by the shape but also by the domain configuration, revealing similar field dependence as a uniaxial anisotropy in lowest-order approximation.

ACKNOWLEDGMENTS

We thank S. Pütter and O. Albrecht for SQUID measurements and M. Scholz and G. Hoffmann for AFM investigation. Financial support by DFG via SFB 668 is gratefully acknowledged.

*akobs@physnet.uni-hamburg.de

[1] R. Wiesendanger, Rev. Mod. Phys. (to be published).
[2] W. Wulfhekel and J. Kirschner, Annu. Rev. Mater. Res. **37**, 69 (2007).
[3] G. Rodary, S. Wedekind, D. Sander, and J. Kirschner, Jpn. J. Appl. Phys. **47**, 9013 (2008).
[4] *Magnetic Microscopy of Nanostructures*, edited by H. Hopster and H. P. Oepen (Springer-Verlag, Berlin, 2004).
[5] B. D. Terris and T. Thomson, J. Phys. D **38**, R199 (2005).
[6] W. Wernsdorfer, K. Hasselbach, A. Benoit, B. Barbara, B. Doudin, J. Meier, J. P. Ansermet, and D. Mailly, Phys. Rev. B **55**, 11552 (1997).
[7] S. S. P. Parkin, M. Hayashi, and L. Thomas, Science **320**, 190 (2008).
[8] D. Atkinson, C. C. Faulkner, D. A. Allwood, and R. P. Cowburn, *Spin Dynamics In Confined Magnetic Structures III* (Springer-Verlag, Berlin, 2006), Vol. 101, p. 207.
[9] M. Brands, R. Wieser, C. Hassel, D. Hinzke, and G. Dumpich, Phys. Rev. B **74**, 174411 (2006).
[10] J. E. Wegrowe, D. Kelly, A. Franck, S. E. Gilbert, and J. P. Ansermet, Phys. Rev. Lett. **82**, 3681 (1999).
[11] L. Vila, L. Piraux, J. M. George, and G. Faini, Appl. Phys. Lett. **80**, 3805 (2002).
[12] U. Ebels, A. Radulescu, Y. Henry, L. Piraux, and K. Ounadjela, Phys. Rev. Lett. **84**, 983 (2000).
[13] A. Aharoni, *Introduction to the Theory of Ferromagnetism* (Oxford University Press, New York, 1996).
[14] T. Wang, Y. Wang, Y. Fu, T. Hasegawa, F. S. Li, H. Saito, and S. Ishio, Nanotechnology **20**, 105707 (2009).
[15] R. A. Silva, T. S. Machado, G. Cernicchiaro, A. P. Guimarães, and L. C. Sampaio, Phys. Rev. B **79**, 134434 (2009).
[16] R. Hertel, J. Magn. Magn. Mater. **249**, 251 (2002).
[17] H. Forster, T. Schrefl, W. Scholz, D. Suess, V. Tsiantos, and J. Fidler, J. Magn. Magn. Mater. **249**, 181 (2002).
[18] R. P. Cowburn, A. O. Adeyeye, and M. E. Welland, Phys. Rev. Lett. **81**, 5414 (1998).
[19] J. Y. Cheng, W. Jung, and C. A. Ross, Phys. Rev. B **70**, 064417 (2004).
[20] D. Stickler, R. Frömter, W. Li, A. Kobs, and H. P. Oepen, Rev. Sci. Instrum. **79**, 103901 (2008).
[21] A. Perin, R. Gupta, G. Principi, C. Tosello, L. M. Gratton, E. Kuzmann, and Z. Klencsar, Surf. Coat. Technol. **103-104**, 93 (1998).
[22] J. Fassbender, J. von Borany, A. Mucklich, K. Potzger, W. Moller, J. McCord, L. Schultz, and R. Mattheis, Phys. Rev. B **73**, 184410 (2006).
[23] T. Miyazaki and T. Ajima, J. Magn. Magn. Mater. **81**, 91 (1989).
[24] A. Yamaguchi, T. Ono, S. Nasu, K. Miyake, K. Mibu, and T. Shinjo, Phys. Rev. Lett. **92**, 077205 (2004).
[25] *Magnetic Microscopy of Nanostructures*, edited by H. Hopster and H. P. Oepen (Springer-Verlag, Berlin, 2004), Chap. 7.
[26] T. R. McGuire and R. I. Potter, IEEE Trans. Magn. **11**, 1018 (1975).
[27] J. M. Garcia, A. Thiaville, J. Miltat, K. J. Kirk, and J. N. Chapman, J. Magn. Magn. Mater. **242-245**, 1267 (2002).
[28] R. Hertel, Z. Metallkd. **93**, 957 (2002).
[29] W. Rave and A. Hubert, IEEE Trans. Magn. **36**, 3886 (2000).
[30] M. Donahue and D. Porter, OOMMF User's Guide, Version 1.0, National Institute of Standards and Technology, Interagency Report No. NISTIR 6376, 1999 (unpublished).
[31] S. Hankemeier, R. Frömter, N. Mikuszeit, D. Stickler, H. Stillrich, S. Pütter, E. Y. Vedmedenko, and H. P. Oepen, Phys. Rev. Lett. **103**, 147204 (2009).
[32] G. Bertotti, *Hysteresis in Magnetism* (Academic, New York, 1998).
[33] M. Bolte, M. Steiner, C. Pels, M. Barthelmess, J. Kruse, U. Merkt, G. Meier, M. Holz, and D. Pfannkuche, Phys. Rev. B **72**, 224436 (2005).

To summarize the contribution of the SEMPA measurements[1] to the publication [P4]: From the statistical investigation of over 600 rectangles it was possible to deduce the remanent states of the single rectangles during the hysteresis loops of the AMR measurement. It was possible to correlate the jumps in electrical resistance during the AMR loops quantitatively to a sudden change of the micromagnetic configuration of a single rectangle. In case of the magnetic field applied along the short axis, the parabolic AMR signature can be attributed to a coherent rotation of the magnetization within the large domains of the Landau and the C/S-state. From the parabolic dependence it was possible to determine the first order anisotropy constant of individual rectangles.

4.3. V-shaped nanowires

In the next section another example of the influences of the magnetic history on the magnetic configuration is presented. Up to now, only rectangles were discussed which are of fundamental importance for the understanding of micromagnetism in general [Hub91, Rep98]. Another major topic within the magnetism community are micromagnetic properties of nanowires in the static regime [Bac07, Bog09, Bro06, San08] as well as the magnetic manipulation via high frequency electrical currents [Yam07, Liu07], modulated magnetic fields [Her07, Kea09, Wei09] and direct currents [Uhl09].

In our submitted article [P5] we investigate the domain wall configuration at the bend in a V-shaped nanowire in dependence of the magnetic history of the wire. As the name suggests, a V-shaped nanowire is a bent wire with a kink in the middle. The angle between the two arms of the wire is referred to as bending angle. This geometry has the advantage that the nucleation of a domain wall is straightforward by utilizing an external magnetic field which is aligned along the symmetry axis of the wire [Tan00]. The application of the magnetic seeding field (one sec field-pulse) causes the magnetization in the arms to align thus creating a domain wall at the bend. The dimensions of the wire were chosen so that the so called "vortex domain wall" is the magnetic ground state [Nak05]. The name "vortex wall" or "vortex domain structure" was first introduced for a planar domain structure in [McM97]. Before this, the term "vortex wall structure" was used for a volume Bloch wall configuration separating to vast domains, e.g. in [Sch91a]. The x-z-plot of such a Bloch wall is quite similar to the x-y-plot of a planar vortex domain wall, thus probably giving the inspiration for the name. As the term "vortex structure" usually implies a homogenous rotation of the magnetization, it is a bit misleading to use it for a vortex domain structure in a planar wire as the majority of the magnetization actually rotates as discrete 90° walls [McM97]. However, nowadays the term "vortex wall" has settled in literature for a domain wall in a nanowire and with this meaning it is also used in the following throughout this work.

A vortex wall in a V-shaped nanowire has four characteristic features of the possible remanent magnetic configuration: Head-to-head or tail-to-tail wall, position

[1] The SEM images shown in [P4, Fig. 1 and Fig. 2] were also acquired with the SEMPA experiment during the measurement session.

of the vortex core with respect to the kink [Bro06], the sense of rotation [1] of the in-plane magnetization and the polarity of the vortex core. In publication [P5] we show that these four characteristics are interconnected. The knowledge about two of the first three characteristics plus the information about the polarity define the remanent state of the vortex wall. Furthermore the configuration of the remanent state can be controlled via the exact orientation of the external seeding field with respect to the symmetry axis of the wire.

[1] The sense of rotation is also often referred to as chirality in literature.

Controlling properties of vortex domain walls via magnetic seeding fields

S. Hankemeier, A. Kobs, R. Frömter, and H.P. Oepen

submitted to *Phys. Rev. B.*; 28th April 2010

accepted for publication in *Phys. Rev. B.*; 19th July 2010

published on 12th August 2010 in *Phys. Rev. B.* **82**, 064414

Preprint

P5

The numbers by which citations are referenced in the following article are only valid within the article.

APS/123-QED

Controlling properties of vortex domain walls via magnetic seeding fields

S. Hankemeier,* A. Kobs, R. Frömter, and H.P. Oepen
Institut für Angewandte Physik, Universität Hamburg,
Jungiusstr. 11, 20355 Hamburg, Germany

(Dated: July 15, 2010)

The seeding of vortex domain walls in soft magnetic V-shaped nanowires by magnetic fields has been investigated via Scanning Electron Microscopy with Polarization Analysis (SEMPA) and micromagnetic simulations. It is found that the orientation of the magnetic seeding field determines the sense of rotation and the position of single vortex domain walls in the state of remanence. The topology of the magnetic microstructure in combination with symmetry considerations give the key for the explanation of this behavior.

I. INTRODUCTION

A concept for potential applications as memory devices [1, 2] is based on the micromagnetic vortex configuration, which is composed of a curling magnetization around a sharp core, where the magnetization is forced out-of-plane to minimize exchange energy. Stable magnetic vortices can be found as remanent state in circular microstructures as well as in nanowires as so called vortex domain walls in head-to-head or tail-to-tail domain arrangements [3]. In microstructures it has been found that the sense of rotation of the vortex is affected by magnetic structures in the vicinity [4–7]. The ability to switch or set the sense of rotation and the polarity, i.e. the magnetization orientation of the vortex core, is a field of intense research. Recent publications demonstrate the possibility to change the sense of rotation in asymmetric single nanorings [8–10] and nanodisks [11] by applying external fields. The polarity can be manipulated via high frequency electrical currents [12, 13] or modulated magnetic fields [14–16]. While the change of vortex properties in small structures is already on the agenda of research, the seeding of vortex walls with defined properties has not yet been widely addressed. The reproducible manipulation of vortex domain wall properties is a necessary prerequisite for a storage concept based on vortex walls in combination with current induced domain wall movement, like in the racetrack memory device [17].

A common approach to introduce a domain wall into a V-shaped nanowire is to apply a magnetic field along the line of intersection of the two arms of the wire, which is the symmetry axis (see Fig. 1) [18, 19]. Depending on the direction of the external field, a head-to-head or a tail-to-tail wall nucleates at the kink as a vortex or a transverse wall depending on the dimensions of the wire [3, 20]. While the influence of the seeding field on the magnetization orientation of the domains is well understood, it is still an open question what determines the vortex domain wall characteristics, i.e. the sense of rotation and position of the core with respect to the symmetry axis: For vortex walls in V-shaped wires and in wires with notches the core is slightly shifted out of the symmetry axis which is caused by the additional geometrical element [21], while transverse walls are centered on the symmetry axis. In this paper it is demonstrated that for V-shaped wires the orientation of the seeding field is the control that determines the sense of rotation and the location of vortex walls. To investigate and explain that behavior, we have carried out experiments via Scanning Electron Microscopy with Polarization Analysis (SEMPA) [22] and performed simulations with the OOMMF code [23].

*shankeme@physnet.uni-hamburg.de

II. EXPERIMENTS AND SIMULATIONS

Experimentally, V-shaped wires of 400 nm width and a bending angle of δ=150° have been carved out of an 18 nm thick, soft magnetic $Co_{39}Fe_{54}Si_7$ (atomic percentage) film via focused ion beam milling (Fig. 1). Fig. 2 shows a SEMPA micrograph of two wires and the adjacent ferromagnetic film. The film has been grown via electron beam evaporation on a silicon single crystal substrate. It has been experimentally verified that the wire dimensions favor the vortex wall over the symmetric transverse wall for this film system [24].

To investigate the influence of the orientation of the magnetic field on the vortex wall properties, wires have

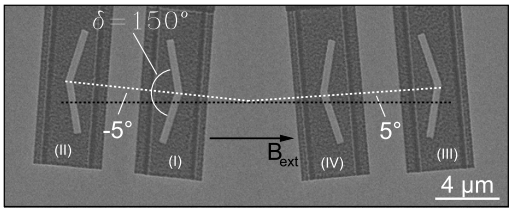

FIG. 1. Scanning Electron Microscope image of V-shaped wires of 400 nm width. The symmetry axis (bisection) is indicated by the white dotted line. The black arrow gives the direction of the external field used for seeding the domain walls.

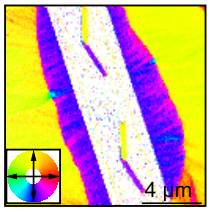

FIG. 2. SEMPA micrograph showing two wires carved out of a continuous film via FIB milling. The orientation of the magnetization is color coded according to the color wheel. In the bright region where the ferromagnetic material has been removed no magnetic signal could be found within the uncertainty of the experiment. The adjacent film shows a domain pattern caused by the sharp edges of the structuring.

been created with tilt angles of ±5° ((I) and (III)) and ±175° ((II) and (IV), Fig. 1) with respect to the axis along which the magnetic field is applied in the experiment (see black arrow in Fig. 1). Such an arrangement of wires allows to investigate all four generic cases of field orientation simultaneously. To nucleate the domain walls at the bend, a magnetic seeding field of $B_{\mathrm{ext}} = 60$ mT is applied. After switching off the field the domain patterns of several wires were imaged via SEMPA technique with a spatial resolution of 20 nm and an angular resolution of 4° [22]. SEMPA micrographs of the predominant vortex wall structures for the four different orientations are shown in Fig. 3(a)-(d). It has to be mentioned that no other vortex domain configuration besides the four shown in Fig. 3 (a)-(d) has been found in the experiments.

Head-to-head and tail-to-tail vortex walls are seeded depending on the direction of the magnetic field as already known from literature. The position and sense of rotation of the walls, however, depends on the exact orientation of the magnetic field. In Fig. 3(a) ($B_{\mathrm{ext}} = +60$ mT at $-5°$) the vortex core of the head-to-head wall is moved into the lower arm and the sense of rotation is clockwise. Reversing the direction of the seeding field creates a tail-to-tail wall in remanence. The vortex core is again placed in the lower arm, while the sense of rotation is switched from clockwise to counter-clockwise (see Fig. 3(b)). In Figs. 3(c),(d) the orientation of the seeding field ($B_{\mathrm{ext}} = \pm 60$ mT) was applied at +5° with respect to the symmetry axis. The remanent configuration shows again a head-to-head / tail-to-tail wall, respectively. The vortex, however, nucleates in the upper part of the wire for both field directions. The sense of rotation again depends on the sign of the applied field, a counter-clockwise / clockwise orientation is found for the two cases (Figs. 3 (c), (d)). To summarize the experimental results: Both, the orientation of the external seeding field with respect to the symmetry axis and the sign determine which of the four micromagnetic configurations (Figs. 3(a)-(d)) occurs. The four states can be transferred into each other by symmetry operations. A mirroring at the dashed line transfers state (a) into state (c) and (b) into (d), respectively. The states (a) and (b) can be mapped onto each other by means of a time-inversion ($\vec{M} \rightarrow$ -$\vec{M}$, $\vec{H} \rightarrow$ -$\vec{H}$) operation, equally (c) and (d).

We have strictly proven our results experimentally by measuring overall 47 independent domain arrangements (three *in situ* re-magnetization processes). A 64% majority of all examined magnetization processes give vortex patterns that agree with the proposition for the four different vortex configurations (Fig. 3(a)-(d)), which is a reasonable success rate compared to similar statistics on vortex wall behavior [5, 25]. A wrong vortex configuration is found with a probability of 11%, i.e. when state (a)/(b) is found instead of state (c)/(d) and vice versa. Besides vortex walls, we find transverse walls (14%) and 11% of the magnetization processes do not show a domain wall at all. Considering only the cases when vortex walls are generated the proposed structures appears with a probability of 86%.

To emphasize the experimental results we have also performed micromagnetic simulations using OOMMF [23]. We have simulated the microstructure in remanence after switching off a magnetic field of $B_{\mathrm{ext}} = \pm 60$ mT, tilted ±5° out of the symmetry axis, corresponding to the four situations in the experiments. The micromagnetic configurations are plotted in Figs. 3(e)-(h). The input parameters for the simulations were M_{S}=1.43 · 10^6 $\frac{\mathrm{A}}{\mathrm{m}}$, A=3.5 · 10^{-11} $\frac{\mathrm{J}}{\mathrm{m}}$, which agree very well with the magnetic properties of the film [24]. Further parameters for the simulations were: cell-size 4 nm x 4 nm x 45 nm, wire width 400 nm, thickness 45 nm, bending angle 150°, and damping constant α=0.5. We simulated a system with higher thickness than in the experiment. The reason for this approach is to overcome the well known problem that simulations at T = 0 K do not necessarily find the total energy minimum (vortex wall), as long as there exists an energy barrier to the local energy minimum for the transverse wall [26].

Comparing the SEMPA images (Fig. 3(a)-(d)) and the results of the micromagnetic simulation (Fig. 3(e)-(h), it is evident that the experiments and simulations give the same magnetic structures, i.e. the sense of rotation and position of the vortex. Even the magnetic fine structure in simulation and experiment shows the same characteristic features of the wall. Due to the high spatial resolution of the measurements, the position of the vortex core can be measured with a quite high accuracy and can be compared with the numerical investigation. The simulation gives a distance of the core to the symmetry axis of 212 nm and a lateral shift towards the outer edge of 20 nm, respectively. In the SEMPA images, we find slightly varying core positions. On the average, the SEMPA images reveal a distance of the core to the symmetry axis of 215 nm (±50 nm), while the lateral shift is 33 nm (±30 nm). Within the experimental uncertainty, both values are in very good agreement with the numbers found in the simulations. Thus we may conclude that the

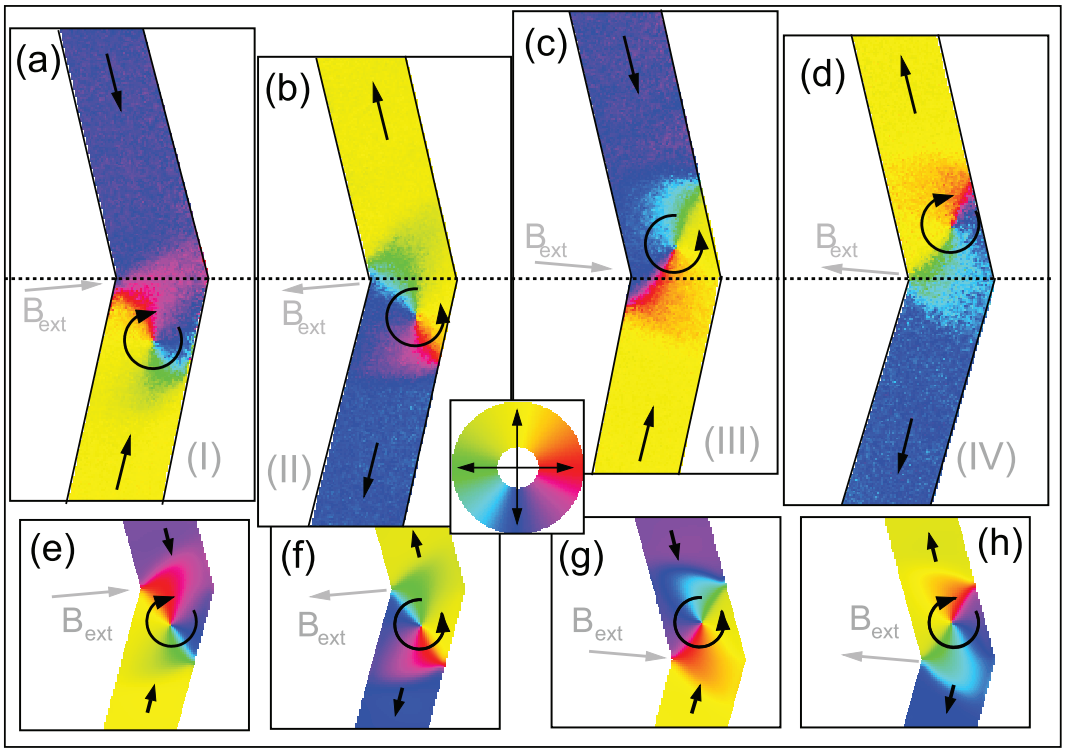

FIG. 3. (Color online) (a)-(d) SEMPA images of vortex domain walls in V-shaped wires after field application in the indicated directions (gray arrows). The labels (I)-(IV) refer to the four arrangements shown in Fig. 1. The orientation of the magnetization is indicated by the black arrows and color coded according to the color wheel. The images have been rotated so that the bisections of the wires are aligned with the black dotted line. In the images only the signal of the wire, i.e. within the black solid lines, is displayed. (e)-(h) Micromagnetic simulation of the corresponding geometries from (a)-(d) after pretreatment in an external field of $B_{\text{ext}} = 60$ mT in the directions of the gray arrows.

input parameters for the numerical simulation represent the experimentally studied system quite well and we can use the simulation to understand the relaxation into the zero field magnetic configurations.

III. DISCUSSION

Before we discuss the relaxation process, we would like to recapitulate some general features of the vortex wall, which give some hint to the link between sense of rotation and wall position. Recently, the domain wall structures in soft magnetic wires were investigated from a topological point of view [27]. In the limit of preponderant magnetostatic energy it has been shown that the vortex wall consists of three topological defects: The vortex core within the wire (winding number +1) and two topological "edge defects" with winding number $-\frac{1}{2}$, i.e. two anti-vortex structures fixed at the edges (see Fig. 4) [28, 29].

The three papers [27–29] give the key to a good understanding of details of the vortex wall structures in ultra-thin, narrow wires. At first, they clearly reveal the fact that in wires the rotation of the vortex is not continuous as it is inherently conjectured form drawing the parallelism to the vortices in nanodisks. The most prominent feature of the vortex wall is a center wall that runs diagonally across the wire crossing the vortex core (Fig. 4). This wall consists of two 90° Néel walls in series with same sense of rotation connected at the core [20]. At the edges, the center wall is terminated by edge defects. Additionally, starting at the edge defects, a kind of 90° wall is built on either side of the center wall acting as borderline to the adjacent domains. The magnetization rotation across the latter borderlines gets smaller when moving from the edge defect towards the opposite side of the wire (Fig. 4(b), (d)). For the sake of clarity we call the borderlines to the adjacent domains transition lines. The center wall is tilted against the main axis of the straight wire to allow for the transition lines to start under 90° to the center wall at the edge defects. Around

the edge defects the magnetization at the edge is perfectly aligned parallel to the edge of the wire preventing any stray field.

All experimental studies and simulations of vortex domain walls in small wires show these features with more or less accuracy [3, 26, 30, 31]. Aforementioned Néel-wall-like fragments of the vortex wall are very well resolved in Lorentz microscopy studies, as the 90° walls appear as bright or dark stripes in the images [21, 32, 33]. As the two 90° walls building the center wall give the same contrast in the Lorentz micrographs (Fig. 4(b), (d)), the center wall is usually labeled as 180° wall.

Another important feature of vortex walls in nanowires is the correlation between the tilting direction of the center wall and the sense of magnetization rotation. Not considered so far is the fact, that the symmetry of the magnetic structure fixes the location of the edge defects with respect to the magnetization rotation around the central topological defect (vortex core). This originates from the edge defect that separates 180° orientated magnetic structures and decomposes into two 90° domain walls at the very position of the edge defect. Changing the sense of rotation of the vortex core has the immediate consequence that the center wall will reverse its angle to the wire and the edge defects appear on the opposite edges. The two possible configurations for head-to-head walls in straight wires are shown in Fig. 4. They can be transferred into each other by mirror operation at the plane through the vortex core perpendicular to the plane of drawing and parallel / perpendicular to the wire axis, respectively. No further combination of sense of rotation and wall tilt is possible as other combinations enforce the creation of two 180° domain walls as transition lines to the adjacent domains. Exactly the same is found for tail-to-tail walls, where the combination of sense of rotation and wall tilt is opposite to the case of head-to-head walls (time inversion). This special symmetry of head-to-head (tail-to-tail) walls is responsible for effects found in magnetotransport measurements that have been appointed to the sense of rotation [30, 34]: As the sense of rotation and the tilt of the center wall lifts the high symmetry of the domain wall structure, any symmetry breaking element (e.g. notches, kinks) in a wire will cause different pinning of the vortex wall and different properties for clockwise and counter-clockwise sense of rotation.

Next we want to come back to our results of seeding domain walls in V-shaped wires. The questions that have to be answered are: Why is the sense of rotation connected to the location of the core and why does the direction of the magnetic field determine both, the location and the sense of rotation?

Edge defects are very special features of the vortex wall structure. The edge defect is the location along the edge of the wire where the magnetization rotates fastest and thus contains most exchange energy. This peculiarity is the reason for an edge defect to localize at the inner kink in the case of a V-shaped wire. Here, the angle of magnetization rotation is reduced by 30° compared to a wall position in a straight wire segment and thus, exchange energy of the vortex wall configuration is most efficiently reduced. The reason is the correlation between sense of rotation and center wall tilt: Imagine the two straight wire configurations of a head-to-head wall shown in Fig. 4(a), (c) that nucleate in a upward bent wire. Two generic edge defects appear that can settle at the inner (A) or outer (B) edge kink. A sketch of the remaining magnetization orientation around the edge defect is shown Fig. 4(e). Obviously, in case of settling at the outer / inner kink the rotation angle is enhanced / reduced (by 30°) as the magnetization is aligned parallel to the edge in the arms and the magnetization in the interior determines the direction of magnetization rotation. Thus, the very special structure of the edge defects causes one defect to be fixed at the inner kink due to minimization of exchange energy. The magnetostatic energy contribution of the edge defect is the same for a location at the outer or inner kink as the reduction of any pole density at the wire edges is identical. Assuming that this edge defect gives a fix-point for the center wall, it remains the question in which direction the center wall will be tilted or equivalent what determines the sense of rotation.

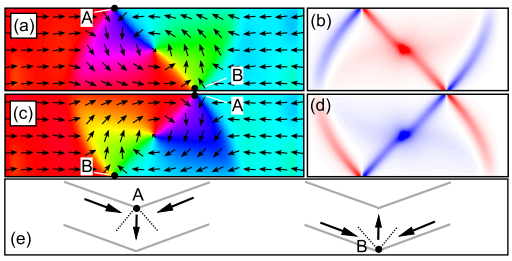

FIG. 4. (Color online) Possible configurations of a head-to-head vortex wall. In (a)/(c) the counter-clockwise/ clockwise configuration is displayed, respectively. The direction of magnetization is indicated by black arrows (obtained via OOMMF). In (b), (d) the z-component of the curl of the vector fields of (a),(c) is shown, red denotes positive values, blue negative values and white is equal to zero. In (e) a sketch of the magnetization orientation around the edge defects located at the kinks is shown.

In the following we consider just one experimental geometry as the other arrangements can be directly traced back to the described situation via symmetry considerations, as discussed above. Due to the very good accordance of simulated results and experiments it appears justified to use the relaxation steps in the micromagnetic modeling to understand the mechanism that drives the center wall into one particular direction. To reproduce the experimental situation where the magnetic field is reduced slowly compared to the intrinsic magnetodynamic time scale in the simulations, one has to reduce the field in several steps to zero using a realistic damping constant. Otherwise, unrealistic dynamical effects could influence

the results. An alternative is to choose a high damping constant and switching off the field in a single step. We performed both procedures with similar results, in particular the evolving remanent domain configuration. As the first method is very time consuming, we present the relaxation steps using the second method, where a large damping constant of α=0.5 is utilized. To demonstrate that the determination of the sense of rotation is caused by the symmetry violation of the seeding field we present the results for the starting configuration with perfectly field aligned moments.

Some of the general steps of the relaxation process are displayed in Fig. 5(a)-(e). Fig. 5(a) gives the start situation, where all moments are aligned five degree towards the right-hand side with respect to the symmetry axis (vertical direction). The relaxation is driven by the shape anisotropy which is most effectively reduced by rotating the moments into the direction parallel to the edges. The torques acting in the two arms are opposite as the angles between the moments and the edges are opposite in the field aligned state. The rotation into the directions along the wire axis appears at first in the vicinity of the edges (Fig. 5). The magnetization within the arm of the wire that has the smaller angle to the field direction (right-hand side) relaxes first while in the arm on the opposite side the relaxation has just started at the edges (Fig. 5(b)). The configuration in Fig. 5(b) is quite similar to the microstructure that is achieved in a static field of $B_{\text{ext}} = 60$ mT. In the bend region the magnetization is preferentially oriented in the former field direction with a continuous transition to the magnetization in the arms of the wire. A slight asymmetry appears as the relaxation on the right-hand side is stronger than on the left-hand side, which pushes the transition region slightly into the left arm. Consequently, the magnetization around the symmetry axis is tilted farther to the right (see white dot in Fig. 5(b)) which is the first indication of a certain sense of rotation that is induced by the relaxation and the initial asymmetric field orientation. In the next step (Fig. 5(c)) the magnetization in the interior of the two arms has further relaxed towards the wire axes. This relaxation step defines the transition lines and drives them closer into the bend region which causes a stronger rotation here. The sense of rotation is determined by the tendency to keep the magnetization parallel to the edges, while around the symmetry axis nearly no shape induced torque is effective. Here the magnetization rotates to establish the continuous transition between the oppositely magnetized arms, while the former sense of rotation is maintained and the asymmetry is even enhanced. In the next step (Fig. 5(d)) the transition line on the right-hand side continues to move into the bend region while the magnetization rotation appears also across the transition line (see white dot in Fig. 5(d)). At this step the sense of rotation of the vortex is clearly visible and the first structure that tags the center wall is established. As the sense of rotation and the tilting of the center wall are strongly correlated (see above), the center wall has to move into the right arm, as the edge defect has to settle at the inner kink. Next (Fig. 5(e)), a combined vortex core/edge defect is created at the end of the sharp transition line on the right-hand side, thus generating all structures needed for the center wall. Finally, vortex core and edge defect separate and the center wall is pushed further away from the bend region to allow for the second 90°-segment at the edge defect to form, acting as transition line to the domain in the arm on the right-hand side (Fig. 3(h)). In contrast, the transition line on the left-hand side is almost unchanged, during relaxation after the step shown in Fig. 5(c).

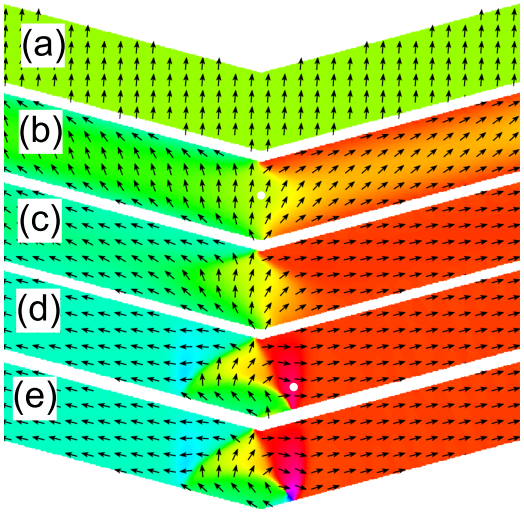

FIG. 5. (Color online) Details of the simulation of the relaxation from the fully saturated state (a) with a high damping constant of $\alpha = 0.5$. The field is aligned 5° towards the right hand side of the symmetry axis. The relaxation steps shown are: 50 steps (b), 80 steps (c), 300 steps (d) and 400 steps (e). The simulation converges after 11647 steps, yielding the configuration of Fig. 3(h). The white dots are marker points which are discussed in the text.

In brief, the driving force of the relaxation process stems from the shape anisotropy that acts first on the moments at the edges. Inside the bend region the net torque is vanishingly small or the opposite torques on both sides compensate, which lets the moments stay almost in the field aligned orientation, e.g. towards the right hand side. The shape-aligned moments along the edges and the former field-aligned moments in the bend region then define the sense of rotation of the vortex. As the sense of rotation and the tilt of the center wall are linked, the vortex core settles in the arm that is closer to the seeding field direction.

The core nucleation process (Fig. 5(e)) was predicted from topologic considerations for the reversed case, the annihilation of the center wall with field [29]. In Ref. [29] the transition from a vortex wall to a transverse wall is

postulated. We find a transition of a transverse-wall-like configuration into the vortex wall during the relaxation process, when the same simulation is carried out for a reduced wire width (e.g. 300 nm), where the transverse wall becomes energetically more favorable and can be clearly observed during the relaxation process.

The results presented here are not limited to the discused geometry. They can be seen as a more universal behavior for the seeding of vortex walls in bend nanowires in a particular span of geometries. At first, vortex walls must be energetically more favorable than transverse walls which depend on the wire dimensions [26] as well as on the bending angle [24]. The tilting angle of the seeding field θ with respect to the symmetry axis is limited. The lower bound is given by the fact that the symmetry has to be broken, i.e. $\theta > 0$. The upper bound is given by the fact that the direction of the external field θ must not be perpendicular to one arm, i.e. $\theta < \frac{180° - \delta}{2}$, where δ is the bending angle, as for higher values of θ no domain wall would nucleate at all.

IV. CONCLUSION

Following the general considerations about topology we find that the symmetry of the vortex head-to-head (tail-to-tail) domain walls allow for two generic geometries only. The two principal vortex structures have an opposite sense of rotation that is inherently connected to an opposite tilting angle of the center wall to the wire axis (Fig. 4).This symmetry property of vortex domain walls is the key link to the understanding of the behavior of the vortex wall in V-shaped wires. By means of SEMPA investigations and micromagnetic simulations it is shown that the sense of rotation / location of the vortex wall in V-shaped wires can be tuned via magnetic fields that are slightly tilted out of the symmetry axis of the wire. The simulations allow for an understanding of the relaxation process which reveals that the shape anisotropy induced relaxation in the arms and the field alignment in the bend region fix the sense of rotation in the beginning of the relaxation process. The possibility to purposely control the sense of rotation and the polarity of a vortex domain wall gives more flexibility in future concepts of vortex based memory devices: A V-shaped injection wire can be used to define a single vortex configuration which acts as a four state bit element and can be moved into a memory array utilizing the spin torque effect, in analogy to the working principle of the racetrack memory [17].

Acknowledgments

Financial support by DFG via SFB 668 is gratefully acknowledged.

[1] R. P. Cowburn. *Nat. Mater.* **6**, 255 (2007).
[2] S. Bohlens, B. Krüger, A. Drews, M. Bolte, G. Meier, and D. Pfannkuche. *Appl. Phys. Lett.* **93**, 142508 (2008).
[3] A. Thiaville, Y. Nakatani, F. Piéchon, J. Miltat, and T. Ono. *Eur. Phys. J. B* **60**, 15 (2007).
[4] S. Y. H. Lua, S. S. Kushvaha, Y. H. Wu, K. L. Teo, and T. C. Chong. *Appl. Phys. Lett.* **93**, 122504 (2008).
[5] M. Konoto, T. Yamada, K. Koike, H. Akoh, T. Arima, and Y. Tokura. *J. Appl. Phys.* **103**, 023904 (2008).
[6] S. Hankemeier, R. Frömter, N. Mikuszeit, D. Stickler, H. Stillrich, S. Pütter, E. Y. Vedmedenko, and H. P. Oepen. *Phys. Rev. Lett.* **103**, 147204 (2009).
[7] T. J. Hayward, M. T. Bryan, P. W. Fry, P. M. Fundi, M. R. J. Gibbs, M.-Y. Im, P. Fischer, and D. A. Allwood. *Appl. Phys. Lett.* **96**, 052502 (2010).
[8] W. Jung, F. J. Castano, and C. A. Ross. *Phys. Rev. Lett.* **97**, 247209 (2006).
[9] R. Nakatani, T. Yoshida, Y. Endo, Y. Kawamura, M. Yamamoto, T. Takenaga, S. Aya, T. Kuroiwa, S. Beysen, and H. Kobayashi. *J. Appl. Phys.* **95**, 6714 (2004).
[10] M. Kläui, J. Rothman, L. Lopez-Diaz, C. A. F. Vaz, J. A. C. Bland, and Z. Cui. *Appl. Phys. Lett.* **78**, 3268 (2001).
[11] Y. Gaididei, D. D. Sheka, and F. G. Mertens. *Appl. Phys. Lett.* **92**, 012503 (2008).
[12] K. Yamada, S. Kasai, Y. Nakatani, K. Kobayashi, H. Kohno, A. Thiaville, and T. Ono. *Nat. Mater.* **6**, 270 (2007).
[13] Y. Liu, S. Gliga, R. Hertel, and C. M. Schneider. *Appl. Phys. Lett.* **91**, 112501 (2007).
[14] R. Hertel, S. Gliga, M. Fähnle, and C. M. Schneider. *Phys. Rev. Lett.* **98**, 117201 (2007).
[15] D. J. Keavney, X. M. Cheng, and K. S. Buchanan. *Appl. Phys. Lett.* **94**, 172506 (2009).
[16] M. Weigand, B. Van Waeyenberge, A. Vansteenkiste, M. Curcic, V. Sackmann, H. Stoll, T. Tyliszczak, K. Kaznatcheev, D. Bertwistle, G. Woltersdorf, C. H. Back, and G. Schütz. *Phys. Rev. Lett.* **102**, 077201 (2009).
[17] S. S. P. Parkin, M. Hayashi, and L. Thomas. *Science* **320**, 190 (2008).
[18] T. Taniyama, I. Nakatani, T. Namikawa, and Y. Yamazaki. *Phys. Rev. Lett.* **82**, 2780 (1999).
[19] T. Taniyama, I. Nakatani, T. Yakabe, and Y. Yamazaki. *Appl. Phys. Lett.* **76**, 613 (2000).
[20] R. McMichael and M. Donahue. *IEEE Trans. Magn.* **33**, 4167 (1997).
[21] C. Brownlie, S. McVitie, J. N. Chapman, and C. D. W. Wilkinson. *J. Appl. Phys.* **100**, 033902 (2006).
[22] R. Frömter, S. Hankemeier, H. P. Oepen, and J. Kirschner. *to be published* (2010).
[23] M. Donahue and D. Porter. *OOMMF User's Guide Version 1.0, Interagency Report NISTIR 6376, National Institute of Standards and Technology, Gaithersburg* (1999).
[24] A. Kobs, S. Hankemeier, R. Frömter, and H. P. Oepen. *to be published* (2010).

[25] D. Backes, C. Schieback, M. Kläui, F. Junginger, H. Ehrke, P. Nielaba, U. Rüdiger, L. J. Heyderman, C. S. Chen, T. Kasama, R. E. Dunin-Borkowski, C. A. F. Vaz, and J. A. C. Bland. *Appl. Phys. Lett.* **91**, 112502 (2007).
[26] M. Kläui. *J. Phys.: Condens. Matter* **20**, 313001 (2008).
[27] O. Tchernyshyov and G.-W. Chern. *Phys. Rev. Lett.* **95**, 197204 (2005).
[28] G.-W. Chern, H. Youk, and O. Tchernyshyov. *J. Appl. Phys.* **99**, 08Q505 (2006).
[29] H. Youk, G.-W. Chern, K. Merit, B. Oppenheimer, and O. Tchernyshyov. *J. Appl. Phys.* **99**, 08B101 (2006).
[30] M. Hayashi, L. Thomas, C. Rettner, R. Moriya, X. Jiang, and S. S. P. Parkin. *Phys. Rev. Lett.* **97**, 207205 (2006).
[31] W. C. Uhlig, M. J. Donahue, D. T. Pierce, and J. Unguris. *J. Appl. Phys.* **105**, 103902 (2009).
[32] D. McGrouther, S. McVitie, J. N. Chapman, and A. Gentils. *Appl. Phys. Lett.* **91**, 022506 (2007).
[33] K. J. O'Shea, S. McVitie, J. N. Chapman, and J. M. R. Weaver. *Appl. Phys. Lett.* **93**, 202505 (2008).
[34] E.-S. Wilhelm, D. McGrouther, L. Heyne, A. Bisig, and M. Kläui. *Appl. Phys. Lett.* **95**, 252501 (2009).

4.4. Properties of $Co_{39}Fe_{54}Si_7$

The experimental investigation presented in the last publication [P5] is based on SEMPA images of nanowires carved from a $Co_{39}Fe_{54}Si_7$ thin film. For details on the magnetic properties of $Co_{39}Fe_{54}Si_7$, a reference to a future publication is given. The publication is in preparation and its content in regard to the magnetic properties of $Co_{39}Fe_{54}Si_7$ is summarized in first part of the next chapter. The second part deals with a comparison of the electrical characteristics of $Co_{39}Fe_{54}Si_7$ and Permalloy. After that, an outlook on the main topic of the forthcoming publication is given which is the influence of the bending angle on the predominant domain wall type in a V-shaped wire.

4.4.1. Magnetic properties

An ideal soft magnetic material for the study of the magnetic fine structure of submicron elements via SEMPA would have to fulfill the following requirements:

- high spin polarization of the secondary electrons for high contrast images
- zero or low anisotropy, thus magnetocrystalline anisotropy effects can be neglected
- low coercive fields for easy in-situ switching of the magnetization
- the grain size of the material should be much smaller as the magnetic structures of interest to neglect its influence
- high resilience against oxidation in air, as ex-situ transfer from the evaporation UHV chamber to the SEMPA chamber is necessary
- evaporation of the thin film should be possible from a single source via electron beam evaporation to be compatible with the nanostencil technique for structuring small elements through a shadow mask [Des99]
- the remanent domain pattern should be similar to that in Permalloy (Py), as Py is the "standard" material in the community and the results should be applicable to Py

The reason for not using Py ($Ni_{80}Fe_{20}$) in the first place is that for high quality SEMPA images of Py, a dusting of the sample with 1-2 ML of iron is necessary [see chapter 1], as nickel has a very low spin polarization of the secondary electrons compared with Fe [Oep05] and $Ni_{80}Fe_{20}$ gives therefore only a small contrast in the images. In order to avoid the iron dusting the sample, material with an intrinsic high spin polarization of the secondary electrons is necessary. Iron, cobalt and their alloys are possible candidates, as this material class gives a high contrast in SEMPA images [All94]. After some testing, it turned out that a thin film of a $Co_{39}Fe_{54}Si_7$ alloy is a good compromise for fulfilling the above mentioned requirements.

The selected film composition ratio was Fe 54 %, Co 39 %, Si 7 % (atomic percent), as checked via energy dispersive x-ray spectroscopy (EDX) [Jos03]. The film

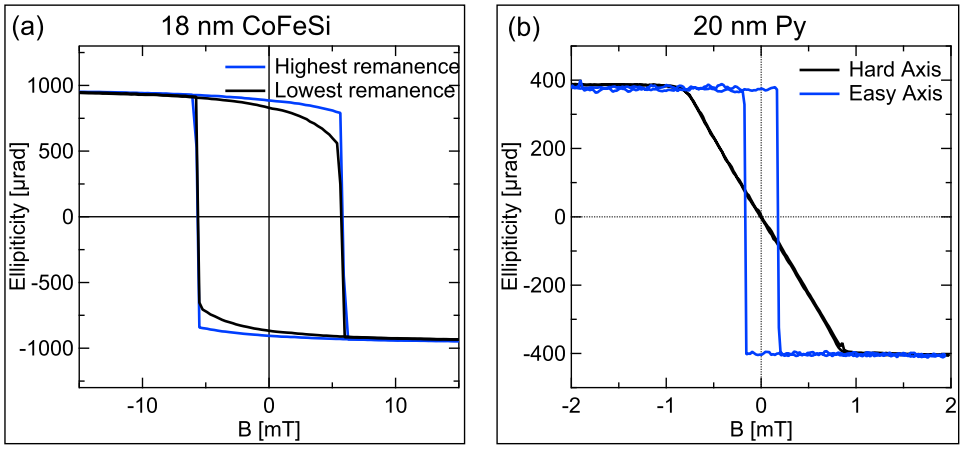

Figure 4.6.: Longitudinal MOKE measurements of an 18 nm thick $Co_{39}Fe_{54}Si_7$ film (a) and of a 20 nm thick Permalloy film (b).

was evaporated by means of electron-beam evaporation from a single source which consisted of 0.3 g cobalt, 0.12 g iron and 0.12 g silicon. Due to the difference in the vapor pressure of cobalt, iron and silicon the above mentioned film composition after evaporation was achieved. The film was deposited with a thickness of 18 nm on a naturally oxidized silicon wafer substrate at a rate of 0.05 nm/s at a base pressure of 1×10^{-8} mbar.

MOKE measurements of the so fabricated $Co_{39}Fe_{54}Si_7$ thin film and for comparison of a Py thin film are shown in Fig. 4.6 (a) and (b). In (a) the blue and the black curve denote the hysteresis along the sample axis with the highest and lowest remanence, respectively. The angle between both axes is 90° and the hysteresis loops for all other directions are framed by the blue and black curve. It is evident that $Co_{39}Fe_{54}Si_7$ has nearly a vanishing uniaxial anisotropy and can be interpreted as magnetically isotropic, giving $Q \simeq 0$. For Py a uniaxial anisotropy of 285 J/m^3 was determined from slope of the hard axis MOKE measurement in Fig. 4.6(b). The value agrees well with the literature [Cer96]. $Co_{39}Fe_{54}Si_7$ has a coercive field of 5.6 ±0.2 mT which is more than a magnitude higher as observed for Py, but still small enough that the magnetization can be switched in-situ with the electromagnet available in the SEMPA chamber. The saturation ellipticity of $Co_{39}Fe_{54}Si_7$ determined from the MOKE hysteresis is roughly twice as large as of Py. M_s was quantitatively determined via ferromagnetic resonance measurements and a value of $M_s = 1.44 \times 10^6$ A/m was obtained, which is comparable with the value published for $Fe_{65}Co_{35}B_4$ in [Pla01] with $M_s = 1.6 \times 10^6$ A/m.

Similar to the addition of B to CoFe [Pla01], the addition of a slight amount of Si probably results in a smaller grain size (<10 nm) which was found via high resolution SEM measurements. For Permalloy and $Co_{39}Fe_{54}Si_7$, the magnetocrystalline and magnetostrictive anisotropy terms can be neglected when considering the energy of a micromagnetic configuration of a nanowire [McM97]. The energy of a micromagnetic configuration is therefore determined by magnetostatic- and exchange energy only. In case of a straight wire geometry, these energy contributions are only affected by

the film thickness, the width of the wire and the magnetostatic exchange length delta, which is defined as [McM97]:

$$\delta_{\mathrm{ex}} = \sqrt{\frac{A}{\mu_0 \cdot M_{\mathrm{s}}^2}} \tag{4.6}$$

From [Liu94] the exchange stiffness A is known for $Fe_{53}Co_{47}$; using this value as approximation for $Co_{39}Fe_{54}Si_7$, the exchange length delta can be calculated. The result and other relevant values for $Co_{39}Fe_{54}Si_7$ and Py are specified in Tab. 4.1.

	$Co_{39}Fe_{54}Si_7$	Py	Co	Ni	Fe
M_{s} [A/m]	14.4×10^5	8×10^5	14×10^5	4.9×10^5	17×10^5
A [J/m]	3.5×10^{-11}	1.3×10^{-11}	3.0×10^{-11}	0.9×10^{-11}	2.1×10^{-11}
δ_{ex} [nm]	3.7	4	3.5	5.5	2.4

Table 4.1.: Saturation magnetization M_{s}, exchange stiffness A and exchange length δ_{ex} for different materials. The values for Py were taken from [Bre08] and for Co, Ni and Fe from [Don99].

It is evident that the exchange length for both materials is nearly identical with a difference smaller 10 %. Therefore the magnetic energy landscape of the remanent state with a given wire geometry should also be similar, i.e. the parameters needed to favor the transverse wall or the vortex wall configuration which are discussed in the next chapter in detail.

The thickness and width dependent transition of the energy landscape, which favors the vortex or transverse wall has been calculated and discussed earlier for straight Py wires [Thi07, Nak05, McM97, Klä08]. The result from [Nak05] is plotted in Fig. 4.9 as black dotted line of equal energy. An analogue phase diagram for $Co_{39}Fe_{54}Si_7$ was calculated via OOMMF [Don99] using the parameters specified in Tab. 4.1. The result for a straight wire is added as red curve to Fig. 4.9. As expected from the nearly identical exchange lengths of both materials, the lines of equal energy show not only the same characteristics but are nearly congruent. As the transition between the vortex wall and the transverse wall is of interest in the following, one can assume that the general results for $Co_{39}Fe_{54}Si_7$ are also valid for Permalloy nanowires.

4.4.2. Electrical properties

To complete the chapter about $Co_{39}Fe_{54}Si_7$, the electrical properties of the thin film are discussed and compared with Permalloy and bulk values in the following. The resistivity is important if e.g. magnetotransport measurements utilizing high current densities are in the focus of interest. Tab. 4.2 gives an overview of the resistivity of $Co_{39}Fe_{54}Si_7$ and Py thin films and for comparison some selected bulk values. The electrical resistance of thin films is generally about a factor of 2-3 higher, compared to their bulk values and increases with a decreasing film thickness [May74] due to

evolving surface scattering effects [Mar06] and the stronger influence of impurities or defects on very thin films [Rij95].

The resistivity is strongly dependent on the temperature and has in case of ferromagnetic $3d$-metals a parabolic dependence on a temperature increase up to the Curie temperature [Ho83, Fer76]. The resistivity of a 20 nm thin Py film for example drops 22 % during cooling from room temperature to 80 K (Tab. 4.2 and for example [P6, Fig. 2]). The bulk value even drops 70 % during the cooling procedure. For $Co_{39}Fe_{54}Si_7$ thin films, the lowering of the resistance is less distinct, a decrease of only 8 % was observed.

Another important effect on the resistivity of thin films is annealing of the sample, which occurs when the temperature rises above the deposition temperature of the film [Miy89]. Tab. 4.2 shows that the resistivity of the Py thin film at 80 K after annealing at 590 K for one hour was reduced by 23 % [Han08]. Similar values of annealing-induced resistance reduction are published in [Kro73, Nah09] and a general discussion of the Py resistivity of nanostructures can be found in [Sac08].

material	T [K]	ρ [Ωm]	comment
$Co_{39}Fe_{54}Si_7$ 18 nm	293	8.1×10^{-7}	as deposited[1]
$Co_{39}Fe_{54}Si_7$ 18 nm	80	7.5×10^{-7}	as deposited[1]
Py 20 nm	293	4.5×10^{-7}	as deposited[1]
Py 20 nm	80	3.5×10^{-7}	as deposited[1]
Py 20 nm	80	2.7×10^{-7}	after annealing at 590 K
Py bulk	293	1.5×10^{-7}	from [Ho83]
Py bulk	80	4.9×10^{-8}	from [Ho83]
Co bulk	293	5.0×10^{-8}	from [Lan10]
Fe bulk	293	1.7×10^{-7}	from [Lan10]
Ni bulk	293	6.0×10^{-8}	from [Lan10]

Table 4.2.: Resistivity of selected materials.

In general the resistivity of $Co_{39}Fe_{54}Si_7$ thin films is more then twice as high as of Py thin films. The influence of annealing on $Co_{39}Fe_{54}Si_7$ has to be further investigated but has probably a similar effect as observed for Py thin films. Direct current densities of 3×10^{12} A/m^2 were achieved for an 18 nm thick $Co_{39}Fe_{54}Si_7$ nanowire on a ℓN_2 cooled diamond substrate. Surprisingly, that is nearly the same threshold current density which was achieved with comparable Py nanowires [Han08], although Py has a lower resistivity at room temperature (see chapter 5.2).

[1] The thin film was deposited via electron beam evaporation from a single source onto a diamond substrate. The average evaporation rate was 0.1 nm/s and the vacuum base pressure 1×10^{-8} mbar. The resistivity measurement was carried out at nanowire sample.

4.5. Influence of the bending angle on the domain wall configuration

In magnetic nanowires three different types of domain wall configuration are stable: The symmetric- and asymmetric transverse wall and the vortex wall configuration (excluding exotic states like multiple vortices [Klä06]). The wall type with lowest energy for a given nanowire depends on the geometric properties, i.e. width, thickness, edge roughness, et cetera and on the magnetic properties of the wire material (saturation magnetization, anisotropy, exchange stiffness). For straight Permalloy wires, the state of lowest energy was calculated for different values of width and thickness and so a phase diagram was obtained, where a line of equal energy denotes the transition from the symmetric transverse- to the vortex wall configuration [Nak05, McM97]. In the transition region, in the vicinity of the line of equal energy, the asymmetric transverse wall configuration was found to be the third stable domain wall configuration [Thi07, Nak05]. These calculated phase diagrams were compared to experimental observations of the predominant domain wall configurations found in nanorings of different size [Klä04, Lau06]. The general trend of the line of equal energy was confirmed, but the transition line was slightly shifted to higher thicknesses in the experiment. This was attributed to slightly differing geometries (rings / straight wires) and to the fact that the simulation not necessarily gives the global energy minimum as a 0 K situation is modeled while the experiments are usually done at room temperature [Lau06]. This is especially of importance when local and global minima are nearly equal in energy, as it is the case near the line of equal energy in the domain wall phase diagram. The dependence on other geometric parameters, however, was not further investigated. Zigzag and V-shaped wires, for example, are frequently employed as experimental systems [Van08, Tsa02, Tan00, Tan99, Klä05a, Klä08, Jub06, Hey08a, Gar02a, Bro06] as it is very easy to introduce a domain wall via an external seeding field. Surprisingly, to my knowledge there is no publication which deals with the influence of a bent wire geometry on the predominant domain wall configuration. The consideration of the additional geometrical parameter, i.e. the bending angle α, is therefore an important aspect, which is discussed in the following.

To get a basic impression of the energy dependence of a transverse wall on the bending angle α, as first approximation for the transverse wall the energy of two different types of Néel wall configuration are considered: A single Néel wall following the symmetry axis of the wire with a wall angle α, as shown in Fig. 4.7(a) and second, the separation of the single wall into two $\alpha/2$ walls merging at the inner kink as shown in Fig. 4.7(b). The energy of both configurations can be analytically calculated. The energy density of a Néel wall [Née53] in dependence of the wall angle can be approximated by

$$\gamma_{\text{Néel}}(\alpha) = \gamma_{\text{Néel}}^{180} \cdot \left(1 - \cos\frac{\alpha}{2}\right)^2, \tag{4.7}$$

with $\gamma_{\text{Néel}}^{180}$ denoting the energy density of the full 180° wall (set to one in the following).

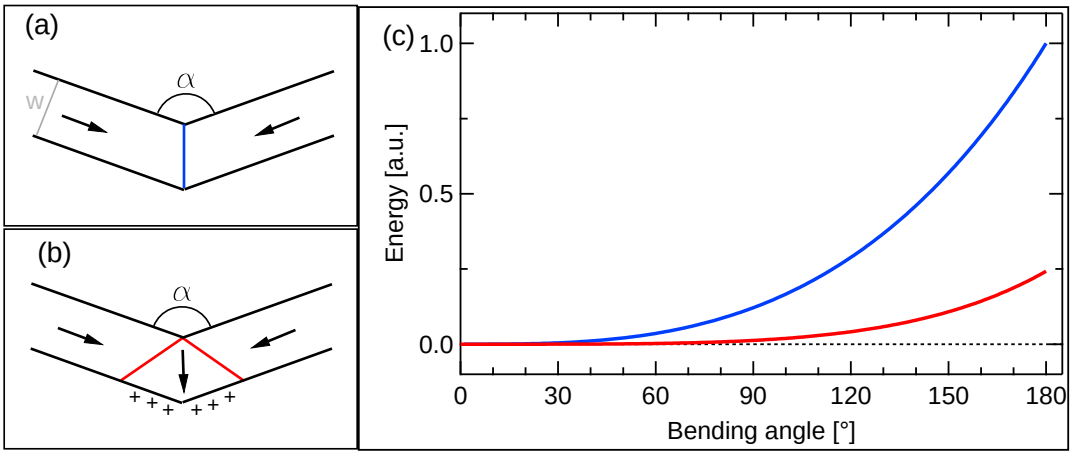

Figure 4.7.: Sketch of two approximations of a Néel wall in a bent nanowire. In (a) a single α wall is plotted, (b) shows a configuration with two $\alpha/2$ walls. The energy for both configurations in dependence of the bending angle is plotted in (c). The blue line denotes E_α and the red is $2E_{\frac{\alpha}{2}}$.

In principle this formula only applies to walls with an infinite length, so in case of a wall in a nanowire with a length of around 500 nm it seems questionable if this model fits reality, but the calculation will give a first impression of the strong impact of the bending angle on the energy landscape: In calculating the energy, the lengths of the walls have to be taken into account, which also depends on the bending angle. Considering this, the energy of the single α wall (Fig. 4.7(a)) yields:

$$E_\alpha(\alpha) = \frac{1}{\sin\frac{\alpha}{2}} \cdot E_{\text{Néel}}^{180} \cdot \left(1 - \cos\frac{\alpha}{2}\right)^2 \tag{4.8}$$

To calculate the length of the two $\alpha/2$ walls (Fig. 4.7(b)), one has to consider the direction of the $\alpha/2$ walls: To minimize the stray-field of the wall, the allowed wall normal $\vec{n}$ is derived from demanding zero net magnetic charge of the wall [Hub98] (p119):

$$\vec{n} \cdot (\vec{M}_1 - \vec{M}_2) = 0 \tag{4.9}$$

This criterion defines the wall direction as $\vec{M}_1$ and $\vec{M}_2$ are the magnetization orientations in one arm and the bend region, respectively. The total energy of two $\alpha/2$ walls can then be derived to:

$$2E_{\frac{\alpha}{2}}(\alpha) = \frac{2}{\cos\frac{\alpha}{4}} \cdot E_{\text{Néel}}^{180} \cdot \left(1 - \cos\frac{\alpha}{4}\right)^2 \tag{4.10}$$

Both energy curves are plotted in Fig. 4.7(c). A strong energy dependence on the bending angle is obvious and the energy of the $\alpha/2$ wall configuration is generally lower compared to the single α wall, giving a hint to the actual structure of the transverse wall. As mentioned before, an important contribution which is not taken into account are the magnetic poles that are generated at the edge of the wire

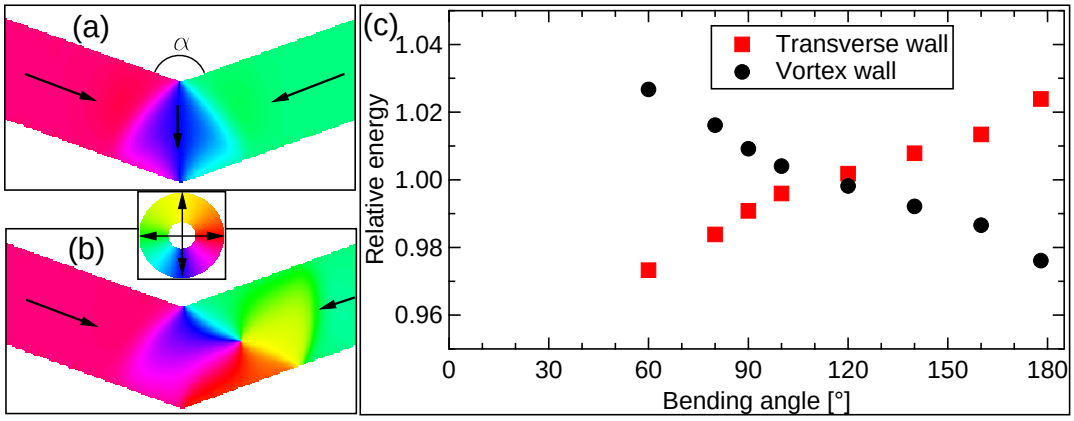

Figure 4.8.: OOMMF simulation of the transverse wall (a) and the vortex wall configuration (b) in a $Co_{39}Fe_{54}Si_7$ wire with w=400 nm, h=10 nm and α=140°. The color wheel and the black arrows give the direction of magnetization. The relative energy for both configurations in dependence on the bending angle α is plotted in (c).

(see Fig. 4.7(b)). To get hand on the energy landscape with a more sophisticated approach, micromagnetic simulations are mandatory.

In Fig. 4.8, the micromagnetic configurations of a transverse wall (a) and a vortex wall (b), obtained via the "Object Oriented MicroMagnetic Framework" (OOMMF) [Don99], are shown. The width of the wire is 400 nm, the thickness 10 nm. The cell size of the simulation was 5 x 5 x 10 nm^3; $M_s = 1.44 \cdot 10^6$ A/m and $A = 3.55 \cdot 10^{-11}$ J/m was used to mimic $Co_{39}Fe_{54}Si_7$.

The actual domain configuration of the transverse wall obtained by the simulations is quite similar to the basic sketch shown in Fig. 4.7(b). In the bend region a quasi domain is visible as blue area in analogy to the $\alpha/2$ wall configuration in Fig. 4.7(b). To avoid / minimize the magnetic poles at the outer edge of the bend region, the magnetization in the vicinity of the edge is aligned along the latter. The so generated exchange energy between the edge-region and the blue domain is minimized by decreasing the size of the blue domain compared to the $\alpha/2$ configuration shown in Fig. 4.7(b). The twisted $\alpha/2$ domain wall configuration is in contradiction with Eq. 4.9 and charged walls are created. The charged walls counterbalance the tendency to shrink the blue area, resulting in the domain configuration of the transverse wall, which can be interpreted as a mixed state of the two basic configurations shown in Fig. 4.7(a) and (b). For the geometrical configuration of the wire shown in Fig. 4.8(a) two transverse wall configurations are stable and have the same energy, a head-to-head and tail-to tail arrangement, which can be transferred into each other by a geometric / time inversion symmetry operation.

The vortex wall configuration 4.8(b) with its different possible states is discussed in detail in [P5]. Combining head-to-head (tail-to tail) arrangement, sense of rotation and polarity of the core yields eight different compositions of the domain structure, which have in absence of any anisotropy the same energy and can be transferred into each other by symmetry considerations [P5]. One possible configuration of a head-to-head vortex wall for a wire with a bending angle of 150° is plotted again in

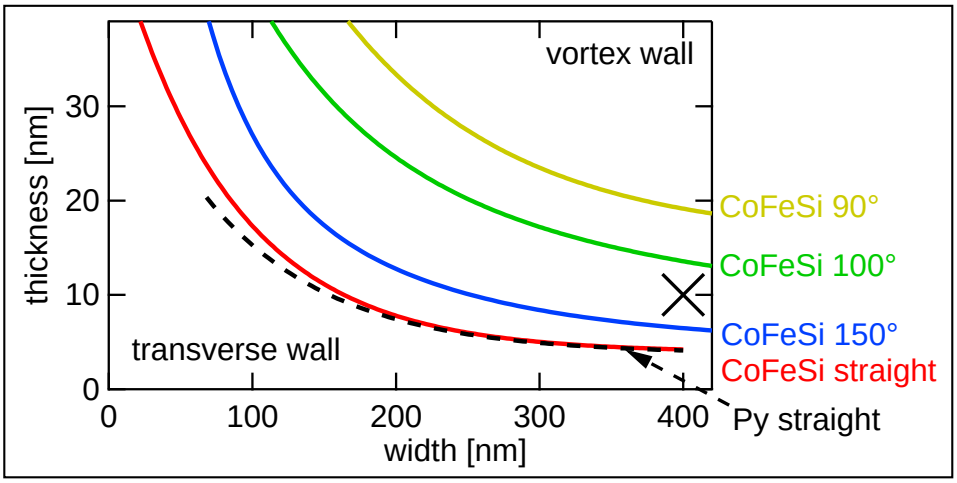

Figure 4.9.: Lines of equal energy for the vortex wall and transverse domain configuration in straight and bent Py / $Co_{39}Fe_{54}Si_7$ nanowires. In the upper right part of the graph the vortex wall has the lower energy; in the lower left part the transverse wall is lower in energy. The graph has been calculated using OOMMF [Don99].

Fig. 4.8(b) for the sake of convenience.

In Fig. 4.8(c), the relative energy of the transverse- and the vortex wall configurations are plotted in dependence on the bending angle. In the case of α=180° the vortex wall is ∼4.5 % lower in energy than the transverse wall. With a decrease of the bending angle, the energy of the transverse wall decreases, mostly due the decrease of the energy of the two $\alpha/2$ walls as displayed in Fig. 4.7. The relative energy of the vortex configuration on the other hand increases with a decrease of the bending angle: To maintain the vortex structure at low bending angles, magnetic poles have to be created at the outer edge in the bend region. Additionally, the total rotating area of the vortex has to be stretched over the symmetry line of the wire for smaller bending angles, thus resulting in a larger amount of volume charges and exchange energy. The energy increase of the vortex wall cumulates in the fact that below α=50° the vortex wall is no longer a stable micromagnetic configuration, i.e. an energy minimum.

This also raises the question if one can still speak of a domain wall in case of a very small bending angle: The classical definition of a domain wall is that of a sharp boundary between domains of opposite direction introduced as magnetic discontinuity [Six31]. If this definition still applies in a bent wire with α=30° inhibiting a transverse wall which is then in fact a region of nearly homogeneous rotation of just 30°, is at least a question to bear in mind, especially when one thinks about spin transfer torque experiments in bent wires.

Coming back to the energy dependence of the domain wall configurations shown in Fig. 4.8(c), we see that at a bending angle of 115° both wall configurations are equal in energy. This angle of course depends on the width and thickness of the simulated wire, the value of 115° only applies for the case of 400 nm width and 10 nm thickness (black cross Fig. 4.9). By additionally varying the thickness as well

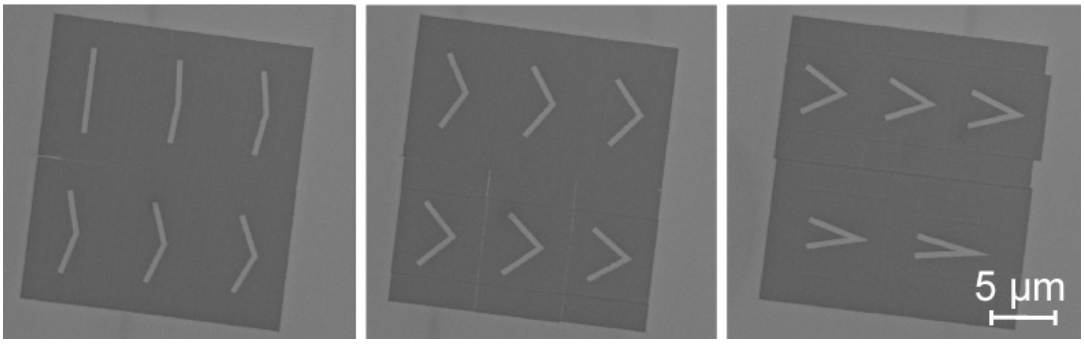

Figure 4.10.: SEM image of V-shaped wire with different bending angles carved via FIB milling from a 18 nm thick $Co_{39}Fe_{54}Si_7$ film.

as the width of the simulated wire, one obtains a 3D-phase diagram which shows the energy dependence on the three geometrical parameters (Fig. 4.9). The region where the vortex wall is the ground state (upper right part) is separated from the transverse wall region by a line of equal energy. Different lines of equal energy are plotted for different bending angles. On lowering the bending angle, the vortex area shrinks and the transverse wall becomes more stable, in accordance to the trend shown in Fig. 4.8(c) for a single set of width and thickness.

As the phase diagram suggests a significant impact of the bending angle on the predominant domain wall configuration, an experiment was designed to confirm the assumption in an experimentally robust way: Analog to the approach in [P5] a $Co_{39}Fe_{54}Si_7$ film was evaporated and V-shaped wires have been structured via focused ion beam milling. The thickness and width of the wires were kept constant (h=18 nm, w=400 nm) while the bending angle was varied from 180° to 20° in 17 steps. The symmetry axes of all wires are tilted 9° with respect to the horizontal. SEM micrographs of the fabricated wires are shown in Fig. 4.10.

To nucleate a domain wall in each wire a magnetic field of 60 mT was applied along the x-axis. SEMPA images of all wires showed that the first three wires with a bending angle of 180°, 170° and 160° did not contain a domain wall thereafter, as the symmetry axis of the wires is slightly tilted upwards and the projection of the magnetic field on the wire arm was not sufficient to switch their magnetization. In all other wires the nucleation of the domain wall was successful, as can be seen from the SEMPA images shown in Fig. 4.11(a)-(j). In (a) and (b) a vortex wall located in the lower arm of the wire with a clockwise sense of rotation is visible. The position of the core and the sense of rotation induced by the orientation of the seeding field (Fig. 4.11(a); red arrow) with respect to the symmetry axis (gray dotted line) are in accordance with the findings of [P5]. As expected from the simulations, for smaller bending angles we find a transverse wall-like configuration. The highly symmetric transverse wall configuration shown in Fig. 4.8(a) is observed for rather small bending angles below 100° (see Fig. 4.11(h)-(j)). This is in accordance with the simulations which give a transition from the vortex to the transverse wall between 90° and 100° (yellow and green curve in Fig. 4.9). For bending angles between 100°-135° (Fig. 4.11(c)-(g)), however, we do not find the vortex wall as suggested by the

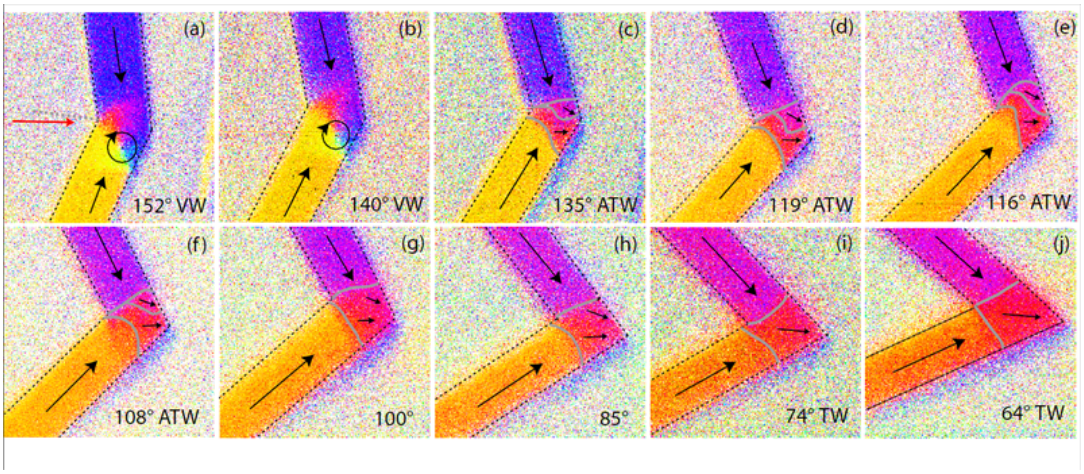

Figure 4.11.: Series of SEMPA images of nanowires with varying bending angle α. The orientation of magnetization is aligned along the black arrows, low-angle domain walls are indicated by gray lines. The edges of the wires are traced by dashed lines.

simulations; but an asymmetric transverse-wall-like configuration, which was not apparent in the first place as we calculated and compared the energy for the two principal cases of the vortex wall and the symmetric transverse wall.

The observed asymmetric configuration is called the asymmetric transverse wall (ATW) which was first predicted in 2005 [Nak05] as metastable state in straight wires and was first observed in a curved wire geometry containing a notch [Bac07]. Further numerical investigations [Thi07] showed that the ATW can be a stable (lowest energy) domain configuration in case the wire parameters are so chosen that the vortex- and transverse wall are nearly equal in energy, i.e. in the vicinity of the line of equal energy in the phase diagram. Simulations show that two mirror symmetric configurations of the asymmetric transverse wall are possible for a head-to-head domain arrangement, the simulation of both plotted in Fig. 4.12(b) and (c) [Thi07]. The reason, however, for the occurrence of the one or the other configuration was not further investigated, nor was the numerical "generation" of the two states described. The micromagnetic structure of the ATW is also discussed in [You06b] from a topological point of view, by comparing the ATW structure with a mutated vortex wall: If the vortex core is shifted on the center wall towards one edge defect so that the core is located (nearly) on the edge itself and the arising domain pattern (Fig. 4.12(d)) matches the numerical simulation of an ATW (Fig. 4.12(e)). In other words: If the vortex core has failed to nucleate at the edge during a relaxation process [P5, Fig. 5], the remaining domain pattern resembles a half finished vortex wall with the vortex core located "outside" the wire. This becomes clear when comparing the ATW configuration plotted in Fig. 4.12 (c) and (e) with the associated vortex wall configuration in Fig. 4.12(a) although it is probably not the ground state.

The tight connection between the ATW and the vortex wall also explains the observed transition between the vortex wall and the transverse wall of Fig. 4.11. The energy difference between both magnetic structures for $100° < \alpha < 135°$ is so small that the vortex core fails to nucleate during the relaxation process and the

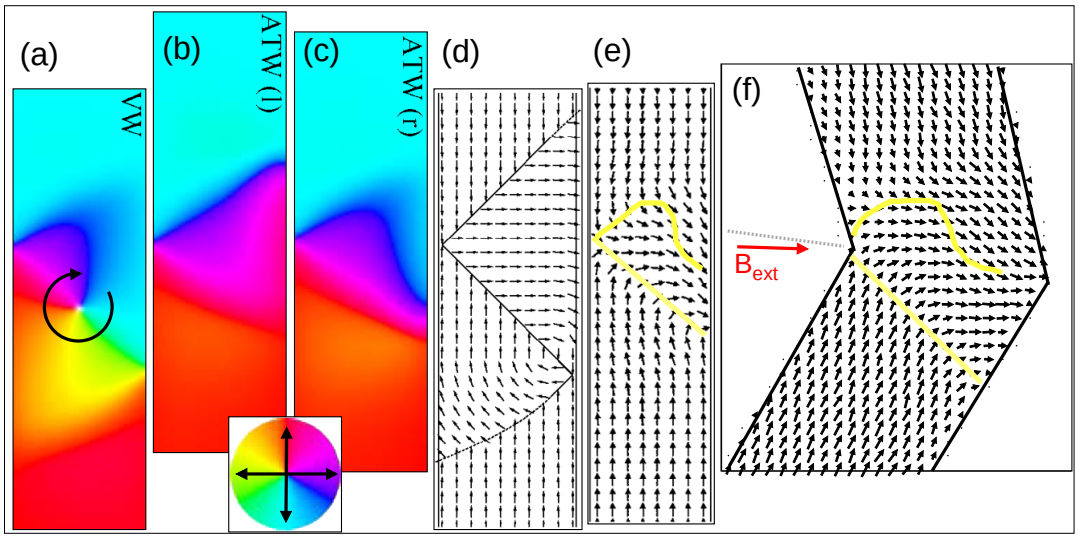

Figure 4.12.: (b) and (c) show the two configurations of the asymmetric transverse wall for a head-to-head wall, for comparability one vortex wall is also plotted in (a). (a)-(c) are reprinted from A. Thiaville et al. [Thi07] with permission from Springer. (d) and (e) are taken from H. Youk et al. [You06b], where the asymmetric transverse wall is discussed from a topological point of view. Reprinted with permission from AIP. (e) shows the same domain pattern as (c). In (f) an arrow-plot of the SEMPA measurement shown in Fig. 4.11(c) is given, the red arrow indicates the direction of the seeding field. The sub-images have been aligned that the edge defects are located on a common horizontal line.

asymmetric transverse wall structure remains as remanent magnetic configuration.

The connection between the vortex wall and the ATW explains also the exact magnetic fine structure observed in the SEMPA images, i.e. which of the two possible tilting directions of the ATW occurs (Fig. 4.12(b), (c)). In Fig. 4.12(f) a zoom into the ATW configuration of Fig. 4.11(c) (α=135°) is plotted with arrows indicating the direction of magnetization. The similarity between the measurement (f) and the calculations shown in (c)-(e) is evident, as the important features match (yellow lines are guide to the eye). From the topological comparison we can see that the virtual half vortex is located at the right edge in the lower arm (Fig. 4.12(d)). If the core had nucleated we would therefore expect it to be in the lower arm of the wire with a clockwise sense of rotation (compare Fig. 4.12(d),(a)). This is exactly what we observe for a slightly higher bending angle of 140° (Fig. 4.11(b)), when the vortex wall is energetically more favorable the core is able to nucleate thus forming the clockwise vortex structure. The nucleation of the core at the outer edge of the lower arm (Fig. 4.12(d)) is also in exact agreement with the dynamical simulation shown in [P5, Fig. 5].

In brief, the influence of the bending angle of a V-shaped nanowire on the predominant domain configuration in remanence has been investigated via SEMPA measurements and numerical simulations. A strong impact of the bending angle on the actual domain pattern was found in the SEMPA micrographs and explained by

energy calculations for different wire geometries. The, in the first place, unexpected occurrence of the asymmetric transverse wall in a symmetrically wire geometry was explained via the symmetry breaking by the external seeding field in analogy to the seeding of different types of vortex walls in [P5]: The tilting direction of the asymmetric transverse wall is, as the tilting of the vortex wall, sensitive to the exact direction of the external seeding field with respect to the symmetry axis of the wire.

4.6. Summary

The technical prerequisite for the results shown in this chapter is the quantitative angular information supplied by the SEMPA experiment. In the SEMPA images it is possible to assign a specific direction of magnetization to each acquired pixel with an angular error of only $\pm 4^\circ$. Due to this high angular resolution, imaging of soft magnetic rectangles and nanowires have revealed unexpected magnetic properties. The Landau structure does not consist of four, but of six domains in case of rectangles with dimensions to mimic the standard problem # 1 [P3]. The statistical investigation of hundreds of rectangles and a detailed investigation of their fine structure supplied the necessary information to interpret magnetotransport measurements of single rectangles [P4]. Finally, the seeding of vortex walls in V-shaped nanowires is sensitive to the exact direction of the seeing field. It could be experimentally confirmed that the sense of rotation and the position of the core are strongly interconnected and both can be adjusted by the orientation of the external field [P5]. Furthermore, the influence of the bending angle of V-shaped wires on the domain wall structure was investigated. A strong impact was observed: Starting with a straight wire and by lowering α the predominant domain wall type changes from the vortex wall to the asymmetric transverse wall and finally to the symmetric transverse wall (Fig. 4.11). It was possible to resolve the fine structure of the ATW (Fig. 4.12) and confirm as well as explain its occurrence in V-shaped wires.

The findings about the predominant domain wall configuration may have some relevance for a "Current-Controlled Magnetic Domain-Wall Nanowire Shift Register" [Hay08a]: Here, a domain wall is introduced into a nanowire via the Oersted field of an on-top fabricated perpendicular wire. The investigation was conducted with straight wires only. By using bent wires as shift register and two seeding wires with different orientation in respect to the kink, the sense of rotation of the vortex wall could be controlled and possibly utilized as additional storage-bit in analogy to the proposed vortex-RAM memory concept [Boh08].

5. Spin Torque Investigation via Direct Current

In the previous sections, which dealt with static investigations of micromagnetic structures, it was argued with energy- and symmetry-considerations in a hand waving manner. The benefit of such arguments is that they are easily accessible, usually straightforward and produce an intuitive picture of the situation. On the other hand, when dynamic effects come into play, static energy considerations must necessarily fail. Then a dynamic theory for the description of micromagnetism is mandatory which must give the same results as energy considerations in the static case. The dynamic theory is expressed by the so called Landau-Lifshitz-Gilbert equation of motion which describes the change of magnetization in time.

5.1. The Landau-Liftshitz-Gilbert equation

The Landau-Liftshitz-Gilbert equation (LLG) was first introduced in 1933 by Landau and Lifshitz [Lan35] and modified by Gilbert in 1955 [Gil04] by a phenomenological damping term. The so improved LLG equation (Eq. 5.1) portrays a single magnetic moment $\vec{m}$ subject to an external magnetic field $\vec{H}$. The first term in Eq. 5.1 describes a precessional motion of the magnetic moment on a circular trajectory around the direction of the field. The second part is the damping term which causes the amplitude of the precession to decay until $\vec{m}$ reaches its equilibrium orientation, parallel aligned to $\vec{H}$. Only recently, it has been shown that the damping term can be derived analytically from first-principles by a nonrelativistic expansion of the Dirac equation [Hic09]. γ_0 denotes the gyromagnetic ratio given by $\gamma_0 = \frac{g|e|\mu_0}{2m}$, where e is the electron charge, m the electron mass and g the Landé factor [Lan21], which is 2 when the magnetic moment is only due to the electron spin[1]. The dimensionless factor α is called damping parameter and typically taken to be a constant, although its determination is a rather complex problem and it is not just a material constant but a sample parameter, which depends on e.g. noise in the system [Hei05]. However, typical experimentally obtained values for the damping constant of thin Permalloy nanostructures are in the range of $\alpha = 0.008 - 0.013$ [Hie97, San99]. It should be noted that the damping has a maximum for $\alpha = 1$ and exhibits a symmetric behavior around the maximum, thus higher values can be considered unphysical [Gli09].

From a non relativistic point of view, moving charges cause an Oersted field which may influence the magnetic structure of a current carrying ferromagnetic sample.

[1] For Fe in absence of an external field $g \backsimeq 1.9$ [Sco55], indicating that the contribution of orbital moment is negligible as the Landé-g factor is defined via the sum of orbital and spin momenta.

In addition, J. Slonczewski [Slo96] and L. Berger [Ber96] have predicted in 1996 independently from each other that the magnetization can be directly influenced by the current flow via the so called spin transfer torque (STT). The effect of an in-plane current flow acting on a localized ferromagnetic structure, e.g. a domain wall, can be described as follows. The spin polarized electron flow exerts a torque on the sample magnetization proportional to the current density in case magnetization and polarization differ from each other in direction. This was first experimentally confirmed for lateral structures by A. Yamaguchi et al. [Yam04], who measured a domain wall displacement via MFM imaging in a Permalloy nanowire after application of microsecond current pulses. In the same manner SEMPA was utilized to get hands on the wall displacement [Klä05b] and for an investigation of the domain wall velocity [Jub06].

To account for STT effects in the theory, two terms have to be added to the LLG: The adiabatic spin torque term (Eq. 5.2) phenomenologically described above and introduced by G. Tatara et al. [Tat04] and the non adiabatic term (Eq. 5.3) proposed by S. Zhang and Z. Li [Zha04] in 2004, which is related to the spatial mistracking of spins between conduction electrons and local magnetization [Thi05].

$$\frac{\mathrm{d}\vec{M}}{\mathrm{d}t} = \underbrace{-\gamma_0 \left[\vec{M} \times \vec{H}_{\mathrm{eff}}\right]}_{\text{precession}} \underbrace{- \frac{\alpha}{M_\mathrm{s}} \vec{M} \times \left[\vec{M} \times \vec{H}\right]}_{\text{damping}} \tag{5.1}$$

$$\underbrace{-\frac{1}{M_\mathrm{s}^2} \vec{M} \times \left[\vec{M} \times (\vec{u} \cdot \nabla)\, \vec{M}\right]}_{\text{adiabatic spin-torque}} \tag{5.2}$$

$$\underbrace{-\frac{\beta}{M_\mathrm{s}^2} \vec{M} \times (\vec{u} \cdot \nabla)\, \vec{M}}_{\text{non-adiabatic spin-torque}} \tag{5.3}$$

Here $\vec{u}$ is given by

$$\vec{u} = \frac{JPg\mu_\mathrm{B}}{2eM_\mathrm{s}} \cdot \vec{j_\mathrm{e}} \tag{5.4}$$

where J is the current density, P the degree of polarization, g the Landé factor, μ_B the Bohr magneton, e the electron charge and $\vec{j_\mathrm{e}}$ the direction of the electron flow. The non-adiabatic term was introduced to resolve discrepancies between experimental observations and theoretical predictions [Li04]. Its influence is determined by the dimensionless parameter β which is known as the "degree of non-adiabaticity" and defined as [Lep09a]:

$$\beta = \frac{\hbar}{J_\mathrm{ex}\tau_\mathrm{sf}} \tag{5.5}$$

Here, J_ex is the *s-d* exchange interaction energy and τ_sf the spin-flip time. Although the LLG with the two additional terms seems to be accepted within the community, the exact value of β for various materials and sample geometries is under intense debate. Some theoretical models suggest that $\beta = \alpha$ [Bar05, Tse06, Sti07]

while others propose $\beta \neq \alpha$ [Koh06]. However, an experimental PEEM investigation could only be reproduced via numerical simulations when $\beta \neq \alpha$ was assumed [Hey08b]. An investigation of domain wall depinning in Py nanowires via current pulses and a following comparison to micromagnetic modeling [Hay08b] yielded values of $\beta = 0.016$, $P = 0.6$ for $\alpha = 0.008$. A similar approach for Py stripes was best reproduced with $\beta = 0.04$ and $P = 0.4$ for $\alpha = 0.02$ [Thi05] and an investigation of Py wires with notches acting as pinning sites yielded $\beta = 0.04$ and $P = 0.5$ [Lep09b].

Recently, a robust measurement scheme for the determination of β was proposed using the displacement of a vortex core in a Permalloy square [Krü10, Naj09]: A steady direct current in the range of 1×10^{12} A/m^2 flows through the rectangle with a size of 5 µm x 5 µm x 10 nm, thus deflecting the vortex core. From the shift of the core in six independent measurements with different initial magnetic configurations of the vortex, i.e. variation of sense of rotation and polarity, one can derive the individual contributions of adiabatic, non-adiabatic and Oersted field effect. The measurement has to be done under equilibrium conditions, thus dynamic effects are nonexistent and the outcome is independent of the damping constant α. For the realization of the method the position of the vortex core has to be resolved with a high lateral resolution as the expected vortex shift is in the range of some 10 nm [Krü10].

To observe a significant influence of the STT effect, e.g. the displacement of a domain wall in a nanowire, relatively high current densities in the range from 5×10^{11} A/m^2 [Yam06] up to 3×10^{12} A/m^2 [Par08] are necessary. Usually these current densities can only be achieved via microsecond (or shorter) current pulses as then the electrical and thermal stress on the wires is much lower than in the static case [Klä05b]. Thus, to perform experiments in the static regime with a direct current requires the technological prerequisite for ultrahigh current densities ($> 1 \times 10^{12}$ A/m^2) in Permalloy nanowires, stable at least for several minutes. This obstacle, however, was overcome [Han08] which will be the topic of the next section.

5.2. Technological prerequisite: Ultrahigh direct current densities

Bulk metals fail because of Joule heating at current densities of $\sim 10^7 - 10^8$ A/m^2 [Ho89]. The current density applicable to a nanowire depends on its thickness [Hua08] and width [Kar09] as wires with smaller cross section can typically sustain a higher current density. For example, a 5 nm thick and 120 nm wide Py wire was able to carry 6×10^{11} A/m^2 without destruction [Ver04] while a 24 nm thick and 300 nm wide Py wire achieved 4×10^{11} A/m^2[Uhl09]. Only carbon nanotubes [Dai96] and superconducting bridges [Jia91] are able to sustain "supercurrents" $> 1 \times 10^{13}$ A/m^2.

Electromigration and thermal stress due to Joule heating are usually responsible for destruction of current carrying thin-film elements [Dur08]. Electromigration, which is the thermally assisted motion of ions under the influence of an electric field, was identified as the major effect causing failures well below the melting temperature of the material due to the so called Rayleigh instability [Kar06]. It has been found that the average mean time t_{50} it takes for a wire to fail under a constant current

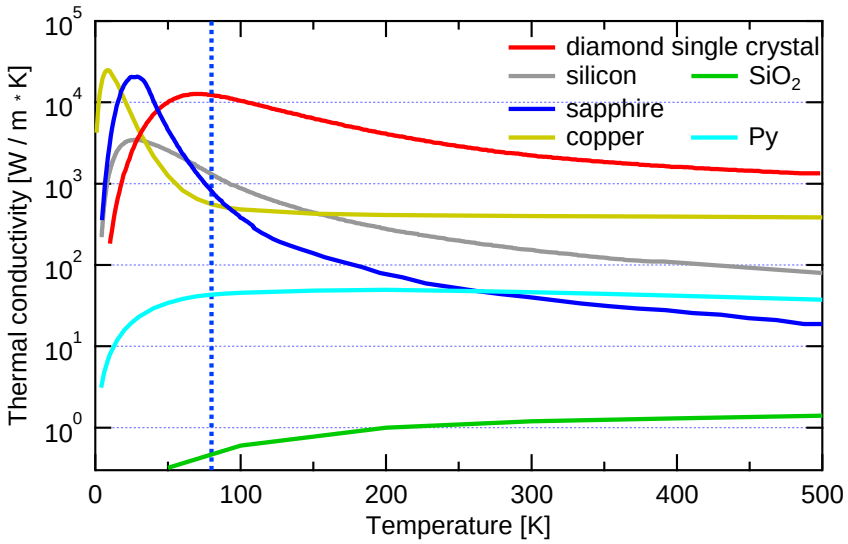

Figure 5.1.: Thermal conductivity of selected materials. The data is taken from [Bar07] (diamond); [Gla64] (silicon); [Lee97] (silicon dioxide); [Bur94, Tom02] (sapphire); [Wea04] (copper); [Ho78] (Permalloy). The blue dotted line denotes the temperature of ℓN_2, i.e. the working point.

density due to electromigration is given by the so called "Black's equation" [Bla69]:

$$t_{50} = CJ^{-n} e^{\frac{E_a}{k_b T}}, \tag{5.6}$$

where the constant C is a material property, J the current density, E_a the electromigration activation energy (0.5-0.7 eV for Al [Ber69]), n an integer which is in most cases two and T the temperature. The main conclusion from the equation becomes clear when considering the following numbers: Increasing the temperature from 300 K to 400 K for a given current density will reduce t_{50} by a factor of 100! Thus, the message is: Keep the temperature as low as possible to reach the maximum current density.

To obtain low temperatures under current carrying condition, efficient cooling of the wire is mandatory. The thermal conductivity of the substrate material is here of central importance. In Fig. 5.1 the thermal conductivities of selected substrate materials as well as copper and Permalloy for comparison are plotted. The material with the highest thermal conductivity above $\sim$ 50 K is a diamond single crystal, although a sapphire single crystal has a slightly higher peak around 25 K but decreases much faster for higher temperatures. For cooling the substrate with liquid nitrogen (78 K, blue dotted line), diamond is the best material for most effective cooling of a thin sample fabricated on-top. Over the whole temperature range up to the Curie temperature of Py, diamond has an approx. 100 times better thermal conductivity than Py, thus an optimum heat flow from the Py / diamond interface into the cryostat is ensured. A silicon single crystal substrate has also a higher thermal conductivity than Py and would be suitable as heat spreader; but to undergo current carrying experiments a relatively thick SiO_2 layer ($>$ 4 nm [Sac08]) is necessary for electrical insulation. SiO_2 on the other hand has generally a ten

times lower thermal conductivity than Py, thus heat accumulates within the wire and cooling would be ineffective.

Generally the heat transfer in solids is carried by the lattice- and the charge carrier thermal conductivity. In case of metals and temperatures above 25 K the dominating factor is the electrical thermal conductivity which is connected to the electrical conductivity via the Wiedemann-Franz relationship [Fra53]. A detailed discussion of the thermal conductivity of metals and alloys can be found in [Ho78]. In electrical insulators the lattice thermal conductivity via propagating phonons is the leading contribution. Especially in single crystals with a highly ordered inflexible lattice the heat transport capability is pronounced. This is also the reason why diamonds with impurities or polycrystalline CVD[1] diamonds have a significantly reduced thermal conductivity [Bar07] due to enhanced scattering of phonons. The theory of lattice thermal conductivity can be expresses by Callaway's theoretical model for an isotropic continuum phonon dispersion. A good introduction into the theory can be found in [Bar07].

We were successful in the preparation of Permalloy nanowires on single crystal diamond substrates. Direct current densities of 2×10^{12} A/m^2 were achieved with ℓN_2 cooling for hours without degradation of the sample as discussed in the following article [P6][2].

[1] Chemical Vapor Deposition (CVD) of thin diamond films from the gas phase [Koi03]

[2] It is probably interesting to note that we also tried to achieve ultrahigh current densities with copper nanowires on diamond. The possible current densities, however, were generally lower than with Py wires [Sac08] maybe due to a lower C constant in the electromigration Eq. 5.6.

Ultrahigh current densities in Permalloy nanowires on diamond

S. Hankemeier, K. Sachse, R. Frömter, and H.P. Oepen

Appl. Phys. Lett. **92**, 242503 (2008)

P6

The numbers by which citations are referenced in the following article are only valid within the article.

APPLIED PHYSICS LETTERS **92**, 242503 (2008)

Ultrahigh current densities in Permalloy nanowires on diamond

S. Hankemeier,[a] K. Sachse, Y. Stark, R. Frömter, and H. P. Oepen
Institute of Applied Physics, Hamburg University, Jungiusstraße 11, 20355 Hamburg, Germany

(Received 18 March 2008; accepted 8 May 2008; published online 17 June 2008)

To study the forces of spin polarized currents on domain walls in the microscopic scale, dc densities in the order of 10^{12} A/m^2 are required. In general, current densities of this magnitude cause a rapid destruction of metallic wires. We present a device that allows us to apply current densities of 1.5×10^{12} A/m^2 for more than an hour without degradation in the wire, using a diamond substrate as heat spreader. Annealing effects are observed and the wire temperature is measured and modeled as function of the current density. © *2008 American Institute of Physics*. [DOI: 10.1063/1.2937842]

Current induced domain wall movement for magnetization switching is a big issue in todays basic research and is discussed as a concept for storage or logic devices in the field of spintronics.[1–3] The magnetization switching via spin momentum transfer is a promising alternative for writing in "one bit/one structure devices," such as the spin momentum transfer magnetic random access memory.[3] Common to all approaches of current driven magnetization reversal is the fact that high current densities are required to provide a sufficient torque to induce switching of a defined number of spins.

In particular, the exact process of current induced domain wall movement is still under debate. Today's investigations are so far performed in a pulsed mode and the effect of the electrical current on wall displacement, wall velocity, and wall transformation are studied in retrospect.[4–6] The pulse mode is chosen to keep the load on the thin film wires as low as possible.[7] Current densities in the range of 10^{12} A/m^2 have been reported to cause displacement of a domain wall.[4] On the other hand, it would be most advantageous to study the equilibrium situation to obtain a better insight into the competing interactions. For such experiments, a static investigation is necessary. Therefore, a ferromagnetic wire with a length that is large compared to the characteristic magnetic length is needed, which has to withstand a current density in the range of 10^{12} A/m^2 for minutes.

Ultrahigh dc densities larger than 1×10^{12} A/m^2 have been put through carbon nanotubes[8] or superconducting constrictions,[9] while normal metals are generally destroyed due to heating and electromigration.[10–13] The highest dc current of 4×10^{12} A/m^2 has been applied to a Au nanoconstriction for several minutes. Hence, it is obvious that a formidable technological problem has to be solved before the experiments can be conducted. In this paper, a preparation method is introduced that overcomes most of the abovementioned problems and thus allows us to perform static experiments. In particular, ferromagnetic wires are fabricated that withstand dc densities in the range of 10^{12} A/m^2 for more than an hour.

The main problem one has to face using nonsuperconducting wires is Ohmic heating as elevated temperatures increase the effects of electromigration.[14] Thus the stability can be enhanced when the device temperature is kept low. The latter means that the system has to be attached to a heat sink and the heat has to be instantaneously dissipated through the substrate. Therefore, a substrate with a high thermal conductivity is mandatory while the material should be insulating to prevent electrical shunting. The latter conditions are best fulfilled by a diamond single crystal, as diamond is the insulating material with the highest known thermal conductivity over a wide temperature range.[15] The geometry of our test setup is as follows. Pt pads are evaporated on the (100) surface of a diamond crystal as contacts. The separation of the Pt contacts is 25 μm. A permalloy (Py, $Ni_{80}Fe_{20}$) wire is evaporated across the gap using the static nanostencil method.[16] The wire dimensions are: width of 650 nm, height of 22.5 nm, and length of 25 μm (Fig. 1). Three aluminum wires are bonded to each Pt pad, which has a similar thickness as the wire. The wires can carry currents up to 30 mA each, without any change in properties. The substrate is firmly attached to a liquid nitrogen bath cryostat that has a temperature sensor close to the diamond substrate. The experiments are performed under high vacuum conditions with a base pressure of 5×10^{-6} mbar to prevent oxidation and thus degrading in the properties of the nanowire.

After fabrication, the initial electrical resistance of the nanowire is determined. Here, we report on a wire setup with an overall resistance of 776 Ω at 300 K, including 17/3 Ω for Pt pads/bond contacts. This leaves 756 Ω as wire resistance, which is roughly three times larger than the resistance one would calculate from bulk properties of Py for this geometry[17] (red solid line in Fig. 2). On cooling to 84 K the wire resistance is determined as function of temperature. As the whole system is in thermal equilibrium (wire and cooling facility), we take the temperature that is indicated by the sensor at the cryostat as the wire temperature. From that experiment, we obtain the calibration curve in Fig. 2. The resistance has been determined via the voltage drop when applying a dc current of 0.1 mA. This procedure is applied for all the resistance measurements we will report throughout this paper. The Ohmic heating due to the latter current, which

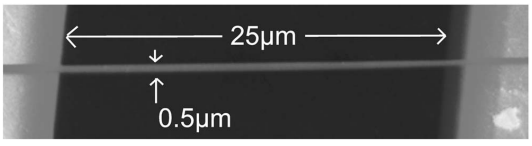

FIG. 1. SEM image of a Permalloy nanowire between platinum contact pads on a diamond substrate.

[a]Electronic mail: shankeme@physnet.uni-hamburg.de.

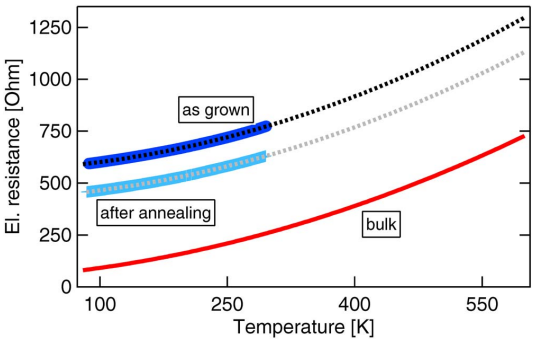

FIG. 2. (Color online) Electrical resistance of the nanowire as grown and after annealing (1.91×10^{12} A/m^2) vs temperature of the cryostat during quasi-static cooling of the system. The dotted lines show the used calibration fit for the temperature of the wire and the solid line represents bulk values for the wire geometry

corresponds to a power in the range of some microwatts, is negligibly small. From the temperature dependence we can extrapolate to the temperature range above 300 K using a parabolic dependence.[17] The obtained calibration curve is displayed as black dotted line in Fig. 2. This calibration curve is used to calculate the wire temperature when currents are applied that cause a temperature increase above room temeprature. For that estimation, it is assumed that the temperature is the same along the wire, which is a reasonable approximation according to numerical simulations of a solitary wire on the diamond substrate using COMSOL MULTIPHYSICS.[18] From the simulation, we obtain an average temperature variation of 6% within the first 5 μm of the wire, which gives in worst case an underestimation of the average temperature in the range of 2%.

When a dc current of 2.5 mA is driven through the wire, a total resistance change of 0.8% is observed, which is due to instantaneous heating. The temperature at the sensor does not show any change. Applying dc currents >7.5 mA causes a response at the sensor. While the temperature change of the wire is instantaneous and proportional to the current, the sensor exhibits a slow creeping to slightly higher temperatures. For currents exceeding 20 mA, the properties of the wire start to change. A typical measurement sequence is shown in Fig. 3(a) for a current of 25 mA. When the current is switched on, we observe a steep rise in the nanowire's resistance, which appears instantaneously within the dwell time (0.3 s) of the measurement. The temperature of the sensor increases very slowly and reaches the equilibrium within about 150 s. Contrary to the temperature evolution of the cryostat, the resistance of the wire drops when the current is kept constant. When the current is switched off, the wire resistance drops to a level lower than before. This indicates that the resistance has changed and the material quality has become better due to annealing. The annealing only takes place when the high current is applied to the wire for the first time. In Fig. 3(a) it is obvious that the resistance decrease in the wire happens within the first few minutes after the current is switched on and becomes constant thereafter. Applying a current of the same magnitude for a second time, a different behavior is found. After the instantaneous jump in resistance, a slow increase with time to an equilibrium is

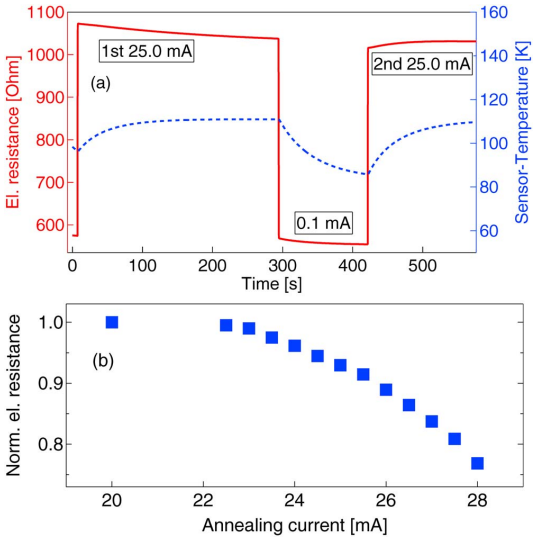

FIG. 3. (Color online) (a) Electrical resistance of the nanowire (solid) and temperature of cryostat (dotted) vs time during annealing at I=25 mA. (b) Electrical resistance at 84 K as function of peak annealing current.

time constant as the cryostat approaches its equilibrium. The latter behavior is the same as that found when applying small currents. We can therefore conclude that the annealing is completed and the base resistance is stable. Such annealing effects are again observed for any further current increase. The onset of annealing occurs for a current of 22 mA, that causes a rise in temperature beyond 400 K.

We have raised the current up to 28 mA, which corresponds to a temperature of approximately 590 K. The annealing allows the resistance to drop by 20% from 594 to 455 Ω at 84 K in accordance with Ref. 14. The change of resistance versus applied current is shown in Fig. 3(b).

After annealing for 10 min, we cooled down to 84 K and an adapted calibration curve for the annealed wire was taken (Fig. 2). The fact that both calibration curves are only shifted by a constant value with respect to the calculated bulk behavior of Py proves that the thermal dependence of the resistance is entirely determined by the Py wire, while a change in contact resistance can be excluded. A measurement with stepwise increase in the current up to 27.5 mA was performed, in which the adapted calibration curve is used to determine the average wire temperature within an error margin of 1%. The sequence is shown as an inset in Fig. 4. After every current change, the current is kept constant until the temperature at the sensor does not change anymore. At that point, thermal equilibrium is reached, which takes typically some minutes. After 20 and 27.5 mA, the current was switched to 0.1 mA to check for changes in the base resistance. The temperature drops instantaneously and falls to exactly the same value as the temperature that is given by the sensor at the cryostat. The latter indicates that the resistance of the wire has not changed during the procedure.

Utilizing atomic force microscopy and scanning electron microscopy, we have crosschecked the wire dimensions and calculated the current densities. The temperature versus cur-

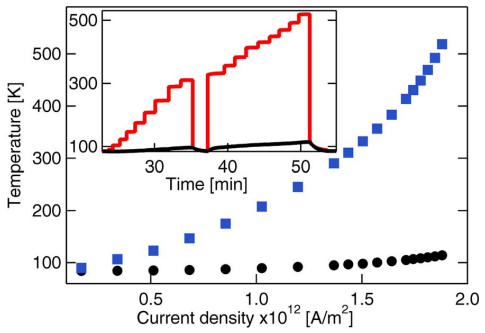

FIG. 4. (Color online) Calculated temperature of the nanowire (squares) and temperature of the cryostat (disks) in equilibrium vs current density. Inset: measurement sequence of the calculated wire (red) and sensor (black) temperature within 2.5–27.5 mA.

sities up to 1.9×10^{12} A/m^2 have been applied during that sequence for several minutes. We are not aware of any publication about comparable densities, that have been applied to ferromagnetic, metallic wires for minutes. Nonetheless, the latter current densities are in the range where domain wall movement is observed for pulsed currents. The fact that the temperature of the Py wire remains well below the Curie temperature is important to mention. The simulations mentioned before show a significant vertical temperature gradient in the wire with a steep increase at the interface and a leveling off at the surface attaining the maximum temperature of 1.3 times the average.

In conclusion, we can summarize that high current densities beyond 1.5×10^{12} A/m^2 have been applied to magnetic metallic thin film wires for more than an hour. These current densities have not caused any degradation in material properties due to electromigration or material evaporation. The essential ingredient for the realization of such stable metallic wires is the thermal coupling of the wire via a single crystal diamond substrate to a low temperature bath, which enables the extremely high current carrying capability of the wire over a large temperature and time span. Diamond appears to be a promising alternative as substrate. The surface quality of the single crystal diamond (rms roughness <1 nm) is comparable to that of standard oxidized silicon. The sample handling is equally easy if not simpler when considering the special properties of diamond, such as hardness, acid fastness, and reusability.

We gratefully acknowledge funding from "Deutsche Forschungsgemeinschaft" via "Sonderforschungsbereich 668." We thank Germar Hoffmann and Matthias Scholz for performing the atomic force microscopy measurements.

[1]R. Allenspach and P. O. Jubert, MRS Bull. **31**, 395 (2006).
[2]D. A. Allwood, G. Xiong, C. C. Faulkner, D. Atkinson, D. Petit, and R. P. Cowburn, Science **309**, 1688 (2005).
[3]S. Wolf, D. Treger, and A. Chtchelkanova, MRS Bull. **31**, 400 (2006).
[4]A. Yamaguchi, T. Ono, S. Nasu, K. Miyake, K. Mibu, and T. Shinjo, Phys. Rev. Lett. **92**, 077205 (2004).
[5]M. Kläui, P.-O. Jubert, R. Allenspach, A. Bischof, J. A. C. Bland, G. Faini, U. Rüdiger, C. A. F. Vaz, L. Vila, and C. Vouille, Phys. Rev. Lett. **95**, 026601 (2005).
[6]G. Meier, M. Bolte, R. Eiselt, B. Krüger, D.-H. Kim, and P. Fischer, Phys. Rev. Lett. **98**, 187202 (2007).
[7]M. Kläui, C. A. F. Vaz, J. A. C. Bland, W. Wernsdorfer, G. Faini, E. Cambril, L. J. Heyderman, F. Nolting, and U. Rüdiger, Phys. Rev. Lett. **94**, 106601 (2005).
[8]B. Q. Wei, R. Vajtai, and P. M. Ajayan, Appl. Phys. Lett. **79**, 1172 (2001).
[9]H. Jiang, Y. Huang, H. How, S. Zhang, C. Vittoria, A. Widom, D. B. Chrisey, J. S. Horwitz, and R. Lee, Phys. Rev. Lett. **66**, 1785 (1991).
[10]P. S. Ho and T. Kwok, Rep. Prog. Phys. **52**, 301 (1989).
[11]D. R. Strachan, D. E. Smith, D. E. Johnston, T.-H. Park, M. J. Therien, D. A. Bonnell, and A. T. Johnson, Appl. Phys. Lett. **86**, 043109 (2005).
[12]M. L. Trouwborst, S. J. van der Molen, and B. J. van Wees, J. Appl. Phys. **99**, 114316 (2006).
[13]F. O. Hadeed and C. Durkan, Appl. Phys. Lett. **91**, 123120 (2007).
[14]S. Krongelb, A. Gangulee, and G. Das, IEEE Trans. Magn. **9**, 568 (1973).
[15]S. Barman and G. P. Srivastava, J. Appl. Phys. **101**, 123507 (2007).
[16]M. M. Deshmukh, D. C. Ralph, M. Thomas, and J. Silcox, Appl. Phys. Lett. **75**, 1631 (1999).
[17]C. Y. Ho, M. W. Ackerman, K. Y. Wu, S. G. Oh, and T. N. Navill, J. Phys. Chem. Ref. Data **12**, 183 (1983).
[18]See http://www.comsol.com/ for details on the software.

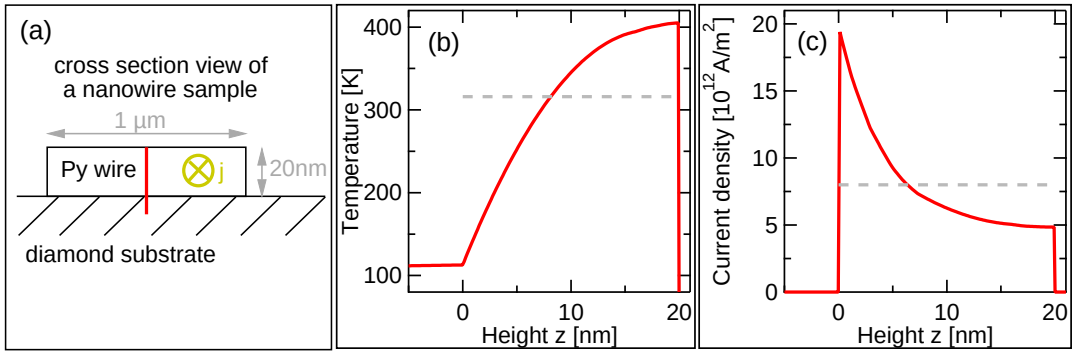

Figure 5.2.: (a) shows a sketch of the profile through a nanowire on a diamond substrate, the red line denotes the path of the line profiles shown in (b) and (c). In (b) and (c) simulated [Com10] line profiles of temperature and current density are plotted. Dotted lines denote the average values.

5.3. Temperature profile of a wire under current

The resistance measurements discussed in [P6] give the average temperature of the nanowire. Numerical simulations of Joule heating combined with a classical model of thermal conductivity utilizing a finite elements method [Com10] indicate that an inhomogeneous temperature profile and thus an inhomogeneous current density is present within the wire. Fig. 5.2 shows the results for a wire carrying a current of 8×10^{12} A/m^2 on a ℓN_2 cooled diamond substrate. The simulation has been carried out for a 20 nm thick and 1000 nm wide Py wire and included the temperature dependence of the thermal- and electrical conductivities [Ho83] of Permalloy wire and diamond. The temperature profile for the path through the wire sketched in Fig.5.2(a) is plotted in (b). The average temperature of the wire is 316 K (gray dotted line in (b)). The maximum temperature of 410 K is reached on the Py surface, while the interface between Py and diamond is at 110 K. The temperature gradient causes a strong local variation of the current density which is plotted in Fig. 5.2(c). The highest current density is reached at the interface and then decays exponentially throughout the wire. Unfortunately, the simulation does not fit the experiment very well. In [P6] an average temperature of the wire of 320 K was reached at a current density of 1.5×10^{12} A/m^2 while in the simulation the corresponding current density was five times higher. Possible reasons for the divergence of experiment and simulation are:

- A thermal resistor is present at the Py / diamond interface which was not included in the simulations. The transition from the electrical thermal conductivity in the Py to the lattice conductivity in the diamond could cause such a resistor which would effectively reduce the heat transport.

- Surface scattering effects of the electrons are not taken into account, which would effectively reduce the current flow as well as the heat flow in the interface region.

- The temperature gradient in the Py wire of 300 K over a range of 20 nm is a quite exceptional situation and results in maximum variation of 5 K per monolayer which probably stretches the bulk theory of thermal conductivity used in the simulations far over the admitted limit. A chain of coupled harmonic oscillators representing the atoms along the red line in Fig. 5.2(a) would probably be a better model.

The inconsistency between experiment and simulation shows one thing: The usual situation of a metal wire with a high thermal conductivity on-top of a low thermal conductivity substrate, giving a constant temperature within the wire and the temperature gradient in the substrate is not applicable here. Thus, recently published analytical models for the estimation of the wire temperature with- [You07] or without [You06a] thermal insulating layer (e.g. SiO_2) and approaches for the assessment of the substrate temperature gradient [Hua08] may not fit this situation. The problem of the temperature gradient of nanowires on diamond substrates needs a different theoretical approach which is out of the scope of this work. The important message, however, is that this is a novel system which exhibits surprising effects like the strong current density gradient which may result in a significant Oersted field as discussed later on.

5.4. SEMPA of a wire under current

After ultrahigh direct current densities were achieved, the next step was to image a current carrying wire via SEMPA. Fig 5.3(a) shows a SEM image of V-shaped $Co_{39}Fe_{54}Si_7$ wire with 18 nm thickness and a width of 900 nm at the kink. The wire was fabricated via evaporation through a FIB structured Si_3N_4 membrane, also called nano-stencil technique [Des99, Gro07], as lithographic methods are hardly compatible with diamond substrates[1]. The arms of the wire lead into elliptical contact pads which have a large overlap with the adjacent electrical contact pad to reduce the overall sample resistance. The V-shaped geometry was used again for the easy introduction of a domain wall via an external magnetic field.

In Fig. 5.3(b)-(e) SEMPA images of the wire under current are displayed. Unfortunately, the type of domain wall is a very uncommon zig-zag domain wall due to the large width and high thickness of the wire which favors complex domain states [Uhl09]. For a current density of 7.4×10^{11} A/m^2 a distortion of the domain pattern is visible as white area in the central part of the wire in Fig. 5.3(e). For lower current densities the distortion is hardly recognizable and a quantitative analysis is impossible due to the relatively low quality of the measurement and the unknown pinning potential for the domain wall.

The experiment shows that it is possible to magnetically image a wire under current. It also showed that there is hand full of technological as well as physical

[1] The challenge is that photo-resist usually does not stick homogenously on the diamond surface which makes a seed layer for the resist e.g. a thin titanium film necessary. Then a multi step liftoff for the removal of both the resist and the titanium is probably necessary. The development of the process, however, was out of the scope of this work due to the time consuming nature of the optimization.

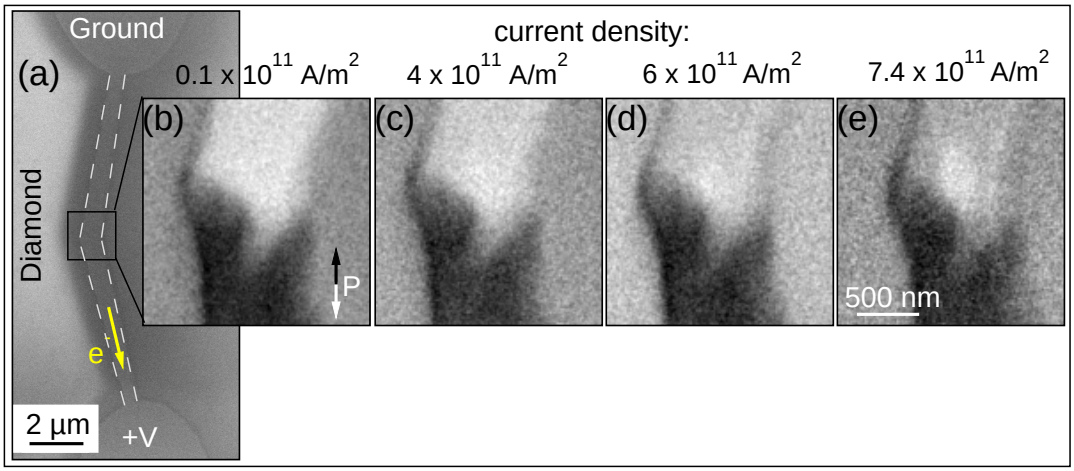

Figure 5.3.: (a) shows the SEM image of a V-shaped $Co_{39}Fe_{54}Si_7$ nanowire with elliptical contact-pads and a width of approx. 900 nm at the kink. The gray dashed lines indicate the edge of the wire. In (b)-(e) SEMPA images of the bend region under a direct current are displayed. Changes in the magnetic microstructure in the central region are visible.

challenges which have to be addressed before another approach is recommendable. The technological aspects which need a solution are:

- During evaporation of iron for contrast enhancement an electrical shunt forms which results in a dramatically reduced overall resistance of the sample after coating with ≈1 nm Fe. Thus, an applied current flows mainly through the Fe layer instead of the wire.

- We used $Co_{39}Fe_{54}Si_7$ in the experiment as Ar soft sputtering is then sufficient for a high SEMPA contrast (see section 4.4.1). During sputtering of the wire sample, which comes with simultaneous sputtering of the diamond substrate, the topmost layers of the diamond transform to a graphite like structure [Oli05, Yan07] and again an electrical shunt forms.

- The used wire was probably too wide at the bend. A smaller width in combination with lower thickness would yield a better defined vortex- or transverse wall as discussed in section 4.5 (see also Fig. 4.9) which would be better to compare to other experiments e.g. [Uhl09].

- The experiment was designed so that one electrical contact is grounded. By applying a current to the wire the other end of the wire is at a potential of e.g. 10 V. Thus, the central region of interest is at ≈5 V. The potential shift changes the transmission of the SEMPA electron optics and the optimal scattering voltage of the tungsten crystal. Each change of wire current needs a time consuming re-tuning of the spin detector during which the contrast degrades due to contamination of the surface.

- Cooling with ℓN_2 causes an image drift analogue to the effect observed during

imaging of $NdCo_5$. (Real-time) software compensation of the drift is mandatory for high quality images.

Most of the mentioned points have been solved via a re-design of parts of the experiment but the actual maintenance is not yet completed which hinders the presentation of better results.

Recently, W. Uhlig et al. conducted a similar SEMPA experiment with more success [Uhl09]. They imaged vortex- and transverse domain walls in Py wires with different widths under current. They achieved a maximum direct current density of 4×10^{11} A/m^2 on a silicon wafer substrate without cooling. At such current densities which are much lower than the usual current densities required for domain wall propagation, the walls showed current induced distortions of the domain structure. They conclude: "The observed distortions appear to be an intrinsic effect with a distinctive tilting of the wall magnetization which is independent of the pinning site. We have been able to qualitatively reproduce some of these distortions using micromagnetic simulations which include presently accepted models of spin transfer torques. A quantitative comparison was not possible because we do not know the location and strength of pinning sites in these stripes" [Uhl09]. The images they show are of high quality and they have obviously solved the technological problems mentioned above. They mention that they keep the imaging position of the wire at ground potential by tuning the potential at both ends of the wire, but they do not comment on how they solved the problem of the evolving shunt due to Fe evaporation.

Both experiments show that some physical questions have to be solved before another approach of SEMPA imaging promises to produce additional insights into the basic physics. Beside the aforementioned investigation of the strength of pinning sites and their influence on SST effects the following questions need to be addressed:

- What is the exact current density needed to move or disturb a domain wall in a Py /$Co_{39}Fe_{54}Si_7$ wire on diamond?
- What is the most promising geometry for an investigation? V-shaped, notch, curved wires...
- It was reported that different types of walls behave differently under current pulses. Some observe that vortex walls "just" move under current pulses [Yam04, Par08]. Others observe a movement and transformation of the vortex wall during the current pulse [Klä05a, Hay06, Jub06]. Transverse walls can also be moved by current pulses [Van08] while a transformation of the initial transverse wall probably due to heating was published in [Hey08a]. Furthermore, different pinning potentials for different domain wall types were observed at the same pinning site [Im09]. The pinning potential seems also to have a significant impact on the threshold current density to move a domain wall [Hey08a, Lep09b]. So, which type of domain wall is most promising for a static SEMPA investigation of the spin transfer torque effect?
- What is the exact influence of pinning sites, e.g. edge roughness of the wire, which was pointed out by previous publications [Van08, Nak03, Uhl09, Ied10]?

It was for example suggested that the field needed for depinning of a domain wall is correlated to the threshold current density [Mal10].

- How large are Oersted field effects caused by the inhomogeneous current density due to the proposed temperature gradient visible in the simulation, as even Oersted fields from adjacent wires are known to influence the depinning behavior of domain walls [Ilg08, Klä09]. Only one robust approximation of the influence of Oersted fields for the case of a spin polarized tunneling current flowing from a STM tip into a ferromagnetic sample is published [Kra07]. They estimate the Oersted field effect to be 1/10 of the SST effect.

To select a physical system which is suitable and promising for a static SEMPA investigation, to learn more about the peculiarities of the diamond sample setup and to easily access the question for the pinning sites it was decided to create a "satellite" experiment where the different wire geometries can be probed utilizing the AMR effect in an in-plane magnetic vector field. After a short comment on necessary improvements of the nanostencil technique a selected result of the investigation is presented in section 5.6.

5.5. Improved Nanostencil Technique

In [P6, Fig. 1] a straight nanowire with a width of 500 nm is shown. It is hardly visible in the SEM image that the wire is 50 nm wider in the center. The SEM image of a V-shaped wire in Fig. 5.3 shows also an unintended increase of the wire width in the bent region indicated by the gray dashed lines. The reason is that during evaporation of Permalloy the FIB-cut slot in the membrane widens due to stress induced by the additional Py film which settles on the membrane. The stress can become so strong that when the membrane rips apart under a mechanical influence, the membrane rolls up which can be seen in a SEM image displayed in Fig. 5.4(a). The bending of the membrane is prominent in case V-shaped shadow mask is used as displayed in Fig. 5.4(b): The triangle at the top side of the cut-out is only supported by one side, so when the triangle rolls up during Py evaporation a blurred wire edge is formed at the top side.

To reduce the stress which acts on the membrane during evaporation, a 100 nm thick Py film was deposited onto the membrane before FIB milling. Furthermore, parallel lines have been milled into the Py film before cutting the wire mask. A FIB image of the finished membrane mask is shown in Fig. 5.4(b). The V-shaped wire is visible as black contour while the parallel cuts have a dark grey color. A cross section of the design is shown in Fig. 5.4(c). The purpose of the Cr/Au film on the other side of the membrane is to prevent the accumulation of electrical charges during the FIB milling process. A widening of the so fabricated shadow mask during repeated evaporation of 20 nm was not observed. The wires have now a well defined edge and the masks can be reused for the successive fabrication of multiple wires. An example of a V-wire fabricated with this technique can be seen in Fig. 5.5(a).

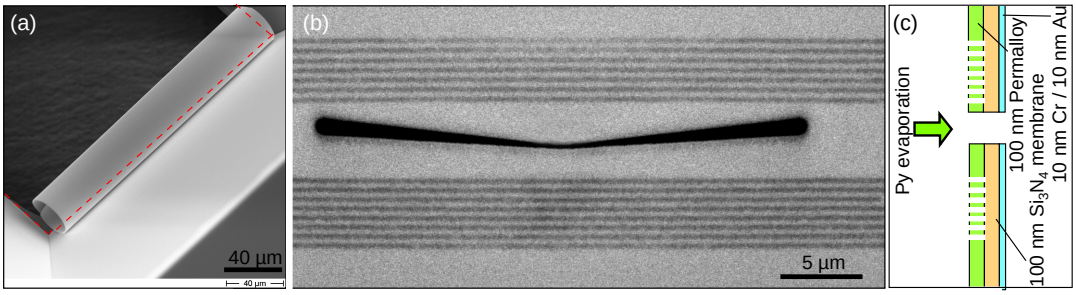

Figure 5.4.: SEM image of a rolled up Si_3N_4 membrane still attached on one side to its supporting frame (a). The red dotted line indicates the frame of the membrane. (b) shows a FIB image of Si_3N_4 shadow mask for the fabrication of a V-wire (shown by courtesy of Y. Stark). The removed V-wire geometry is black and the darker parallel lines are FIB-cuts to release stress from the membrane. The cross section in (c) shows the layer system and the cutting depth of the parallel lines.

5.6. Current supported switching processes

The basic idea of the aforementioned satellite experiment is to create and annihilate domain walls in different wire geometries via an external in-plane vector field. The overall resistance of the wire is measured during the procedure and the presence of a DW can be detected via the AMR signature. Variation of the current density changes the AMR signature due to spin torque and Oersted field effects. Furthermore, the response of the system to a variation of substrate temperature and direction of the external field can be investigated. The details of the experimental setup and a discussion of the results obtained so far can be found in the Diploma Thesis of B. Beyersdorff [Bey10]. In this chapter a selected result is highlighted with an additional interpretation of the measurements based on recent micromagnetic simulations, SEMPA measurements and a detailed discussion of Oersted field effects and the influence of pinning sites on the magnetic microstructure.

5.6.1. Wire geometry & Oersted field

A SEM image of the wire used throughout the following investigation is displayed in Fig. 5.5(a). The wire is 18 nm thick and fabricated by electron beam evaporation of the Py film through a Si_3N_4 shadow mask onto a single crystal diamond substrate. The electrical contact is realized via two Cr (10 nm) / Pt (10 nm) contact pads visible in the SEM image as lighter areas on the left and right side of the image. The electrically active part of the wire between the contact pads has a length of 20 µm. The sample fabrication procedure is identical to the method described in [P6] but with incorporation of the improved FIB milling technique for the membrane. A sketch of the wire geometry is displayed in Fig. 5.5(b). The angle between the two arms of the V-shaped wire is 170°. The wire has the smallest width at the kink with $\approx$ 350 nm and the arms have an opening angle of 2°. Thus, the current density is highest at the bend where the domain wall is located after creation by an external field. The edge roughness of the wire has maximum values of (peak-to-peak) 40 nm

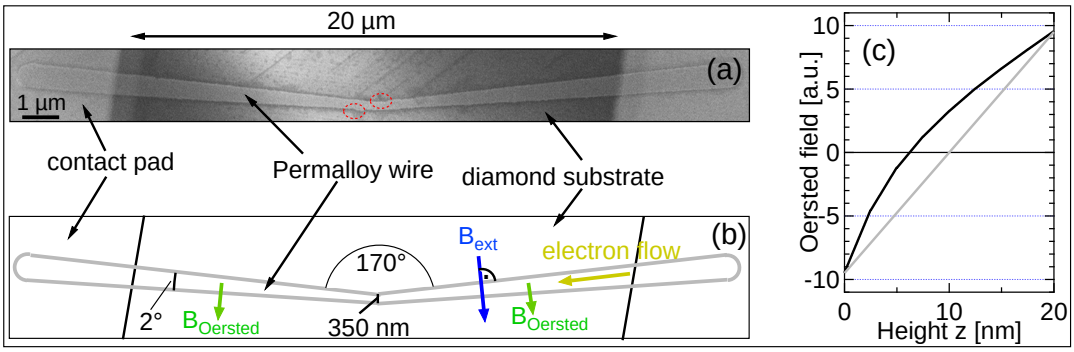

Figure 5.5.: In (a) a sketch of the experimental wire geometry is displayed. The blue arrow indicates the direction of the external magnetic field and the green arrows show the direction of the Oersted field based on the current direction indicated by the yellow arrow. A SEM micrograph of the V-shaped wire used for the following measurements is shown in (b). The Oersted field in the direction indicated by the green arrow in (a) caused by the inhomogeneous current density shown in Fig. 5.2(c) is plotted in (c) as black line. The gray line gives the Oersted field for a homogenous current density.

caused by an identical edge roughness of the shadow mask which comes from the FIB milling process[1].

All in all five samples with the geometry shown in Fig. 5.5 were fabricated from five different shadow masks. The general results of all samples are the same [Bey10]. Only slight variations between the samples were observed which are probably caused by slight edge irregularities i.e. a variation of the mask contour of the in principle identical masks.

In the following, an exemplary set of measurements from a single sample and for a fixed orientation of the external field is presented. The orientation of the external field is indicated by the blue arrow in Fig. 5.5(b). The angle between the magnetic field and the right-hand-side arm of the wire is 90°, thus the field is only able to irreversibly switch the magnetization in the left arm of the wire but not in the right.

On application of high current densities an inhomogeneous distribution throughout the cross section of the wire is expected, as discussed in chapter 5.3 thus creating an Oersted field inside the wire. The main component of the Oersted field is along the direction indicated by the green arrows in Fig. 5.5(b). The contribution of the current flowing in a layer at height z to the total Oersted field is plotted in (c). The black curve gives the Oersted field caused by the inhomogeneous current density shown in Fig 5.2(c). For comparison the gray line displays the Oersted field from a homogenous current density. In both cases the Oersted field contribution changes sign within the wire and under the assumption that the magnetic moments are interconnected throughout the 18 nm thickness of the wire, the majority of the field cancels out, but in contrast to a homogenous current density, a residual Oersted field remains which acts on the magnetization inside the wire. Considering the previous discussion about the validity of the simulated current distribution, it should

[1] At the time of membrane fabrication some problems occurred with the FIB experiment resulting in a 40 nm lateral jitter of the FIB beam.

be noted that the argumentation about the Oersted field presented here can only be of qualitative nature. It is not certain that the inhomogeneous current density is caused solely by the temperature distribution within the wire. Another possible reason could be different boundary / surface scattering of the electrons at the interface / surface which would also create an inhomogeneous current density and thus a residual Oersted field.

5.6.2. Single hysteresis loop

A single hysteresis loop implementing the before mentioned experimental situation is plotted in Fig.5.6(a). The correlating initial magnetization in remanence is shown in (b). A tail-to-tail transverse domain wall is the starting configuration for the field loop. Remember: The magnetic field is perpendicular to the right-hand-side arm, thus only the left arm will irreversibly switch during the loop. The overall form of the curve is caused by the $\cos^2$ dependence of the AMR effect as discussed in section 4.2.

We start with the remanent configuration on the black AMR curve. Increasing the field causes the magnetization in both arms to tilt out of the easy axis towards the field axis and the resistance decreases. Comparing the micromagnetic structure at 11 mT and 12 mT in (b) we see a purple "ledge" to creep from the left end of the wire to the center. The fix point of the ledge at the lower edge jumps rapidly from one pinning site to the next during the field ramp due to edge roughness. The rapid jumps of the ledge are correlated to small negative steps in the AMR signature which are marked by red dots in (a). Furthermore, we see a transformation of the initial transverse wall to the vortex wall between 11 mT and 12 mT.

During further increase of the field the vortex core shifts to the top edge of the wire and the purple ledge reaches the bend region. At ≈20 mT the ledge merges with the domain wall which is then annihilated. The process is accompanied by a large positive step in magnetoresistance marked by the blue dot. It is not only the vanishing domain wall which causes the resistance variation, but large areas near the wire edge switch simultaneously as they are no longer stabilized by the domain wall. On further increase of the magnetic field the magnetization aligns with the field direction via continuous rotation and exhibits a $\cos^2$-signature according to Eq. 4.4.

During relaxation of the field the signature of continuous rotation is visible again (gray line, right side). The remanent state is plotted in (b) ($B_{\mathrm{ext}} = 0$ mT). The magnetization in both arms points to the right-hand side and is aligned along the main axis of the arms. The absence of a domain wall is also apparent in the AMR measurement. The gray curve has a 0.2 Ω higher resistance in remanence as the black one due to the AMR signal of the domain wall itself.

During increase of the field into the opposite direction a similar situation is observed: A green ledge moves towards the bend region from the left end of the wire. Then, at ≈-25 mT the edge region of the left are switches when the green area reaches the kink accompanied by a jump in electrical resistance (blue dot on left side in (a)). A following relaxation of the magnetic field yields the initial magnetic configuration with a transverse domain wall in remanence.

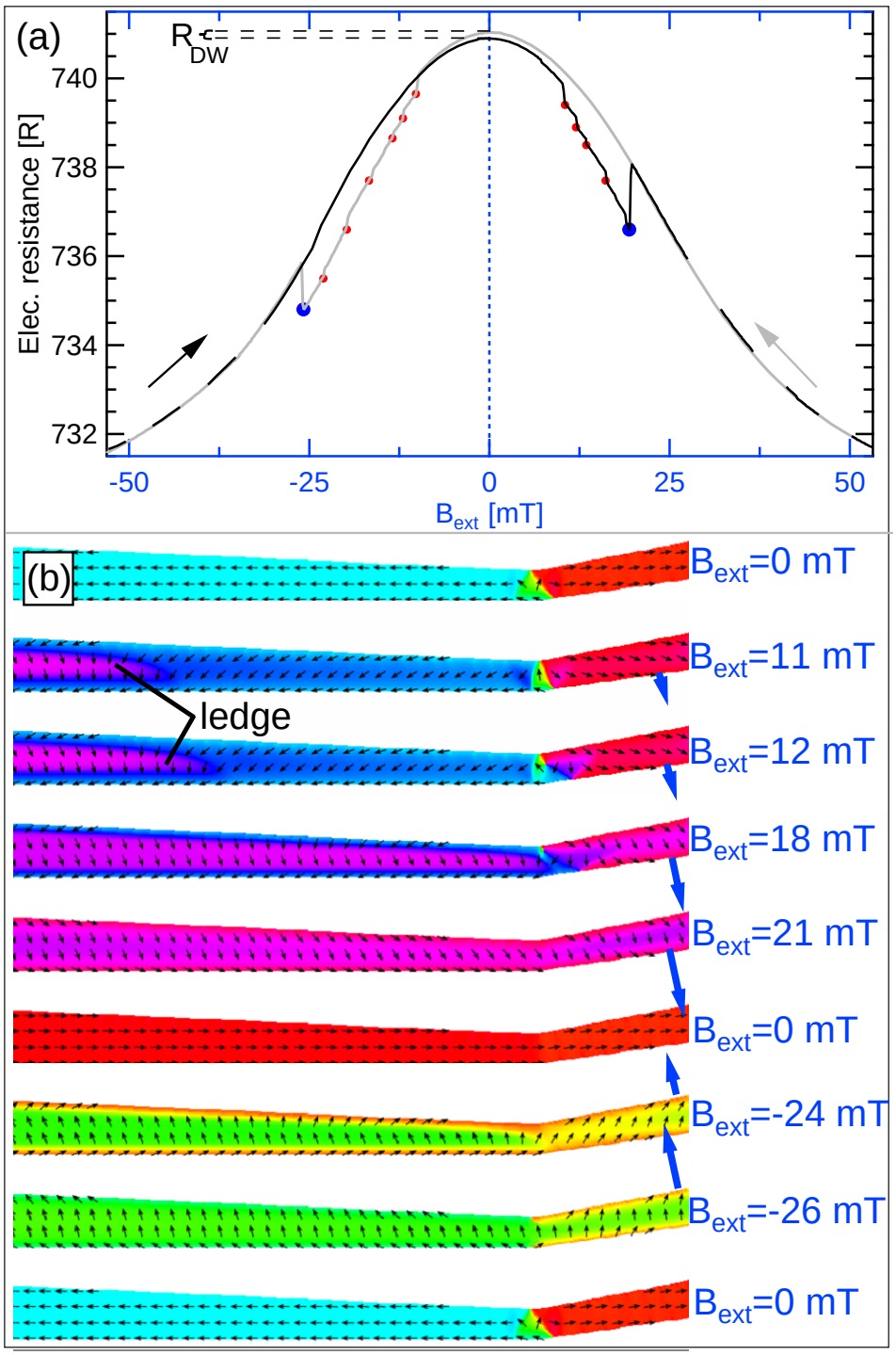

Figure 5.6.: A single AMR-hysteresis of the V-shaped wire is plotted in (a). The black and gray arrows indicate the ramp direction of the field. Blue and red circles mark steps in the resistance which are important for the following discussion. In (b) the correlating magnetic microstructures according to micromagnetic simulations is shown. The direction and strength of the magnetic field are indicated by blue arrows.

The fact that in the remanent state a transverse wall remains is a bit surprising as the phase diagram in Fig. 4.9 suggests that a vortex wall is energetically more favorable. The explicit simulation of the V-wire structure gives also a 5 % lower total energy of the vortex wall with $E_{\mathrm{VW}} = 1.67 \times 10^{-16}$ J and $E_{\mathrm{TW}} = 1.76 \times 10^{-16}$ J. The uniform decrease of the magnetic field during the loops probably prevents the nucleation of the vortex core and the transverse wall remains. The failed nucleation of the vortex core in the simulation could also be due to neglecting temperature effects. To check this point, a hysteresis loop according to Fig. 5.6 was applied to a V-wire with the same geometry as in Fig. 5.5 followed by SEMPA imaging of the wire. Fig. 5.7 shows the sum image of the wire (a) and the magnetization map in (b). The measurement confirms the simulation, a transverse wall is visible at the bend in the remanent state.

Coming back to the hysteresis loop of Fig. 5.6(a). The measurement shows that the magnetic switching of the left arm marked by the two blue dots happens not at the same absolute field value. For positive fields the arm switches at 20 mT while with a negative field 25 mT are necessary. Thus, it is "easier" to push the vortex core out of the wire, i.e. to annihilate the domain wall, than to create the domain wall during the backward field ramp. The asymmetry of switching fields is confirmed by the simulations with nearly the exact values (see Fig. 5.6).

A feature which is observed in the measurements and not in the simulation of a wire with perfect edges are the negative jumps in resistance marked by the red dots. We assume that they are caused by the edge roughness of the wire. According to the simulations of a wire with perfect edges, the purple ledge moves continuously towards the bend during the field ramp. The real wire in contrast has a irregular saw-tooth like edge with a maximum peak-to-peak distance of 40 nm (see Fig.5.7(a)). The small notches act as pinning sites for the apex of the purple ledge which leaps from one notch to the other during the field ramp thus creating steps in resistance. These resistance steps have the same reproducible position in repeated hysteresis loops. Recently, the AMR measurement was repeated with a wire with smaller edge roughness (peak-to-peak < 5 nm). Here the curve is totally smooth except for the switching of the whole arm (blue dots) and no resistance steps (red dots) are visible [Röß10]. Due to the reproducible manner of the steps they are included into the following data analysis of temperature and spin transfer torque effects and it will be shown that their positions indicate a longitudinal temperature distribution throughout the wire.

5.6.3. Temperature variation

The blue and red solid dots which indicate features of the AMR signature in Fig.5.6(a) are utilized in the following to visualize the variation of the AMR hysteresis with changing measurement parameters. First, the influence of the substrate temperature is investigated. Fig. 5.8 shows the position i.e. the field value of the dots versus substrate temperature. Each vertical slice through the graph represents a single AMR loop at a different temperature. Red dots mark negative jumps in resistance blue dots mark positive steps, respectively. The dot area corresponds to the magnitude of the resistance jump as indicated by the legend. The general trend for all

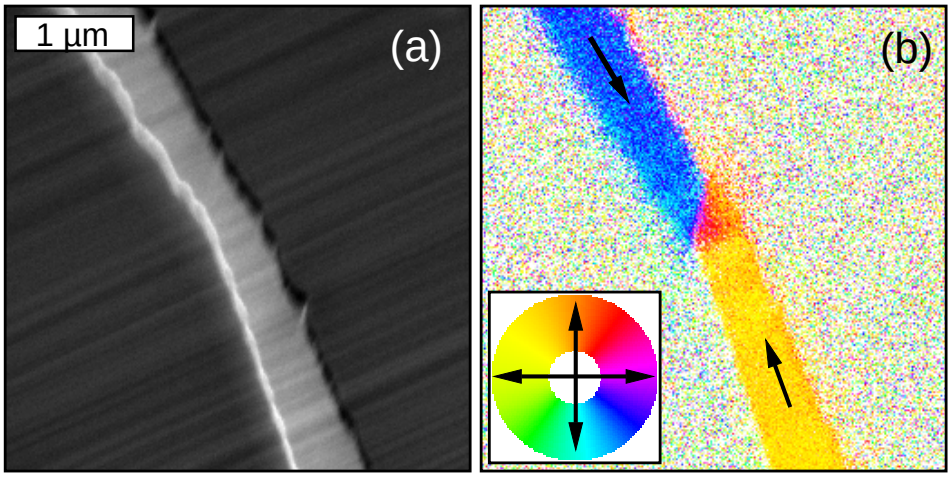

Figure 5.7.: SEMPA image of a V-shaped wire with the geometry of Fig. 5.5 after a hysteresis as shown in Fig. 5.6(a). In (a) the sum image is plotted and (b) shows the magnetization map according to the color wheel. A transverse wall is visible as remanent state in accordance to the results of the simulations shown in Fig. 5.6(b)

points is a decrease of the switching field with increased temperatures in accordance to previous findings, as thermal excitation in general supports depinning processes [Him05, Dag07, Len08].

The blue dots i.e. the annihilation of the domain wall in case of positive fields and the nucleation in case of negative fields have been fitted (blue dotted line) according to the Kurkijärvi model [Kur72] with:

$$H(T) = H_0 \cdot \left(1 - \left(\frac{k_B T}{E} \cdot ln\left[\frac{\Gamma_0 k_B H_0 T}{1.5\nu E_0 \sqrt{1 - H/H_0}}\right]\right)^{2/3}\right) \tag{5.7}$$

Here, H_0 and E_0 are free fit parameter, Γ_0 is the so called attempt frequency, ν is the field ramp rate set to 0.84 mT/sec and H/H_0 was set to 0.8 [1]. The model describes the physical situation of a particle in a potential well which "tries" to escape at a certain frequency Γ_0 assuming an escape probability which is correlated to H. The model was originally developed for phase slip events occurring in Josephson junctions and first employed to describe the temperature dependence of the escape field of a domain wall from a potential well in 1994 [Gun94, Gar95]. The domain wall is treated as quasi particle trapped in a parabolic potential well which is altered by temperature and the external field in this model. A good review of the theory and of the following application for depinning processes of domain walls can be found in [Lok99].

For the fit procedure a $\Gamma_0 = 10^{10}$ sec^{-1} was assumed according to [Len08]. A variation of Γ_0 between $10^8 - 10^{12}$ sec^{-1} did not produce a significant variation of

[1] H/H_0 does not change dramatically in the studied temperature range. Thus, neglecting the magnetic field dependence in the denominator of the logarithmic term does not introduce a significant error as discussed in [Lok99]

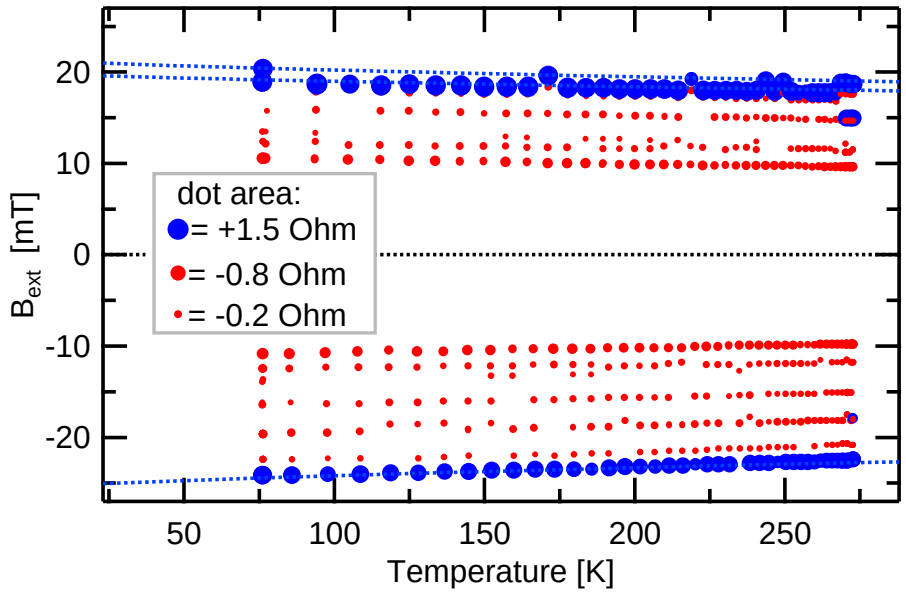

Figure 5.8.: Positive and negative steps indicated by blue and red dots from single hysteresis loops vs. sample temperature. The area-size of the markers corresponds to the step high.

the results as also observed in [Him05]. The two fits for positive fields (two parallel dotted lines) have been introduced due to the fact that some of the blue dots are slightly increased. The reason is probably the existence of two different pinning sites for the domain wall near the bend of the wire which are visible in the SEM image and additionally marked with red circles in Fig. 5.5. The domain wall stochastically nucleates at the one or the other position both with different pinning strengths.

The fitting procedure yields for the switching field at zero temperature $H_0(1) = 21.4$ mT, $H_0(2) = 19.9$ mT and $H_0(3) = -25.6$ mT. For ≈500 nm wide Py wires the literature reports values for H_0 of 3.5 mT[Ilg08], 11 mT[Him05] and 24 mT[Len08]. The barrier height at zero Kelvin is expressed by E_0. The fit procedure gives: $E_0(1) = 2.07 \times 10^{-18}$ J, $E_0(2) = 2.5 \times 10^{-18}$ J and $E_0(3) = 2.14 \times 10^{-18}$ J. The aforementioned Py wires yielded $E_0 = 1.1 \times 10^{-19}$ J [Ilg08], $E_0 = 4.3 \times 10^{-19}$ J [Him05] and $E_0 = 3.2 \times 10^{-20}$ J [Len08]. The calculated values for the switching field H_0 fit very well the literature values, the height of the energy barrier, however, is roughly one order of magnitude larger as published. This may be caused by the fact that usually a domain wall moves away from the notch towards the end of a wire during annihilation. In case of V-shaped wires with the field geometry as shown in Fig. 5.6 the domain wall stays at its place during the field loop and is finally annihilated by the purple ledge. This process may have a deeper pinning potential as the common case of domain wall depinning by domain wall movement and would explain the discrepancy between literature and the result of our investigation

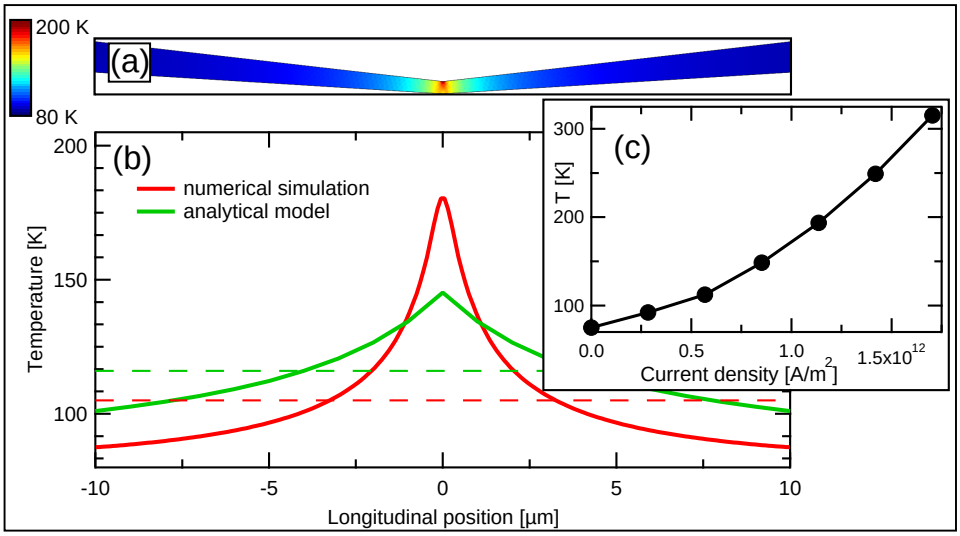

Figure 5.9.: Temperature map of a V-shaped nanowire as indicated by simulations of a metallic wire subject to Joule heating (a). The current density is 6.5×10^{11} A/m^2 at the kink. The longitudinal temperature profile is plotted as red curve in (b). The green curve shows the longitudinal temperature according to an analytical model [Kim08]. The dashed lines indicate the correlating average temperatures. (c) shows a measurement of the average wire temperature versus current density as determined from the resistance measurement.

5.6.4. Longitudinal temperature gradient

In the last chapter, the substrate temperature was varied accompanied by a homogenous temperature throughout the wire. If the wire is subject to Joule heating, an inhomogeneous temperature distribution is expected: On one hand there is the temperature variation in height as discussed in section 5.3, on the other hand the tapered wire geometry causes a longitudinal temperature gradient. The highest temperature will be at the bend where the cross section is smallest in the current density maximum.

Fig. 5.9 shows a simulated temperature map (top view) of the wire in (a) and the associated longitudinal temperature distribution in (b) (red curve). The simulation was carried out with Comsol multiphysics in analogy to section 5.6.1. The simulated current density is 6.5×10^{11} A/m^2. The green curve in (b) shows the result of an analytical model to calculate an average wire temperature of a joule heated metallic wire on a low thermal conductivity substrate considering only perpendicular heat flow [Kim08]. For current densities $> 8 \times 10^{11}$ A/m^2 the simulation no longer converges due to the highly nonlinear character of the problem: With increasing temperature due to Joule heating, the thermal and electrical conductivity of the wire rapidly decrease. A lower electrical conductivity causes more heating, resulting in a lower thermal conductivity and it is difficult for the algorithm to find the equilibrium state.

The strong dependence of the diamond thermal conductivity and the wire proper-

ties on temperature variation is the reason for the pronounced temperature peak at the bend. All other wire positions exhibit more favorable conditions for heat transport due to the lower temperature. As the analytical model only considerers average values of the physical properties, the curve is smoother compared to the simulation. The dotted lines in (b) indicate the average temperature of the wire calculated from the longitudinal temperature profile. The inset (c) shows a graph of the experimentally obtained average temperature of the wire versus current density. The average temperature was determined from the overall electrical resistance which was calibrated with the measured resistance versus substrate temperature dependence. At a current density of 5.7×10^{11} A/m^2 the average wire temperature is 112 K while the simulation gives 105 K for 6.5×10^{11} A/m^2. Reasons for the discrepancy are the same as in section 5.6.1, again the simulation can only give an approximation. The average temperature of 315 K at a current density of 1.7×10^{12} A/m^2 at the bend should be noted, it is much lower compared to a straight wire [P6, Fig. 4] due to tapered geometry of the V-wire configuration.

5.6.5. Variation of current density

In the same manner in which the temperature was varied in section 5.6.3 now the influence of an increasing current density is investigated. Fig. 5.10(a) shows the switching field indicated by blue and red dots versus current density for the geometrical situation described in Fig. 5.6. The dot size is again correlated to the step height of the resistance. Four eye catching features are visible in the graph. First, a parabolic dependence of the blue dots at positive fields. Second, an abrupt decrease of switching field (blue dots in the first quadrant). Third, the red dots show an increasing parabolic behavior with increasing switching field. Fourth, the blue dots at negative fields show a linear signature.

The reason for the individual characteristics is discussed in the following by number. The parabolic behavior of the blue positive dots can be explained by temperature effects. They describe the annihilation of the domain wall and again two slopes marked by the blue dotted lines are visible as in Fig. 5.8 due to two pinning sites near the kink. The reason for the parabolic dependence is that the wire temperature is roughly proportional to the inserted heating power P which is $P = R \cdot I^2 \propto T_{\mathrm{wire}}$. The link between wire temperature and switching field is known from Fig. 5.8 which can be approximated via a linear slope and thus gives the two parabolic fits marked with blue dotted lines. Each switching field at each current density can be now be correlated to a temperature. For the maximum current density and the blue dot marked by the black circle gives for example a temperature of ≈ 460 K from extrapolating the curve in Fig. 5.8 at the position where the domain wall is depinned, i.e. at the kink. The value agrees fairly well with the temperature of a straight wire of 450 K at 1.7×10^{12} A/m^2 as presented in [P6, Fig. 4] and is also in accordance with the average wire temperature of 312 K at this current density (see Fig. 5.9(c)).

The next interesting feature is the abrupt decrease of the positive switching field (blue dots at positive field) at a current density of $\approx +1.2 \times 10^{12}$ A/m^2. After the abrupt decrease a linear decline is visible marked by gray dotted lines which act as a guide to the eyes. The feature is only visible for positive current densities and

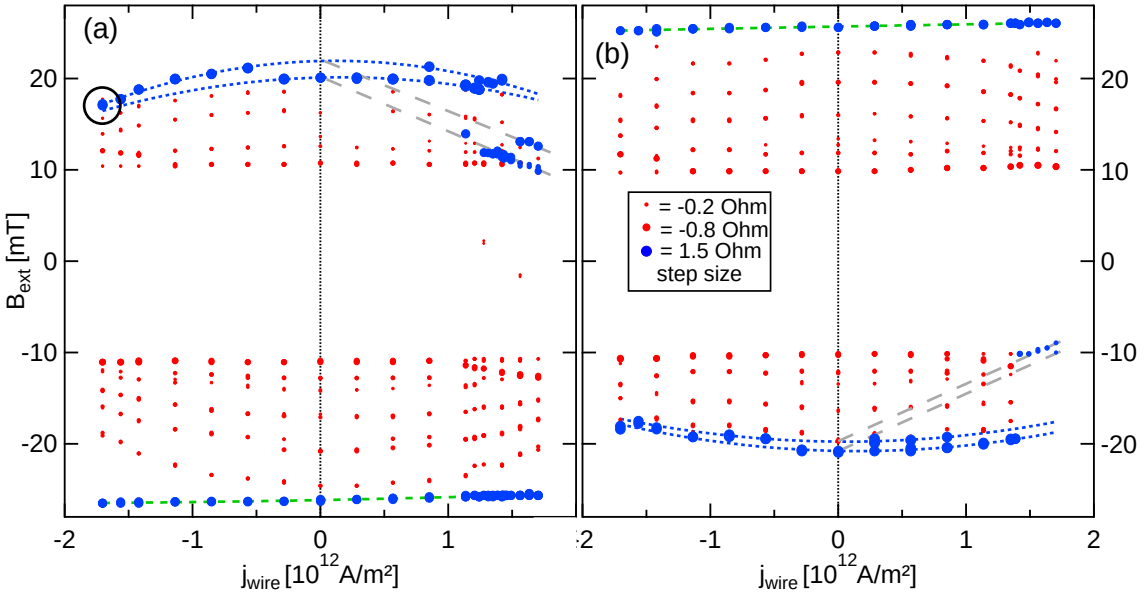

Figure 5.10.: Positive and negative steps from single hysteresis loops vs. current density. In (a) the result for the configuration shown in Fig. 5.6 is plotted. (b) presents the control experiment where the magnetization of the right-hand-side arm is irreversibly switched and the measurement repeated.

can therefore not be attributed to Oersted field effects which would be in a first approximation proportional to the current density and switch sign with the current density. A possible explanation is the spin transfer torque effect which supports the depinning process. But two questions remain: First, why is a threshold current density necessary to observe the effect? The inset of the abrupt decrease happens exactly at the field value ($\approx$ 12 mT) where the simulation shows the transition of the domain wall from the transverse configuration to the vortex wall. Thus, under the assumption that the spin torque acts in this special case only on the vortex wall the abrupt inset of SST effects can be explained. The transverse wall is maybe stabilized by the external field which hinders a current supported depinning of the wall and not until the wall transforms into a vortex wall SST effect can be observed. Second, why is no effect visible for negative current densities? The experimental conditions probe the switching of the left arm of the V-shaped wire (see Fig. 5.6). Thus, when the wall is pushed towards the other arm via a negative current, the switching of the right arm would be supported. The experiment, however, is only sensitive to a switching of left arm thus no SST effect can be observed.

The red dots mark negative steps in resistance during the AMR loop and indicate the stepwise movement of the magnetic ledge (see Fig. 5.6(b)) between pinning sites caused by edge roughness. In Fig. 5.10 they exhibit an increasing parabolic behavior with increasing absolute value of the switching field. Again temperature effects due to Joule heating are responsible for the parabolic dependence. The increasing parabolic dependence can be explained by the fact that the first red dot at $\approx$ 10 mT is furthest away from the kink where the heating is lowest in accordance

to a nearly vanishing parabolic signature. When the ledge moves further towards the kink during the AMR loop the temperature increases as can be seen in Fig. 5.9 and an increasing parabolic dependence of the depinning process is observed.

The blue dots on the lower side of the x-axis show a linear dependence with variation of current density indicated by the green dotted line. The linear fit has a slope of $+0.28\frac{\mathrm{mT}}{1\times10^{12}\mathrm{A/m^2}}$ in (a) and $+0.25\frac{\mathrm{mT}}{1\times10^{12}\mathrm{A/m^2}}$ in (b), respectively. The cause for this signature is probably an Oersted field which is in-plane and perpendicular to the wire axis as shown in Fig. 5.5 caused by an inhomogeneous current density throughout the cross section of the wire. An Oersted field would be proportional to the current density. For positive currents the switching process would be supported and for negative restrained as observed in the measurement shown in Fig. 5.10(a). The assumption of an Oersted field is also supported by the control experiment shown in Fig. 5.10(b). Here the initial magnetization of the right-hand-side arm was reversed and the whole experiment repeated. The same four features as in (a) are visible in (b), partly reversed due to the symmetry of the setup and most of the features are mirrored at the x-axis: Nucleation and annihilation of the domain wall switch places and the SST still effects only the annihilation of the domain wall at positive currents. The Oersted field signature (green dotted line) shows the same slope due to the fact that current direction and direction of the external magnetic field were not changed and now the Oersted field hinders the nucleation of a domain wall for a positive current. The control experiment confirms all previously drawn conclusions and completes the explanation of the effects found in Fig. 5.10.

5.7. Summary & Outlook

Ultrahigh current densities in nanowires were realized in the static mode for hours without degradation of the wire properties. The nanostencil method for wire preparation was improved to produce smaller wires with constriction as well as to allow a multiple use of the shadow masks. SEMPA imaging of a wire under current was demonstrated and compared with a similar recently published experiment [Uhl09]. The technological and physical challenges of such an experiment were discussed in view of a better general understanding of SST effects with the LLG (Eq.5.1-5.3) as theoretical basis. To facilitate the choice of an adequate physical system for a promising SEMPA investigation a satellite experiment was designed to probe the magnetic state of a nanowire via magnetotransport measurements in an external vector field. The field and current supported switching of a V-shaped wire geometry was investigated. A significant influence of edge roughness on the switching process was pointed out in accordance to [Bry04]. The AMR signature in combination with SEMPA measurements, symmetry considerations and comparative OOMMF simulations yielded an understanding of the evolution of the magnetic microstructure during the field assisted switching process. Temperature effects and a variation of current density were investigated with the result that it was possible to separate Oersted field- , spin transfer torque- and temperature effects in the switching behavior of the wire.

Based on our experience with static currents and the common experimental diffi-

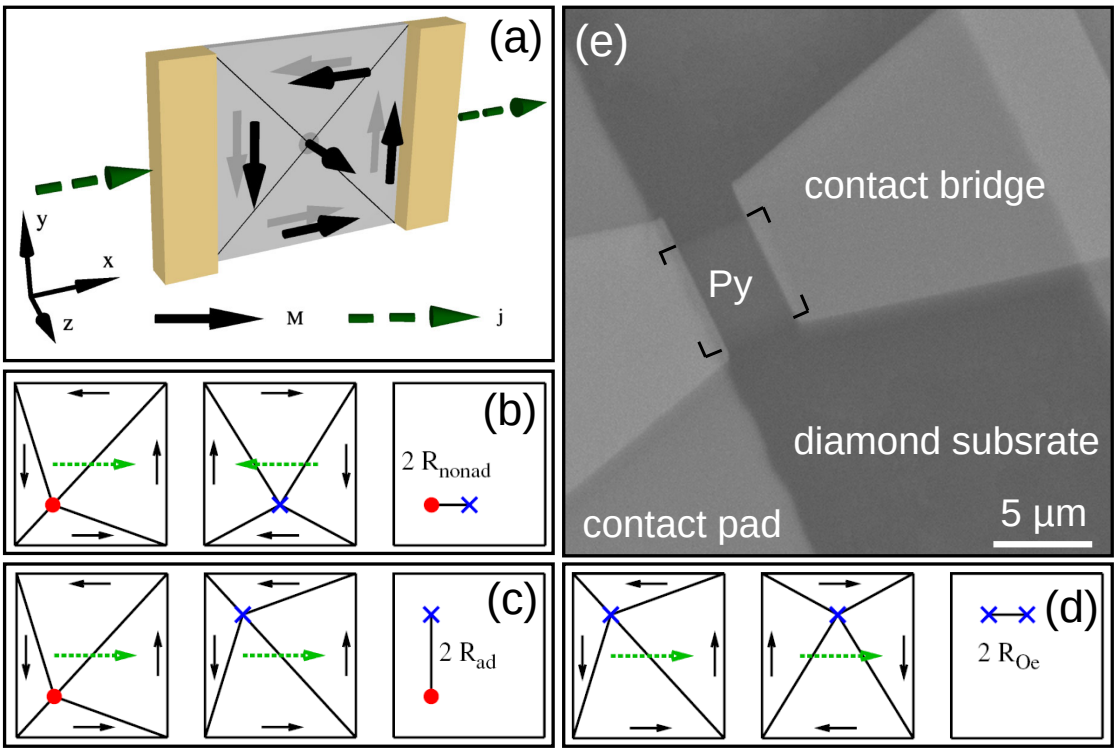

Figure 5.11.: (a) Proposed experiment geometry of a 5 x 5 µm^2 Py square with 10 nm thickness (gray) and current contacts (yellow). (b)-(d) Scheme for the determination of the three different contributions to the vortex displacement according to [Krü10]. (a)-(d) reprinted from [Krü10], copyright (2010) by APS. By measuring the distances between the positions of two different vortices it is possible to separate the displacements (b) due to the nonadiabatic spin torque, (c) the adiabatic spin torque, and (d) the Oersted field. Points and crosses denote cores with positive and negative polarization, respectively. The in-plane magnetization is denoted by the solid arrows. The dashed green arrows denote the current direction. For the sake of illustration the displacements are exaggerated. A SEM image of the technical realization of the proposed experiment on a diamond substrate is shown in (e) by courtesy of S. Rößler. The Py square is emphasized by the black lines marking the corners.

culties to determine the degree of non-adiabaticity β in the Landau-Liftshitz-Gilbert equation, our colleagues B. Krüger et al. within "Sonderforschungsbereich 668" developed and published a "Proposal of a Robust Measurement Scheme for the Nonadiabatic Spin Torque Using the Displacement of Magnetic Vortices" [Krü10]. Fig. 5.11(a) illustrates the proposed experimental setup: A direct current flows through a 5 x 5 µm^2 and 10 nm thick Permalloy square in the vortex state. Adiabatic-, Non-adiabatic spin torque and Oersted field effects cause the vortex to shift into different directions as displayed in Fig. 5.11(b)-(d). Six successive measurements via e.g. SEMPA of the vortex displacement after permutation of current direction, core polarity and sense of rotation of the vortex as indicated in Fig. 5.11(b)-(d) yield R_{ad}, R_{nonad} and R_{Oe}. From these values β can be calculated as presented in [Krü10]. The theory expects with a current density of 1.5×10^{12} A/m^2 values in the range of $2 \cdot R_{\mathrm{ad}} = 1100$ nm and $2 \cdot R_{\mathrm{nonad}} = 20$ nm which is accessible with SEMPA. Recently, it was possible to fabricate such a Permalloy rectangle on diamond and to contact it utilizing contact bridges and an adjacent contact pad via a three step nanostencil process. In Fig. 5.11(e) a SEM image of such a structure is displayed which is currently characterized via AMR in a magnetic vector field by S. Rößler as one topic of his diploma thesis. In a second step it is planned to measure such a sample in the SEMPA experiment which promises to shed some light on the exact value of β.

6. Conclusion

In this thesis the magnetic fine structure of different thin-film systems was investigated via SEMPA and magnetotransport measurements, supported by micromagnetic simulations. The scope of the thesis covers a wide area of physical topics: The characteristics and long time stability of our optimized LEED detector for imaging, as well as a discussion of the improvements to the experiments in chapter two. Chapter three deals with a SEMPA investigation of the temperature driven spin-reorientation transition in $NdCo_5$ thin films. In chapter four a discussion of the magnetic fine structure of Py rectangles is given, followed by an investigation of the predominant type of domain wall found in magnetic nanowires. The last chapter discusses current supported depinning processes of domain walls in aforementioned nanowires.

In particular, several interesting and surprising results were obtained: The characteristics of our newly designed scanning electron microscope with polarization analysis for the acquisition of magnetic images are presented in [P1]. The instrument has been optimized with respect to ease of handling and efficiency and the performance of the LEED detector has been modeled in order to find the optimum operating parameters and to predict the obtainable image asymmetry. We demonstrate experimentally 8.6 % polarization asymmetry in the domain structure of an iron whisker, which corresponds to an image contrast of 17.2 %, in good agreement with the predicted value of the model. A contrast to noise ratio (CNR) of 27 is achieved at 5 ms acquisition time per pixel. The long time stability of the LEED detector is then in the focus: Starting with a clean analyzer crystal, intensity variations of the (2,0) beams are observed. They are explained by a peak shift of the intensity curves due to hydrogen contamination of the tungsten detector crystal [P2]. The intensity variation and peak shift are shown to have only a slight influence on the obtainable image asymmetry within the first 60 minutes after flash cleaning, thus flash cleaning once an hour is sufficient during measurements sessions.

The optimum parameters for sample preparation in order to obtain high quality SEMPA measurements via iron dusting and mild argon-ion sputtering are discussed, together with calibration measurements of the newly designed cryostat component.

The experiment can even be further improved: For the next refit of the vacuum chamber it is planned to mount the sputter gun and the Fe / Co evaporators on a flange which has direct access to the sample without need of moving it during a SEMPA measurement, thus allowing e.g. sample preparation of cooled samples or spin-SEM assisted Fe-dusting. A new data acquisition software which allows variable aspect ratios and drift correction of the images is under development by F. Lofink. A time resolving approach with SEMPA is also on the agenda [Str] which would allow us to image triggered recurring magnetization dynamics like e.g. in [Bol08]. The polarization detection process itself is probably already at the achievable limit

of optimization. Thus to gain a higher image quality ($\propto N \cdot S^2$) which is limited by the Poisson statistics, only the intensity of the primary SEM electron beam can be increased. New, commercially available SEM columns for example reach beam intensities of > 100 nA with high lateral resolution (1.6 nm / 1 kV) [Hit10a] instead of 5 nA [P1].

The newly designed electronics for easier tuning of the experiment and the cryostat permitted a SEMPA investigation of the temperature driven spin-reorientation transition in $NdCo_5$. The evolution of the domain pattern was imaged and a quantitative analysis of the data yielded the temperature dependence of the ratio of the anisotropy constants K_1/K_2. The opportunity for the investigation of such medium anisotropy films is the result of a fruitful cooperation with the Group of R. Schäfer at IFW Dresden from which M. Seifert fabricated the $NdCo_5$ thin films. At present, M. Seifert is performing micromagnetic simulations to reproduce the observed domain pattern in order to solve and quantify the open questions that have arisen from the SEMPA domain images discussed in section 3.9.

The main part of the thesis deals with the magnetic fine structure of patterned soft-magnetic elements. It begins with the investigation of Permalloy rectangles with dimensions to mimic standard problem #1. It was found that the Landau state in such rectangles consists of six instead of four domains, as two of the four expected domains split. The splitting was quantified via the splitting angle, which was found to depend on the exact shape of the rectangle's edges [P3]. Furthermore, the splitting angle is strongly influenced by magnetostatic coupling in an array of such structures. At present, K. Lebecki and coworkers are conducting sophisticated micromagnetic simulations with periodic boundary conditions to quantify the influence of magnetostatic coupling in the arrays.

The magnetization behavior of single rectangles was investigated via magnetotransport measurements supported by SEMPA imaging [P4]. It was possible to derive the firstorder anisotropy constant for individual rectangles from the coherent rotation curves obtained via AMR measurements for the case the rectangles exhibit a Landau or C-/S-state in remanence. A statistical SEMPA investigation of over 600 rectangles yielded the information about the remanent state in case of different magnetic histories. This knowledge gave the necessary hint for the micromagnetic understanding of the AMR curves.

The AMR investigations of single rectangles is continuing: H. Spahr and A. Kobs are at present investigating the influence of magnetostatic coupling on the firstorder anisotropy constants of single rectangles, thus connecting the findings of [P3] and [P4].

In the last part of the thesis V-shaped nanowires were analyzed. The predominant type of domain wall in dependence of wire geometry and initial conditions for the seeding of domain walls was here in the focus of interest. It was shown that the sense of rotation of the vortex wall and its position with respect to the bend are interconnected and both can be tuned by the exact orientation of an external seeding field. The reason for this behavior is the symmetry breaking of the geometry by the external field in combination with topological considerations as discussed in [P5].

The question for the ground state of a domain wall, i.e. is the vortex wall or transverse wall the state of lowest energy, in dependence of the wire geometry is

discussed in the following section 4.5. The influence of wire width and thickness is recapitulated as it is already known from [McM97, Nak05, Klä08]; the influence of the bending angle, however, was not yet addressed in literature. Thus, it is discussed in the subsequent section: It is shown that the bending angle has a strong impact on the predominant domain wall configuration: Almost straight wires favor the vortex wall, while for small bending angles the transverse wall becomes the state of lowest energy. At an angle where both configurations are nearly equal in energy, a third wall type is observed in the SEMPA measurements: The asymmetric transverse wall (ATW). The occurrence and geometrical properties of the ATW are explained and discussed in the context of [P5] and compared to the literature where a similar micromagnetic configuration is discussed from a topological point of view (see Fig. 4.12). The tilting direction of the ATW is sensitive to the exact orientation of the seeding field in analogy to the seeding of vortex walls.

The findings about the predominant domain wall configuration in V-shaped nanowires and the tunability via external fields have direct consequences for applications. It is now feasible to deliberately seed certain types of vortex walls into nanowires and utilize the additional degree of freedom, i.e. the sense of rotation, for the investigation of future memory concepts [Boh08].

Chapter five deals with the manipulation of domain walls in nanowires via an external field supported by a static direct current. The development of a sample setup that sustains the necessary ultra-high current densities in nanowires without degradation is presented in [P6]. SEMPA images of a nanowire with a domain wall that is transformed by an electrical current are presented in section 5.4. A quantitative analysis of the results, however, is difficult as discussed in the context of a similar experimental approach [Uhl09]. To gain a deeper insight into the physical basics of our special sample system and to select a suitable sample design for a SEMPA investigation, a satellite magnetotransport experiment was established for the fast characterization of different geometries. The anisotropic magnetoresistance is here utilized to study the depinning behavior of the domain wall in e.g. a V-shaped nanowire. A selected result is presented where it was possible to understand the complete micromagnetic switching process from the analysis of multiple AMR hysteresis loops at different current densities and temperatures, supported by micromagnetic simulations and SEMPA measurements. The insight into the complete switching process gave the possibility to separate the influence of temperature, Oersted-field and spin-torque-effects which act on the depenning process of the domain wall.

S. Rößler continues the work with static direct currents and first promising results for the realization of the proposed robust measurement scheme for the degree of non-adiabaticity [Krü10] were presented.

I am happy to continue the exciting work in this group for an additional year and look forward to contribute in finding new interesting results in the variety of fields and ongoing investigations mentioned throughout this thesis [Que91].

A. Circuit diagram

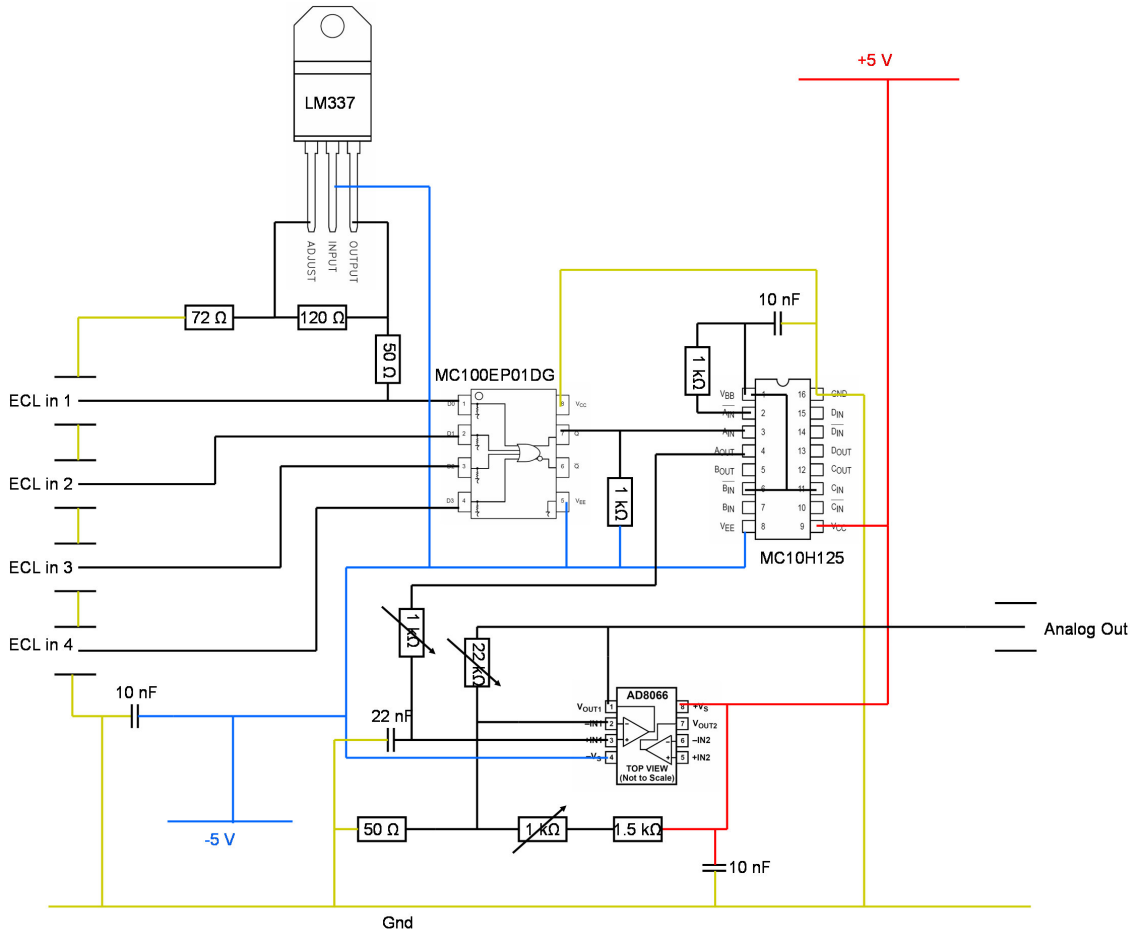

Figure A.1.: Circuit diagram for the self-developed electronics for adding up the signal outputs of the four ECL preamplifier pulses and the conversion of the count rates into a real-time analog signal.

Bibliography

[Aha96] A. Aharoni, *Introduction to the theory of ferromagnetism*, Oxford University Press (1996)

[Aha01] A. Aharoni, "Micromagnetics: past, present and future", *Physica B*, **306**, 1 (2001)

[All90] R. Allenspach, M. Stampanoni, and A. Bischof, "Magnetic Domains in thin Epitaxical Co/Au(111) films", *Phys. Rev. Lett.*, **65**, 3344 (1990)

[All92] R. Allenspach, A. Bischof, M. Stampanoni, D. Kerkmann, and D. Pescia, "Growing thin magnetic films with a mask: Distinguishing between magnetic and instrumental asymmetries", *Appl. Phys. Lett.*, **60**, 1908 (1992)

[All94] R. Allenspach, "Ultrathin films: magnetism on the microscopic scale", *J. Magn. Magn. Mater.*, **129**, 160 (1994)

[All06] R. Allenspach and P. O. Jubert, "Magnetic domain walls in nanowires", *Mrs Bulletin*, **31**, 395 (2006)

[Arr05] A. Arrott, *"Introduction to Micromagnetics" in "Ultrathin Magnetic Structures IV"*, Springer, Berlin (2005)

[Bac07] D. Backes, C. Schieback, M. Kläui, F. Junginger, H. Ehrke, P. Nielaba, U. Rüdiger, L. J. Heyderman, C. S. Chen, T. Kasama, R. E. Dunin-Borkowski, C. A. F. Vaz, and J. A. C. Bland, "Transverse domain walls in nanoconstrictions", *Appl. Phys. Lett.*, **91**, 112502 (2007)

[Bar04] M. Barthelmess, C. Pels, A. Thieme, and G. Meier, "Stray fields of domains in permalloy microstructures - Measurements and simulations", *J. Appl. Phys.*, **95**, 5641 (2004)

[Bar05] S. E. Barnes and S. Maekawa, "Current-Spin Coupling for Ferromagnetic Domain Walls in Fine Wires", *Phys. Rev. Lett.*, **95**, 107204 (2005)

[Bar07] S. Barman and G. P. Srivastava, "Temperature dependence of the thermal conductivity of different forms of diamond", *J. Appl. Phys.*, **101**, 123507 (2007)

[Bed07] D. Bedau, M. Kläui, U. Rüdiger, C. A. F. Vaz, J. A. C. Bland, G. Faini, L. Vila, and W. Wernsdorfer, "Angular dependence of the depinning field for head-to-head domain walls at constrictions", *J. Appl. Phys.*, **101**, 09F509 (2007)

[Ber] D. Berkov, *MicroMagus*, INNOVENT Technology Development e.V., Prüssingstr. 27B, D-07745 Jena, Germany

[Ber69] L. Berenbaum and R. Rosenberg, "Surface topology changes during electromigration in metallic thin film stripes", *Thin Solid Films*, **4**, 187 (1969)

[Ber96] L. Berger, "Emission of spin waves by a magnetic multilayer traversed by a current", *Phys. Rev. B*, **54**, 9353 (1996)

[Bey10] B. Beyersdorff, "Stromunterstützte Ummagnetisierungsprozesse in Permalloy-Nanodrähten", *Diplomarbeit Uni Hamburg* (2010)

[Bit32] F. Bitter, "Experiments on the Nature of Ferromagnetism", *Phys. Rev.*, **41**, 507 (1932)

[Bla69] J. Black, "Electromigration - A brief survey of some recent results", *IEEE Trans. Electron Devices*, **ED-16**, 338 (1969)

[Bod08] M. Bode, O. Pietzsch, A. Kubetzka, W. Wulfhekel, D. McGrouther, S. McVitie, and J. N. Chapman, "Comment on "Three-Dimensional, Spin-Resolved Structure of Magnetic Vortex and Antivortex States in Patterned Co Films Using Scanning Ion Microscopy with Polarization Analysis"", *Phys. Rev. Lett.*, **100**, 029703 (2008)

[Bog09] L. K. Bogart, D. Atkinson, K. O'Shea, D. McGrouther, and S. McVitie, "Dependence of domain wall pinning potential landscapes on domain wall chirality and pinning site geometry in planar nanowires", *Phys. Rev. B*, **79**, 054414 (2009)

[Boh08] S. Bohlens, B. Krüger, A. Drews, M. Bolte, G. Meier, and D. Pfannkuche, "Current controlled random-access memory based on magnetic vortex handedness", *Appl. Phys. Lett.*, **93**, 142508 (2008)

[Bol08] M. Bolte, G. Meier, B. Krüger, A. Drews, R. Eiselt, L. Bocklage, S. Bohlens, T. Tyliszczak, A. Vansteenkiste, B. Van Waeyenberge, K. W. Chou, A. Puzic, and H. Stoll, "Time-Resolved X-Ray Microscopy of Spin-Torque-Induced Magnetic Vortex Gyration", *Phys. Rev. Lett.*, **100**, 176601 (2008)

[Bre08] L. Breitenstein, P. Lendecke, S. Bohlens, G. Meier, and U. Merkt, "Stray field of a Landau magnetization pattern", *J. Appl. Phys.*, **104**, 083909 (2008)

[Bro56] K. L. Brown and G. W. Tautfest, "Faraday-Cup Monitors for High-Energy Electron Beams", *Rev. Sci. Instrum.*, **27**, 696 (1956)

[Bro62] W. F. Brown, *Magnetostatic Principles in Ferromagnetism*, North Holland (1962)

[Bro06] C. Brownlie, S. McVitie, J. N. Chapman, and C. D. W. Wilkinson, "Lorentz microscopy studies of domain wall trap structures", *J. Appl. Phys.*, **100**, 033902 (2006)

[Bry04] M. T. Bryan, D. Atkinson, and R. P. Cowburn, "Experimental study of the influence of edge roughness on magnetization switching in Permalloy nanostructures", *Appl. Phys. Lett.*, **85**, 3510 (2004)

[Bur94] S. Burghartz and B. Schulz, "Thermophysical properties of sapphire, AlN and $MgAl_2O_4$ down to 70 K", *J. Nucl. Mater.*, **212**, 1065 (1994)

[Bus00] B. L. Busse, "http://www.stanford.edu/ bbusse/work/downloads.html", *Stannford University* (2000)

[Cel82] R. Celotta and D. Pierce, *Microbeam Analysis*, San Francisco Press (1982)

[Cer96] S. Cercelaru, A. M. Nguyen, P. Hesto, G. Tremblay, and J. C. Perron, "A comparative study of the magnetic properties of thin permalloy films", *J. Magn. Magn. Mater.*, **160**, 338 (1996)

[Cha84] J. N. Chapman, "The investigation of magnetic domain structures in thin foils by electron microscopy", *J. Phys. D*, **17**, 623 (1984)

[Che05] S. Cherifi, R. Hertel, J. Kirschner, H. Wang, R. Belkhou, A. Locatelli, S. Heun, A. Pavlovska, and E. Bauer, "Virgin domain structures in mesoscopic Co patterns: Comparison between simulation and experiment", *J. Appl. Phys.*, **98**, 043901 (2005)

[Chi78] S. Chikazumi and S. H. Charap, *Physics of Magnetism*, Wiley (1978)

[Chr88] K. Christmann, "Interaction of hydrogen with solid surfaces", *Surface Science Reports*, **9**, 1 (1988)

[Chu10] S.-H. Chung, R. D. McMichael, D. T. Pierce, and J. Unguris, "Phase diagram of magnetic nanodisks measured by scanning electron microscopy with polarization analysis", *Phys. Rev. B*, **81**, 024410 (2010)

[Coh70] M. S. Cohen, *Handbook of thin film technology*, McGraw-Hill (1970)

[Col57] R. V. Coleman and G. G. Scott, "Magnetic Domain Patterns on Single-Crystal Iron Whiskers", *Phys. Rev.*, **107**, 1276 (1957)

[Com10] Comsol, "Comsol Multphysics 3.4", *Software*, **http://www.comsol.com/** (2010)

[Cor88] B. W. Corb, "Effects of magnetic history on the domain structure of small NiFe shapes", *J. Appl. Phys.*, **63**, 2941 (1988)

[Cow00] R. P. Cowburn, D. K. Koltsov, A. O. Adeyeye, and M. E. Welland, "Lateral interface anisotropy in nanomagnets", **87**, 7067 (2000)

[Cow07] R. P. Cowburn, "Spintronics: Change of direction", *Nat. Mater.*, **6**, 255 (2007)

[Dag07] M. Dagras, M. Laufenberg, D. Bedau, L. Vila, G. Faini, C. A. F. Vaz, and J. A. C. Bland, "The influence of thermal activation and the intrinsic temperature dependence of the spin torque effect in current-induced domain wall motion", *J. Phys. D*, **40**, 1247 (2007)

[Dai96] H. J. Dai, E. W. Wong, and C. M. Lieber, "Probing electrical transport in nanomaterials: Conductivity of individual carbon nanotubes", *Science*, **272**, 523 (1996)

[Dar74] M. Darby and E. Isaac, "Magnetocrystalline anisotropy of ferro- and ferrimagnetics", *IEEE Trans. Magn.*, **10**, 259 (1974)

[Des99] M. M. Deshmukh, D. C. Ralph, M. Thomas, and J. Silcox, "Nanofabrication using a stencil mask", *Appl. Phys. Lett.*, **75**, 1631 (1999)

[Did24] P. H. Didon, "Motto of the 1924 Summer Olympics", (1924)

[Don99] M. Donahue and D. Porter, *OOMMF User's Guide Version 1.0, Interagency Report NISTIR 6376, National Institute of Standards and Technology, Gaithersburg* (1999)

[Dür89] W. Dürr, M. Taborelli, O. Paul, R. Germar, W. Gudat, D. Pescia, and M. Landolt, "Magnetic Phase Transition in Two-Dimensional Ultrathin Fe Films on Au(100)", *Phys. Rev. Lett.*, **62**, 206 (1989)

[Dur08] C. Durkan, *Current at the Nanoscale*, Imperial College Press (2008)

[Dys04] F. Dyson, "A meeting with Enrico Fermi", *Nature*, **427**, 297 (2004)

[Ebe96] H. Ebert, A. Vernes, and J. Banhart, "Anisotropic electrical resistivity of ferromagnetic Co-Pd and Co-Pt alloys", *Phys. Rev. B*, **54**, 8479 (1996)

[Ede97] C. Edelmann, *Vakuumphysik*, Spektrum Akademischer Verlag (1997)

[Eis04] S. Eisebitt, J. Luning, W. F. Schlotter, M. Lorgen, O. Hellwig, W. Eberhardt, and J. Stöhr, "Lensless imaging of magnetic nanostructures by X-ray spectro-holography", *Nature*, **432**, 885 (2004)

[Eis08] S. Eisebitt, "X-ray holography: The hole story", *Nat. Photon.*, **2**, 529 (2008)

[Eng05] B. N. Engel, J. Akerman, B. Butcher, R. W. Dave, M. DeHerrera, M. Durlam, G. Grynkewich, J. Janesky, S. V. Pietambaram, N. D. Rizzo, J. M. Slaughter, K. Smith, J. J. Sun, and S. Tehrani, "A 4-mb toggle MRAM based on a novel bit and switching method", *IEEE Trans. Magn.*, **41**, 132 (2005)

[Fed81] R. Feder and J. Kirschner, "Spin-polarized low-energy electron diffraction: Theory, experiment and analysis of results from W(001)(1 x 1)", *Surf. Sci.*, **103**, 75 (1981)

[Fel67] E. Feldtkeller and K. Stein, "Verbesserte Kerr Technik zur Beobachtung magnetischer Domänen", *Z. Angew. Phys.*, **23**, 100 (1967)

[Fer76] A. Fert and I. A. Campbell, "Electrical resistivity of ferromagnetic nickel and iron based alloys", *J. Phys. F*, **6**, 849 (1976)

[Fey60] R. Feynman, "There's Plenty of Room at the Bottom", *Engineering and Science*, **XXIII**, 22 (1960)

[Fey88] R. P. Feynman, *The Pleasure of Finding Things Out*, Basic Books (1988)

[Fid00] J. Fidler and T. Schrefl, "Micromagnetic modelling - the current state of the art", *J. Phys. D*, **33**, R135 (2000)

[Frö08] R. Frömter, H. Stillrich, C. Menk, and H. P. Oepen, "Imaging the Cone State of the Spin Reorientation Transition", *Phys. Rev. Lett.*, **100**, 207202 (2008)

[Fra53] R. Franz and G. Wiedemann, "Über die Wärme-Leitungsfähigkeit der Metalle", *Ann. Phys. (Leipzig)*, **165**, 497 (1853)

[Gal97] W. J. Gallagher, S. S. P. Parkin, Y. Lu, X. P. Bian, A. Marley, K. P. Roche, R. A. Altman, S. A. Rishton, C. Jahnes, T. M. Shaw, and G. Xiao, "Microstructured magnetic tunnel junctions", **81**, 3741 (1997)

[Gar95] A. Garg, "Escape-field distribution for escape from a metastable potential well subject to a steadily increasing bias field", *Phys. Rev. B*, **51**, 15592 (1995)

[Gar02a] J. M. García, A. Thiaville, and J. Miltat, "MFM imaging of nanowires and elongated patterned elements", *J. Magn. Magn. Mater.*, **249**, 163 (2002)

[Gar02b] J. M. García, A. Thiaville, J. Miltat, K. J. Kirk, and J. N. Chapman, "MFM imaging of patterned permalloy elements under an external applied field", *J. Magn. Magn. Mater.*, **242-245**, 1267 (2002)

[Get96] M. Getzlaff, J. Paul, J. Bansmann, C. Ostertag, G. H. Fecher, and G. Schönhense, "Oxygen adsorbed on rare earth surfaces", *Surf. Sci.*, **352**, 123 (1996)

[Get10] M. Getzlaff, "Private Communication", (2010)

[Gil04] T. Gilbert, "A phenomenological theory of damping in ferromagnetic materials", *IEEE Trans. Magn.*, **40**, 3443 (2004)

[Gla64] C. J. Glassbrenner and G. A. Slack, "Thermal Conductivity of Silicon and Germanium from 3 K to the Melting Point", *Phys. Rev.*, **134**, A1058 (1964)

[Gli09] S. Gliga, "Ultrafast vortex core dynamics investigated by finite-element micromagnetic simulations", *PhD Thesis* (2009)

[Gom99] R. D. Gomez, T. V. Luu, A. O. Pak, K. J. Kirk, and J. N. Chapman, "Domain configurations of nanostructured Permalloy elements", *J. Appl. Phys.*, **85**, 6163 (1999)

[Gro07] L. Gross, R. R. Schlittler, G. Meyer, A. Vanhaverbeke, and R. Allenspach, "Fabrication of ultrathin magnetic structures by nanostencil lithography in dynamic mode", *Appl. Phys. Lett.*, **90**, 093121 (2007)

[Gun94] L. Gunther and B. Barbara, "Quantum tunneling across a domain-wall junction", *Phys. Rev. B*, **49**, 3926 (1994)

[Guo97] L. Guo, E. Leobandung, and S. Y. Chou, "A Silicon Single-Electron Transistor Memory Operating at Room Temperature", *Science*, **275**, 649 (1997)

[Guo03] Z. J. Guo, J. S. Jiang, C. Y. You, V. K. Vlasko-Vlasov, U. Welp, J. P. Liu, and S. D. Bader, "Exchange coupling in epitaxial Sm-Co($1\bar{1}00$)/Nd-Co exchange-spring bilayers", *J. Appl. Phys.*, **93**, 8122 (2003)

[Gus04] K. Y. Guslienko and V. Novosad, "Vortex state stability in soft magnetic cylindrical nanodots", *J. Appl. Phys.*, **96**, 4451 (2004)

[Han08] S. Hankemeier, K. Sachse, Y. Stark, R. Frömter, and H. P. Oepen, "Ultra-high current densities in Permalloy nanowires on diamond", *Appl. Phys. Lett.*, **92**, 242503 (2008)

[Han09] S. Hankemeier, R. Frömter, N. Mikuszeit, D. Stickler, H. Stillrich, S. Pütter, E. Y. Vedmedenko, and H. P. Oepen, "Magnetic Ground State of Single and Coupled Permalloy Rectangles", *Phys. Rev. Lett.*, **103**, 147204 (2009)

[Har91] U. Hartmann, T. Göddenhenrich, and C. Heiden, "Magnetic force microscopy: Current status and future trends", *J. Magn. Magn. Mater.*, **101**, 263 (1991)

[Haw10] P. W. Hawkes and J. C. Spence (Editors), *Science of Microscopy*, Springer New York (2010)

[Hay06] M. Hayashi, L. Thomas, C. Rettner, R. Moriya, X. Jiang, and S. S. P. Parkin, "Dependence of Current and Field Driven Depinning of Domain Walls on Their Structure and Chirality in Permalloy Nanowires", *Phys. Rev. Lett.*, **97**, 207205 (2006)

[Hay08a] M. Hayashi, L. Thomas, R. Moriya, C. Rettner, and S. S. P. Parkin, "Current-Controlled Magnetic Domain-Wall Nanowire Shift Register", *Science*, **320**, 209 (2008)

[Hay08b] M. Hayashi, L. Thomas, C. Rettner, R. Moriya, and S. S. P. Parkin, "Dynamics of domain wall depinning driven by a combination of direct and pulsed currents", *Appl. Phys. Lett.*, **92**, 162503 (2008)

[Hei05] B. Heinrich, *"Spin Relaxation in Magnetic Metallic Layers and Multilayers" in "Ultrathin Magnetic Structures III"*, Springer, Berlin (2005)

[Her87] D. A. Herman, Jr., B. E. Argyle, and B. Petek, "Bloch lines, cross ties, and taffy in permalloy", *J. Appl. Phys.*, **61**, 4200 (1987)

[Her02] R. Hertel, "Thickness dependence of magnetization structures in thin Permalloy rectangles", *Z. Metallkd.*, **93**, 957 (2002)

[Her07] R. Hertel, S. Gliga, M. Fähnle, and C. M. Schneider, "Ultrafast Nanomagnetic Toggle Switching of Vortex Cores", *Phys. Rev. Lett.*, **98**, 117201 (2007)

[Hey08a] L. Heyne, M. Kläui, D. Backes, P. Mohrke, T. A. Moore, J. G. Kimling, O. Boulle, U. Rüdiger, L. J. Heyderman, A. F. Rodríguez, F. Nolting, K. Kirsch, and R. Mattheis, "Direct imaging of current-induced domain wall motion in CoFeB structures", *J. Appl. Phys.*, **103**, 07D928 (2008)

[Hey08b] L. Heyne, M. Kläui, D. Backes, T. A. Moore, S. Krzyk, U. Rüdiger, L. J. Heyderman, A. F. Rodríguez, F. Nolting, T. O. Mentes, M. Niño, A. Locatelli, K. Kirsch, and R. Mattheis, "Relationship between Nonadiabaticity and Damping in Permalloy Studied by Current Induced Spin Structure Transformations", *Phys. Rev. Lett.*, **100**, 066603 (2008)

[Hic09] M. C. Hickey and J. S. Moodera, "Origin of Intrinsic Gilbert Damping", *Phys. Rev. Lett.*, **102**, 137601 (2009)

[Hie97] W. K. Hiebert, A. Stankiewicz, and M. R. Freeman, "Direct Observation of Magnetic Relaxation in a Small Permalloy Disk by Time-Resolved Scanning Kerr Microscopy", *Phys. Rev. Lett.*, **79**, 1134 (1997)

[Him05] A. Himeno, T. Okuno, T. Ono, K. Mibu, S. Nasu, and T. Shinjo, "Temperature dependence of depinning fields in submicron magnetic wires with an artificial neck", *J. Magn. Magn. Mater.*, **286**, 167 (2005)

[Hit10a] "Hitachi High-Technologies Europe GmbH; Field Emission SEM with Ultra High Resolution SU-70", *http://www.hht-eu.com/cms/2911.html* (2010)

[Hit10b] Hitachi, "Specifications: Deskstar 7K2000, 2TB, 3.5-Inch Hard Disk Drive", *http://www.hitachigst.com/deskstar-7k2000* (2010)

[Ho78] C. Y. Ho, M. W. Ackerman, K. Y. Wu, S. G. Oh, and T. N. Havill, "Thermal conductivity of ten selected binary alloy systems", *J. Phys. Chem. Ref. Data*, **7**, 959 (1978)

[Ho83] C. Y. Ho, M. W. Ackerman, K. Y. Wu, T. N. Havill, R. H. Bogaard, R. A. Matula, S. G. Oh, and H. M. James, "Electrical Resistivity of Ten Selected Binary Alloy Systems", *J. Phys. Chem. Ref. Data*, **12**, 183 (1983)

[Ho89] P. S. Ho and T. Kwok, "Electromigration In Metals", *Rep. Prog. Phys.*, **52**, 301 (1989)

[Hop83] H. Hopster, R. Raue, E. Kisker, G. Güntherodt, and M. Campagna, "Evidence for Spin-Dependent Electron-Hole-Pair Excitations in Spin-Polarized Secondary-Electron Emission from Ni(110)", *Phys. Rev. Lett.*, **50**, 70 (1983)

[Hop89] H. Hopster and D. L. Abraham, "Spin-dependent inelastic electron scattering on Ni(110)", *Phys. Rev. B*, **40**, 7054 (1989)

[Hos06] M. Hosomi, "A novel nonvolatile memory with spin torque transfer magnetization switching: Spin-RAM", *Electron Devices Meeting, 2005. IEDM Technical Digest. IEEE International*, page 473 (2006)

[Hua08] Q. Huang, C. M. Lilley, M. Bode, and R. Divan, "Surface and size effects on the electrical properties of Cu nanowires", *J. Appl. Phys.*, **104**, 023709 (2008)

[Hub58] E. E. Huber, Jr., D. O. Smith, and J. B. Goodenough, "Domain-Wall Structure in Permalloy Films", *J. Appl. Phys.*, **29**, 294 (1958)

[Hub86] A. Hubert and F. Schmidt, "Domain observations on CoCr layers with a digitally enhanced Kerr microscope.", *J. Magn. Magn. Mater.*, **61**, 307 (1986)

[Hub91] A. Hubert and M. Rührig, "Micromagnetic analysis of thin-film elements", **69**, 6072 (1991)

[Hub98] A. Hubert and R. Schäfer, *Magnetic Domains*, Springer, Berlin (1998)

[Ied10] J. Ieda, H. Sugishita, and S. Maekawa, "Current-induced domain wall motion in magnetic nanowires with spatial variation", *J. Magn. Magn. Mater.*, **322**, 1363 (2010)

[Ilg08] D. Ilgaz, M. Kläui, L. Heyne, O. Boulle, F. Zinser, S. Krzyk, M. Fonin, U. Rüdiger, D. Backes, and L. J. Heyderman, "Selective domain wall depinning by localized Oersted fields and Joule heating", *Appl. Phys. Lett.*, **93**, 132503 (2008)

[Im09] M.-Y. Im, L. Bocklage, P. Fischer, and G. Meier, "Direct Observation of Stochastic Domain-Wall Depinning in Magnetic Nanowires", *Phys. Rev. Lett.*, **102**, 147204 (2009)

[Jia91] H. Jiang, Y. Huang, H. How, S. Zhang, C. Vittoria, A. Widom, D. B. Chrisey, J. S. Horwitz, and R. Lee, "Observation of ultrahigh critical current densities in high-T_c superconducting bridge constrictions", *Phys. Rev. Lett.*, **66**, 1785 (1991)

[Jos03] G. Joseph, D. E. Newbury, D. C. Joy, P. Echlin, C. E. Lyman, and E. Lifshin, *Scanning electron microscopy and x-ray microanalysis*, Springer, Berlin (2003)

[Jub06] P.-O. Jubert, M. Kläui, A. Bischof, U. Rüdiger, and R. Allenspach, "Velocity of vortex walls moved by current", *J. Appl. Phys.*, **99**, 08G523 (2006)

[Jun07] F. Junginger, M. Kläui, D. Backes, U. Rüdiger, T. Kasama, R. E. Dunin-Borkowski, L. J. Heyderman, C. A. F. Vaz, and J. A. C. Bland, "Spin torque and heating effects in current-induced domain wall motion probed by transmission electron microscopy", *Appl. Phys. Lett.*, **90**, 132506 (2007)

[Kar06] S. Karim, M. E. Toimil-Molares, A. G. Balogh, W. Ensinger, T. W. Cornelius, E. U. Khan, and R. Neumann, "Morphological evolution of Au nanowires controlled by Rayleigh instability", *Nanotechnology*, **17**, 5954 (2006)

[Kar09] S. Karim, K. Maaz, G. Ali, and W. Ensinger, "Diameter dependent failure current density of gold nanowires", *J. Phys. D*, **42**, 185403 (2009)

[Kea09] D. J. Keavney, X. M. Cheng, and K. S. Buchanan, "Polarity reversal of a magnetic vortex core by a unipolar, nonresonant in-plane pulsed magnetic field", *Appl. Phys. Lett.*, **94**, 172506 (2009)

[Kim08] K.-J. Kim, J.-C. Lee, S.-B. Choe, and K.-H. Shin, "Joule heating in ferromagnetic nanowires: Prediction and observation", *Appl. Phys. Lett.*, **92**, 192509 (2008)

[Kin80] D. A. King and G. Thomas, "Displacive surface phases formed by hydrogen chemisorption on W 001", *Surf. Sci.*, **92**, 201 (1980)

[Kir84] J. Kirschner, "On the Role of the Electron-Spin in Scanning Electron-Microscopy", *Scanning Electron Microsc.*, **III**, 1179 (1984)

[Kir85a] J. Kirschner, "Direct and Exchange Contributions in Inelastic Scattering of Spin-Polarized Electrons from Iron", *Phys. Rev. Lett.*, **55**, 973 (1985)

[Kir85b] J. Kirschner, *Polarized Electrons at Surfaces*, Springer, Berlin (1985)

[Kit49] C. Kittel, "Physical Theory of Ferromagnetic Domains", *Rev. Mod. Phys.*, **21**, 541 (1949)

[Kit96] O. Kitakami, T. Sakurai, Y. Miyashita, Y. Takeno, Y. Shimada, H. Takano, H. Awano, K. Ando, and Y. Sugita, "Fine Metallic Particles for Magnetic Domain Observations", *Jpn. J. Appl. Phys.*, **35**, 1724 (1996)

[Klä04] M. Kläui, C. A. F. Vaz, J. A. C. Bland, L. J. Heyderman, F. Nolting, A. Pavlovska, E. Bauer, S. Cherifi, S. Heun, and A. Locatelli, "Head-to-head domain-wall phase diagram in mesoscopic ring magnets", *Appl. Phys. Lett.*, **85**, 5637 (2004)

[Klä05a] M. Kläui, P.-O. Jubert, R. Allenspach, A. Bischof, J. A. C. Bland, G. Faini, U. Rüdiger, C. A. F. Vaz, L. Vila, and C. Vouille, "Direct Observation of Domain-Wall Configurations Transformed by Spin Currents", *Phys. Rev. Lett.*, **95**, 026601 (2005)

[Klä05b] M. Kläui, C. A. F. Vaz, J. A. C. Bland, W. Wernsdorfer, G. Faini, E. Cambril, L. J. Heyderman, F. Nolting, and U. Rüdiger, "Controlled and Reproducible Domain Wall Displacement by Current Pulses Injected into Ferromagnetic Ring Structures", *Phys. Rev. Lett.*, **94**, 106601 (2005)

[Klä06] M. Kläui, M. Laufenberg, L. Heyne, D. Backes, U. Rüdiger, C. A. F. Vaz, J. A. C. Bland, L. J. Heyderman, S. Cherifi, A. Locatelli, T. O. Mentes, and L. Aballe, "Current-induced vortex nucleation and annihilation in vortex domain walls", *Appl. Phys. Lett.*, **88**, 232507 (2006)

[Klä08] M. Kläui, "Head-to-head domain walls in magnetic nanostructures", *J. Phys.: Condens. Matter*, **20**, 313001 (2008)

[Klä09] M. Kläui, D. Ilgaz, L. Heyne, J.-S. Kim, O. Boulle, C. Schieback, F. Zinser, S. Krzyk, M. Fonin, U. Rüdiger, D. Backes, and L. Heyderman, "Concepts for Domain Wall Motion in Nanoscale Ferromagnetic Elements due to Spin Torque and in Particular Oersted Fields", *Journal of magnetics*, **14**, 53 (2009)

[Kle75] H. Klein, A. Menth, and R. Perkins, "Magnetocrystalline anisotropy of light rare-earth cobalt compounds", *Physica B+C*, **80**, 153 (1975)

[Kob09] A. Kobs, H. Spahr, D. Stickler, S. Hankemeier, R. Frömter, and H. P. Oepen, "Magnetic energies of single submicron permalloy rectangles determined via magnetotransport", *Phys. Rev. B*, **80**, 134415 (2009)

[Koh] T. Kohashi and K. Koike, "A Spin-Polarized Scanning Electron Microscope with 5-nm Resolution", *Jpn. J. Appl. Phys.*, **40**, L1264

[Koh06] H. Kohno, G. Tatara, and J. Shibata, "Microscopic Calculation of Spin Torques in Disordered Ferromagnets", *J. Phys. Soc. Jpn.*, **75**, 113706 (2006)

[Koi84] K. Koike, H. Matsuyama, and K. Hayakawa, "Spin-Polarized Scanning Electron Microscope Equipped with a Thumb-Size Spin Detector", *Jpn. J. Appl. Phys.*, **27**, L1352 (1984)

[Koi87] K. Koike, H. Matsuyama, and K. Hayakawa, "Spin-Polarized Scanning Electron Microscopy for Micro-Magntic Structure Observation", *Scanning Microsc. Suppl.*, **1**, 241 (1987)

[Koi03] P. M. Koinkar, P. P. Patil, M. A. More, V. N. Tondare, and D. S. Joag, "Field emission studies of CVD diamond thin films: effect of acid treatment", *Vacuum*, **72**, 321 (2003)

[Kon04] M. Konoto, T. Kohashi, K. Koike, T. Arima, Y. Kaneko, T. Kimura, and Y. Tokura, "Direct Imaging of Temperature-Dependent Layered Antiferromagnetism of a Magnetic Oxide", *Phys. Rev. Lett.*, **93**, 107201 (2004)

[Kon08] M. Konoto, T. Yamada, K. Koike, H. Akoh, T. Arima, and Y. Tokura, "Formation and control of magnetic vortex chirality in patterned micromagnet arrays", *J. Appl. Phys.*, **103**, 023904 (2008)

[Krü10] B. Krüger, M. Najafi, S. Bohlens, R. Frömter, D. P. F. Möller, and D. Pfannkuche, "Proposal of a Robust Measurement Scheme for the Nonadiabatic Spin Torque Using the Displacement of Magnetic Vortices", *Phys. Rev. Lett.*, **104**, 077201 (2010)

[Kra07] S. Krause, L. Berbil-Bautista, G. Herzog, M. Bode, and R. Wiesendanger, "Current-Induced Magnetization Switching with a Spin-Polarized Scanning Tunneling Microscope", *Science*, **317**, 1537 (2007)

[Kro73] S. Krongelb, A. Gangulee, and G. Das, "Annealing of thin magnetoresistive permalloy films", *IEEE Trans. Magn.*, **9**, 568 (1973)

[Kry09] M. Kryder and C. S. Kim, "After Hard Drives - What Comes Next?", *IEEE Trans. Magn.*, **45**, 3406 (2009)

[Kur72] J. Kurkijärvi, "Intrinsic Fluctuations In A Superconducting Ring Closed With A Josephson Junction", *Phys. Rev. B*, **6**, 832 (1972)

[Lan21] A. Landé, "Anomalous zeeman effect", *Z. Phys.*, **5**, 231 (1921)

[Lan35] L. Landau and E. Lifshitz, "On the theory of the dispersion of magnetic permeability in ferromagnetic bodies", *Phys. Z. Sowjetunion*, **8**, 153 (1935)

[Lan10] *The Landolt-Börnstein Database*, Springer Berlin (2010)

[Lau06] M. Laufenberg, W. Buhrer, D. Bedau, P.-E. Melchy, M. Kläui, L. Vila, G. Faini, C. A. F. Vaz, J. A. C. Bland, and U. Rüdiger, "Temperature Dependence of the Spin Torque Effect in Current-Induced Domain Wall Motion", *Phys. Rev. Lett.*, **97**, 046602 (2006)

[Leb08] K. M. Lebecki, M. J. Donahue, and M. W. Gutowski, "Periodic boundary conditions for demagnetization interactions in micromagnetic simulations", *J. Phys. D*, **41**, 175005 (2008)

[Lee97] S.-M. Lee and D. G. Cahill, "Heat transport in thin dielectric films", *J. Appl. Phys.*, **81**, 2590 (1997)

[Len08] P. Lendecke, R. Eiselt, G. Meier, and U. Merkt, "Temperature dependence of domain-wall depinning fields in constricted Permalloy nanowires", *J. Appl. Phys.*, **103**, 073909 (2008)

[Lep09a] S. Lepadatu, M. C. Hickey, A. Potenza, H. Marchetto, T. R. Charlton, S. Langridge, S. S. Dhesi, and C. H. Marrows, "Experimental determination of spin-transfer torque nonadiabaticity parameter and spin polarization in permalloy", *Phys. Rev. B*, **79**, 094402 (2009)

[Lep09b] S. Lepadatu, A. Vanhaverbeke, D. Atkinson, R. Allenspach, and C. H. Marrows, "Dependence of Domain-Wall Depinning Threshold Current on Pinning Profile", *Phys. Rev. Lett.*, **102**, 127203 (2009)

[Li04] Z. Li and S. Zhang, "Domain-wall dynamics driven by adiabatic spin-transfer torques", *Phys. Rev. B*, **70**, 024417 (2004)

[Li06] J. Li and C. Rau, "Three-Dimensional, Spin-Resolved Structure of Magnetic Vortex and Antivortex States in Patterned Co Films Using Scanning Ion Microscopy with Polarization Analysis", *Phys. Rev. Lett.*, **97**, 107201 (2006)

[Lil50] B. A. Lilley, "Energies and widths of domain boundaries in ferromagnetics", *Phil. Mag.*, **41**, 792 (1950)

[Liu94] X. Liu, R. Sooryakumar, C. J. Gutierrez, and G. A. Prinz, "Exchange stiffness and magnetic anisotropies in bcc $Fe_{1-x}Co_x$ alloys", *J. Appl. Phys.*, **75**, 7021 (1994)

[Liu07] Y. Liu, S. Gliga, R. Hertel, and C. M. Schneider, "Current-induced magnetic vortex core switching in a Permalloy nanodisk", *Appl. Phys. Lett.*, **91**, 112501 (2007)

[Lok99] J. G. S. Lok, A. K. Geim, U. Wyder, J. C. Maan, and S. V. Dubonos, "Thermally activated annihilation of an individual domain in submicrometer nickel particles", *J. Magn. Magn. Mater.*, **204**, 159 (1999)

[Lua08] S. Lua, S. Kushvaha, Y. Wu, K. L. Teo, and T. C. Chong, "Effect of FIB Trimming on the Spin Configurations of Hexagonal-Shaped Elements Characterized by SEMPA Imaging", *IEEE Trans. Magn.*, **44**, 3229 (2008)

[Mal10] G. Malinowski, A. Lörincz, S. Krzyk, P. Möhrke, D. Bedau, O. Boulle, J. Rhensius, L. J. Heyderman, Y. J. Cho, S. Seo, and M. Kläui, "Current-induced domain wall motion in Ni_80 Fe_20 nanowires with low depinning fields", *J. Phys. D*, **43**, 045003 (2010)

[Mar87] Y. Martin and H. K. Wickramasinghe, "Magnetic imaging by "force microscopy" with 1000 Å resolution", *Appl. Phys. Lett.*, **50**, 1455 (1987)

[Mar06] H. Marom and M. Eizenberg, "The effect of surface roughness on the resistivity increase in nanometric dimensions.", *J. Appl. Phys.*, **99**, 123705 (2006)

[Mat91] H. Matsuyama and K. Koike, "A data acquisition and display system for spin-polarized scanning electron microscopy (spin SEM)", *Rev. Sci. Instrum.*, **62**, 970 (1991)

[May74] A. F. Mayadas, J. F. Janak, and A. Gangulee, "Resistivity of Permalloy thin films", *J. Appl. Phys.*, **45**, 2780 (1974)

[McG75] T. McGuire and R. Potter, "Anisotropic Magnetoresistance in Ferromagnetic 3*d* Alloys", *IEEE Trans. Magn.*, **4**, 1018 (1975)

[McM97] R. McMichael and M. Donahue, "Head to head domain wall structures in thin magnetic strips", *IEEE Trans. Magn.*, **33**, 4167 (1997)

[McM10] B. J. McMorran, A. C. Cochran, R. K. Dumas, K. Liu, P. Morrow, D. T. Pierce, and J. Unguris, "Measuring the effects of low energy ion milling on the magnetization of Co/Pd multilayers using scanning electron microscopy with polarization analysis", *J. Appl. Phys.*, **107**, 09D305 (2010)

[McV88] S. McVitie and J. Chapman, "Magnetic structure determination in small regularly shaped particle using transmission electron microscopy", *IEEE Trans. Magn.*, **24**, 1778 (1988)

[Mil96] Y. Millev and J. Kirschner, "Reorientation transitions in ultrathin ferromagnetic films by thickness- and temperature-driven anisotropy flows", *Phys. Rev. B*, **54**, 4137 (1996)

[Miy89] T. Miyazaki, T. Ajima, and F. Sato, "Dependence of magnetoresistance on thickness and substrate temperature", *J. Magn. Magn. Mater.*, **81**, 86 (1989)

[Möl63] G. Möllenstedt and F. Lenz, *"Electron Emission Microscopy" in "Advances in Electronics and Electron Phyics"*, London: Academic Press (1963)

[ML06] J. Mejia-Lopez, D. Altbir, A. H. Romero, X. Batlle, I. V. Roshchin, C.-P. Li, and I. K. Schuller, "Vortex state and effect of anisotropy in sub-100-nm magnetic nanodots", *J. Appl. Phys.*, **100**, 104319 (2006)

[Moo65] G. E. Moore, "Cramming more components onto integrated circuits", *Electronics*, **38**, 8 (1965)

[Nah09] G. Nahrwold, L. Bocklage, J. M. Scholtyssek, T. Matsuyama, B. Krüger, U. Merkt, and G. Meier, "Current-induced domain-wall depinning in curved Permalloy nanowires", *J. Appl. Phys.*, **105**, 07D511 (2009)

[Naj09] M. Najafi, B. Krüger, S. Bohlens, M. Franchin, H. Fangohr, A. Vanhaverbeke, R. Allenspach, M. Bolte, U. Merkt, D. Pfannkuche, D. P. F. Möller, and G. Meier, "Proposal for a standard problem for micromagnetic simulations including spin-transfer torque", *J. Appl. Phys.*, **105**, 113914 (2009)

[Nak03] Y. Nakatani, A. Thiaville, and J. Miltat, "Faster magnetic walls in rough wires", *Nat Mater*, **2**, 521 (2003)

[Nak05] Y. Nakatani, A. Thiaville, and J. Miltat, "Head-to-head domain walls in soft nano-strips: a refined phase diagram", *J. Magn. Magn. Mater.*, **290**, 750 (2005)

[Nat05] National Physics Laboratory, "Argon Sputter Table", *http://resource.npl.co.uk/* (2005)

[Née53] L. Néel, "Energies des parois de Bloch dans les couches minces", *Comp. Rend. Acad. Sci. Paris*, **237**, 1468 (1953)

[NIS] "National Institute of Standards and Technology (NIST), 100 Bureau Drive, Stop 1070, Gaithersburg, MD 20899-1070",

[Nov03] V. Novosad, M. Grimsditch, J. Darrouzet, J. Pearson, S. D. Bader, V. Metlushko, K. Guslienko, Y. Otani, H. Shima, and K. Fukamichi, "Shape effect on magnetization reversal in chains of interacting ferromagnetic elements", *Appl. Phys. Lett.*, **82**, 3716 (2003)

[Oep89] H. P. Oepen and J. Kirschner, "Magnetization Distribution of 180° Domain Walls at Fe(100) Single-Crystal Surfaces", *Phys. Rev. Lett.*, **62**, 819 (1989)

[Oep91] H. Oepen and J. Kirschner, "Imaging of magnetic microstructures at surfaces - The scanning electron microscope with spin polarization analysis", *Scanning Microsc.*, **5**, 1 (1991)

[Oep05] H. Oepen, *Magnetic Microscopy of Nanostructures*, Springer, Berlin (2005)

[Oep07] H. Oepen and R. Frömter, *"Chapter XX: Scanning Electron Microscopy with Polarization Analysis" in "Handbook of Magnetism III"*, Wiley (2007)

[O'H99] R. C. O'Handley, *Modern Magnetic Materials: Principles and Applications*, Wiley-Interscience (1999)

[Oli05] P. Olivero, S. Rubanov, P. Reichart, B. C. Gibson, S. T. Huntington, J. Rabeau, A. D. Greentree, J. Salzman, D. Moore, D. N. Jamieson, and S. Prawer, "Ion-Beam-Assisted Lift-Off Technique for Three-Dimensional Micromachining of Freestanding Single-Crystal Diamond", *Adv. Mater.*, **17**, 2427 (2005)

[Ono79] S. Ono and K. Kanaya, "The energy dependence of secondary emission based on the range-energy retardation power formula", *J. Phys. D*, **12**, 619 (1979)

[Par08] S. S. P. Parkin, M. Hayashi, and L. Thomas, "Magnetic Domain-Wall Racetrack Memory", *Science*, **320**, 190 (2008)

[Pat06] A. K. Patra, V. Neu, S. Fahler, H. Wendrock, and L. Schultz, "Phase formation, texture, and magnetic properties of epitaxial Pr–Co films grown on MgO(100)", *J. Appl. Phys.*, **100**, 043905 (2006)

[Pen85] D. R. Penn, S. P. Apell, and S. M. Girvin, "Theory of spin-polarized secondary electrons in transition metals", *Phys. Rev. Lett.*, **55**, 518 (1985)

[Pla01] C. Platt, N. Minor, and T. Klemmer, "Magnetic and structural properties of FeCoB thin films", *IEEE Trans. Magn.*, **37**, 2302 (2001)

[Plo93] R. Ploessl, J. N. Chapman, A. M. Thompson, J. Zweck, and H. Hoffmann, "Investigation of the micromagnetic structure of cross-tie walls in permalloy", *J. Appl. Phys.*, **73**, 2447 (1993)

[Pot74] R. I. Potter, "Magnetoresistance anisotropy in ferromagnetic NiCu alloys", *Phys. Rev. B*, **10**, 4626 (1974)

[Que91] Queen, "The show must go on", *Song from the album "Innuendo"* (1991)

[Rößl10] S. Rößler, "Private Communication", (2010)

[Rav00] W. Rave and A. Hubert, "Magnetic ground state of a thin-film element", *IEEE Trans. Magn.*, **36**, 3886 (2000)

[Rei85] L. Reimer and A. Schmidt, "The Shrinkage of Bulk Polymers by Radiation damage in a SEM", *Scann.*, **7**, 47 (1985)

[Rei88] L. Reimer, *Scanning Electron Microscopy: Physics of Image Formation and Microanalysis, Second Edition* (1988)

[Rei10] R. Reichelt, *"Scanning Electron Microscopy" in "Science of Microscopy"*, Springer New York (2010)

[Rem08] A. Remhof, A. Schumann, A. Westphalen, H. Zabel, N. Mikuszeit, E. Y. Vedmedenko, T. Last, and U. Kunze, "Magnetostatic interactions on a square lattice", *Phys. Rev. B*, **77**, 134409 (2008)

[Rep98] "National Institute of Standards and Technology, Micromagnetic Modeling Activity Group, Report on "standard problem 1"", *http://www.ctcms.nist.gov/ rdm/std1/prob1report.html* (1998)

[Rij95] T. Rijks, R. Sour, D. Neerinck, A. De Veirman, R. Coehoorn, J. Kools, M. Gillies, and W. de Jonge, "Influence of grain size on the transport properties of $Ni_{80}Fe_{20}$ and Cu thin films", *IEEE Trans. Magn.*, **31**, 3865 (1995)

[Rus31] E. Ruska, "The Development of the Electron Microscope and of Electron Microscopy", *Nobel Lecture held in 1986* (1931)

[Sac08] K. Sachse, "Ultrahohe Gleichstromdichten in magnetischen Nanodrähten auf Diamant-Substrat", *Diplomarbeit Uni Hamburg* (2008)

[San99] G. M. Sandler, H. N. Bertram, T. J. Silva, and T. M. Crawford, "Determination of the magnetic damping constant in NiFe films", *J. Appl. Phys.*, **85**, 5080 (1999)

[San08] C. W. Sandweg, N. Wiese, D. McGrouther, S. J. Hermsdoerfer, H. Schultheiss, B. Leven, S. McVitie, B. Hillebrands, and J. N. Chapman, "Direct observation of domain wall structures in curved permalloy wires containing an antinotch", *J. Appl. Phys.*, **103**, 093906 (2008)

[Sat06] K. Sato, T. Yamamoto, T. Tezuka, T. Ishibashi, Y. Morishita, A. Koukitu, K. Machida, and T. Yamaoka, "MFM observation of spin structures in nano-magnetic-dot arrays fabricated by damascene technique", *J. Magn. Magn. Mater.*, **304**, 10 (2006)

[Saw92] J. Sawler and D. Venus, "Effects of hydrogen adsorption on the performance of the W(001) spin-polarized low-energy electron diffraction electron polarimeter", *J. Vac. Sci. Technol. A*, **10**, 388 (1992)

[Sch89a] M. R. Scheinfein, D. T. Pierce, J. Unguris, J. J. McClelland, R. J. Celotta, and M. H. Kelley, "Improved low-energy diffuse scattering electron-spin polarization analyzer", *Rev. Sci. Instrum.*, **60**, 1 (1989)

[Sch89b] M. R. Scheinfein, J. Unguris, R. J. Celotta, and D. T. Pierce, "Influence of the surface on magnetic domain-wall microstructure", *Phys. Rev. Lett.*, **63**, 668 (1989)

[Sch90] M. R. Scheinfein, J. Unguris, M. H. Kelley, D. T. Pierce, and R. J. Celotta, "Scanning electron microscopy with polarization analysis (SEMPA)", *Rev. Sci. Instrum.*, **61**, 2501 (1990)

[Sch91a] M. Scheinfein, J. Unguris, M. Aeschlimann, D. Pierce, and R. Celotta, "Scanning electron microscopy with polarization analysis (SEMPA) – studies of domains, domain walls and magnetic singularities at surfaces and in thin films", *J. Magn. Magn. Mater.*, **93**, 109 (1991)

[Sch91b] M. R. Scheinfein, J. Unguris, J. L. Blue, K. J. Coakley, D. T. Pierce, R. J. Celotta, and P. J. Ryan, "Micromagnetics of domain walls at surfaces", *Phys. Rev. B*, **43**, 3395 (1991)

[Sch93] G. Schönhense and H. Siegmann, "Transmission of electrons through ferromagnetic material and applications to detection of electron spin polarization", *Ann. Phys. (Leipzig)*, **2**, 465 (1993)

[Sco55] G. G. Scott, "Gyromagnetic Ratio of Iron at Low Magnetic Intensities", *Phys. Rev.*, **99**, 1241 (1955)

[Sea79] M. P. Seah and W. A. Dench, "Quantitative electron spectroscopy of surfaces: A standard data base for electron inelastic mean free paths in solids", *Surface and Interface Analysis*, **1**, 2 (1979)

[Sei76] H. Seiler, "Determination of the "information depth" in the SEM", *Scanning Electron Microscopy*, **1**, 9 (1976)

[Sei09] M. Seifert, L. Schultz, and V. Neu, "Magnetization processes and spin reorientation in epitaxial $NdCo_{5\pm x}$ thin films", *J. Appl. Phys.*, **106**, 073915 (2009)

[Sha06] P. Shah and A. Gavrin, "Synthesis of nanoparticles using high-pressure sputtering for magnetic domain imaging", *Journal of Magnetism and Magnetic Materials*, **301**, 118 (2006)

[Sin06] A. Singh, V. Neu, R. Tamm, K. Rao, S. Faehler, W. Skrotzki, L. Schultz, and B. Holzapfel, "Pulsed laser deposited epitaxial SmCo thin films with uniaxial magnetic texture", **99**, 08E917 (2006)

[Six31] K. J. Sixtus and L. Tonks, "Propagation of Large Barkhausen Discontinuities", *Phys. Rev.*, **37**, 930 (1931)

[Slo96] J. C. Slonczewski, "Current-driven excitation of magnetic multilayers", *J. Magn. Magn. Mater.*, **159**, L1 (1996)

[Smi51] J. Smit, "Magnetoresistance of ferromagnetic metals and alloys at low temperatures,", *Physica*, **17**, 612 (1951)

[Stö93] Y. Stöhr, J.and Wu, B. Hermsmeier, M. Samant, G. Harp, S. Koranda, D. Dunham, and B. Tonner, "Element-Specific Magnetic Microscopy with Circularly Polarized X-rays", *Science*, **259**, 658 (1993)

[Ste02] G. Steierl, G. Liu, D. Iorgov, and J. Kirschner, "Surface domain imaging in external magnetic fields", *Rev. Sci. Instrum.*, **73**, 4264 (2002)

[Sti07] M. D. Stiles, W. M. Saslow, M. J. Donahue, and A. Zangwill, "Adiabatic domain wall motion and Landau-Lifshitz damping", *Phys. Rev. B*, **75**, 214423 (2007)

[Sti10] D. Stickler, R. Frömter, H. Stillrich, C. Menk, C. Tieg, S. Streit-Nierobisch, M. Sprung, C. Gutt, L.-M. Stadler, O. Leupold, G. Grübel, and H. P. Oepen, "Soft x-ray holographic microscopy", *Appl. Phys. Lett.*, **96**, 042501 (2010)

[Sto47] E. Stoner and W. E., "A mechanism of magnetic hysteresis in heterogenous alloys", *Philos. Trans. R. Soc. London*, **240**, 74 (1947)

[Str] "Struck Innovative Systeme", *http://www.struck.de/*

[Suc54] W. Sucksmith and J. E. Thompson, "The Magnetic Anisotropy of Cobalt", *Proc. R. Soc. London, Ser. A*, **225**, 362 (1954)

[Tan99] T. Taniyama, I. Nakatani, T. Namikawa, and Y. Yamazaki, "Resistivity due to Domain Walls in Co Zigzag Wires", *Phys. Rev. Lett.*, **82**, 2780 (1999)

[Tan00] T. Taniyama, I. Nakatani, T. Yakabe, and Y. Yamazaki, "Control of domain structures and magnetotransport properties in patterned ferromagnetic wires", *Appl. Phys. Lett.*, **76**, 613 (2000)

[Tat04] G. Tatara and H. Kohno, "Theory of Current-Driven Domain Wall Motion: Spin Transfer versus Momentum Transfer", *Phys. Rev. Lett.*, **92**, 086601 (2004)

[Thi05] A. Thiaville, Y. Nakatani, J. Miltat, and Y. Suzuki, "Micromagnetic understanding of current-driven domain wall motion in patterned nanowires", *Europhys. Lett.*, **69**, 990 (2005)

[Thi07] A. Thiaville, Y. Nakatani, F. Piéchon, J. Miltat, and T. Ono, "Transient domain wall displacement under spin-polarized current pulses", *Eur. Phys. J. B*, **60**, 15 (2007)

[Tom02] T. Tomaru, T. Suzuki, T. Uchiyama, A. Yamamoto, T. Shintomi, C. T. Taylor, K. Yamamoto, S. Miyoki, M. Ohashi, and K. Kuroda, "Maximum heat transfer along a sapphire suspension fiber for a cryogenic interferometric gravitational wave detector", *Phys. Lett. A*, **301**, 215 (2002)

[Tsa02] J. L. Tsai, S. F. Lee, Y. D. Yao, C. Yu, and S. H. Liou, "Magnetoresistance study in thin zig zag NiFe wires", *J. Appl. Phys.*, **91**, 7983 (2002)

[Tse06] Y. Tserkovnyak, H. J. Skadsem, A. Brataas, and G. E. W. Bauer, "Current-induced magnetization dynamics in disordered itinerant ferromagnets", *Phys. Rev. B*, **74**, 144405 (2006)

[Uhl09] W. C. Uhlig, M. J. Donahue, D. T. Pierce, and J. Unguris, "Direct imaging of current-driven domain walls in ferromagnetic nanostripes", *J. Appl. Phys.*, **105**, 103902 (2009)

[Ung86] J. Unguris, G. Hembree, R. Celotta, and D. Pierce, "Investigations of magnetic microstructures using scanning electron microscopy with spin polarization analysis", *J. Magn. Magn. Mater.*, **54**, 1629 (1986)

[Van90] T. VanZandt and R. Browning, "Determination of spin-polarized secondary-electron escape depth through oxidation of iron", *J. Appl. Phys.*, **68**, 5835 (1990)

[Van91] T. VanZandt, R. Browning, and M. Landolt, "Iron overlayer polarization enhancement technique for spin-polarized electron microscopy", *J. Appl. Phys.*, **69**, 1564 (1991)

[Van08] A. Vanhaverbeke, A. Bischof, and R. Allenspach, "Control of Domain Wall Polarity by Current Pulses", *Phys. Rev. Lett.*, **101**, 107202 (2008)

[vdB85] H. A. M. van den Berg, "Self-consistent domain theory in soft ferromagnetic media. I. Solenoidal distributions in elliptical thin-film elements", *J. Appl. Phys.*, **57**, 2168 (1985)

[vdB86] H. A. M. van den Berg, "Self-consistent domain theory in soft-ferromagnetic media. II. Basic domain structures in thin-film objects", *J. Appl. Phys.*, **60**, 1104 (1986)

[vdB87] H. A. M. van den Berg and A. H. J. van den Brandt, "Self-consistent domain theory in soft-ferromagnetic media. III. Composite domain structures in thin-film objects", *J. Appl. Phys.*, **62**, 1952 (1987)

[Ved02] E. Y. Vedmedenko, H. P. Oepen, and J. Kirschner, "Microstructure of the spin reorientation transition in second-order approximation of magnetic anisotropy", *Phys. Rev. B*, **66**, 214401 (2002)

[Ver04] N. Vernier, D. A. Allwood, D. Atkinson, M. D. Cooke, and R. P. Cowburn, "Domain wall propagation in magnetic nanowires by spin-polarized current injection", *Europhys. Lett.*, **65**, 526 (2004)

[vG10] J. W. von Goethe, "Zur Farbenlehre", (1810)

[Vog10] A. Vogel, A. Drews, T. Kamionka, M. Bolte, and G. Meier, "Influence of Dipolar Interaction on Vortex Dynamics in Arrays of Ferromagnetic Disks", *Phys. Rev. Lett.*, **105**, 037201 (2010)

[Wan06] R. F. Wang, C. Nisoli, R. S. Freitas, J. Li, W. McConville, B. J. Cooley, M. S. Lund, N. Samarth, C. Leighton, V. H. Crespi, and P. Schiffer, "Artificial spin ice in a geometrically frustrated lattice of nanoscale ferromagnetic islands", *Nature*, **439**, 303 (2006)

[Wea04] R. C. Weast (Editor), *CRC Handbook of Chemistry and Physics 85th edition*, CRC Press (2004)

[Wei09] M. Weigand, B. Van Waeyenberge, A. Vansteenkiste, M. Curcic, V. Sackmann, H. Stoll, T. Tyliszczak, K. Kaznatcheev, D. Bertwistle, G. Woltersdorf, C. H. Back, and G. Schütz, "Vortex Core Switching by Coherent Excitation with Single In-Plane Magnetic Field Pulses", *Phys. Rev. Lett.*, **102**, 077201 (2009)

[Wie94] R. Wiesendanger, *Scanning Probe Microscopy and Spectroscopy: Methods and Applications*, Cambridge University Press (1994)

[Wol06] S. Wolf, D. Treger, and A. Chtchelkanova, "Spintronics: The Future of Data Storage?", *Mrs Bulletin*, **31**, 400 (2006)

[Yam04] A. Yamaguchi, T. Ono, S. Nasu, K. Miyake, K. Mibu, and T. Shinjo, "Real-Space Observation of Current-Driven Domain Wall Motion in Submicron Magnetic Wires", *Phys. Rev. Lett.*, **92**, 077205 (2004)

[Yam06] A. Yamaguchi, K. Yano, H. Tanigawa, S. Kasai, and T. Ono, "Reduction of threshold current density for current-driven domain wall motion using shape control", *Jap. J. Appl. Phys.*, **45**, 3850 (2006)

[Yam07] K. Yamada, S. Kasai, Y. Nakatani, K. Kobayashi, H. Kohno, A. Thiaville, and T. Ono, "Electrical switching of the vortex core in a magnetic disk", *Nat. Mater.*, **6**, 270 (2007)

[Yan07] J. Yang, C. F. Wang, E. L. Hu, and J. E. Butler, "Lift -off process to get free-standing high quality single crystal diamond films and suspended single crystal diamond devices", *Mater. Res. Soc. Symp. Proc.*, **956**, 0956 (2007)

[You06a] C.-Y. You, I. M. Sung, and B.-K. Joe, "Analytic expression for the temperature of the current-heated nanowire for the current-induced domain wall motion", *Appl. Phys. Lett.*, **89**, 222513 (2006)

[You06b] H. Youk, G.-W. Chern, K. Merit, B. Oppenheimer, and O. Tchernyshyov, "Composite domain walls in flat nanomagnets: The magnetostatic limit", *J. Appl. Phys.*, **99**, 08B101 (2006)

[You07] C.-Y. You and S.-S. Ha, "Temperature increment in a current-heated nanowire for current-induced domain wall motion with finite thickness insulator layer", *Appl. Phys. Lett.*, **91**, 022507 (2007)

[Yu07] D. Yu, C. Math, M. Meier, M. Escher, G. Rangelov, and M. Donath, "Characterisation and application of a SPLEED-based spin polarisation analyser", *Surf. Sci.*, **601**, 5803 (2007)

[Zav00] F. Zavaliche, W. Wulfhekel, H. Xu, and J. Kirschner, "Suppression of silicide formation in Fe films grown on Si(001)", *J. Appl. Phys.*, **88**, 5289 (2000)

[Zha04] S. Zhang and Z. Li, "Roles of Nonequilibrium Conduction Electrons on the Magnetization Dynamics of Ferromagnets", *Phys. Rev. Lett.*, **93**, 127204 (2004)

Publications

Published

S. Hankemeier, K. Sachse, R. Frömter, and H.P. Oepen, "Ultrahigh current densities in Permalloy nanowires on diamond", *Appl. Phys. Lett.* **92**, 242503 (2008) [**P6**]

S. Hankemeier, R. Frömter, N. Mikuszeit, D. Stickler, H. Stillrich, S. Pütter, E.Y. Vedmedenko, and H.P. Oepen, "Magnetic ground state of single and coupled Permalloy rectangles", *Phys. Rev. Lett.* **103**, 147204 (2009) [**P3**]

A. Kobs, H. Spahr, D. Stickler, S. Hankemeier, R. Frömter, and H.P. Oepen, "Magnetic energies of single submicron permalloy rectangles determined via magnetotransport", *Phys. Rev. B.* **80**, 134415 (2009) [**P4**]

Accepted

S. Hankemeier, A. Kobs, R. Frömter, and H.P. Oepen, "Controlling properties of vortex domain walls via magnetic seeding fields", accepted for publication in *Phys. Rev. B.*; 19th July 2010 [**P5**]

Submitted

R. Frömter, S. Hankemeier, H.P. Oepen and J. Krischner, "Optimizing a LEED spin polarization analyzer for imaging of magnetic structures", submitted to *Review of Scientific Instruments* in July 2010 [**P1**]

In Preparation

F. Lofink, S. Hankemeier, R. Frömter, and H.P. Oepen, "Long time stability of an optimized SPLEED-detector for magnetic imaging / SEMPA", to be submitted to *Vacuum Science and Technology* in 2010 [**P2**]

C. Tieg, R. Frömter, D. Stickler, S. Hankemeier, A. Kobs, S. Streit-Nierobisch, C. Gutt, G. Grübel, and H.P. Oepen, "Imaging the in-plane magnetization in a Co microstructure by Fourier transform holography", to be submitted to *Appl. Phys. Lett.* in 2010

Acknowledgments

Sincere thanks to all who contributed to this work.
In particular I would like to acknowledge:

Prof. H.P. Oepen for the chance to do research in his group, his encouragement and for the introduction to the world of physics in his lecture during my first term at university in 2002.

Robert Frömter for the excellent supervision of my PhD thesis and his always solid advice during in the last three years.

André Kobs for the brilliant teamwork which was the basis for two shared publications. Ich hofffe, da geht noch was...

Marietta Seifert, Volker Neu and Rudolf Schäfer from Dresden for supplying the $NdCo_5$ samples.

Konrad Sachse, Björn Beyersdorff and Stefan Rößler for the dedication to their Diploma thesae which produced valuable results.

Yulyia Stark for FIB milling of the silicon nitride membranes used in the nanostencil process.

Matthias Hille for his permission to reprint some results of his MOKE investigation of iron thin films.

Nikolai Mikuszeit for supplying OOMMF simulations of coupled rectangles.

Daniel Stickler for valuable suggestions, the common time in office, his choice in music and for repairing the printer.

Hendrik Spahr for valuable discussions and proofreading of the manuscript.

Christian Menk for the experimental introduction to the SEMPA experiment.

Germar Hoffmann for enabling the AFM measurements.

André Drews and Benjamin Krüger for valuable advice concerning the spin transfer torque effect from a theoretical point of view.

Wolfgang Pfützner for technical advise.

everyone else from *Group G* not mentioned by name.

Jesco Topp for the FMR measurements of CoFeSi thin films, general advice, help with the Latex coding and supplying gossip during the weekly squash sessions.